3D Printed FDM Composites: Fabrication, Microstructure and Properties

A thesis submitted in fulfilment of the requirements for the degree of

Doctor of Philosophy

Yiwei Hu

Bachelor of Aerospace Engineering (NPU, China)

School of Engineering

College of Science, Technology, Engineering and Maths

RMIT University

September 2022

DECLARATION

I certify that except where due acknowledgement has been made, this research is that of the author alone; the content of this research submission is the result of work which has been carried out since the official commencement date of the approved research program; any editorial work, paid or unpaid, carried out by a third party is acknowledged; and, ethics procedures and guidelines have been followed.

In addition, I certify that this submission contains no material previously submitted for award of any qualification at any other university or institution, unless approved for a joint-award with another institution, and acknowledge that no part of this work will, in the future, be used in a submission in my name, for any other qualification in any university or other tertiary institution without the prior approval of the University, and where applicable, any partner institution responsible for the joint-award of this degree.

I acknowledge that copyright of any published works contained within this thesis resides with the copyright holder(s) of those works.

I give permission for the digital version of my research submission to be made available on the web, via the University's digital research repository, unless permission has been granted by the University to restrict access for a period of time.

Yiwei Hu

07 September 2022

ACKNOWLEDGEMENTS

This co-tutelle PhD project was supported by RMIT University and NPU University, which included two-year research in Australia and two-year research in China. Without this, I would not have thoroughly enjoyed the valuable opportunity to broaden my horizon and incorporate my overseas experience into my academic research.

I would like to sincerely thank my Senior Supervisor, Distinguished Professor Adrian P. Mouritz for his excellent guidance and support throughout the research project. He is a very knowledgeable, experienced and caring supervisor. He showed me how to be a professional academic researcher, and shaped my capabilities in critically and analytically thinking and solving scientific engineering problems. Professor Mouritz is also very encouraging and patient in helping me to improve my academic writing skills. Without his endless help, I would never have been able to accomplish this PhD project.

I would also like to thank my Associate Supervisor - Dr Raj B. Ladani of RMIT University. He is very supportive, encouraging and patient. He taught me how to get a start on the PhD project, helped me get used to the research process in Australian universities, and consistently provided feedback and advice on my study and life overseas.

I would like to thank my Chinese supervisor - Professor Yazhi Li - for his guidance and academic and financial support in helping me complete the PhD project in China. He is very knowledgeable and patient, and he is a respected academic for his dedication to teaching and guiding students. Without his care and help, I would be unable to continue my research during this hard COVID time.

I would also like to extend my greatest gratitude to my friend Mr Paul Muscat, Technican Office – Composites at RMIT University. He provided excellent technical support throughout the research project. He is experienced, creative, responsible and considerate. I learned a lot from his work and the life experience he shared. His encouragement and enthusiasm gave me a meaningful research and living experience in Australia. I also want to thank my colleagues and friends, especially Dr Jacquelynn Tian, Mr Lloyd John, Mr Nathaphon Buddhacosa, Dr Koranat Pattarakunnan, Mr Huanxin Zhang, Dr Anil Ravindran, Ms Jia-Wun Shih, Dr Reza Omrani, Dr Suraj Suresh Bijjahalli at RMIT, Weiqian Song of the RMIT University Technical Services team, Mary Tomlinson of the RMIT Administration

Team, as well as Ms Minge Duan, Mr Fan Yang, Mr Xuan Yang and Mr Yifan Ma in NPU, for being caring and supportive during my PhD. I also want to appreciate Professor Chao Zhang and his team at NPU for their equipment and technical support of my experimental works in China.

I would like to thank my boyfriend, Jiye Zhang, for accompanying and encouraging me during the final period of my PhD project. His emotional support is crucial for me to overcome the setbacks I suffered during the hard COVID time and complete this PhD thesis. More important, I would like to appreciate my family who have been my faithful supporters whenever I need them. Their understanding and encouragement have helped me through all the difficulties faced during overseas living and my entire academic career. My achievements would not have been possible without the tireless help I have received from my parents and grandparents, to whom I am indebted beyond measure.

TABLE OF CONTENT

LIST OF FIGURE

LIST OF TABLES

SUMMARY

Fused deposition modelling (FDM) is an additive manufacturing process commonly used for the 3D printing of continuous fibre-polymer composites. However, a major limitation of using the FDM process is the relatively low mechanical properties of 3D printed composites compared to materials made using conventional fabrication processes such as vacuum bag resin infusion of fabric composites and autoclave curing of prepreg-based composites. The 3D printed composites have low fibre content and often contain a relatively high volume fraction of voids and polymer-rich regions at the fusion interface between the adjacent filaments in a single ply and between ply layers. The voids can act as geometric stress raisers that can initiate cracks in the polymer matrix phase, resulting in the susceptibility of 3D printed composites to delamination and matrix cracking under load. Furthermore, the FDM process can cause other defects including fibre misalignment and fibre damage that can compromise the dimensional accuracy and mechanical properties of 3D printed composites with intricate shapes.

This PhD project investigates the causes and effects of microstructural damage in 3D printed continuous fibre/polymer composites fabricated using the FDM process. The changes to the microstructure and mechanical properties of continuous fibre filaments used to 3D print composites is investigated at multiple steps of the FDM process. The FDM steps investigated spanned from the stock filament material in the as-received (original) condition, through different stages of the FDM process including heating and extrusion, to the final step involving deposition of individual filaments in the 3D layer-by-layer printing of composites. The study was conducted at the fibre, filament, ply and composite length-scales to gain a complete understanding of the material changes caused by the FDM process. The composite materials investigated in this PhD project were 3D printed using FDM filaments of continuous carbon-polyamide, glass-polyamide and aramid-polyamide, which experience different types and amounts of microstructural and property changes. The expected outcome of the PhD project is to systematically identify the causes of material damage and the resultant reductions in the mechanical properties of continuous fibre/polymer composites during 3D printing using the FDM process.

The literature review chapter in this PhD thesis presents a critical and comprehensive overview of published research into the microstructural and mechanical properties of 3D

printed fibre/polymer composites using the FDM process. Included in the review is an assessment into how these properties are controlled by the 3D printing parameters using the FDM process. The review considers the effects of the FDM process parameters on the microstructure of 3D printed composites. The literature review also reports that the mechanical properties of 3D printed composites can be improved via surface modification of fibres or adding functionalities. The review considers the effect of voids in 3D printed composites, including how their size and content can be reduced by optimising the FDM process. Published research reveals that the mechanical properties of 3D printed composites are determined by the microstructure and print direction of the filaments and the layup direction of the ply layers. A research gap analysis presented in Chapter 2 reveals there is limited understanding of the effect of the multiple stages of the 3D printing process using FDM on the microstructural damage to composites (matrix, fibres, matrix-fibre interface) and the resultant reduction to mechanical properties.

The first two research chapters present experimental investigations into the changes to the microstructural and mechanical properties of FDM filaments using a Markforged® MarkTwo printer during different stages of the FDM process, from the initial feedstock filament material to the final deposition of hot filament on the print build platform. Studies are performed on polyamide matrix FDM filaments containing continuous carbon, E-glass or aramid fibres. The surface of the FDM filament is abraded when it passes through the stages of the FDM machine, and it is shown that this damage can be minimised by modifying the filament feed system in the 3D printer. Damage and breakage to the fibres in FDM filament occurs as it passes through the 3D printing process, with most fibre damage occurring when it is bent through 90^{o} during deposition on the print build platform. The degree of fibre damage and the residual strength of FDM filaments depends on the fibre type. Carbon fibres experience the most damage resulting in the largest loss in filament strength from the FDM printing process. Glass fibres are also damaged during 3D printing, but less than carbon fibres, due to their higher flexibility, fracture toughness and failure strain. Aramid fibres are not broken in the FDM resulting in the smallest loss in mechanical properties, although they are crimped by the FDM process.

The next research chapter presents an experimental investigation into the effect of 3D printing curvature on the microstructure and mechanical properties of FDM filaments containing continuous carbon, glass or aramid fibres. Studies are performed on filaments with

printed curved radii between 1 mm and 30 mm. It is discovered that curved printing using the Markforgered® MarkTwo causes significant deformation and damage to filaments, particularly at small radius values. Filament folding and twisting occurs at tight curvatures that cause fibre breakage in the carbon- and glass-reinforced filaments due to the relatively low bending fracture strain of these fibres. Some carbon fibres also pull away from the main filament, with longitudinal tearing of the polyamide matrix between fibres. The aramid fibre filament sustains no fibre breakage during curved printing due to its higher flexibility and failure strain. The effect of fibre breakage and matrix damage caused by curved filament printing on the tensile properties of the 3D printed filaments is determined.

The microstructure and tensile properties of 3D printed unidirectional composites made via the layer-by-layer deposition of carbon, glass or aramid filaments studied in the previous chapters are investigated. The 3D printed composites are compared against equivalent composites containing the same filaments, but fabricated using hot moulding which does not cause the damage of the FDM process (e.g. fibre breakage, voids). Compared to the hot moulded composites, fibre damage caused by the FDM process is a crucial factor in reducing the tensile properties of 3D printed carbon-polyamide and glass-polyamide composites. In addition, cracks and elongated voids occur at the fusion interface between adjacent printed filaments and ply layers, contributing to the lower tensile properties of 3D printed composites.

The final research chapter presents an investigation into the microstructure and mechanical properties of 3D printed hybrid continuous fibre/polymer composites made using the FDM process. The hybrid composites were 3D printed using the combination of carbon + glass or carbon + aramid filaments. The composites were 3D printed with the carbon layer sandwiched between or separated by glass or aramid layers, and the carbon layer ratio was varied between 11% and 50%. Fibre hybridisation can increase the ultimate failure strain of the carbon fibre reinforced layer in 3D printed composites. The measured tensile modulus values for the hybrid composites agree with predictions using rule-of-mixtures. The tensile strength properties of the 3D printed hybrid composites are similar to the 3D printed non-hybrid glass-polyamide or aramid-polyamide composites, with the carbon fibres having little influence. The lower-than-expected tensile strength of the 3D printed hybrid composites containing carbon fibres is attributed to the poor interfacial quality between the different fibre layers and their lower failure strain.

The main conclusions and research findings of the PhD project are presented in the last chapter to the thesis, along with several recommendations for further research into 3D printed composites made using the FDM process.

CHAPTER 1: INTRODUCTION

1.1 Background and Motivation

Fibre-reinforced polymer composites have wide-ranging applications including in aerospace, automotive, marine, construction and sports goods due to their high strength-to-weight ratio, corrosion resistance, good design flexibility and other excellent properties. However, the high costs of materials and manufacturing are limiting the take-up of continuous fibre reinforced polymer composites in some sectors when price is a critical factor in materials selection. For instance, expensive moulds are often needed to form and shape composite components using conventional manufacturing processes such as resin transfer moulding [1-8]. These processes often require long production cycle times for heating, forming and curing of the composite material. Many processes also generate significant material waste, which can be a major problem when using expensive carbon fibres. Therefore, new manufacturing processes which can lower the cost, increase production time and reduce waste are desired.

Additive Manufacturing (AM) has emerged as an alternate processing method for composites with the potential of being cost-effective by enabling rapid prototyping with high precision geometry, and simultaneously reducing material waste. AM technologies are revolutionising many manufacturing industries for producing next-generation high-performance materials [9]. AM refers to a series of manufacturing processes defined as 'discrete – accumulation', i.e., building parts by joining materials, usually layer-by-layer, directly from computer design data to a real product without tooling and often no need for post-fabrication machining. AM results in much less waste and larger internal shape flexibility [10] without the need for expensive tooling and moulding. In some instances, the duration of the design and fabrication process involving AM has been reduced from weeks to several hours [11].

Fused Desposition Modelling (FDM) is an AM technique for the 3D printing of polymer matrix composites containing continuous or discontinuous fibres. The FDM process is a filament-by-filament and layer-by-layer printing process that makes it easier to design and fabricate composite parts with intricate internal geometries and shapes, which would otherwise be challenging or impossible to produce using conventional composite

manufacturing techniques. For example, when mechanical fastening is needed to reinforce composite structures made using conventional processes then the notches and holes require machining processes such as drilling and cutting. Because continuous fibres in fabrics or prepregs are aligned in specific directions, such as the 0° and 90° orientations, it is not practical to deflect the fibres around where cut-outs and holes need to be located. In contrast, the placement of fibre reinforcements using 3D printing can be optimised to follow the desired path and thereby reduce or eliminate the need for drilling and machining of holes.

The FDM method is one of the most common AM techniques for 3D printing continuous fibre-polymer composites. Compared to 3D printed unfilled polymers and short fibre-polymer composites, the continuous fibre reinforced polymer composites made using the FDM process have superior strength, stiffness and other mechanical properties. However, the mechanical properties of 3D printed continuous fibre composite materials are often less than that expected based on rule-of-mixtures (ROM), indicating that the properties are not optimum. For example, **Figure 1-1** presents published tensile property data for 3D printed fibre/polymer composites measured in the filament printing direction, and the strength and modulus are lower (often much lower) than expected from ROM and inferior to composites made using conventional processes such as RTM or autoclave curing.

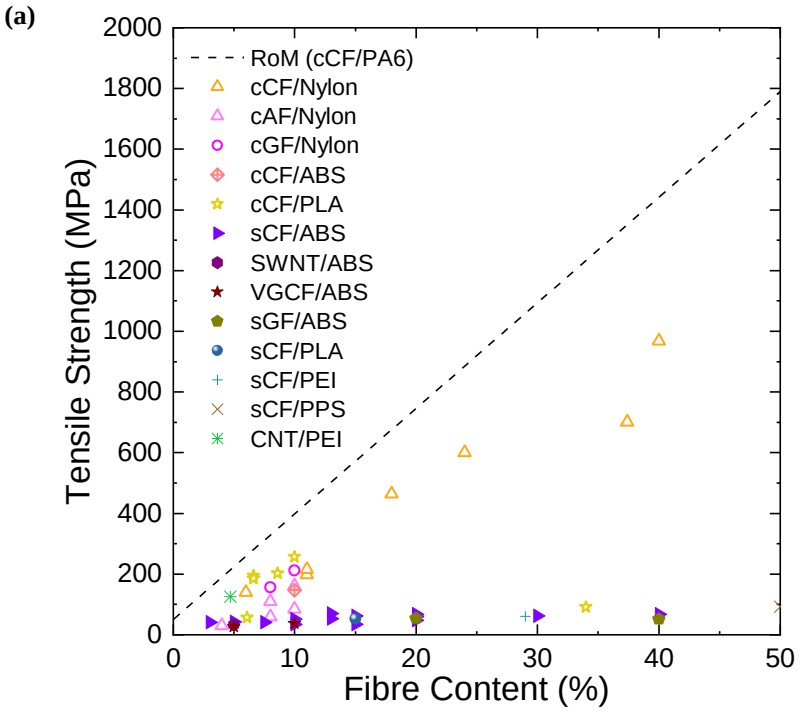

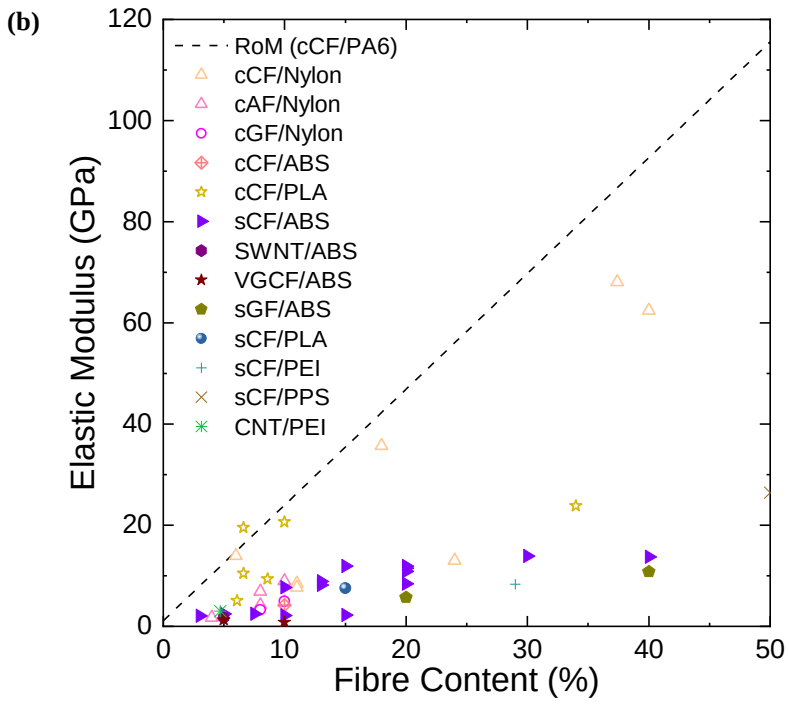

Figure 1-1 *(a) Tensile strength and (b) Young's modulus of 3D printed composites using the FDM process. The dashed line is the calculated values of a carbon-polyamide composite based on rule-of-mixtures [12-30]. Abbreviation: c - continuous, s - short, CF - carbon fibre, GF - glass fibre, AF - aramid fibre, SWNT - single walled carbon nanotube, VGCF – vapor grown carbon fibre, CNT – carbon nanotube.*

The relatively low fibre content, high porosity level and non-uniform microstructure are the most commonly reported reasons for the lower-than-expected mechanical properties of 3D printed continuous fibre composites. The stock filament used in the FDM process consists of continuous fibre and thermoplastic matrix phases. The required viscosity range of the filament material to avoid nozzle clogging in the FDM machine during 3D printing limits the fibre content to ~10-30%. Although higher fibre contents have been achieved [18, 21, 28, 31] through filament modification and printing device adjustment, the fibre fraction of FDM printed composites are still below that of conventionally manufactured composites (V_f ~50%-60%). Additionally, the lack of high consolidation pressure applied to the filaments during deposition on the print build platform of the FDM machine often leads to a non-uniform microstructure to the 3D printed composite, with localised clusters of fibres, polymer-rich regions, and voids of varying shape, size and location [14, 16, 23, 28, 29, 32]. This microstructural inhomogeneity in 3D printed composites can result in large scatter in the mechanical properties. Although efforts have been made to optimise the FDM printing parameters (e.g. print temperature, filament feed rate) and to improve the feedstock material

quality, 3D printing composites with mechanical properties comparable to composites fabricated using conventional processes remains a challenge. Therefore, exploring the FDM process-induced damage on the microstructure and mechanical properties of the filaments – the basic building blocks of 3D printed composites - and determining the relationship between filament damage and the microstructure and properties of 3D printed composites is important.

1.2 Research Aims and Objectives

This PhD project focuses on the causes of damage to continuous fibre/polyamide filaments and composites and the resultant reduction of the mechanical properties when 3D printed using the FDM process. The project is conducted at multi-length scales including the individual fibre level, filament level, ply level and coupon level when continuous fibre composites are 3D printed using a MarkForged® FDM printer. The Markforged® MarkTwo printer is one of the most developed desktop printers for 3D printing continuous fibre polymer composites, which is favoured by small and medium-sized businesses and individuals for prototype designing and mould manufacturing. The Markforged® company provides guaranteed quality of the feedstock materials for 3D printing and affordable prices of the desktop series folders that are lower than other industrial-grade printers for fibre-polymer composites. Therefore, it is worth investigating the effect of the printing process using the MarkTwo printer (the latest model) on the mechanical properties of the 3D printed composites. The research findings from this PhD project can be used for developing further desktop printers and achieving their potential in fabricating high-quality products. The Markforged desktop printers do have many restrictions on varying printing conditions. However, these limitations are necessary for successfully 3D printing the filament materials provided by the Markforged® company. Furthermore, a constant printing condition can exclude the device error and improve the credibility of the results in this work that the damage is caused by the printing process stages.

In achieving the aim of the PhD project, the research work will address the following specific objectives:

- Investigate the effect of the FDM 3D printing process stages on the microstructural and mechanical properties of continuous fibre (carbon, glass and aramid)-polyamide FDM filaments.

- Investigate the effect of 3D printing curvature radius on the microstructure and mechanical properties of continuous fibre (carbon, glass and aramid)-polyamide FDM filaments.
- Investigate the effect of filament damage caused by the FDM process on the microstructure and mechanical properties of continuous fibre (carbon, glass and aramid)-polyamide composites.
- Investigate the effect of layer ratio and layer distribution on the microstructure and mechanical properties of 3D printed hybrid continuous fibre (carbon + glass and carbon + aramid)-polyamide composites produced using the FDM process.

This PhD project aims to provide new fundamental insights into the relationship between the FDM process-related microstructure and the lower-than-expected mechanical properties of 3D printed continuous fibre/polymer composites. The outcome and significance of this project reveal the opportunities for the FDM process modification to reduce the fibre damage and thereby enable the 3D printing of continuous fibre composites with improved mechanical properties. Because this study is focus on the stages of the 3D printing process, the effects of different process variables including printing speed and temperatures are not examined by mimicking the Markforged® printer process.

1.3 Thesis Outline

Chapter 2 of this thesis presents an overview of published research into the FDM process to 3D print fibre/polymer composites. The first part of the literature review explores the advantages and limitiations of the FDM process in 3D printing continuous fibre/polymer composites compared to other 3D printing methods. The chapter also presents a comprehensive review of published research into the microstructural and mechanical properties of 3D printed composites, and how these are affected by the printing process conditions. Key gaps in the published research on the fabrication, microstructure and properties of 3D printed composites are identified.

Chapters 3 and 4 present experimental research studies into the damage caused to continuous fibre filaments during different stages of the FDM process, from the initial feedstock filament material to the final 3D printed filament to determine the causes for the low mechanical properties of 3D printed composites. Chapter 3 investigates the reductions in the tensile and compressive properties of carbon-polyamide composite filaments caused by

the different stages of the FDM process. The causes of the damage and resultant reductions to the mechanical properties of the FDM carbon fibre filament during 3D printing are identified. The study also investigates a modification to the FDM printer to reduce fibre damage caused by the filament feeding gears and thereby minimises the reduction to the tensile properties. Chapter 4 follows the research work presented in Chapter 3 to assess the effect of the different FDM stages on the microstructure and mechanical properties of continuous glass-polyamide and aramid-polyamide filaments.

Chapter 5 presents an experimental investigation into the effect of 3D printing curvature on the microstructural and mechanical properties of FDM filaments. The study was conducted on polyamide-based filaments containing continuous carbon, glass or aramid fibres that were 3D printed as curved filaments with different radii between 1 mm and 30 mm. The causes of the curvature-induced damage to the FDM filaments are identified, and the effect of the damage on the tensile properties of the filaments printed at different radii is determined. The limits on the maximum curvature that can be applied to FDM filaments during 3D printing to avoid damage and property loss are identified.

A study is presented in Chapter 6 into the microstructural and mechanical properties of the 3D printed continuous fibre/polymer composites using the FDM process. A comparative assessment between 3D printed composites and composites made using hot moulding containing the same FDM filaments of carbon-polyamide, glass-polyamide and aramid-polyamide composites is conducted. The hot moulded composites have the same material composition as the 3D printed composites, but do not contain FDM-induced damage (e.g. fibre breakage, voids, cracks). The tensile properties and fracture mechanisms of the 3D printed and hot moulded composites are compared, and the study identifies the effect of the microstructural defects on the tensile properties of 3D printed composites.

Chapter 7 presents an investigation into the mechanical properties of 3D printed hybrid composites made using the FDM process. The carbon fibre/polyamide layers in the 3D printed hybrid composites were sandwiched between or separated by glass or aramid fibre/polyamide layers. The study determines the effect of the carbon layer ratio and layer distribution on the tensile properties of 3D printed hybrid continuous fibre/polymer composites. The hybridising effect on the tensile modulus, failure stress and failure mode of the 3D printed composites are determined. The study also evaluates the efficiency of using

the FDM process to fabricate the hybrid continuous fibre/polymer composites through normalising the tensile properties by the density and cost of materials.

Chapter 8 summarises the major research findings and conclusions of the PhD project. Several recommendations for future research work into 3D printed composites to deepen further our understanding of these materials and the FDM process are given.

CHAPTER 2: LITERATURE REVIEW

The initial concept of 3D printing continuous fibre composites is generally attributed to Coeur d'Alene, CEO of Continuous Composite®, and it is based on the stereolithography (SLA) process [33]. The first published research study on 3D printed continuous fibre-reinforced composites, which used the FDM process, was reported in 2016 by Matsuzaki et al. [20]. Due to a rapid rate of innovation and the diverse amount of research in the field of 3D printing of polymer composites using the FDM process, it is challenging to provide a comprehensive and wide-ranging review of the field. There are many review papers that discuss the mechanical properties, applications, opportunities and challenges of FDM printed composites [9, 24, 34-37].

This chapter presents a literature review focused on state-of-the-art 3D printing using the FDM process and the mechanical properties of FDM-printed continuous fibre composites. The review focused on published research related to 3D printing processes, microstructure and mechanical properties of continuous fibre composites. The first part of this literature review provides an overview of the different AM processes used to manufacture continuous fibre composites, with a focus on the FDM process. In the following two parts, the mechanical properties of FDM-produced continuous fibre-polymer composites as well as the methods used for maximising the properties of these materials are reviewed. This review also identifies key research gaps that need to be addressed to solve the research problems being investigated in this PhD project. In the final section, the advantages of hybrid composites are presented as a reference for widening the novel application of the FDM process.

2.1 Overview of 3D Printing Techniques for Continuous Fibre-Polymer Composites

Parts fabrication and properties of polymer composites made using AM can vary based on different process method, which includes binder jetting, material jetting, direct energy deposition, powder bed fusion, sheet laminations, material extrusion and vat photo-polymerisation, as per ASTM International Technical Committee F42 on AM technologies [38]. The last three categories can be used to produce continuous fibre-reinforced polymer composites, which are discussed in this section.

2.1.1 Vat photo-polymerisation

Vat photo-polymerisation selectively cures liquid photo-polymer in a vat using ultraviolet (UV) light. Stereolithography (SLA, **Figure 2-1**) is a vat photo-polymerisation process used for the 3D printing of polymer composites with continuous fibre bundles or fibre mats [39]. The choice of materials is limited by the curing process for SLA, and the polymers are usually epoxy- or acrylic-based. The addition of continuous fibre reinforcements is achieved via two methods: (i) manual laying [40, 41] and (ii) incorporation fibre laying [42]. In the manual laying method, the continuous fibre tows or mats are placed manually on the build platform and then impregnated with the photosensitive resin. Once cured, fresh fibre tows or mats coated with resin are added successively on top to manufacture composites with multiple fibre layers. In contrast, incorporation fibre laying enables an in-situ addition of fibre tows during the process. It has been reported that the addition of continuous fibre promotes a 1.5x to 3x improvement to the tensile properties of the printed pure polymer [39]. However, the inclusion of fibre tows in the SLA process can lead to incomplete resin curing due to scattering and attenuation of the UV radiation, causing poor fibre-matrix bonding and relatively low matrix properties [41]. The continuous fibre volume content that can be achieved in the composites produced using this process is typically limited to less than ~20%. Furthermore, improper placement of the fibres may cause air entrapment, thereby reducing the printing resolution and weakening the interlayer properties. Some efforts have been made to improve fibre/matrix interfacial bonding via thermal treatment and post-UV curing [41, 42]. However, regions with uncured (liquid) polymer cannot be completely eliminated due to the UV blocking effect of the fibres. Additionally, post-curing of these parts can lead to internal stresses which can cause shrinkage and warpage of the printed composite [43].

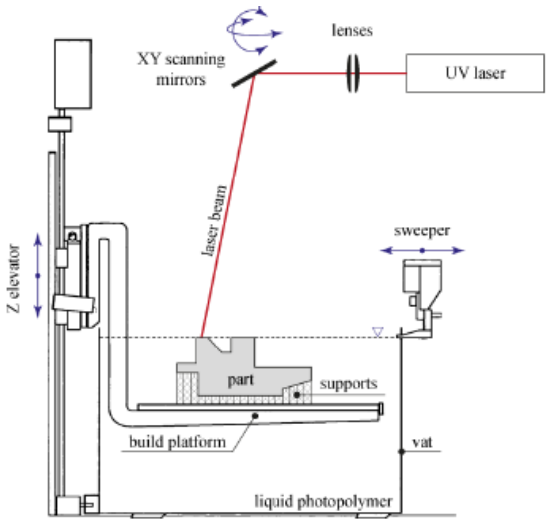

Figure 2-1 *Scheme of the SLA process [38].*

2.1.2 Sheet lamination

Sheet lamination (SL), as the name implies, bonds sheets of material together to form the composite product [44]. The material used in SL is in the form of either prepreg sheet, fibre mat or any other fibrous preform which makes it self-supporting. SL is based on two processes: laminated object manufacturing (LOM) and composite-based additive manufacturing (CBAM). LOM is a commercial process used to make full-scale models and prototypes. The sheets of heat-activated material are laser cut, stacked layer-by-layer, and then all the layers are consolidated using adhesive, pressure and heat to form a final composite part [45]. The fibre content of composites produced using LOM can be relatively high. For example, using prepreg sheets containing 55 vol% unidirectional E-glass fibres in an epoxy matrix, a study [46] reported tensile and flexural strengths of 716 MPa and 1.19 GPa, respectively, for the LOM composite. However, the quality and microstructure of the composites are dependent on a combination of factors including the adhesive type, sheet thickness and consolidation pressure.

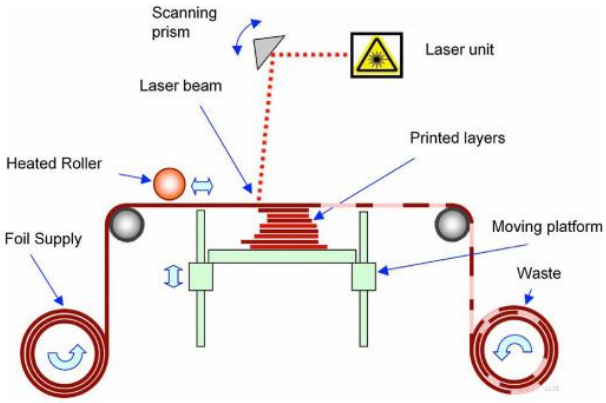

Figure 2-2 *Scheme of the LOM process [47].*

In the CBAM process, which is different from the LOM, the composite structure is controlled by selective deposition of the adhesive [48]. An aqueous-based solution is first deposited on each fibrous sheet layer using an injection method. Thermoplastic powder is subsequently added onto the sheet which adheres to the aqueous solution. The excess matrix powder is removed, and the sheets are stacked layer-by-layer, followed by compression and heating in an oven to fuse the fibres and polymer matrix in the multiple sheets. The consolidated part is then subjected to finishing processes including machining, sanding, etc to achieve the desired form and dimensional tolerance of the final product [48].

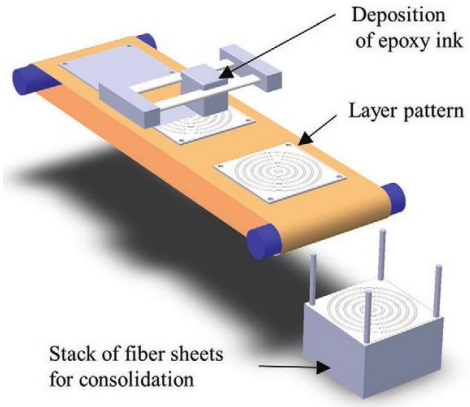

Figure 2-3 *Scheme of the* CBAM *process [9].*

2.1.3 Material extrusion

In material extrusion (ME), a filament, which is either in a semi-solid or soft paste-like state, is selectively deposited through the nozzle onto a print bed. Fused deposition modelling (FDM, **Figure 2-4c, d**) is a commonly used ME process to melt, extrude and bond the filament materials in a filament-by-filament and layer-by-layer process. ME-based

processes are popular for their relatively high printing speed, compatibility with a wide variety of materials, and low-cost of printers compared to other AM processes [49]. In general, the FDM process uses a thermoplastic as the matrix phase since they can be easily converted from a solid filament to a soft molten paste-like state through rapid heating at the desired temperatures, followed by rapid cooling upon contact with the print bed which facilitates the reshaping and layer-by-layer build-up of the part. Two methods have been developed for the FDM process to add the continuous fibre reinforcements to the polymer and realise the fabrication of 3D printed composites, which are (i) in-situ fusion [20, 50-54] and (ii) extrusion of pre-impregnated FDM filament [23, 27-30, 32, 55-60].

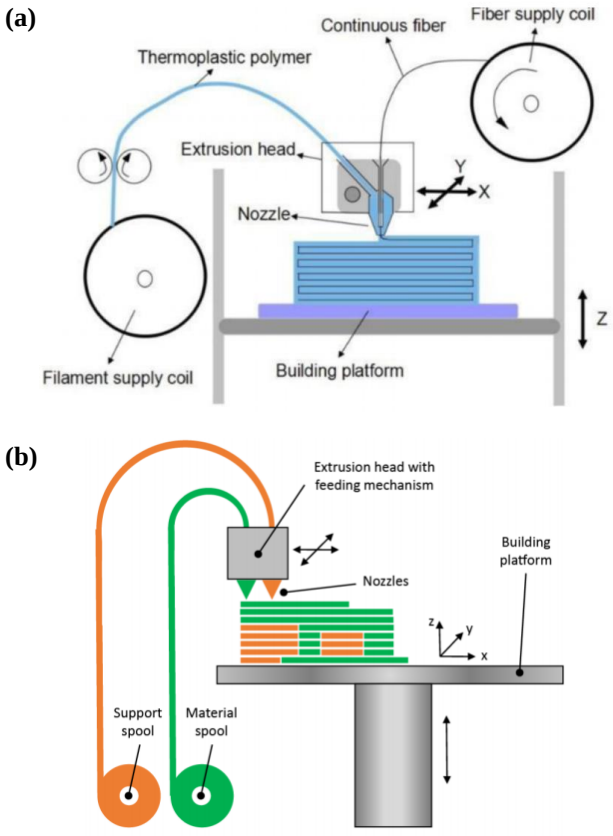

Figure 2-4 *Schemes of the (a) FDM in-situ and (d) FDM pre-impregnated processes [22, 47].*

When using the in-situ fusion process, the viscosity of the polymer and the material feed speed can affect both the volume content and distribution of the fibres [61]. In-situ fusion can fabricate functionally-graded composite parts by varying the material systems and fibre content during deposition. In comparison, the utilisation of commercial FDM filaments provides a more controlled material quality in terms of fibre content and orientation.

The Markforged® desktop printer is the first commercially available 3D FDM printer, and it uses thermoplastic impregnated fibre reinforced filaments for printing composite parts. It has separate printing nozzles for the thermoplastic matrix and pre-impregnated fibre filaments. The filaments are fed through the Bowden mechanism which uses a set of gears to force them into the FDM printer nozzle, where they are rapidly heated to ~260°C to soften the thermoplastic matrix. As the filaments exit the nozzles, they come in contact with the nozzle tip which simultaneously heats them to the desired deposition temperature and compresses them into a flat ribbon on the print bed to the FDM machine. This deposition process promotes matrix fusion between adjacent printed filaments/layers. The continuous fibre composites printed using the FDM process can have tensile properties about five times higher than the unreinforced polymer [27]. However, the fibre loading that can be achieved using FDM process is generally limited to 10-30% due to the clogging of the nozzle that occurs at higher fibre loading.

2.2 Physical and Mechanical Properties of Continuous Fibre-Polymer Composites Produced by FDM Process

The quality, dimensional accuracy, microstructure and properties of composite parts produced using the FDM process depend on many factors which can be generally classified into two groups: (i) material parameters and (ii) printing parameters.

2.2.1 FDM material parameters

The FDM process uses thermoplastics (rather than thermosets) as the matrix phase since they can be melted and re-solidified at the high rates needed for 3D printing. Thermoplastics such as PLA, ABS, polyamide and phosphorylcholine [62-67] are often used. For high temperature applications, thermoplastics such as PEEK [68-70], PEI and UL-TEM1000 are used, but they require higher FDM processing temperatures. The most commonly used continuous fibre reinforcements are carbon, glass and aramid [27, 29, 55-58, 71], while other reinforcements such as natural fibres are rarely used [72]. The flexibility of the FDM process offer the functionality to print hybrid continuous fibre reinforcement materials with a combination of carbon, glass and/or aramid [73].

The mechanical properties of FDM continuous fibre composites are superior to the neat polymer or short fibre-polymer composites with an equivalent fibre content. For

example, Matsuzaki et al. [20] reported that continuous carbon fibre/PLA manufactured using the in-situ fusion FDM process had a tensile strength that was 6 times higher than the unreinforced PLA polymer. As another example, continuous carbon fibre reinforced polyamide fabricated using pre-impregnated FDM filaments achieved 12 fold increase in the flexural strength of neat PA [74]. Tensile strength values for FDM continuous fibre composites comparable to some aluminium alloys have been reported [21].

The commercial pre-impregnated FDM filament consists of a thermoplastic matrix and unidirectional continuous fibres, as shown for example in **Figure 2-5**. The as-received FDM filament has a circular-like cross-section with continuous fibres dispersed in the matrix phase. The filaments often show material inhomogeneity with fibre clusters and polymer-rich regions, and micro-voids can occur along or near fibre/matrix interfaces. The selected fibre and polymer must be compatible physically (good wettability of polymer to fibre), chemically (no chemical reaction occurs between fibre and polymer) and thermally (similar thermal expansion coefficient of fibre to polymer) [75].

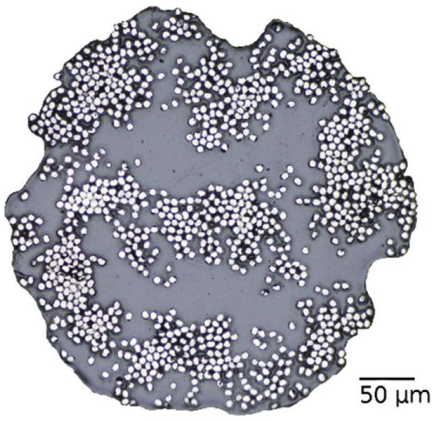

Figure 2-5 *Cross-section of an as-received FDM filament consisting of continuous carbon fibre and polyamide matrix [58].*

Limited research has been reported on the use of different materials and additives for improving the mechanical properties of FDM printed fibre-polymer composites. Additive materials are commonly used in 3D printed composites reinforced with short fibres or fillers to control the rheological and/or thermal properties. A lower melt temperature and higher glass transition temperature (T_g) and degradation temperature is ideal [76, 77]. In contrast, fibre surface treatment is an alternative for improving the fibre/matrix interfacial strength in 3D printed continuous fibre polymer composites. Studies have reported an improvement in the bond strength by replacing the epoxy-based sizing commonly applied to carbon fibres

with a more chemically compatible thermoplastic-based sizing [21, 67, 78]. Alternatively, Luo et al. [79] used plasma treatment of carbon fibres before the dry fibre bundle was impregnated with PEEK to form an FDM filament. Lou and colleagues measured an improvement to the interfacial bonding between the carbon fibres and PEEK matrix due to the plasma treatment, which also reduced micro-voids formed along the fibre/matrix interface (void content decreased from 4.6% to 3.0%) and thereby improved the interlaminar shear strength (ILSS) of the 3D printed composite, as shown in **Figure 2-6.**

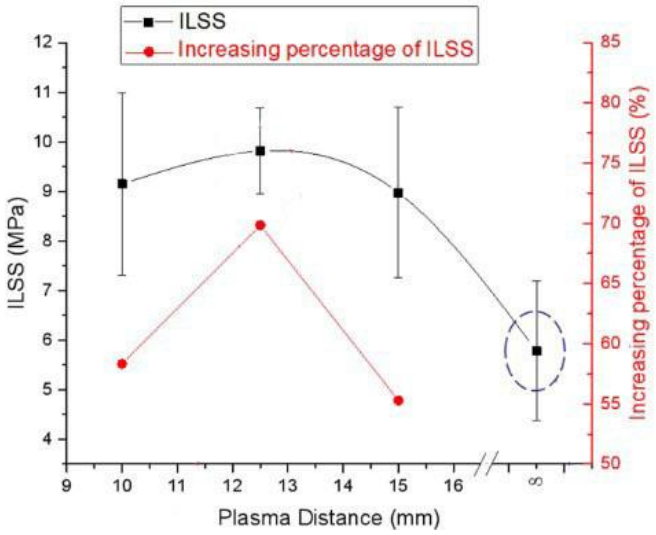

Figure 2-6 *Effect of plasma treatment on the ILSS of 3D printed CF/PEEK composite. Data point in the circle is the composite without plasma treatment [79].*

2.2.2 FDM printing parameters

The FDM process has the flexibility to adjust multiple printing parameters to control the microstructure and mechanical properties of 3D printed composites, and significant effort have been dedicated to this research topic as reported in numerous studies in the literature. The printing parameters can be classified into three types: environment, process and equipment.

Humidity is one of the most important environmental parameters, as the moisture sensitivity of the thermoplastic polymer matrix could limit the application of 3D printed continuous fibre-polymer composites, especially in environments with frequent changes in temperature and moisture. It has been reported that moisture-induced orthotropic hygroscopic swelling can cause mechanical property degradation in the direction transverse to fibres in a unidirectional 3D printed composite, as shown in **Figure 2-7** [58]. When employing the

moisture-sensitive polymer as the matrix to the FDM filament, specimens with higher resin content are more susceptible for application in humid environments.

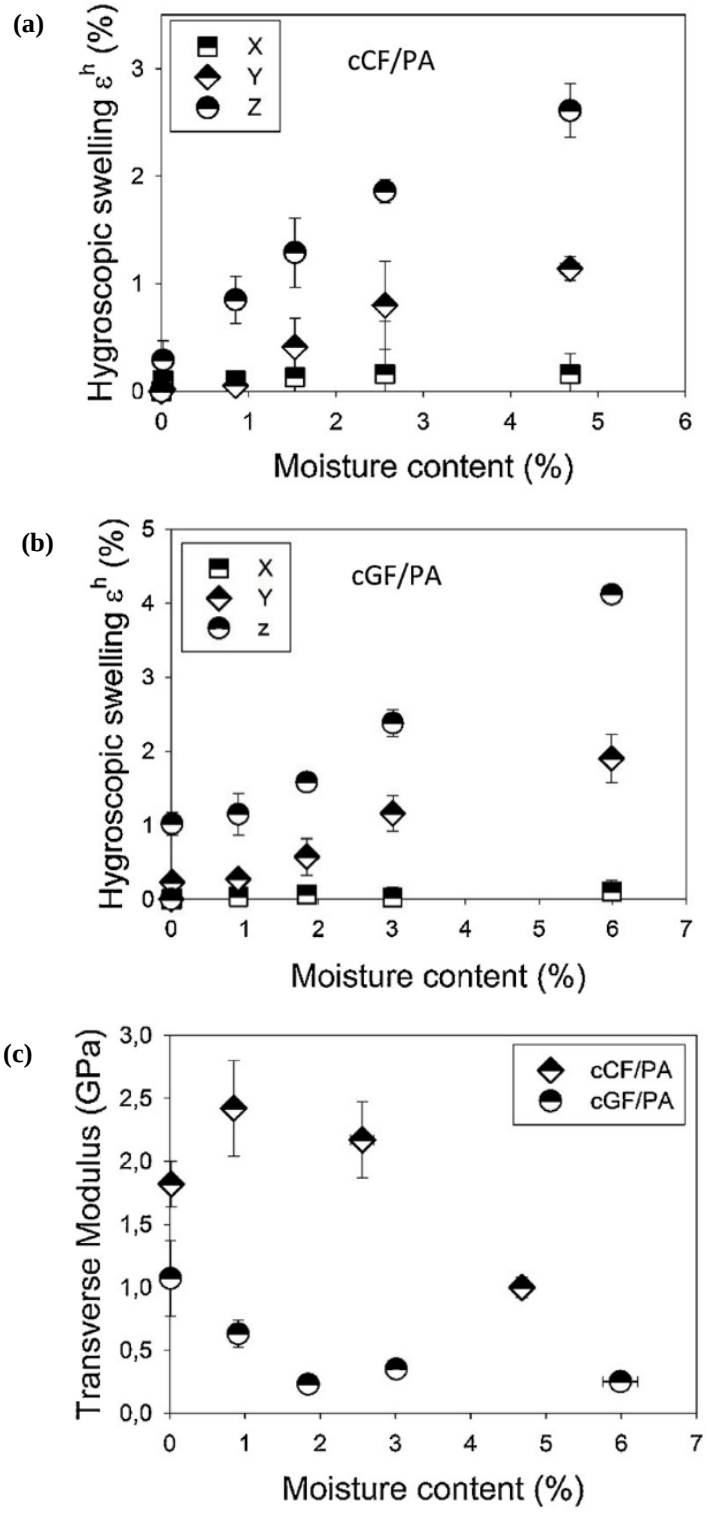

(d)

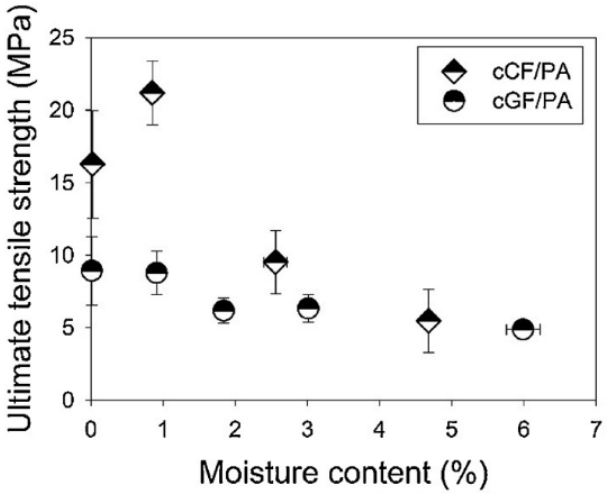

Figure 2-7 *Hygroscopic swelling (a, b), transverse tensile modulus (c) and ultimate strength (d) of continuous CF/PA and continuous GF/PA, respectively, as a function of moisture content. The moisture content of the tensile specimen was controlled by the relative humidity of a saturated solution in the storage chamber [58].*

Process parameters include resin infill pattern (e.g. rectangle, hexagon, triangle, etc) and density (i.e. percentage coverage), printing direction and build orientation. The infilled resin is the matrix material deposited within the outer contour of a printed part to maintain the overall shape of the structure; with examples shown in **Figure 2-8**. The infill pattern controls the amount of filament material being added to the part which in turn governs the mechanical properties of the 3D printed composite [80-83]. For example, Mei et al. [54] reported that polyamide parts made using a rectangular infilled pattern have higher tensile properties at low fibre content compared to the hexagonal or triangular infilled patterns, as shown in **Figure 2-9**. This is possibly due to the high load-bearing capacity of the rectangular infilled structure in the longitudinal direction. Pertuz et al. [84] reported that the triangular 20% infill pattern exhibits better energy dissipation and improved fatigue properties of 3D printed carbon-polyamide composite compared to triangular 50% and hexagonal infill patterns. Additionally, the material costs, weight of the printed structure, and printing time should also be considered [85].

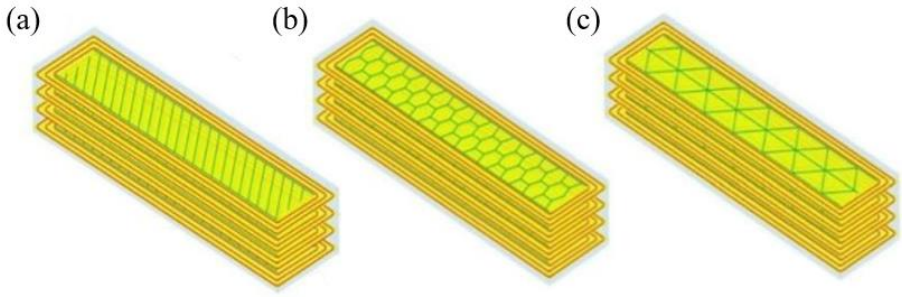

Figure 2-8 *3D printed composite specimens with concentric fibre rings, fibre layers, and various complex polyamide in-fill of (a) rectangular, (b)hexagonal and (c) triangular filled patterns [54].*

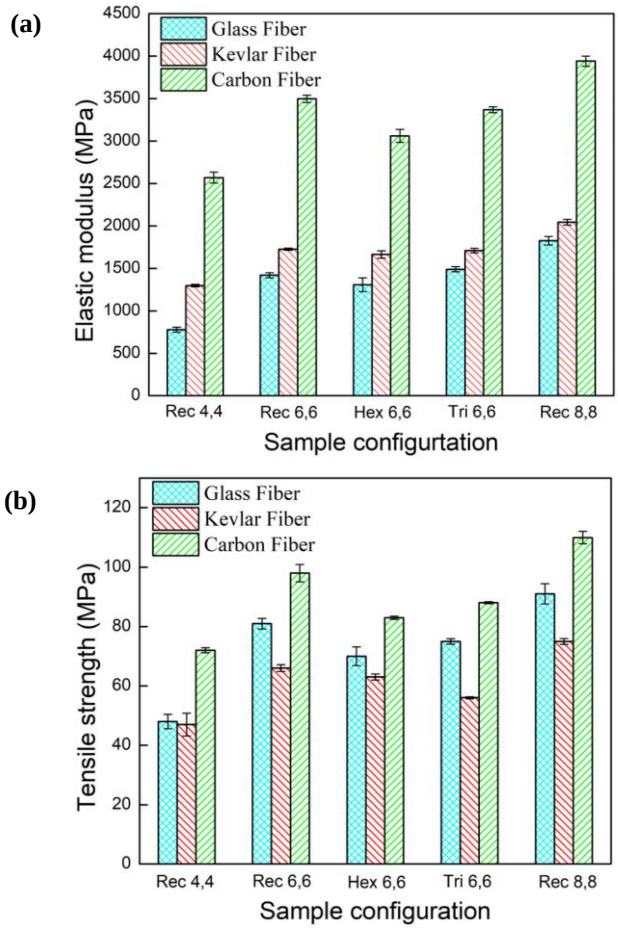

Figure 2-9 *(a) Tensile modulus and (b) tensile strength of 3D printed carbon-, glass-, and Kevlar-polyamide composites with different polymer infilled patterns. 'Rec', 'Hex' and 'Tri' are rectangular, hexagonal and triangular infilled patterns, respectively. The first number is the number of fibre rings in the layer. The last number is the number of layers in the printed composite. The carbon-polyamide composite has 32 layers in each sample while the glass and Kevlar composites have 40 layers [54].*

Due to the layer-by-layer building process where the filaments can only be laid in the in-plane direction, 3D printed composites exhibit anisotropic microstructural and mechanical

properties and are susceptible to damage in the through-thickness direction. The optimum design can be achieved by maximising the content and placement of the fibre reinforcement and their orientation. This can be achieved by varying the print direction (i.e. filament deposition direction and layer build-up direction) and increasing the fibre content (i.e. the number of fibre filaments in a ply and/or the number of fibre layers in a part). **Figure 2-10** shows schematics of specimen conditions with different 3D printing build orientations. Take a dog-bone shaped specimen as an example: 'flat' is the condition of a composite laid-up in the thickness direction; 'on-edge' is laid-up in the width direction; and 'upright' is in the length direction. Caminero et al. [59] reported that the glass-polyamide 'on-edge' sample exhibited the highest Charpy impact toughness of the three build orientations. High performance sandwich composite parts can also be created by depositing fibre reinforced layers on the top and bottom surfaces of a porous polymer-based core with an infill pattern. Fibre orientation is another key factor controlling the mechanical properties, which is similar to the ply orientation of traditional fibre-reinforced composites. For instance, Justo et al. [28] showed that the tensile strength of a 3D printed [90°] glass-polyamide composite was only 1/60 that of the [0°] composite.

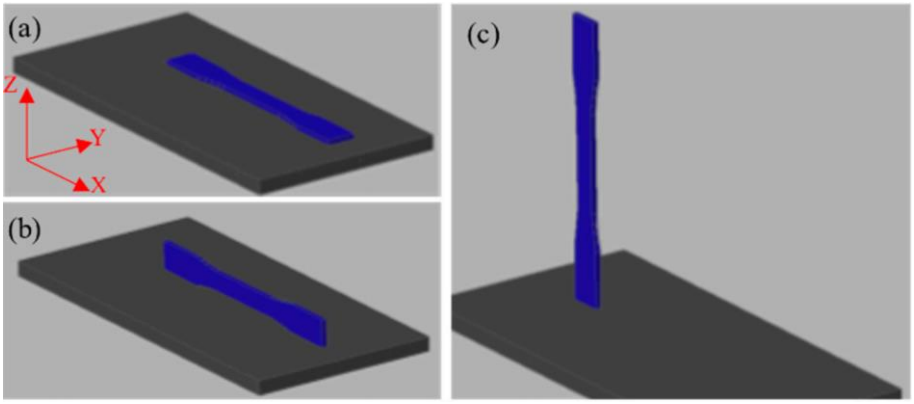

Figure 2-10 *Building orientation definitions: (a) flat, (b) on-edge, (c) upright [86].*

Equipment parameters are related to the FDM printer settings, including filament feeding speed, printing speed, nozzle temperature, build platform temperature, etc. When 3D printing with continuous fibre filaments using the FDM process, the printing speed and filament feeding speed should be set at the same value for successful printing. The printing speed is expected to have limited influence on the mechanical properties. At present, however, there are no published studies into the effect of printing speed on the mechanical properties of 3D printed composite materials using impregnated fibre filaments. It is expected that low

printing speed can prolong the contact time of the melted filament to the deposited material and thereby promote adhesive bonding, however it will reduce the production rate and thereby increase the part cost. When employing the in-situ fusion process, the optimum combination of printing and feeding speeds is critical for achieving complete melting of the polymer to promote impregnation of the fibre tows, which will in turn controls the matrix-to-fibre ratio in a deposited layer and the fibre distribution throughout the printed composite structure.

The nozzle temperature, which can also be referred to as the material extrusion temperature, depends on the T_g and melt temperature of the polymer matrix. The heat distribution in printed filaments is illustrated in **Figure 2-11**. A freshly deposited filament with high temperature can heat the previously laid-up filaments through conduction. Enough heat energy combined with low polymer viscosity allows adjacent filaments to fuse, and the polymer chains can intermingle in the fusion zone before the polymer matrix cools. An optimum nozzle temperature is required to allow the polymer matrix to the filament to soften and fuse to the previously deposited filaments in a layer without degrading the polymer. During printing, heat conduction through the deposited layers can enhance the bonding between adjacent filaments and layers [87]. In addition, the printing temperature can affect the chemical structure of the polymer matrix. It is reported that increasing the print temperature increases the crystallinity of the printed PLA (due to the faster cool-down rate) and thereby increases the tensile strength [62]. However, excessively high temperatures can lead to excessive and rapid flow of the melt polymer through the nozzle thereby compromising the accuracy of the printed geometry of continuous fibre-polymer composites [64]. Also, Ning et al. [87] reported that a completely melted state of the polymer could increase the void content in the printed material, which can reduce the strength of printed parts.

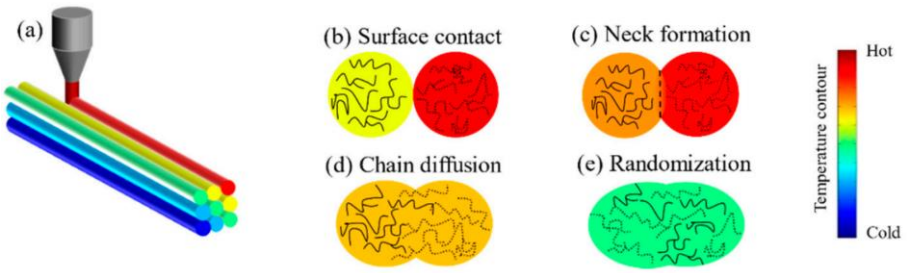

Figure 2-11 *(a) Temperature distribution of printed filaments from the highest temperature (red) of the current printing to cold filament (blue) away from the nozzle. Filament fusion after deposition from (b) initial surface contacting of filaments; (c) heat dissipation from the current deposition and neck growth; (d) molecular chain diffusion between filaments; (e) chain randomisation in cold filaments [35].*

The ambient and print bed temperatures are used to control the cooling rate of the deposited materials. Yang et al. [69] reported that heating of the ambient and print bed to temperatures below the T_g of the material could increase adhesion between the printed structure and the build platform, increase the crystallinity of the PEEK polymer, improve the fusion between filaments and layers, and relieve the residual heat stress upon cooling. However, there is no published study investigating its effect on the microstructure and mechanical properties of 3D printed continuous fibre-polymer composite.

2.2.3 Process-induced microstructure

The mechanical properties of 3D printed continuous fibre-polymer composites using the FDM process reported in the literature are summarised in **Figure 1-1**. As can be seen in this figure, the improvements to the Young's modulus and tensile strength of these composites with increasing fibre volume fraction does not follow the rule-of-mixtures (ROM). As expected, the reported increases to the tensile properties of 3D printed short fibre reinforced polymer composites are significantly lower than expected from ROM. This is likely due to the length of the short fibres being less than the critical length necessary for effective stress transfer to promote high load-carrying capacity. Continuous fibre reinforced composites also exhibit on average ~20-35% lower tensile properties compared to the RoM for the range of fibre volume contents. One of the possible attributing factors is the high porosity level. On the one hand, the fibre reinforcement with a higher thermal conductivity than the polymer matrix could improve the heat transfer rate between the adjacent printed filaments and layers, thereby lowering the void content and increasing the properties. On the other hand, however, the reinforcing phase can cause micro-cracks and voids at the

fibre/matrix interfaces due to poor compatibility of the polymer matrix to the fibres [23, 88], thereby increasing the probability of crack initiation and propagation under external loading.

In the in-situ fusion process, the void distribution and content are both highly dependent on the impregnation of matrix to fibre bundles during printing and the interface formation between adjacent printed lines during deposition, which are commonly affected by the combination of polymer feeding rate, printing speed and nozzle temperature (i.e. liquefier temperature). In this process where dry fibre tow is extruded through a polymer liquefier contained in a heated chamber which is located above the nozzle, a moderate-to-high polymer feed rate and fibre filament print rate (e.g. 80-100 mm/min for CF/PLA in [64]) can increase the inner pressure in the liquefier and overlapping contact pressure between adjacent deposited lines due to large unit volume of extruded polymer matrix, leading to better impregnation of matrix to fibre bundles and improved bonding between printed lines. However, further increasing the feed and print speeds reduces the dwell time available for impregnating the fibre tow with polymer, which may result in an inhomogeneous distribution of polymer in the fibre tow causing dry spots in the printed composites. The nozzle temperature can affect the flow and viscosity of the melt thermoplastic and thereby influence the impregnation process of the polymer to fibres. Tian et al. [64] evaluated the flexural strength of 3D printed continuous CF/PLA composites manufactured at different temperatures using the in-situ FDM process. As shown in **Figure 2-12**, delamination occurred in a fractured specimen fabricated at a lower nozzle temperature of 180°C whereas the composite with a temperature of 240°C had better fusion between layers. The higher temperature also increased the melt flow index from 2.0 to 35.6 g/10 min, which significantly improved the impregnation of matrix to fibres, leading to fibre breakage instead of fibre pull-out during loading and thereby increasing the flexural strength of the 3D printed composite.

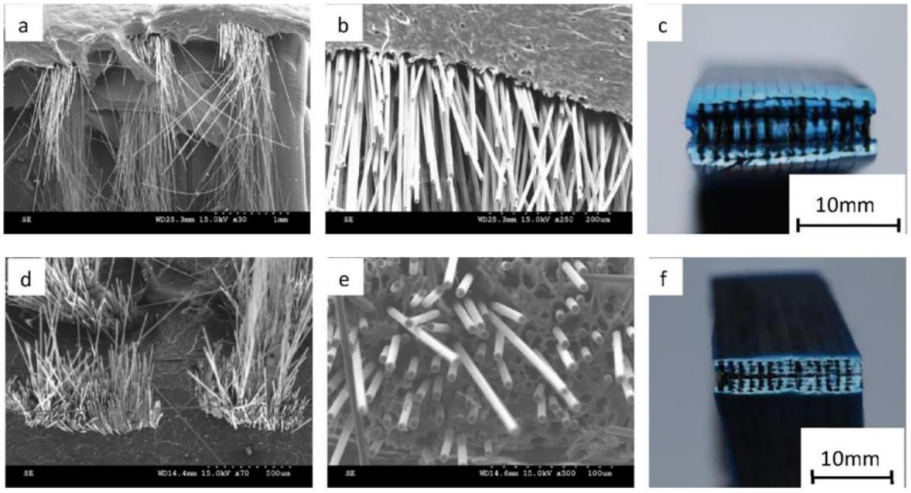

Figure 2-12 *Microstructures of fractured cross-sections of carbon/PLA composites with temperature in the printing head of 180°C (a, b, c) and 240°C (d, e, f), respectively: overall cross-section (a and d), interface (b and e) and fracture pattern (c and f) [64].*

Employment of in-situ pressure is another strategy to improve the quality of impregnation and decrease the void content in 3D printed composites. Liu et al. [31] proposed a micro-screw in-situ extrusion process to increase the impregnation of dry carbon fibre tows with molten PA12; **Figure 2-13** illustrates the 3D printing device. The micro-screw reduces the viscosity of the melt polymer via shear-thinning. The tensioned fibres generate high pressure at the pin surface, assisting the melt polymer to infiltrate the fibre bundle. The device increased the fibre volume fraction from 32% to 50%, with only 2.6% porosity due to good impregnation, resulting in high in-plane tensile properties [31]. By using pre-impregnated FDM filaments, the fibre/matrix bonding of the material could potentially be improved. However, internal porosity of ~2% in fibre-dense regions is common in pre-impregnated FDM filaments (**Figure 2-14**) [58], which can be entrapped after being 3D printed into a composite structure.

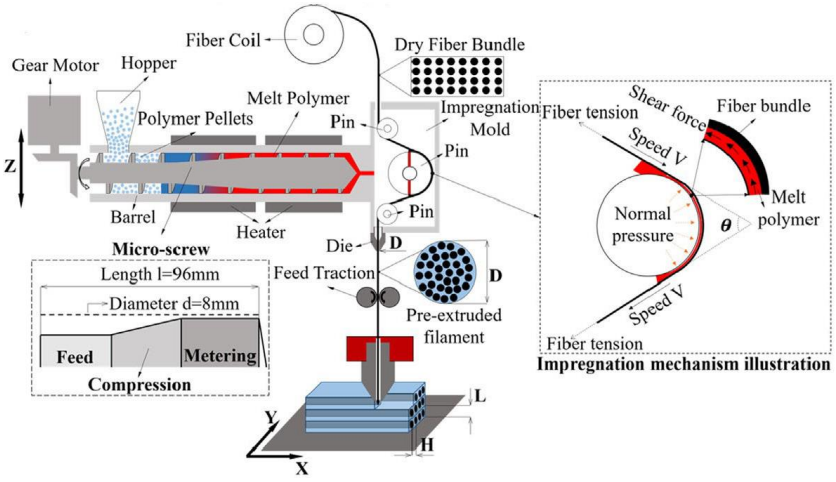

Figure 2-13 *Schematic of micro-screw in-situ extrusion based device for 3D printing continuous fibre reinforced composites [31].*

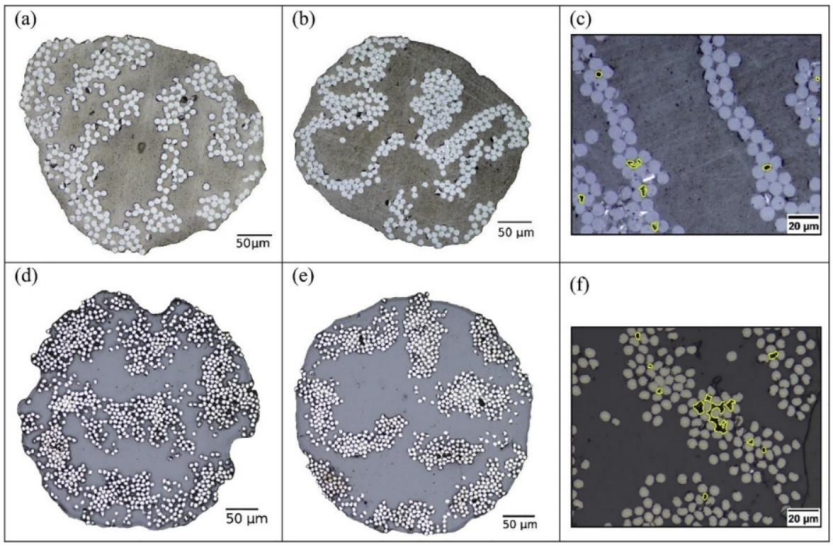

Figure 2-14 *Cross-sectional optical images of (a-c) glass- and (d-f) carbon fibre filaments exhibiting irregular outer lines (a and d), regular circumference (b and e) and magnified views (c and f) [58].*

Large voids can occur at the edges of 3D printed continuous fibre composites due to variations to the print direction. As shown in **Figure 2-15**, as the printer head changes direction at the extremities of the ply it forms a hairpin loop, which often results in a large void at the edge. These loops are an artefact of the printing process, and concentrated at the outer edges. Goh et al. [29] showed that the loop size can vary between different filament or fibre tow materials due to the differences in the fibre diameter and filament sizes. These loops can also affect the inter-filament distance within a ply further away from the periphery, which will be expected to reduce the filament fusion and strength of the printed composite [32].

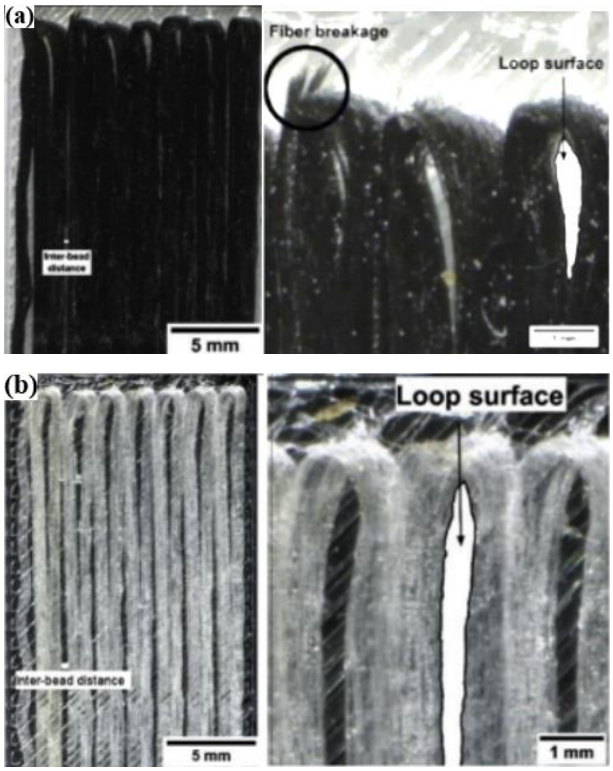

Figure 2-15 *Optical images of a single printed layer of (a) continuous carbon/PA and (b) continuous glass/PA, showing the fibre breakage and loop surface near the edge [58].*

In the filament-by-filament and layer-by-layer build-up process, the lack of sufficient heat and/or pressure can lead to imperfect fusion between the filaments (**Figure 2-16**) which increases porosity in the 3D printed composite. Studies have proposed the use of an in-situ laser heating system to increase the local surface temperature of the printed part above T_g for better interlayer adhesion [52, 79]. Another study reported the use of a compaction system in the printing process which resulted in a ~30% improvement in the tensile modulus and strength of the composite [89]. Post-processing the 3D printed composite using hot-pressing [90, 91] can double the mechanical properties by increasing the fibre volume content and reducing the void size and content. For instance, He et al. [91] reported that post-processing of printed parts using compression moulding increased the tensile strength in the longitudinal and transverse directions by 22% and 78% respectively, whereas the flexural strength and mode I interlaminar fracture toughness increased by 93% and 90%, respectively. He and colleagues showed that compression moulding reduced the void content of the printed part from 12% to 6%. However, the compacting process is not always suitable, particularly for printed structures that feature complex 3D geometry (e.g. lattice). Moreover, the use of

moulds in the post-processing also eliminates the rapid prototyping capability offered by the 3D printing process.

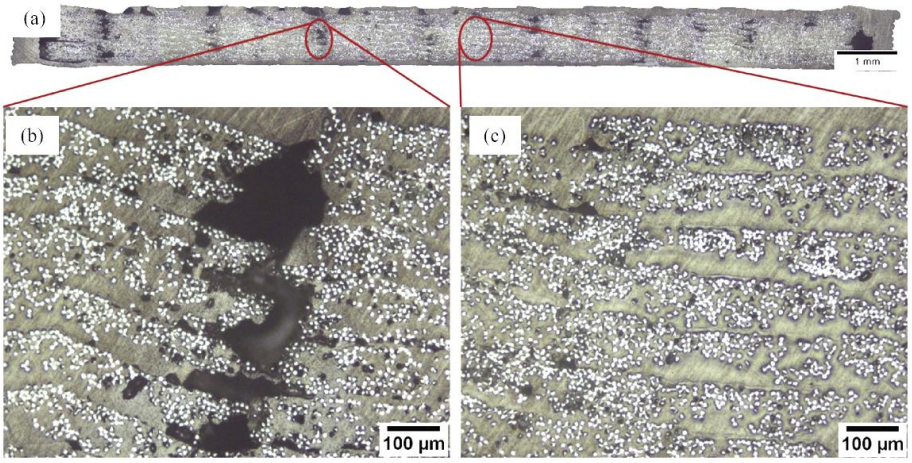

Figure 2-16 *Cross-section of 3D printed glass-polyamide composite. (b-c) are magnifications to highlight the non-overlap between filaments and voids within filaments.*

Fibre alignment is another critical factor affecting the mechanical properties of 3D printed composites. In conventional composites manufactured by stacking unidirectional plies, the desired mechanical properties are achieved through a combination of ply orientation angles [92-94]. In conventional composite structures, the drilling of fastener holes results in fibre discontinuity which reduces the failure stress, thereby requiring a conservative design approach for safety critical structural applications. Similarly, fabrication of complex-shaped structures with double curvatures can cause defects such as reduced dimensional accuracy, fibre waviness and ply wrinkling in traditional composite lay-up process. In the FDM process, a complex-shaped structure with arbitrarily curved fibre reinforcements can be produced more accurately by active control of the fibre path at the filament level. Several studies have reported the development of specialised algorithms using finite element analysis (FEA) to identify the most optimum fibre tow deposition directions within a ply [95-98]. It is important to simplify the optimisation of the fibre paths when using FEA, considering the practicability in the real 3D printing process. As shown in **Figure 2-17**, this process was used for 3D printing of composites with fastener holes without the fibre discontinuity [97] which occurs in conventional manufacturing. This study investigated the effect of fibre placement paths and fibre volume fraction on the mechanical properties of 3D printed composites with an open hole. The mechanical properties of the composites were improved by adopting maximum or middle principal stress trajectories for the placement of continuous fibres

around the fastener holes. The FEA results predicted an improvement to the open hole strength under uniaxial and biaxial loading of the composite utilizing the optimum curved fibre placement method. However, stress concentration still occurred near the fastener hole, albeit at a lower level. This concept was experimentally investigated by Andrew et al. [41], who 3D printed an open-hole carbon/polyamide composite emulating a weft-warp construction. By printing a 0/90 structure into one layer, fibre continuity was maintained around the hole aiding in the stress distribution (**Figure 2-18**). The tensile strength of the 3D printed composite was 93% of the unnotched material, and nearly double that of the traditional die punched sample.

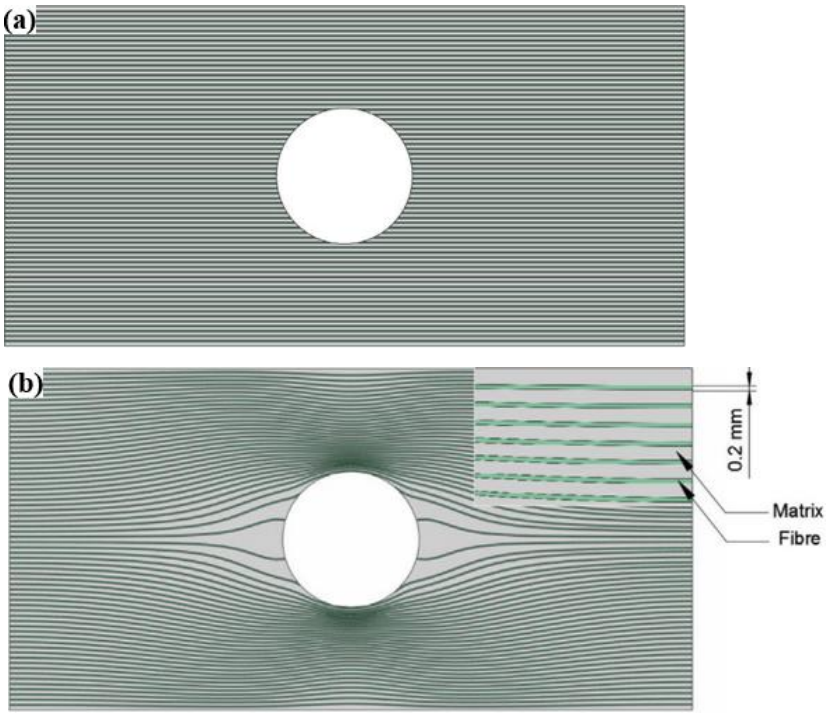

Figure 2-17 *FEM models of (a) conventional and (b) optimised CFRP plate with an equivalent volume fraction of fibres (V_f=27.2%) [97].*

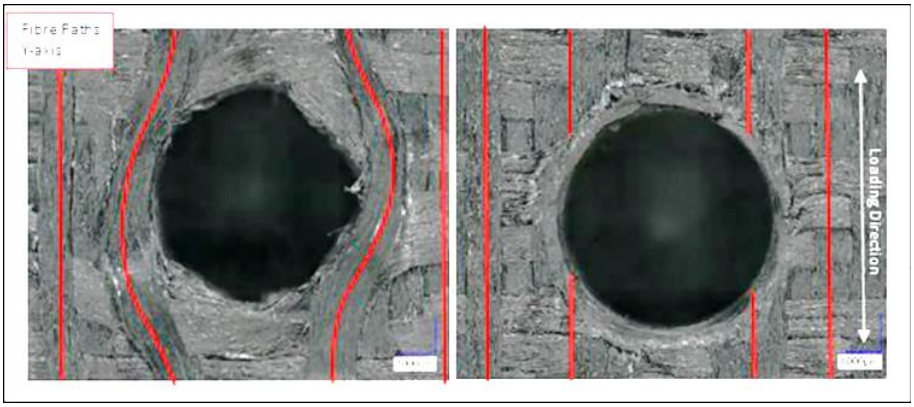

Figure 2-18 *'Tailor Woven' sample (left hand-side) and 'Die Punched' sample (right hand-side). Red lines represent typical fibre paths near the hole [41].*

Some studies have investigated a range of fibre alignment strategies to generate special print patterns by controlling the printer head and tool geometries [99-101]. **Figure 2-19** and **Figure 2-20** illustrate the 3D printing of various core configurations for sandwich structures. Liu et al. [100] investigated a novel print process making use of FDM to produce parts with free-hanging 3D features. While the process used by Liu and colleagues was successful in printing complex free-hanging features using continuous fibre filaments, the dimensional accuracy of the printed part was poor when printing out-of-plane features. It was reported that the dimensional inaccuracy was more pronounced in regions with large curvature, i.e. tight radius or large fibre bundle size, and the printed radius turned out to be lower than the FDM machine set value. Matsuzaki et al. [102] developed a model to predict the nozzle path for the printed radius by accounting for the twist and path length difference of the inner and outer edges using data collected from 3D printing experiments.

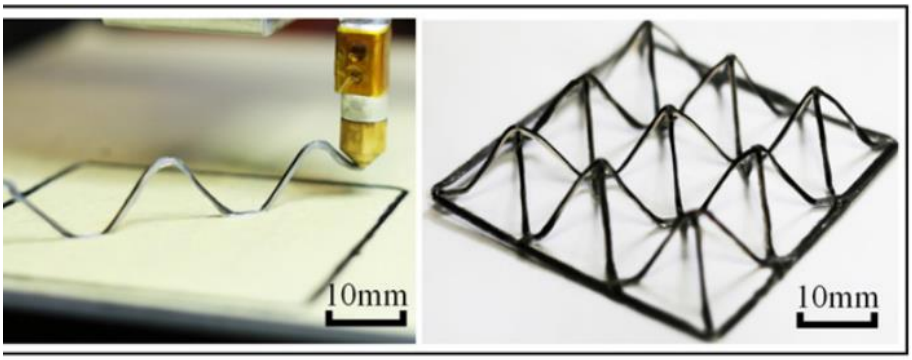

Figure 2-19 *Free-hanging 3D printing process of pyramidal lattice structure [100].*

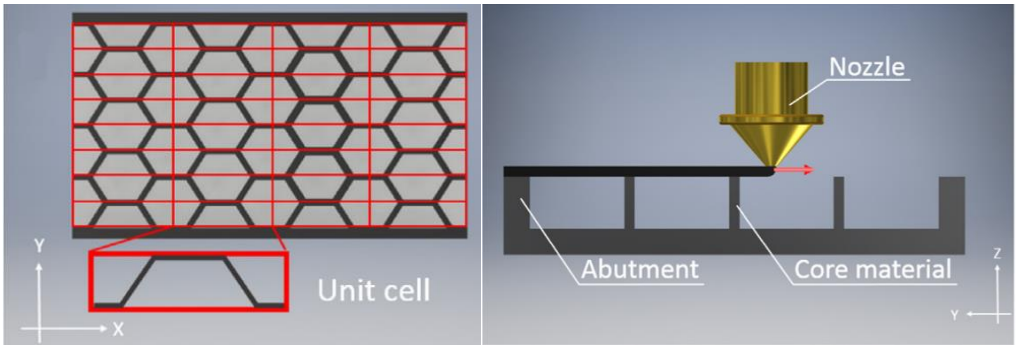

Figure 2-20 *Schematic of printing a wide bridge space using fibre tension [103].*

3D printing of curved features using the FDM process results in several types of microstructural defects, including filament waviness, filament peeling, twisting, folding, or even breakage (**Figure 2-21**) [29, 58, 97, 101, 102, 104-107]. For example, Ishii et al. [104] investigated the bending fracture mechanisms of a carbon fibre FDM filament in curved profiles with different radii. The study proposed that each fibre in the filament after curved printing would be in the state where the tensile and compressive stresses are generated in the outer and inner surfaces. Under the maximum strain rule, the minimum print radius was predicted to be 0.16 mm, below which the carbon fibres in the filament will fail by tensile fracture or compressive rupture. Ishii and colleagues therefore concluded that no fracture could occur during curved printing, as such a small radius is not printable using the typically filament diameter of ~0.37 mm. However, the curved filament specimens investigated by Ishii and colleagues were fabricated without a 3D printer, and the FDM-induced defects such filament folding and twisting were not considered. Shiratori et al. [105] attributed the folding of the filament to the twisting torque generated by two forces: adhesive force to the build platform and tensile force from the printer head. Fibre breakages were observed on the filament surface at the curved section after the polyamide resin was removed by laser processing. Shiratori et al. [105] evaluated the fibre damage via electrical resistance measurements of the filaments, which showed a nonlinear increase with the decrease of the inner radius. Using X-ray computed microtomography, Zhang et al. [106] characterised fibre misalignment and breakage in printed filaments with various turning angles and curvatures. The stress distribution in a printed filament was also investigated using FEA. However, only the elastic properties of the filament were considered in the FE model, and therefore no fibre damage could be predicted using modelling. The literature review reveals that the effect of printing radii size on the mechanical properties of 3D printed composites is yet to be fully

determined, which is the basis of understanding the performance of 3D printed structures with complex geometry.

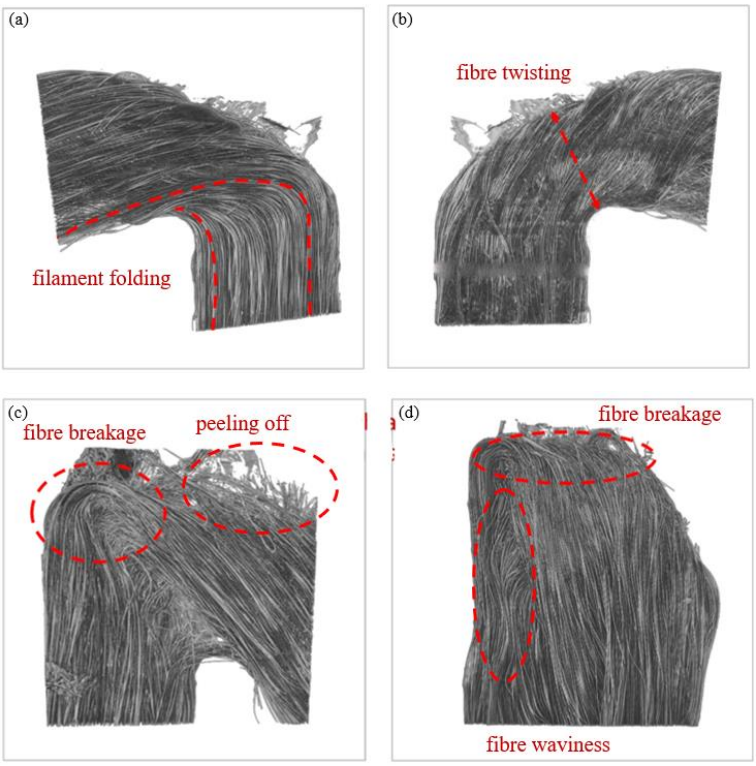

Figure 2-21 *Microstructural defects of (a) filament folding, (b) fibre twisting, (c) filament peeling from the base, (d) fibre breakage and fibre waviness in 3D printed filaments with curvature [106].*

2.3 Mechanical Properties of Continuous Fibre-Polymer Composites Produced by FDM Process

Maximising mechanical properties is one of the main reasons for using continuous fibre reinforcement in the 3D printing of composite materials. Research efforts have been focused on the use of different types of continuous fibre filaments, printing parameters, process conditions, and structure design on the mechanical properties. This section presents a review of published research towards maximising the mechanical properties of 3D printed composites using the FDM process.

2.3.1 Tensile properties

A large number of experimental studies have been published on the tensile properties of 3D printed continuous fibre composites [17, 20, 30, 52, 53, 64, 75, 87, 91, 108-119]. **Figure 2-22** and **Figure 2-23** from [74] present data on the tensile strength and modulus

values for unidirectional composites obtained from various studies. As can be seen, material selection, fibre content and the printing process all influence the tensile properties, resulting in a wide range of tensile property values. The highest tensile strength (of 1400 MPa) yet reported is for a 3D printed composite using conventional carbon fibre filament combined with hot pressing as the post-processing step [90]. The highest reported tensile modulus (of 161 GPa) is for a 3D printed carbon fibre-thermoset matrix system [119].

The filament fusion process without in-situ assist processing or post-processing usually results in relatively low tensile properties; often lower than 250 MPa and 20 GPa for tensile strength and modulus, respectively, for 3D printed carbon fibre composites fabricated using the FDM in-situ impregnation process [21, 120]. However, the mechanical properties of some 3D printed unidirectional composites are comparable to aluminium and titanium alloys [58], although they are still lower than the properties of composites manufactured using conventional processes such as hot moulding or autoclave curing. This is partly due to the limitation to the maximum fibre content of ~30 to 40% that can be achieved using the FDM process, as opposed to the higher fibre contents (of up to ~60%) for conventional composite. Even worse, the maximum fibre content that can be achieved using the in-situ impregnation process is very low (typically under 10%). Moreover, in 3D printing the dry spots and voids increase with the fibre content because fully infiltrating the fibre filament with the polymer filament becomes increasingly difficult at higher fibre content, which limits the improvement to the mechanical properties. Process-induced defects such as dry spots and voids have a larger impact on the tensile properties of 3D printed composites in the direction transverse to the printed filaments, in which the matrix properties and interfacial bond quality are more crucial [121, 122]. For instance, the transverse tensile strength and modulus of a 3D printed continuous glass-polyamide [90°] composite was reported to be only 30% and 12%, respectively, compared to the values for a conventional E-glass/epoxy composite with a fibre volume fraction of 65% [28].

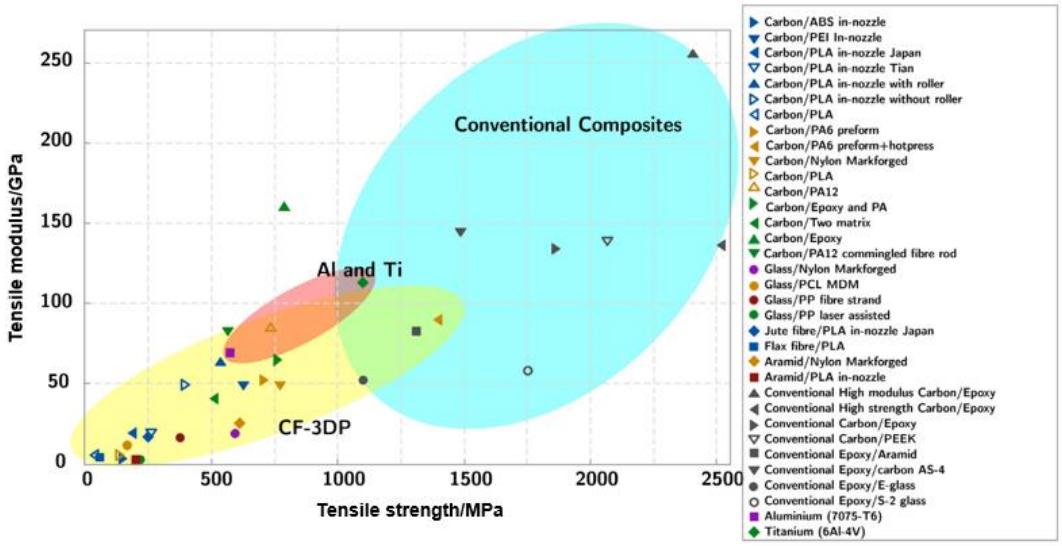

Figure 2-22 *Tensile property map of 3D printed continuous fibre-reinforced composites. Properties for conventional composites and aluminium and titanium alloys are shown for comparison [74].*

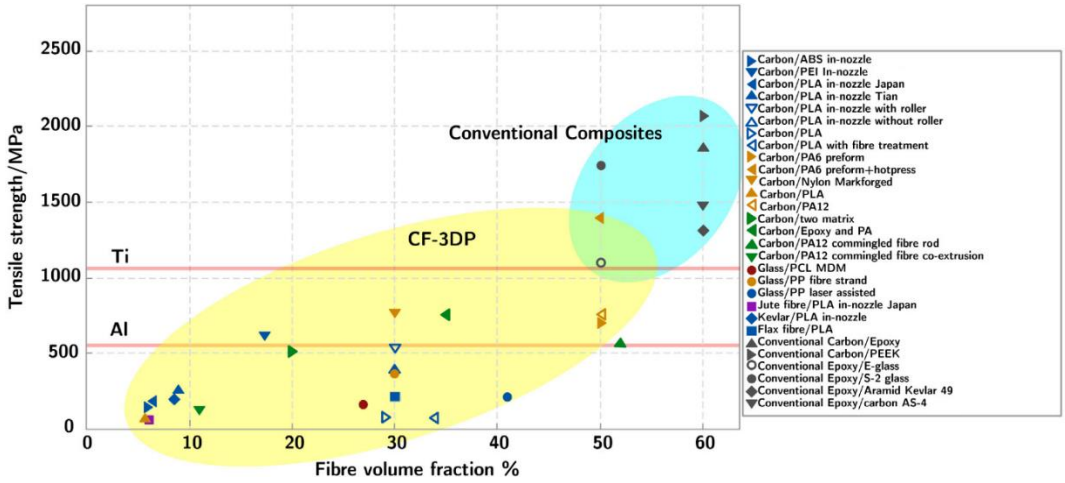

Figure 2-23 *Tensile strength vs fibre volume fraction plots of 3D printed continuous fibre-reinforced composites and conventional composites [74].*

2.3.2 Compressive and flexural properties

For materials used in structural engineering applications, a high resistance to compression and bending loads is desired. Therefore, the compressive and flexural properties of 3D printed composites have also been investigated. The flexural strength increases when continuous fibre reinforcement is added to the 3D printed polymer, which is expected. For example, Andrew et al. [23] measured a flexural strength and modulus of 250 MPa and 13 GPa, respectively, for continuous carbon-polyamide composite [23], which are 6 times and 12.3 times higher than the pure polyamide polymer. By increasing the carbon fibre content to

around 40%, Goh et al. [29] achieved the flexural strength of 430 MPa and modulus of 38 GPa. The flexural properties of continuous carbon fibre composite are more than double compared to the short carbon fibre-reinforced polymer at a similar fibre content of ~15% [32]. The published results show, however, that the improvements to the flexural properties with increasing fibre volume content does not conform to RoM. A larger percentage improvement to the flexural properties is achieved at low-to-moderate fibre volume contents, and as the fibre volume content is increased further the rate of improvement is reduced [123]. The flexural strength and modulus values of 3D printed continuous fibre composites are often much lower than composites fabricated using conventional processes because of poor interfacial adhesion caused by the filament-by-filament and layer-by-layer deposition process together with other process-induced defects (e.g. voids). This is evident from the delamination/de-bonding dominant fracture mode resulted from shear kinking and matrix failure in the compressive layers observed for flexural loading of 3D printed composites [29].

Only a few studies have investigated the compression properties of 3D printed composites [28, 56, 100]. Delamination, fibre-matrix debonding and local fibre buckling are the common damage modes for 3D printed composites subjected to axial compression loading [122]. The effects of fibre type, fibre infill pattern, fibre distribution, fibre content, and print orientation on the compressive properties have been evaluated [28, 56]. It is reported that the equidistant layer distribution, where reinforced layers are placed evenly through the specimen and separated by polymer layers, can improve adhesion resulting in an improvement to the compressive properties of 3D printed parts [56]. Other studies have investigated the effects of modifying the nozzle, printing path and printing parameters on the print accuracy for producing unique geometries, such as composites with in-build fastener holes and truss core sandwich structures. For instance, Liu et al. [100] investigated a free-hanging continuous carbon-PLA lattice truss core sandwich structure which had an average dimensional error of 1.9% compared to the CAD model. This sandwich structure had a relatively high specific out-of-plane compression strength of 0.042 MPa·m^3/kg.

2.3.3 Interlaminar shear, impact and interlaminar fracture toughness properties

A significant disadvantage of 3D printed continuous fibre-polymer composites is their low through-thickness mechanical properties due to the lack of fibre reinforcement in this direction. As 3D printing is a layer-by-layer process, the filaments are usually laid in the in-plane direction. The strength of the final printed composite in the through-thickness direction

depends largely on the bonding quality between adjacent printed layers. Delamination is likely to occur in FDM composites produced without post-process of uniform heating and pressing (**Figure 2-24**).

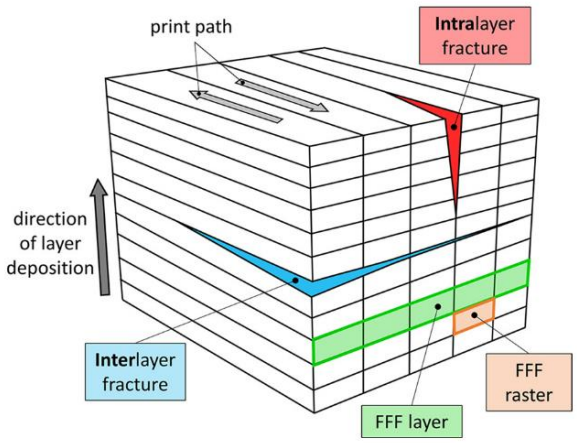

Figure 2-24 *Decohesion between adjacent layers/beads in FDM unidirectional composites [66].*

The interlaminar shear strength (ILSS) is often measured to evaluate the interlayer properties of composites. A few studies have investigated the effects of fibre type and fibre content on the ILSS of 3D printed composites. Caminero et al. [57] reported an ILSS of 32 MPa for a 3D printed carbon-polyamide composite, which was 213% higher than the 3D printed polyamide-only material. The improvement to the ILSS as a function of increasing fibre content is low to moderate due to a higher level of defects induced by high fibre volume content, as discussed previously. Since the ILSS is dependent on tow waviness and the interface region, process modification such as surface treatment and laser heating can increase the interfacial strength of 3D printed composites [52, 78].

High resistance to impact damage is necessary for composites used in aircraft structures, where accidental impact from hailstones, bird strikes, tool drops, runway debris, etc., can cause delamination, matrix cracking and fibre fracture leading to a significant knockdown in the mechanical properties. Few studies have investigated the impact resistance of 3D printed continuous fibre composites made using the FDM process [59, 60, 124]. Caminero et al. [59] experimentally investigated the energy absorption efficiency of composites printed with various fibre reinforcements, fibre contents and build-up orientations using the Charpy impact test. Generally, the ‘on-edge’ (laid-up onto the edge of the specimen on the print bed; see **Figure 2-10**) specimen condition had higher impact energy than ‘flat’ (laid-up in the thickness direction of the composite), even with lower fibre content

(approximately 35% vs 55%). In a subsequent study, Caminero et al. [60] evaluated the impact damage resistance of these 3D printed composites. Higher damaged areas occurred in the 3D printed glass-polyamide composites compared to conventional carbon-epoxy composites, which is indicative of inferior impact damage resistance. This is believed to be due to the low through-thickness strength of 3D printed composites due to the weak interlayer bonding caused by the layer-by-layer build-up process.

Interlaminar delamination resistance of composites depends mainly on the fracture toughness of the matrix material and the fibre-matrix interfacial bond strength, although toughening mechanisms such as fibre bridging and crack bifurcation can increase the delamination resistance at longer crack lengths. At present, very few studies have investigated the interlaminar fracture toughness properties of 3D printed continuous fibre composite systems. Iragi et al. [121] reported that fibre bridging under mode I loading is one of the main toughening mechanisms in 3D printed composites. Unlike the composites manufactured using conventional processes, the lack of high pressure consolidation in 3D printing using the FDM process can lead to a high level of porosity between filaments in a ply and between neighbouring layers in a composite, resulting in lower interlaminar fracture toughness properties compared to composites made using conventional processes [125]. He et al. [91] investigated the effect of voids on the mode I interlaminar toughness of 3D printed carbon-polyamide composites. In this study, post-process using hot pressing decreased the void content of the composite from 12% to 6% which resulted in a 90% increase in the strain energy release rate for crack initiation ($G_{Ic\_initial}$). However, the steady-state fracture toughness ($G_{Ic\_propagation}$) of the unprocessed 3D printed composite was only 1/3 lower than the processed composite, which was due to the reduction in the amount of fibre bridging during delamination growth for the hot-pressed specimens. He and colleagues also reported that the mode II interlaminar fracture toughness of FDM continuous carbon-polyamide composite is lower than the mode I toughness, which is unusual considering the mode II delamination properties for conventional composite is typically higher than mode I.

Goh et al. [125] investigated the effect of printing parameters on the microstructure and mode I fracture toughness of 3D printed continuous carbon fibre-polyamide composites. It was found that an optimum combination of print speed with high nozzle and bed temperatures can increase the mode I toughness properties due to increased fibre bridging along the delamination crack. The study highlighted the necessity of improving interfacial

bonding and reducing void content for improving the resistance of 3D printed composites against delamination crack initiation and propagation.

2.4 Mechanical Properties of 3D Printed Hybrid Composites Using FDM Process

Composites reinforced with continuous carbon fibres are commonly used for structural application requiring high specific stiffness, strength and fatigue resistance. In contrast, aramid fibre reinforced composites are generally preferred for structural applications requiring high impact resistance and in-plane fracture toughness. Glass fibre composites are often used when low material cost and high strength is required. Therefore, hybrid composites containing two or more fibre types to overcome the limitations of a single fibre type are sometimes used; balancing the mechanical and other properties of the fibre types for a given structural application. It is also possible to provide specific properties such as impact or fatigue resistance via fibre hybridising, offering more design freedom for applications. The hybridisation of fibres can be achieved using three configurations [126, 127]: intrayarn (fibre-by-fibre), intralayer (yarn-by-yarn), and interlayer (layer-by-layer) (**Figure 2-25**).

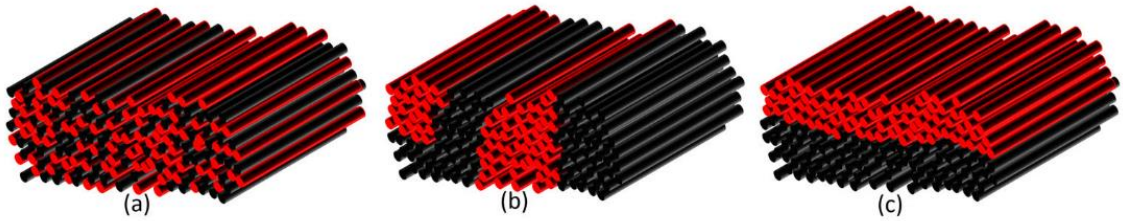

Figure 2-25 *Three different hybrid fibre configurations: (a) intrayarn, (b) intralayer and (c) interlayer [126].*

The extensive design freedom of hybrid fibre composites challenges traditional manufacturing processes. Conversely, the FDM process becomes outstanding with its design flexibility and simplicity of achieving multi-material printing. However, very few studies have investigated the effect of fibre hybridisation on the mechanical and other properties of 3D printed composites. Wang et al. [128] explored the feasibility of simultaneously enhancing the strength and ductility of polyamide-based composites using the combination of short carbon + continuous carbon + continuous aramid fibre reinforcements. They determined the effect of fibre layer distribution on the indentation force and energy absorption capability of the 3D printed hybrid composites. The highest indentation force was obtained when

placing the continuous carbon layer at the front side, while the highest energy absorption was achieved with the aramid layer at the front side. Yavas et al. [129] evaluated the ILSS of 3D printed continuous carbon/short carbon-polyamide composites. They discovered that the ILSS increased by varying the stacking sequence and increasing the number of consecutive short carbon fibre layers. This was accompanied with a transition in the failure mode from brittle matrix cracking of the short carbon fibre-reinforced layers to the interfacial cracking between the continuous and short carbon fibre-reinforced layers, resulting in improved ILSS. Huang et al. [73] investigated the potential of FDM printed hybrid composites with carbon-polyamide layers sandwiched by fibreglass-polyamide layers to exhibit a pseudo-ductile response under tensile loading. 3D printed composites with the carbon layer thickness between 100 and 200 μm were determined to be desired for exhibiting a pseudo-ductile response, which is higher than that required in composites manufactured using thin-ply prepreg (29-84 μm ply thickness). This was attributed to the low fibre volume fraction and tensile failure strain energy of 3D printed carbon plies. Wang et al. [124] enhanced the energy absorption capabilities by hybridising continuous carbon and Kevlar fibres in the polyamide matrix. However, the effect of fibre types, fibre layer distributions and fibre fractions on the 3D printed hybrid continuous fibre-polymer composites have not been investigated.

2.5 Summary and Outstanding Research Gaps

The additive manufacturing of continuous fibre-polymer composites has the potential to increase the production rate and reduce material waste. FDM is one of the simplest and commonly used AM processes to 3D print near-net-shaped composite components with high dimensional accuracy. The FDM process involves extruding polymer filament and co-mingled filament of fibre-polymer via two nozzles within a heated FDM printer device. The filaments are deposited onto the build platform, where they fuse together as they cool rapidly from the extrusion temperature to ambient temperature. The printing head of an FDM machine is typically designed to move laterally (i.e. X-Y directions), and the build platform moves vertically (i.e. Z-direction) to build the composite filament-by-filament and then layer-by-layer. Additive manufacturing of composites via the precise placement of continuous fibre-thermoplastic filaments in an automated build-up process eliminates some of the problems associated with conventional techniques, such as the high amount of manual labour and the potential risk of incorrect ply alignment.

However, a major limitation of using the FDM process is the relatively low mechanical properties of 3D printed composites compared to materials made using conventional processes such as vacuum bag resin infusion of fabric composites and autoclave curing of prepreg-based composites. Although factors including fibre type, matrix type, printing parameters, structural design and material modifications have been considered, the improvement to the tensile properties [23, 28, 32, 56, 59, 130] are lower than expected. This has been attributed to defects that form during the FDM process, such as a high level of porosity and material heterogeneity. Microstructural analysis [95] shows that 3D printed composites made using the FDM process often contain a relatively large volume fraction of voids and polymer-rich regions at the fusion interfaces between adjacent filaments and layers. However, the literature only revealed the effect of void content on the mechanical properties through the comparison of 3D printed composites with and without post-process such as hot pressing. As the post-process can compromise the advantage of the FDM manufacturing and is not suitable in cases where complex geometry is required, understanding the process-induced microstructural features on the fracture behaviour of 3D printed composites is critical for structural design in industrial applications. Additionally, fibre damage incurred during the FDM process is another potential cause of the low mechanical properties of 3D printed composites. Although a few studies have reported fibre waviness and breakage [30, 33-36, 60, 102, 104, 105], limited published research has explored the effect of fibre damage induced by the FDM process on the mechanical properties of composite.

As an efficient process of improving the mechanical properties of fibre-polymer composites, fibre hybridising was reviewed in this chapter. Hybrid fibre reinforcement can alleviate the drawbacks of one type of fibre reinforcement while keeping the benefits of the other fibre type [131-134]. The hybridisation can also lead to synergetic effects or the properties that neither of the constituents possess [135-141]. However, few studies have employed the FDM process in hybrid fibre composite manufacturing and determined the effect of fibre hybridising on the specific mechanical properties of 3D printed continuous fibre composites.

CHAPTER 3: EXPERIMENTAL CHARACTERISATION OF CARBON FIBRE FILAMENT DAMAGE DURING THE FDM PROCESS

Abstract

The damage caused to continuous carbon fibres during different stages of the FDM process from the initial feedstock filament material to the deposition of the filament on the build platform is systematically investigated to determine the causes of the low mechanical properties of 3D printed carbon fibre composites. The effect of the process stages on the damage and mechanical properties of continuous carbon-polyamide filament material is determined. Fibre damage occurs at multiple stages of the FDM process due to abrasion and bending, with most damage occurring in the final deposition stage when the FDM filament is bent to ~90° and flattened on the build platform. The average strength of carbon fibres within the FDM filament evaluated in this study is reduced by ~33% by the FDM process. The tensile strength and compression kinking stress of the FDM filament are reduced by ~44% and ~25%, respectively. The causes of the damage and the resultant reductions to the mechanical properties of the FDM filament during 3D printing are identified. In this study, a modification to the printer was also employed to mitigate abrasion damage caused by the material feeding gears on the FDM filament. The carbon-polyamide filament using the modified feeding system experienced almost no reduction in tensile strength compared to the value of the initial feedstock filament.

3.1 Introduction

The tensile [23, 28, 32, 56, 59, 130], compressive [28, 29, 56], flexural [29, 32] and other mechanical properties [57, 59, 88, 97, 142] of laminates made using the FDM process are much lower than laminate made using conventional manufacturing processes such as vacuum bag resin infusion of fabric laminates or autoclave curing of prepreg-based laminates. As described in the previous chapter, published research has proven that defects and damage to the laminate caused by the FDM process, such as relatively low fibre content of no more than 40% [18, 21, 28], high porosity level, and large volume fraction of polymer-rich regions [14, 16, 23, 28, 29, 32], are often the causes of low mechanical properties. These studies, however, have only investigated the properties of the 3D printed laminate, and not identified what aspects of the FDM process control the creation of defects and other damage. In particular, the effect of the FDM process on the integrity of the fibres has not been investigated.

The study presented in this chapter investigates the damage caused to a carbon-polyamide filament by the FDM process. The filament is a commonly used stock material for the 3D printing of continuous carbon fibre laminates using FDM. The damage caused to the FDM filament, including to the carbon fibres within the filament, as it progresses through the different process stages of a Markforged® FDM machine, starting from the original stock material to the final printing deposition, is determined. The effect of damage incurred in the different FDM process stages on the tensile properties and compressive kinking stress of the FDM filament is determined. The study identifies the stages of the FDM process which cause the most damage and the largest reductions to the mechanical properties of the FDM filament and the carbon fibres within the filament. In addition, a process modification to the material feeding system of the FDM machine is employed in this research to minimise damage to the fibres and filament. The efficiency of the modification towards reducing damage and thereby retaining the tensile properties of the carbon-polyamide FDM filament is evaluated.

3.2 Materials and Experimental Methodology

3.2.1 Material

The filament investigated was a continuous carbon fibre-polyamide material which is representative of a carbon fibre-thermoplastic matrix stock material used for the 3D printing of laminates using the FDM process. The FDM filament was supplied by Markforged®, and

had a nominal diameter of 0.38 mm. A cross-sectional view of the filament in the as-received condition is shown in **Figure 3-1**. The carbon fibres are unevenly distributed in the FDM filament, and the average fibre volume fraction measured using phase-contrast imaging (ImageJ) is 34%. The filament also contains voids, which are typically less than 20 µm in size, and interfacial cracks between some of the fibres and the matrix phase. The manufacturing defects of the feedstock filament in terms of the non-uniform fibre distribution and voids have been reported in other studies [58, 143]. The feedstock filaments were stored in a dry box supplied by Markforged® kept in the laboratory with the humidity at ~35%.

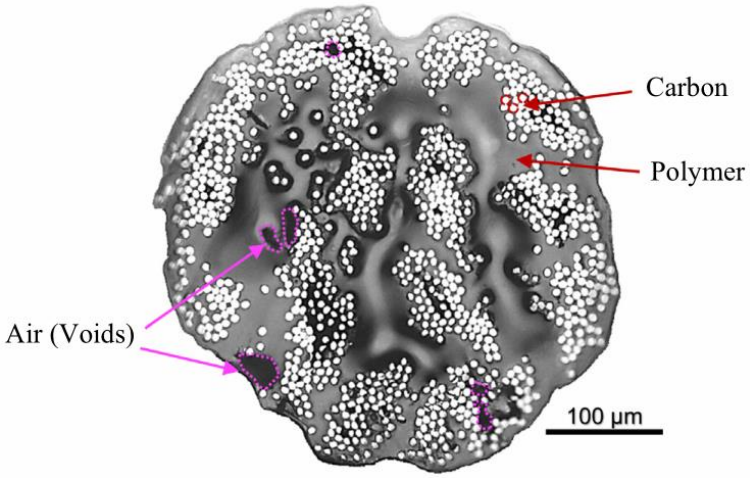

Figure 3-1 *Optical micrograph showing cross-section of the feedstock carbon/polyamide FDM filament in the as-received condition.*

3.2.2 FDM process

A Markforged MarkTwo® FDM printer was used to print a single filament of the carbon-polyamide feedstock. The FDM printer and the printing process are shown in **Figure 3-2**. This FDM printer has a single print head that houses two separate nozzles: one for printing polymer filament material and the other for the fibre-polymer filament material. The print head can only operate one nozzle at any given time, and there is no interaction between the polymer and fibre-polymer filaments.

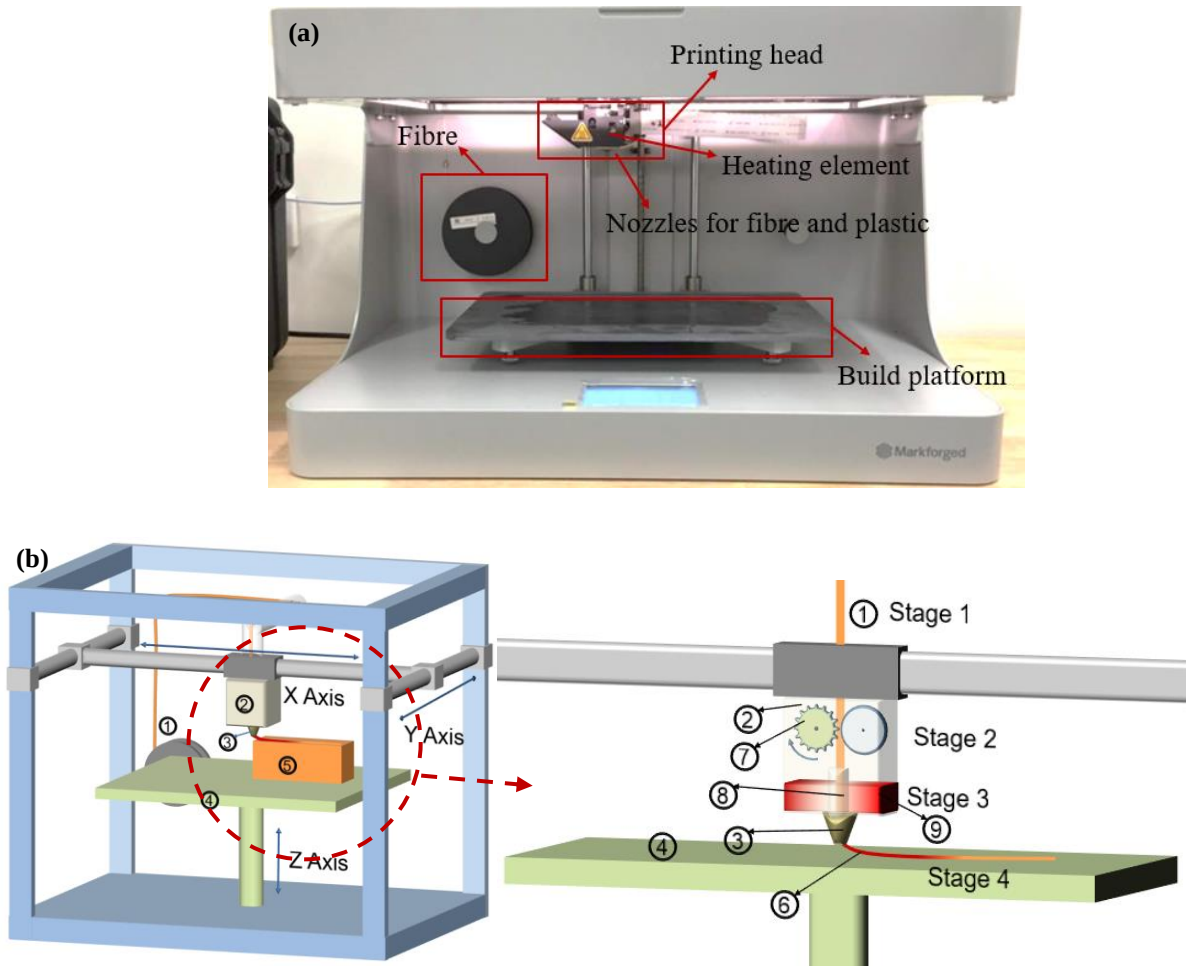

Figure 3-2 *(a) MarkTwo® printer and (b) schematic of the FDM process (① filament stock, ② print head [⑦ serrated driving motor, ⑧ guide PTFE tube, ⑨ heating element], ③ printing nozzle, ④ printing bed, ⑤ printed composites, ⑥ deposited filament).*

The FDM process consists of four consecutive stages performed continuously to print a single FDM filament, which forms the basic 'building block' of a 3D printed laminate using a filament-by-filament, layer-by-layer approach. The stages are summarised in the flowchart in **Figure 3-3**, and each stage is briefly described.

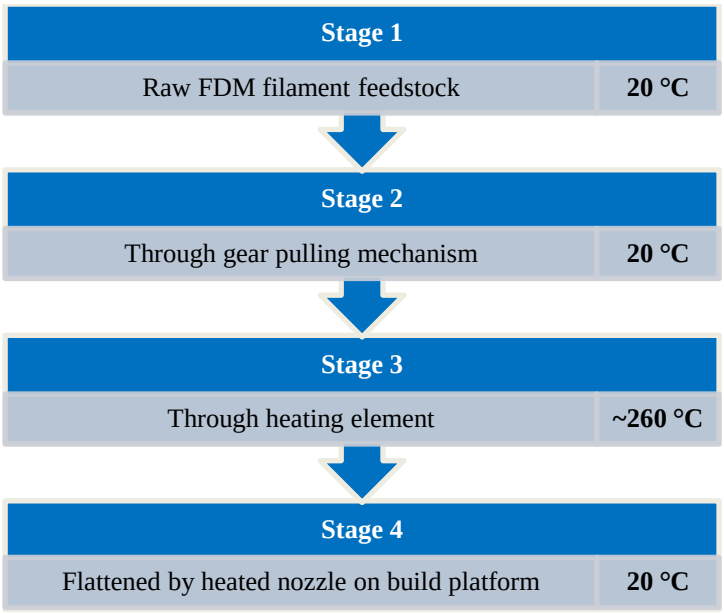

Figure 3-3 *Flowchart of the main stages to the FDM process using the MarkTwo® printer.*

Stage 1: As-received (stock) carbon-polyamide FDM filament.

Stage 2: FDM filament (20°C) is drawn at a feed rate of 15 mm/s into the printer head device using two counter-rotating metal wheels, one of which has serrated teeth (as indicated in the schematic in **Figure 3-4**).

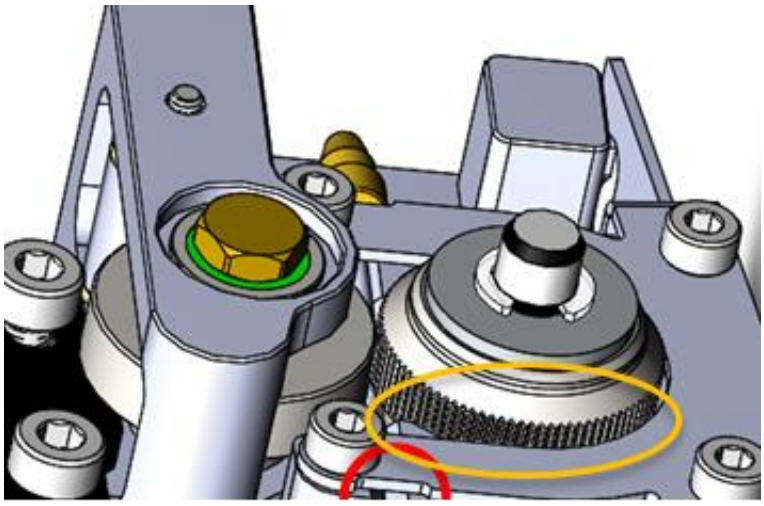

Figure 3-4 *Schematic of metal wheels for filament feeding in the MarkTwo® printer, one of which has serrated teeth on the surface. (Note: Schematic is from the website of Markforged® company).*

Stage 3: The filament is drawn into and through the printer head, where it is rapidly heated to 254°C to soften the polyamide matrix phase. This temperature is fixed for the MarkTwo® printer, and is set by the Markforged® company for polyamide-based filaments. The filament

is guided by a PTFE tube that passes through the full nozzle length, exits the nozzle tip and is then extruded downwards towards the build platform of the printer (**Figure 3-5**). The nozzle has a diameter of 1 mm, which is wider than that of the filament.

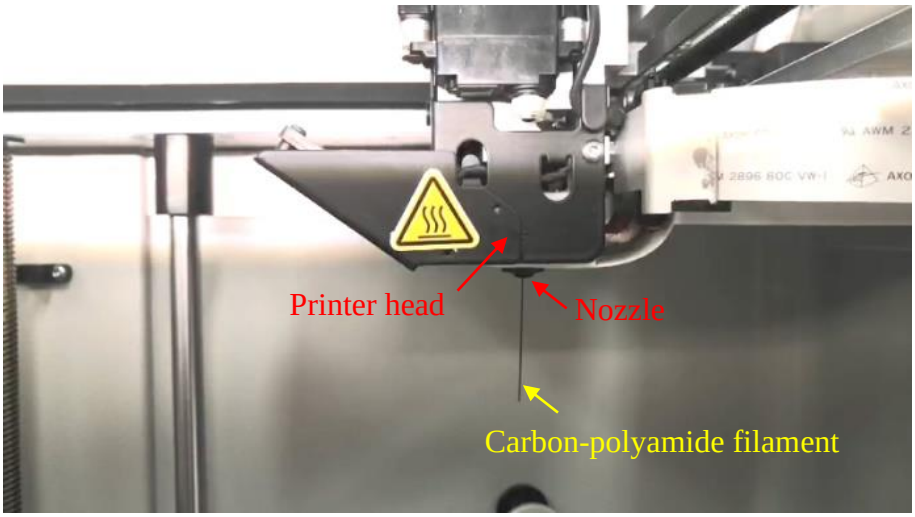

Figure 3-5 *Filament extrusion process in which a filament is heated and pushed out of the printer head.*

Stage 4: The filament is deposited onto a flat build platform, which can move vertically. The gap between the moving nozzle and platform was set at 0.13 mm, as recommended by the printer supplier. This is important because the feedstock filaments used in the research are very thin, any small deviation in the spacing between the printer head and build platform could cause unacceptable printing quality or even failed printing. The printer head drags the FDM filament as it is being deposited and assists in its compaction on the build platform (**Figure 3-6**). The gap between the printer head and the build platform (0.13 mm) is smaller than the initial diameter of the filament (0.38 mm), so the printer head applies pressure onto the filament changing it to a flat shape. The build platform is at room temperature, causing the FDM filament to cool rapidly and thereby solidify the polyamide matrix phase. For the research presented in this chapter, only a single FDM filament was deposited, and layer-by-layer printing was not performed.

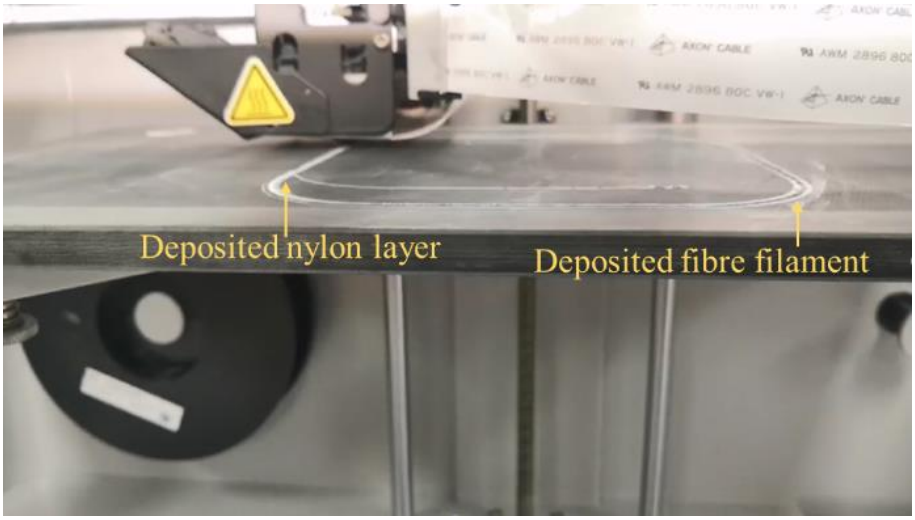

Figure 3-6 *Material deposition process in which the fibre filament is flattened on the build platform.*

3.2.3 Feeding system modification

When the filament feedstock is gripped and drawn into the FDM printer by two counter-rotating metal wheels, the serrated teeth on the metal wheel may abrade the filament surface. Therefore, rubber rings with different diameters were used to replace the metal gears, as illustrated in **Figure 3-7**. Three rubber rings covered each side of the rotating spindles, with the middle creating a groove to guide for the filament through. Slight pressure was applied from the rubber wheels to the filament by adjusting the distance between the two spindles so that the filament could be steadily driven to the printer head. Note that the results and discussion presented below are for the FDM machine containing metal serrated gears, and the modified rings are discussed later in the chapter.

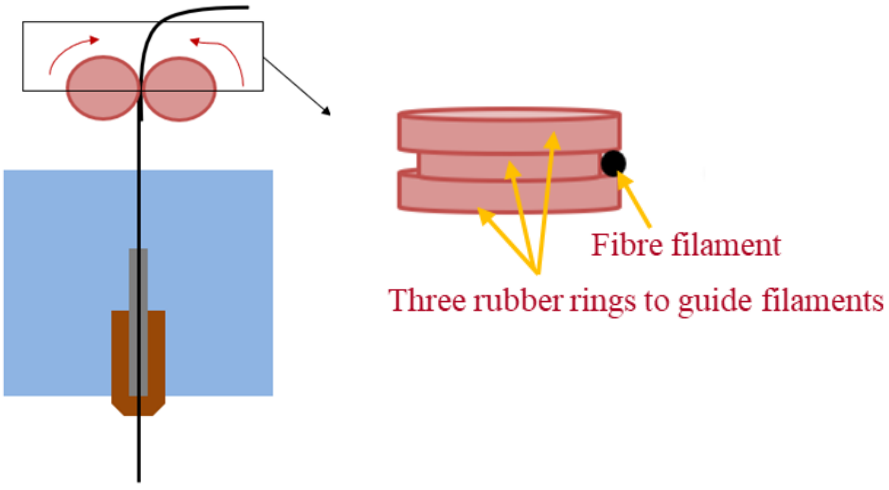

Figure 3-7 *Schematic of material feeding system modification with Marktwo® printer.*

3.2.4 Microstructural examination of FDM filament

The effect of each stage of the FDM process on the damage to the carbon fibres was evaluated by interrupting the printing to extract the filament for examination and mechanical testing. Physical damage to the FDM filament was examined using optical and scanning electron microscopy (SEM). The SEM was performed using an LEO 1530VP-21-32, with the FDM filament coated with a thin iridium film before examination to avoid electron beam charging effects.

3.2.5 Mechanical property testing

3.2.5.1 Tensile testing of single carbon fibre

The tensile failure stress of single carbon fibres extracted from the FDM filament (following removal of the polyamide matrix) was measured at the start (Stage 1) and end (Stage 4) of the FDM process. Single fibres were extracted from the as-received FDM filament (Stage 1) and the printed FDM filament (Stage 4) by heating in a vacuum oven for 5 hours at 500°C to decompose and vaporise the polyamide matrix, thereby creating a bundle of loose fibres. Individual fibres were carefully extracted from the bundle and then mounted on a thin cardboard support frame containing a 65 mm long rectangular cut-out, which defined the fibre specimen gauge length (ASTM C1557 [144]). **Figure 3-8** illustrates the mounted single carbon fibre for the tensile test. The ends of the cardboard frames were gripped by a 2.5 N load capacity Instron (Model 4501). Each fibre was tensile tested at room temperature at a 1 mm/min cross-head displacement rate until failure. Thirty carbon fibres were tensile tested for the as-received FDM filament (Stage 1) and the printed FDM filament (Stage 4).

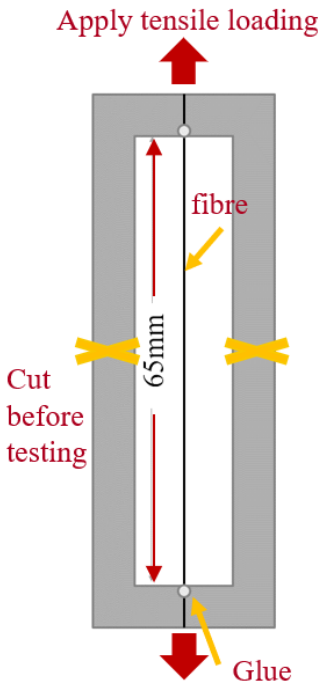

Figure 3-8 *Schematic of specimen preparation for the single fibre tensile test.*

3.2.5.2 Tensile testing of single carbon-polyamide FDM filament

Tensile tests were performed on the carbon fibre-polyamide filament after being extracted from Stages 1 to 4 of the FDM process. The filament was also extracted from the FDM machine with the modified rubber gears at Stage 2 (designated Stage 2_M). The tensile properties of the FDM filament were determined using test specimens that were 200 mm long with a gauge length section of 100 mm. The specimen ends were reinforced within 50 mm long, 1.5 mm thick glass-epoxy tabs to avoid damage when the FDM filament was gripped in the tensile machine. All the filament specimens were marked at the gauge area for measuring the elongation during testing using a high-speed camera. The picture frame rate of the camera was set as 2 Hz. **Figure 3-9** shows the test setup with a schematic of the marked filament specimen on the right. The cross-sectional shape of the FDM filament was approximately cylindrical (e.g. **Figure 3-1**) with a diameter of ~0.38 mm from Stages 1 to 3 of the FDM process. The FDM filament had a flattened rectangular shape after being printed (Stage 4) and was about 0.13 mm thick and 0.90 mm wide. For each stage, the shape and cross-sectional dimensions of the FDM filament used for tensile testing were evaluated using an optical microscope. The results are given in **Table 3-1**.

The FDM filament was tensile tested at room temperature at an extension rate of 0.5 mm/min until failure during a 10 kN load capacity Instron machine (Type 5569). The tensile

modulus of the FDM filament was calculated from the strain values obtained using the digital image correlation (DIC) method through GOM Correlation software. The images were taken using a MER2-2000-19U3M-L industrial digital camera with a lens of HN-2520-20M-C1/1X (Daheng, China). A minimum of fifteen FDM filaments taken from each stage were tested under identical conditions to determine the average and scatter to the tensile properties.

***Table 3-1**. Shape and dimensions for the FDM filament for each stage.*

FDM Stage	Cross-sectional Shape	Dimension (mm)
1	Circular	0.38 ± 0.02
2	Circular	0.38 ± 0.02
3	Circular	0.37 ± 0.04
4	Rectangular	0.13 ± 0.04 × 0.90 ± 0.15

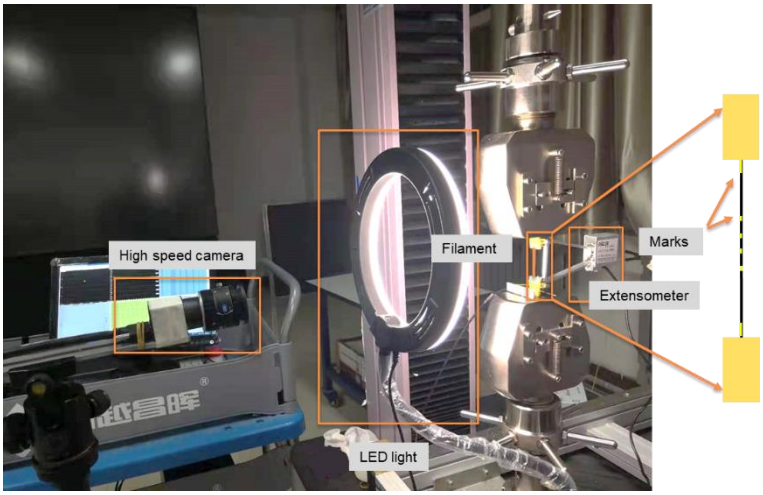

***Figure 3-9** Setup for the filament tensile test.*

3.2.5.3 Compressive testing of single carbon-polyamide FDM filament

To evaluate the effect of fibre damage on the compressive properties of the 3D printed continuous fibre composites, it is necessary to first investigate at a tow level, which does not have defects such as weakened fusion interfaces and large voids. It is not possible to directly compressive test the FDM filament due to its very high shape aspect ratio, which causes

buckling. Therefore, a modified axial compression tests were performed on the FDM filament taken from the different stages of the FDM process. A single FDM filament was mounted in the centre of an epoxy polymer block (which is much softer than the filament itself), as shown in **Figure 3-10**. The polymer was used to provide lateral support to the FDM filament to prevent buckling under the compressive force. In the preparation of the compression samples, a very slight tensile force was applied to the FDM filament to ensure it was straight, and then liquid epoxy resin (105 epoxy resin® / 206 slow hardener®) was moulded around the filament. The resin was cured at room temperature for at least 24 hours before compression testing. The FDM filament bonded to the epoxy with no cracks or other flaws at the interface between the materials. The single FDM filament was then axially compressed at room temperature at an end-shortening rate of 1 mm/min using a 10 kN Instron machine. The test was stopped when cracks appeared at the filament/epoxy interface, which always coincided with compressive failure of the FDM filament. The polymer block was elastically deformed under the load, but did not plastically deform due to the low compressive failure strain of the FDM filament. A minimum of five samples containing a single filament taken from each FDM stage were tested under identical conditions.

This test method does not provide a direct measure of the compressive failure load of the FDM filament, although it can be used as a qualitative ranking of compression strength for the different stages of the FDM process. For comparison, the compressive response of the polymer block without a filament was measured to determine the difference in applied load between this specimen and those specimens containing a single FDM filament.

(a)

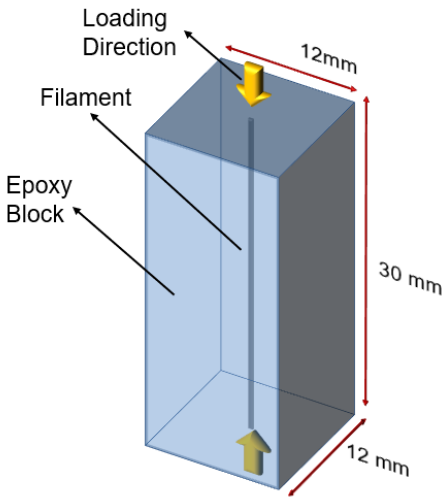

(b)

Figure 3-10 *(a) Schematic and (b) photograph of compression specimen for a single FDM filament.*

Acoustic emission (AE) was used to monitor the filament damage during the compressive test. A single acoustic transducer (Physical Acoustic Corporation, R15 α SNAK67) was mounted on the side of the specimen. The acoustic signals measured by the transducer were amplified and analysed using an AE system (Physical Acoustic Corporation, μDiSP^{TM}). The acquisition parameters of the AE system were set at an amplitude threshold of 40 dB, peak definition time (PDT) of 25 μs, hit definition time (HDT) of 150 μs, and hit lockout time (HLT) of 300 μs.

3.3 Results and Discussion

3.3.1 Effect of FDM stages on damage to carbon-polyamide filament

The FDM filament underwent significant physical changes during the FDM process, from the as-received (stock) material to being printed as a single strand on the build platform before 3D layering. **Figure 3-11** shows the surface texture of the FDM filament for Stages 1-3. The surface showed elongated groove marks as it progressed through the stages, which is attributed to abrasion, particularly caused by the teeth of the gears used for pulling the filament through the machine. The surface showed severe damage as it passed through the hot nozzle (Stage 3), with regions that appear to have been severely abraded (**Figure 3-11c**). It appears that the internal surface of the nozzle orifice abraded the FDM filament, which was in a thermally softened condition. The surface wear resistance of carbon fibre-thermoplastic composites was reduced at the high temperature due to softening of the matrix phase and fibre/matrix interfacial region. Thermal softening of the polyamide matrix of the FDM

filament as it passed through and out of the FDM printer device made it more susceptible to abrasion.

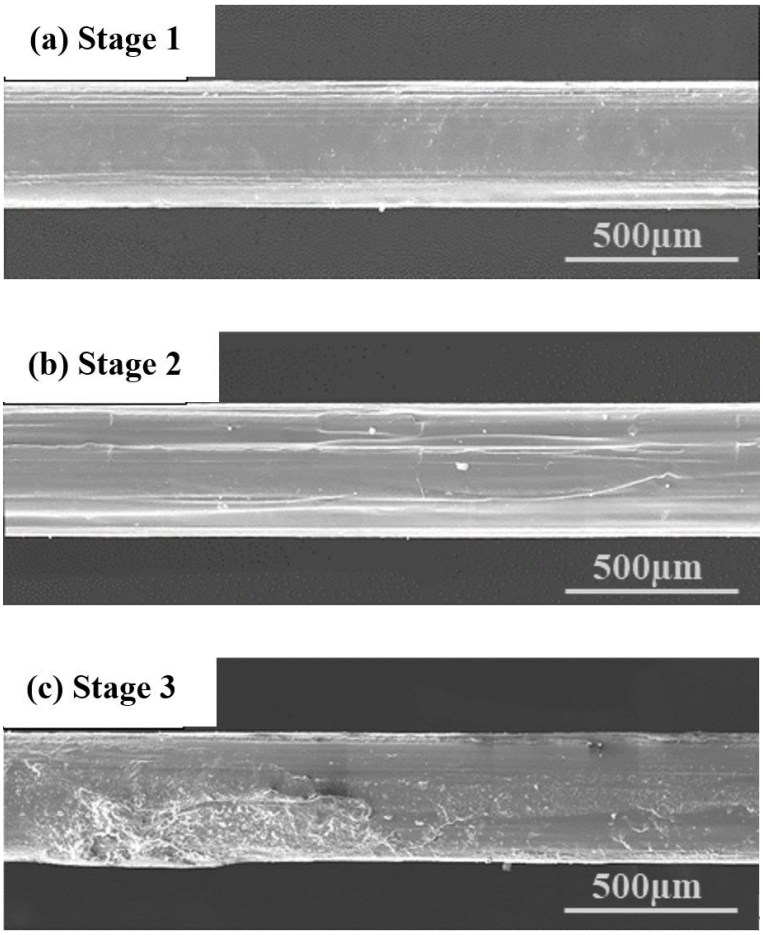

Figure 3-11 *Surface texture of the FDM filament at stages (a) 1, (b) 2 and (c) 3.*

Figure 3-12 shows the upper (contacted with the nozzle) and lower (in contact with the build platform) surfaces of the FDM filament in Stage 4. The surface texture changed abruptly after the filament was flattened by the printer head on the build platform. Fibres with waviness were exposed on the surfaces, and lacking resin can be seen in the fibre clusters. The X-ray CT image in **Figure 3-12c** shows the fibre distribution throughout the filament, where considerable fibre waviness was observed. The thermally softened matrix could not provide sufficient lateral support to the fibres causing them to spread out under the pressure and thereby become wavy. Additionally, fibre breakage occurred at the upper filament surface that was in contact with the nozzle (**Figure 3-12a**).

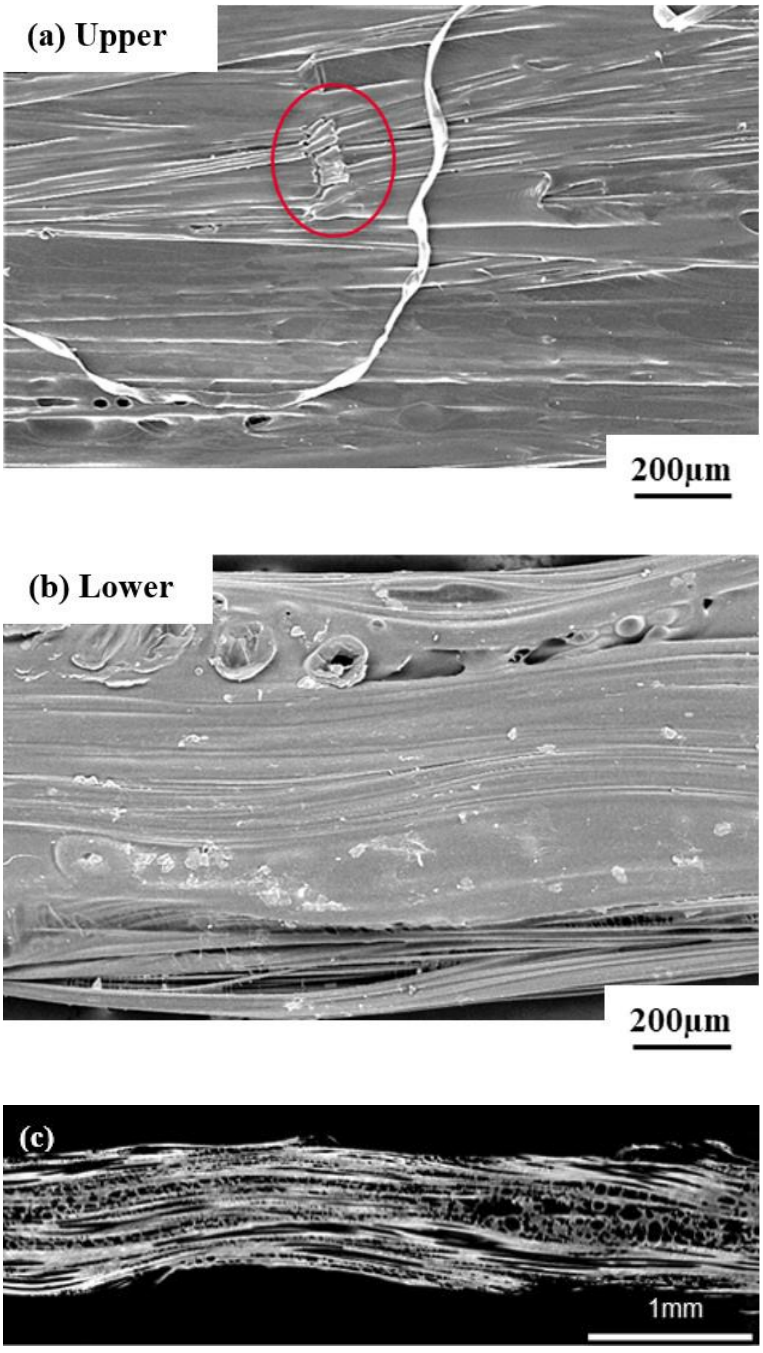

Figure 3-12 *(a-b) SEM and (c) X-CT images of carbon-polyamide FDM filament showing the surface texture and fibre distribution in the longitudinal direction in the as-printed (Stage 4) condition. The brightest regions in (c) are fibres. The circle in (a) indicates where fibres are broken. Upper and Lower indicate upper and lower surfaces, respectively.*

Damage sustained by the FDM filament was investigated by burning off the polyamide matrix to expose the carbon fibres. Carbon fibres at the FDM filament surface for each stage are shown in **Figure 3-13**. The broken carbon fibres at the filament surface for four stages were counted using the SEM images. Five samples with a gauge length of 30 mm

for each stage were examined. The fibre breakage in each stage was evaluated using the number density of broken fibres at the filament surface, which is the number of the broken fibres divided by the examined area. The result in **Figure 3-14** show that the number density of broken carbon fibres increased as the FDM filament progressed through the different stages, with a significant increase when the filament exited the printer nozzle (Stage 3). The abrasion to the hot FDM filament as it passed through the printer nozzle in a matrix softened condition broke many carbon fibres. A much greater number of fibres were broken when the FDM filament was finally printed (Stage 4), which was due to the increased fibre/device and fibre/fibre interactions caused by the involved printing device pressing and sliding against the filament. The filament being bent through an angle of 90^{o} is another reason. As shown schematically in **Figure 3-15**, the fibres bent with the filament at the nozzle tip. The surface strains have been calculated to be as high as ~1.6% [10], which exceeds the failure strain of carbon fibre (~0.5%). Therefore, bending the filament through a tight angle broke some fibres, particularly those close to the surface where the strains are the highest.

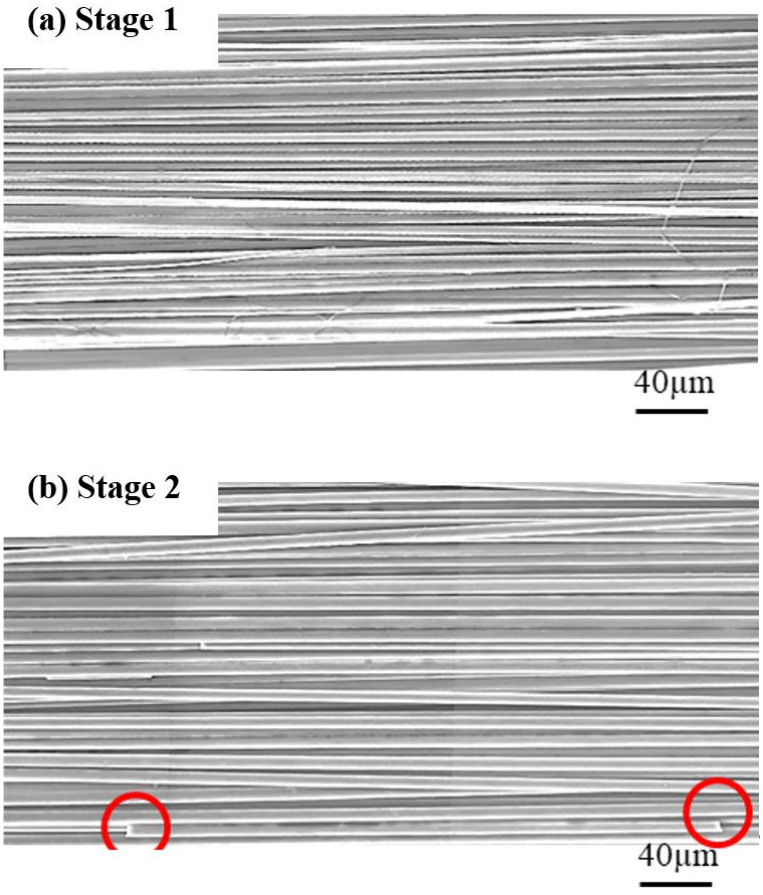

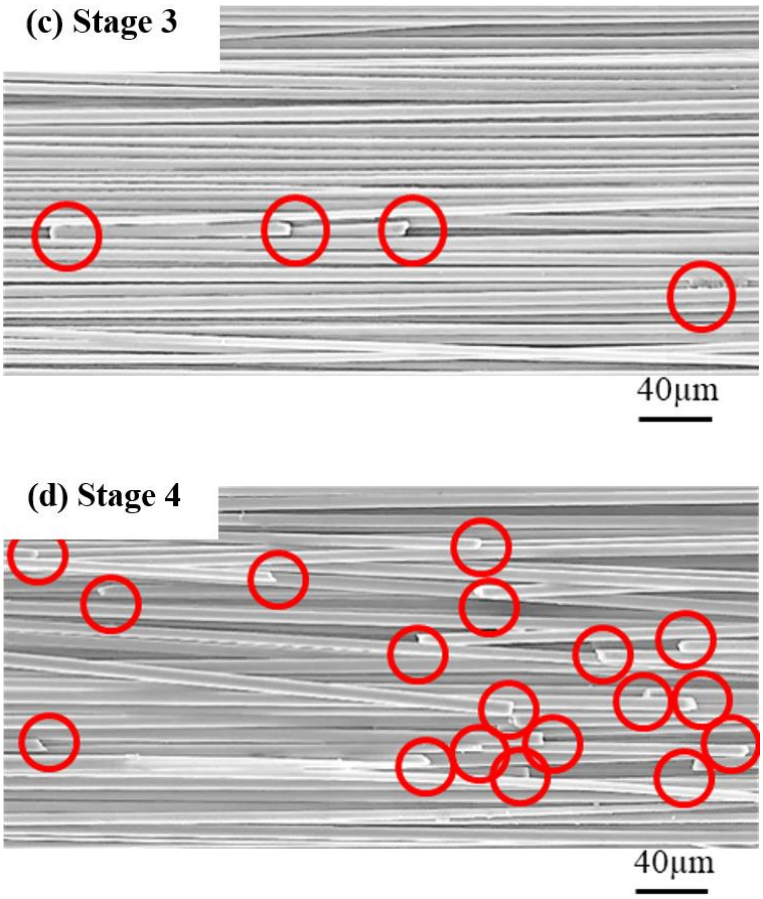

Figure 3-13 *Longitudinal images of the FDM filament (with the matrix removed) in stages (a) 1, (b) 2, (c) 3 and (d) 4. The circles indicate where fibres are broken.*

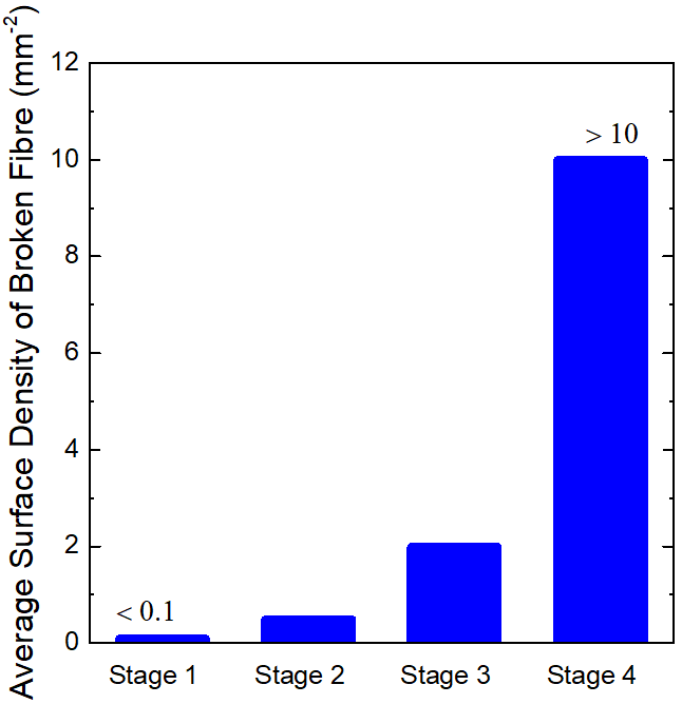

Figure 3-14 *Surface density of broken fibres for the FDM filament for each stage determined from five samples. The gauge length of a filament specimen is 30 mm.*

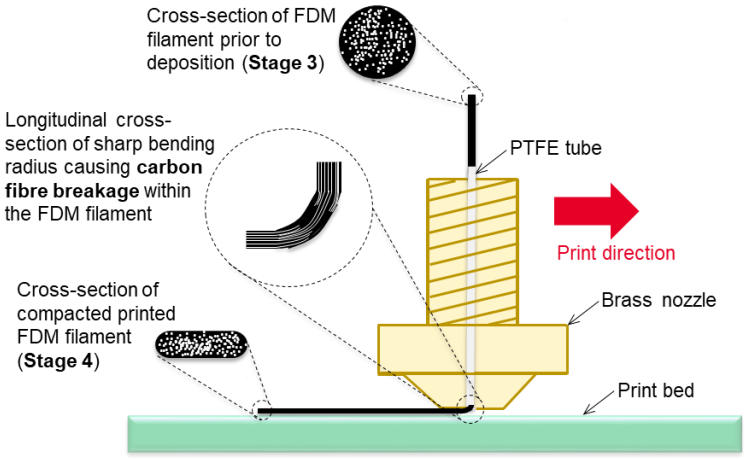

Figure 3-15 *Schematic showing bending and compaction of the filament in Stage 4 of the FDM process. (Note: Schematic created by Dr. Joel Galos, RMIT University).*

The internal microstructure of the FDM filament also underwent changes as it progressed through the FDM machine. Typical cross-sectional images of the FDM filament at each stage are presented in **Figure 3-16**. As mentioned, the as-received FDM filament consisted of a non-uniform distribution of carbon fibres within the polyamide matrix, which itself contained voids (as shown in **Figure 3-1**). This microstructure was retained through the different stages of the FDM process before the filament was deposited onto the build platform (Stage 4), with many small voids in the fibre clusters caused by insufficient rein infiltration. The fibres were spread out and voids were reduced when the filament was deposited on the build platform (Stage 4) due to the consolidation pressure applied by the printer head.

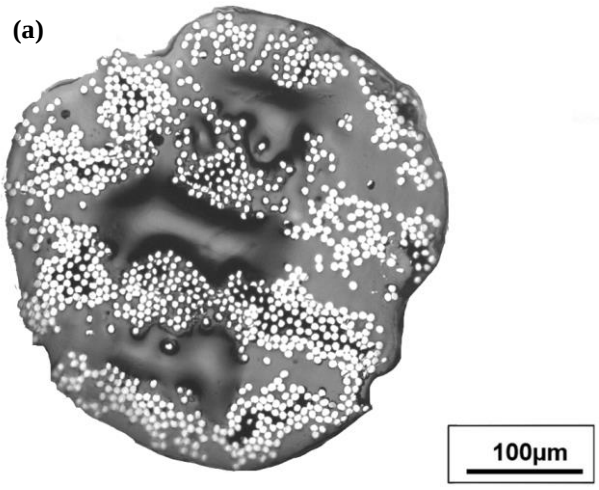

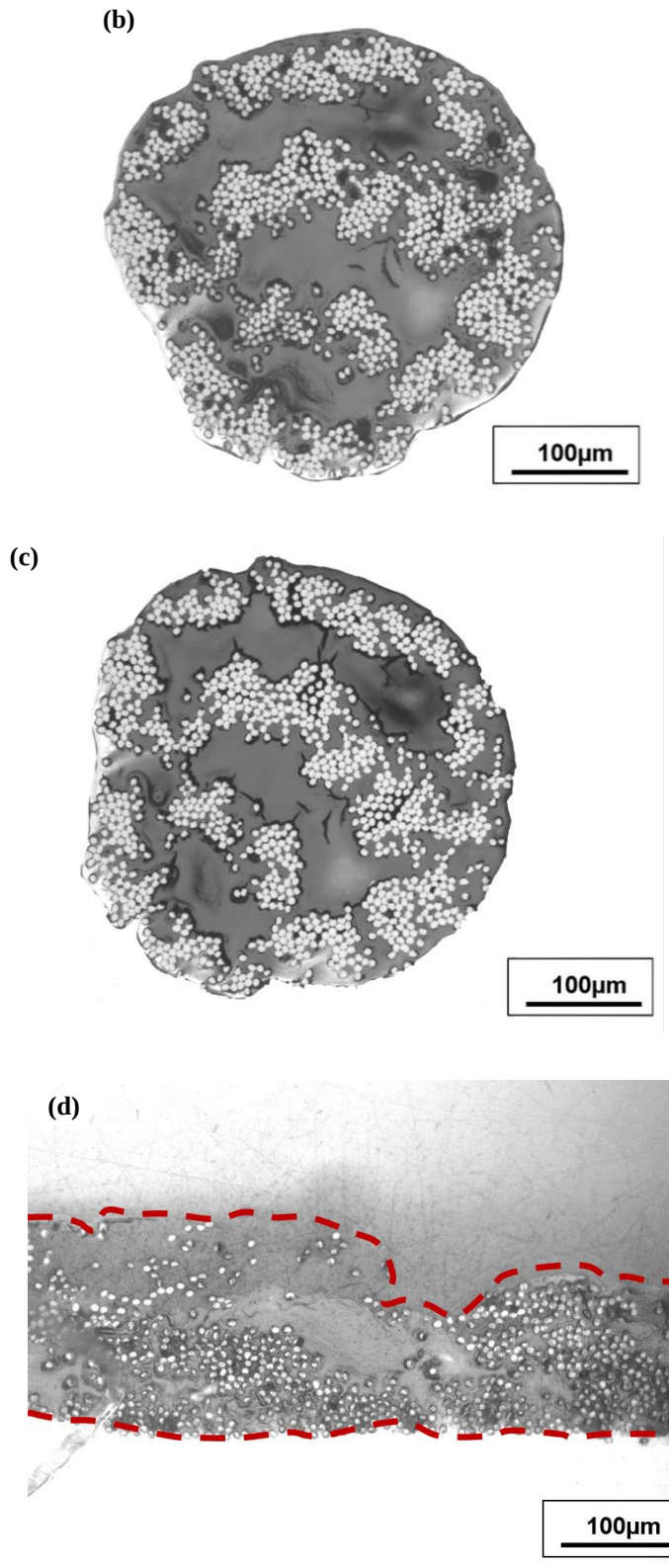

Figure 3-16 *Cross-sectional images of the FDM filament in stages (a) 1, (b) 2, (c) 3 and (d) 4. Dash lines indicate the filament boundary.*

Multiple (30) single fibre tensile tests were performed on carbon fibres extracted from the as-received feedstock FDM filament (Stage 1) and following the printing of the FDM filament (Stage 4) to investigate further the damage caused by the FDM process. As mentioned, these fibres were removed from the filament following thermal decomposition of the polyamide matrix in the vacuum oven. Plots of the failure stress distribution and the Weibull strength distribution for the carbon fibre in its original and printed conditions are shown in **Figure 3-17**. The average value ($\sigma_{av,f}$) and standard deviation value ($\hat{s}_f$) for the fibre failure stress were calculated using:

$$\sigma_{av,f} = \sigma_0 \Gamma\left(1 + \frac{1}{m}\right) \text{ and} \quad (1)$$

$$\hat{s}_f = \sigma_0 \left[\Gamma\left(1 + \frac{2}{m}\right) - \Gamma^2\left(1 + \frac{1}{m}\right)\right] \quad (2)$$

where Γ is the statistical Γ -function. The subscript f signifies a single fibre. The Weibull strength for the single fibres was calculated based on the two-parameter Weibull strength distribution:

$$P_f = 1 - \exp\left(-\left(\frac{\sigma}{\sigma_0}\right)^m\right) \quad (3)$$

where P_f is the failure probability and σ_0 and m are the Weibull parameters. The failure stress of the fibre following printing (1191 ± 174 MPa) was much lower than the original strength (1792 ± 57 MPa). This reduction shows that significant fibre damage is caused by the FDM process, in addition to the breakage of fibres within the FDM filament (**Figure 3-13**). **Figure 3-17b** shows that the carbon fibres in both the as-received and printed conditions have a two-parameter Weibull distribution. This indicates that the strength is controlled by a single type of flaw (e.g. crack) in the fibre. The m value for the fibre following printing (2.7) was lower than in the original condition (6.8), indicating that the FDM process increases significantly the distribution of failure stress values for the fibres, which is also observed in **Figure 3-17a**.

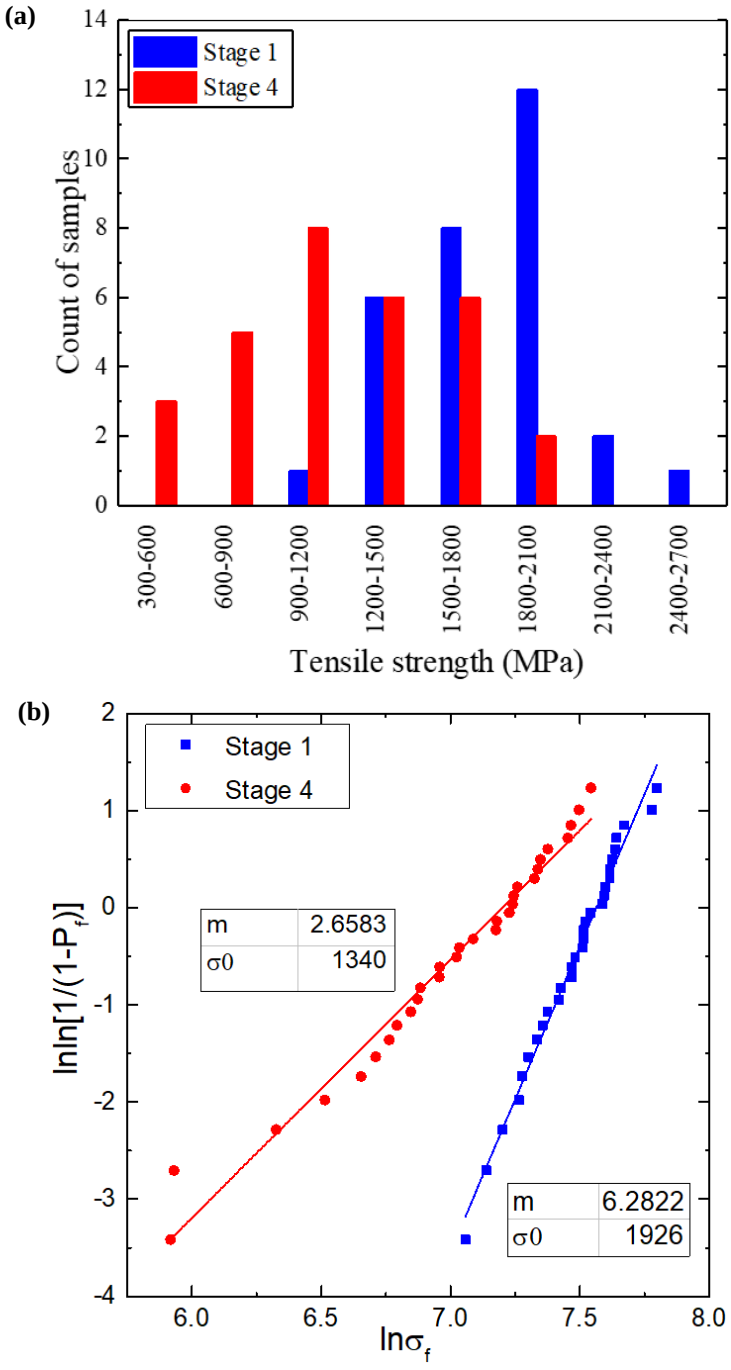

Figure 3-17 *Failure stress of single carbon fibres in the original (Stage 1) and printed (Stage 4) conditions. (a) Histogram and (b) Weibull distribution of fibre strength. The Weibull parameters of* σ_0 *and* m *are given in (b).*

Examination of the broken ends of the original and printed carbon fibres using SEM indicates that tensile fracture was initiated at the surface rather than from within the fibre. The flaw type could not be reliably identified using SEM because of its small size. However, the critical flaw size (c) in carbon fibre can be calculated from the measured fibre strength (σ_f) using linear elastic fracture mechanics:

$$c = \frac{1}{\pi}\left(\frac{K_{Ic}}{\sigma_f Y(c,R)}\right)^2 \quad (4)$$

where K_{Ic} is the mode I fracture toughness, which for PAN-based carbon fibre is ~1.0 MPa.m$^{0.5}$ [145]. *Y(c,R)* is the geometric stress concentration factor. *Y(c,R)* equals $2/\pi$ for a semicircular surface flaw, provided it is much smaller than the fibre radius. Using this analysis, **Figure 3-18** shows the calculated distribution of critical flaw sizes (assuming a semi-circular surface crack) for the carbon fibre in the original (Stage 1) and printed (Stage 4) conditions. The average critical flaw size of the fibre in the original condition is calculated to be 177 ± 88 nm, which is typical for as-received carbon fibres. After printing, the average critical size is calculated to have increased to 1018 ± 313 nm. The calculations reveal that only relatively small increases in the surface flaw size (<800 nm), which can be caused by abrasion from the FDM process, are needed to account for the large reduction in fibre strength. However, in this nanometer-size range, the concept of a sharp crack with a semicircular shape most likely does not hold, and therefore the calculations of the flaw sizes should not be considered highly quantitatively accurate. However, the calculations do indicate that a very small increase in the flaw size due to surface damage can account for the large reduction in fibre strength that occurs in the FDM process.

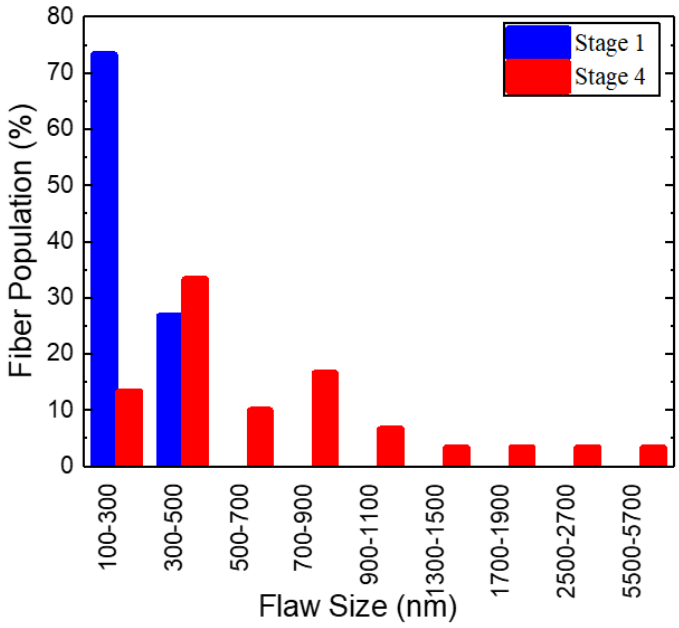

Figure 3-18 *Calculated distribution of critical flaw sizes in single carbon fibres in the original (Stage 1) and printed (Stage 4) conditions.*

3.3.2 Effect of FDM stages on tensile properties of carbon-polyamide filament

The tensile properties of the FDM filament were reduced as it proceeded from the original stock material through the FDM machine to be printed on the build platform. Tensile stress-axial displacement curves for the FDM filament taken at the different stages are shown in **Figure 3-19**. The tensile stiffness, ultimate strength and elongation-to-failure of the filament are reduced by the FDM process. The changes to the tensile modulus and failure stress of the FDM filament at the different stages of the process are shown in **Figure 3-20**. The modulus of the FDM filament remained constant (within the bounds of experimental scatter as defined by the error bars) as it proceeded through the stages until it was heated and exited the printer nozzle (Stage 3), when a small but significant reduction occurred (~10%). A further reduction (another 11%) occurred when the FDM filament was deposited on the build platform (Stage 4). The FDM filament strength shows a different dependence on the process stages than that measured for modulus. The failure stress dropped (by ~8%) after being drawn into the printer head (Stage 2). After the FDM filament was contacted with the nozzle of the FDM machine (Stage 3), the strength dropped by 14% compared to the original value. The failure stress dropped even further (another 30%) after the FDM filament was printed on the build platform. These results reveal that no single stage of the FDM process caused the reduction in the tensile properties of the FDM filament; instead, multiple stages are responsible.

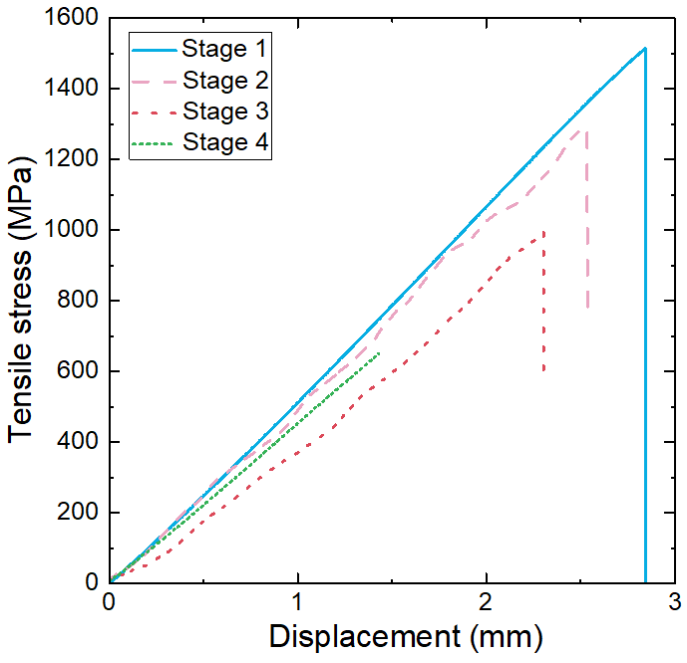

Figure 3-19 *Tensile stress-displacement curves for the FDM filament at the different stages.*

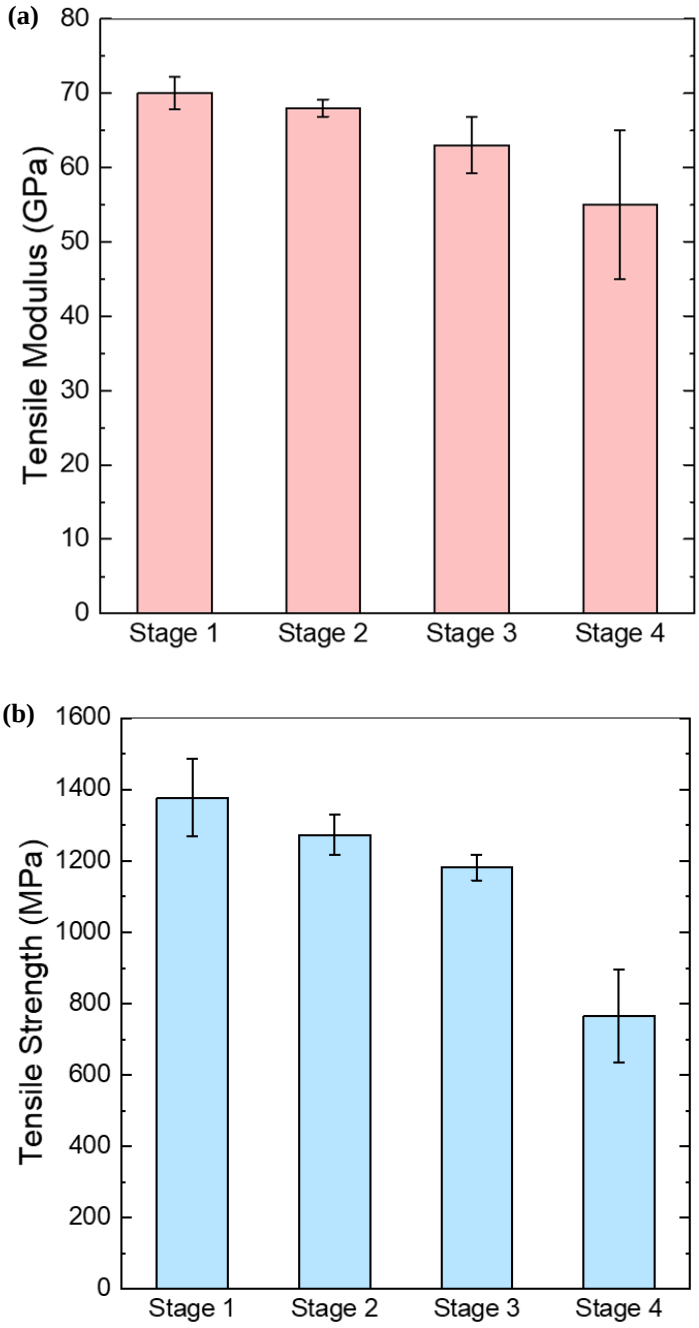

Figure 3-20 *(a) Tensile modulus and (b) tensile strength values of the FDM filament at the different stages.*

Figure 3-21 shows a typical fracture surface of the failed FDM filament in Stage 1 and Stage 4. From **Figure 3-21a**, textured microflows indicating crack growth direction in the resin-rich areas of the Stage 1 filament are present. The arrows indicate the local crack growth directions. The defects such as voids, microcracks at the fibre/matrix interface and broken fibres appear to initiate the fracture, which spreads through the filament. Fibrillation patterns (shown in the red circles) reveal the typical ductile-type fracture in a thermoplastic

matrix. Fibre breakage with some fibre pull-out occurs on the fractured surface of the Stage 1 filament. The fracture surface of the Stage 4 filament (**Figure 3-21b**) was similar to Stage 1.

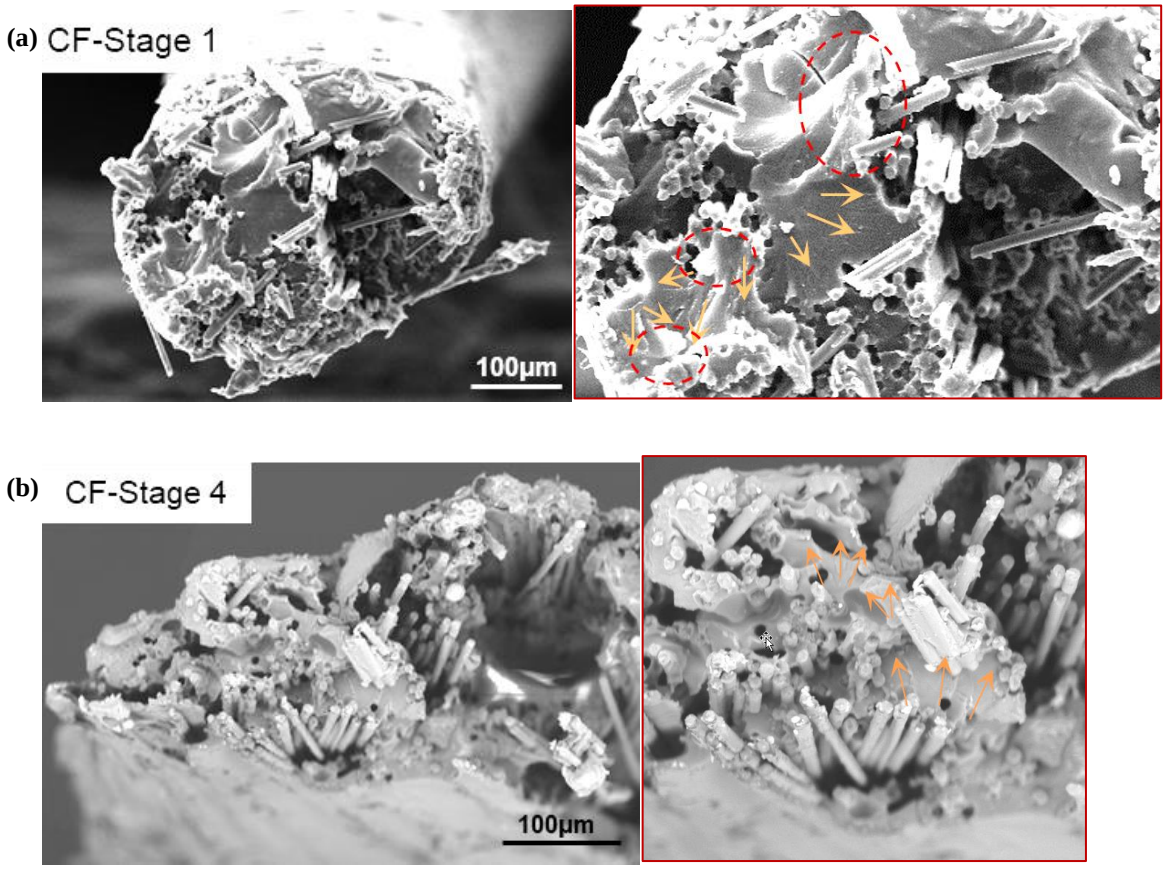

Figure 3-21 *Failure surface of the FDM filament at (a) Stage 1 and (b) Stage 4. Images with red border on the right are the closer inspection showing the fracture growing through the resin.*

3.3.3 Effects of feeding device modification on tensile strength of carbon-polyamide filament

As reported above, the serrated metal gear mechanism used to draw the filament into and through the FDM printer causes some fibre damage which reduces the tensile failure stress. It is believed that the hard tip of the gears abrade the filaments during the gripping action which damages and breaks fibres at the surface. To overcome this problem, the gear was replaced in the FDM machine with a rubber device (**Figure 3-7**). The effect of the modified gear mechanism on the tensile strength of the carbon-polyamide filament following Stage 2 of the FDM process (material feeding process) is shown in **Figure 3-22**. The tensile strength of the FDM filament in Stage 2_M (i.e. using the rubber device) was the same as the original filament, and ~7% higher than the standard Stage 2 filament (i.e. serrated steel gear).

The flexible contact surface (rubber) in the modified feeding system eliminated abrasion to the FDM filament in Stage 2. The results demonstrate that the modification strategy on the printer in this study can stop abrasion and thereby improve the tensile properties of 3D printed filaments.

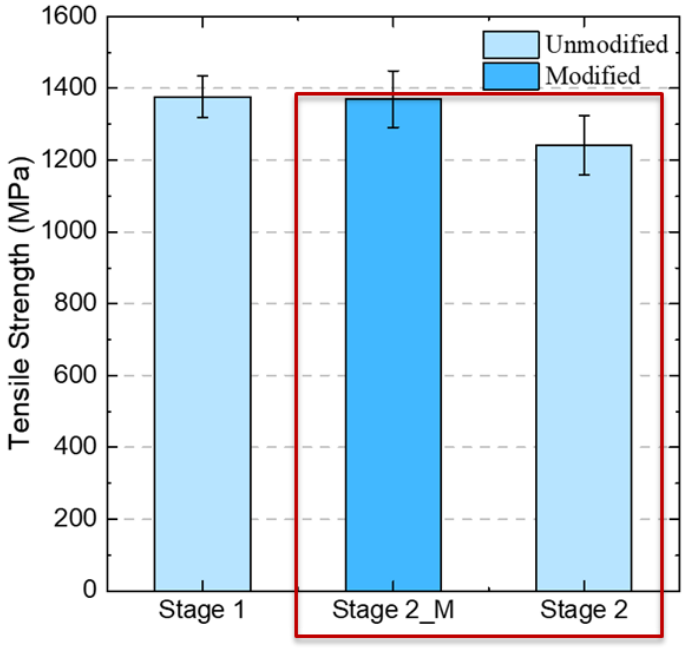

Figure 3-22 *Tensile strength of the Stage 2 filament using modified material feeding system. The original (Stage 1) filament strength is shown for comparison.*

3.3.4 Effect of FDM stages on compressive properties of carbon-polyamide filament

The effect of the different stages of the FDM process on the compressive failure stress of the FDM filament is shown in **Figure 3-23**. In all cases, the FDM filament failed by carbon fibre kinking within a well-defined kink band, as shown for example in **Figure 3-24**. Failure by kinking indicates that the compression test method provides a measure of the material strength, and is not determined by geometric effects such as global buckling of the filament. Furthermore, the AE technique did not detect any fibre failures until the onset of kinking, when the FDM filament failed instantaneously with an immediate and large rise in the recorded number of AE events. This suggests that the kinking process was unstable, with all the fibres failing at the same time as the kink band propagated rapidly across the load-bearing section of the filament.

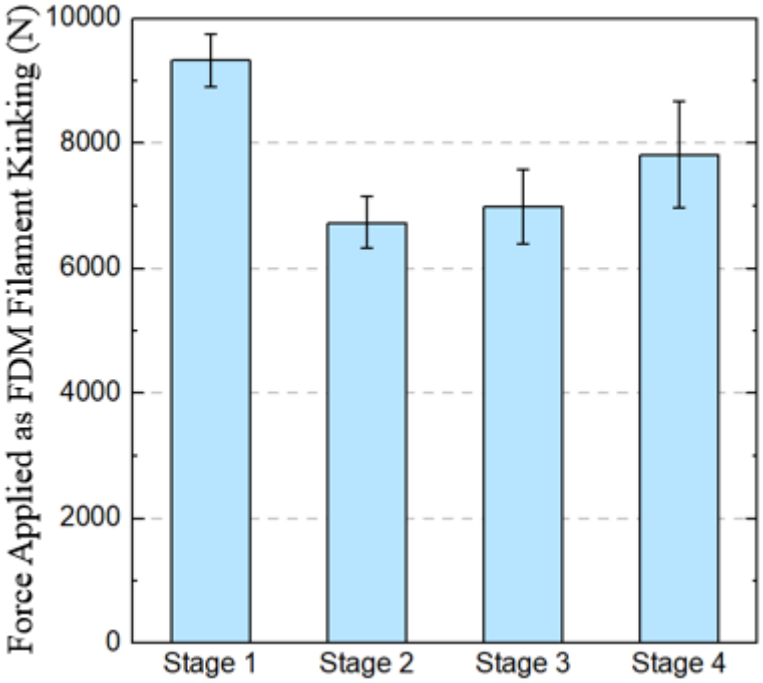

Figure 3-23 *Compressive kinking load of the FDM filament at the different stages.*

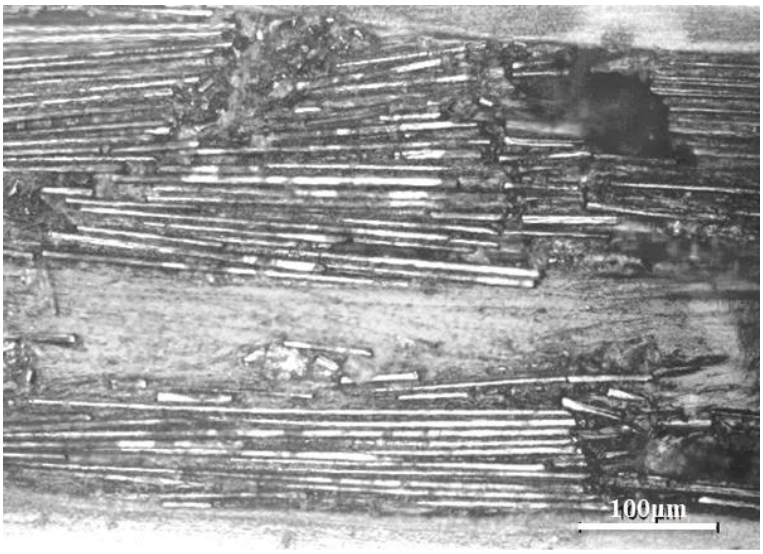

Figure 3-24 *Optical micrograph of filament kink band.*

Figure 3-23 shows that the kinking failure load for the FDM filament dropped as it came into contact with the gear mechanism (Stage 2). The scratches caused by gear abrasion can act as geometric stress raisers to initiate the kinking failure process. Therefore, it is believed that the abrasion caused by the gears is responsible for the reduced kinking load of the FDM filament. Following this reduction in Stage 2, the failure load of the FDM filament remained constant (within the bounds of experimental scatter) for the remainder of the FDM

process. It appears that the large increase in fibre breaks that occurred in Stages 3 and 4 does not significantly reduce the compressive load limit.

3.4 Conclusions

This study has demonstrated that the FDM process using a Markforged® printer causes significant damage to the carbon fibre-thermoplastic filament used for 3D printing of continuous fibre laminates. The surface of the FDM filament is abraded when it passes through the different stages of the FDM process by the gripping action of the serrated gear mechanism used to pull the filament (Stage 2) and during contact with the nozzle (Stage 3). Damage is also caused when the FDM filament is bent through 90^{o} and pressed onto the build platform (Stage 4). Abrasion grooves are formed on the FDM filament, which includes broken and damaged carbon fibres. Abrasion and bending effects cause a rapid increase in the number of broken fibres in the filament towards the end of the FDM process (Stage 4). Also, surface damage to fibres by the FDM process increases the flaw size. This damage is sufficient to reduce the average failure stress of single carbon fibres within the FDM filament by about 33%. FDM-induced damage also reduces the tensile and compressive kinking stress values of the FDM filament studied here by ~44% and ~25%, respectively. It is worth noting that this modified compressive test is a qualitative method to compare the response of fibre filament at different stages under compressive loading. However, the results can also be affected by the specimen shape (Stage 1-3 filaments are circular and Stage 4 is flat), which is difficult to be excluded using experimental methods. Therefore, this test was not further conducted on other fibre types investigated in the following chapters, and only on the carbon fibre filament (which have more significant fibre damage caused by 3D printing process).

The study also employed a feeding system modification to the printer to mitigate abrasion to the FDM filament in Stage 2. The tensile strength of the filament was not reduced in Stage 2 using the modified feed device. Opportunities also exist to modify the FDM process to reduce filament damage and thereby 3D print continuous fibre laminates with improved mechanical properties.

The study shows that the spacing between the printer head and the build platform is critical as it deforms the circular cross-section of the filament into a flat ribbon. The effect of the distance between the printer head and built platform on the mechanical properties of the 3D printed composites is an important research topic if the gap spacing can be precisely

controlled. Decreasing the distance can help the matrix to spread out and improve the fibre/matrix interface due to the higher consolidation pressure, but might cause more damage to fibres due to more serious compaction and abrasion from the printer and fibres themselves. Also, if the distance is too small, the filament is unable to be extruded out of the nozzle. If the distance is large, the interaction between fibres and the device and fibres themselves can decrease and thereby decrease the fibre damage. Also, the printed materials cannot stick on the platform when the distance is too large. For this reason, the gap spacing used in this research was set to a constant value as recommended by the MarkForged company, and was not varied.

Additionally, the non-uniformity of the fibre distribution, polymer-rich areas and voids within the composite filament used in this study are also factors governing the mechanical properties of the 3D printed composites. These imperfections might be reduced during the manufacturing process for the pre-impregnated filament. For example, an appropriate tension force applied to the fibre bundle can control the distance between fibres and thereby improve the fibre distribution after polymer impregnation. The pressure for the resin to infill the fibre bundle is another critical factor, with higher pressure expected to reduce the void content. Furthermore, it is also possible to improve the fibre distribution during the printing process when the filament is flattened onto the build platform. Methods like using a thinner nozzle, adjusting the printing temperature, and adjusting the nozzle/platform distance might help in improving the fibre distribution through matrix spread out, as well as decrease the void content.

While the research findings presented in this chapter are specific to the Markforged® machine used in this study, the FDM-induced damage to the carbon fibre-polyamide filament indicates that other types of filament materials may be damaged using the FDM process. To explore this further, the next chapter presents a study into the effect of the FDM process on the microstructural and mechanical properties of polyamide filaments containing continuous glass or aramid fibres. The effect of the FDM process on glass and aramid filaments is compared to the carbon filament studied in this chapter.

CHAPTER 4: DAMAGE TO GLASS AND ARAMID FIBRE FILAMENTS USING THE FDM PROCESS

Abstract

The previous chapter presented an experimental investigation in the damage and tensile properties of continuous carbon fibre-polyamide filament during the 3D printing of composites using the FDM process. In this chapter, damage to and changes to the mechanical properties of continuous glass-polyamide and aramid-polyamide filaments caused by the FDM process using a MarkForged printer are determined. Using a similar experimental approach to that used in the previous chapter, it was found that glass fibre damage occurs at multiple stages of the FDM process with the final stage, in which the filament is extruded from the printer nozzle and deposited on the built platform, causing the most severe damage. The average tensile modulus and strength of the glass-polyamide filament decreased by 15% and 32% due to fibre damage caused by the FDM process. In contrast, no fibre damage occurred to the aramid-polyamide filament, including in the final deposition stage, and this is due to the high toughness, high failure strain and flexibility of Kevlar fibres. As a result, the 3D printed aramid-polyamide filament experienced a relatively small loss in tensile properties in the FDM process. The causes of the fibre damage and other defects introduced by the 3D printing process and the resultant reductions to the mechanical properties of the glass and aramid filaments are identified, and compared to those of the carbon filament (as investigated in the previous chapter).

4.1 Introduction

Several studies have investigated the mechanical properties of 3D printed continuous glass- and aramid fibre-polymer composites fabricated using the FDM process, including the tension [23, 28-30, 54, 55, 58, 99], compression [28, 56], interlaminar shear [57], fatigue [146] and other properties [29, 59]. The mechanical properties of these composites are usually much lower than glass and aramid fibre composites fabricated using conventional techniques, such as autoclave processing and vacuum bag resin infusion, as reported in **Chapter 2**. The effect of the 3D printing process on the microstructure and resultant property changes of FDM composite materials have also been investigated. For instance, Chabaud et al. [58] reports 8x higher porosity in 3D printed composites than in the stock filament used in the FDM process, and attributes the reduction in composite properties to the higher void content. Cagri et al. [99] identified multiple types of microstructural defects in 3D printed continuous fibre-polymer composites which reduce the properties, including imperfect interfaces between printed layers, voids and incomplete fill density. Despite these studies, the effect of the 3D printing process on the microstructure and mechanical properties of polymer-based filaments containing continuous glass or aramid fibres is not fully understood.

The previous chapter presented an experimental study characterising the fibre damage to continuous carbon-polyamide filament during different stages of the FDM printing process, starting with the original stock filament to the final deposited filament. In this chapter, the damage caused to continuous glass-polyamide and aramid-polyamide FDM filaments as they pass through the different stages of the Marktwo® FDM printer are determined. The effect of fibre damage caused by the different FDM process stages on the tensile properties of the filaments are determined. The study compares the microstructural damage and tensile properties of the glass and aramid-based filaments to those of the carbon filament presented in the previous chapter.

4.2 Materials and Methodology

4.2.1 Materials

The FDM filaments used in this study were continuous glass fibre-polyamide and aramid fibre-polyamide, which are the stock materials for the 3D printing of composite laminates. The filaments were supplied by MarkForged® company. The nominal diameters of the as-received glass- and aramid-fibre filaments are 0.32 mm and 0.33 mm, respectively,

although they are not perfectly cylindrical in cross-section. Cross-sectional images of the as-received stock filaments before FDM printing are presented in **Figure 4-1**. The number of fibres within the glass and aramid filaments are ~400 and ~270, with the single fibre diameters measured to be 9 µm and 12 µm, respectively. The glass-polyamide filament shows uneven fibre distribution, with localised regions of high fibre density and other regions that are polyamide-rich. The aramid fibres are more evenly distributed within the FDM filament, although regions rich in fibres or polyamide exist. Microcracks at fibre/matrix interfaces occurred in both filaments. The average fibre volume fraction of the glass-polyamide filament, which was determined by the polymer burn-off test performed in a vacuum furnace under 500°C, was ~32%. The fibre content of the aramid-polyamide filament, measured by phase-contrast imaging (ImageJ), was ~41%. (The pyrolysis method was not employed to measure the aramid fibre content because of the temperature used is close to the degradation temperature of the aramid [143]).

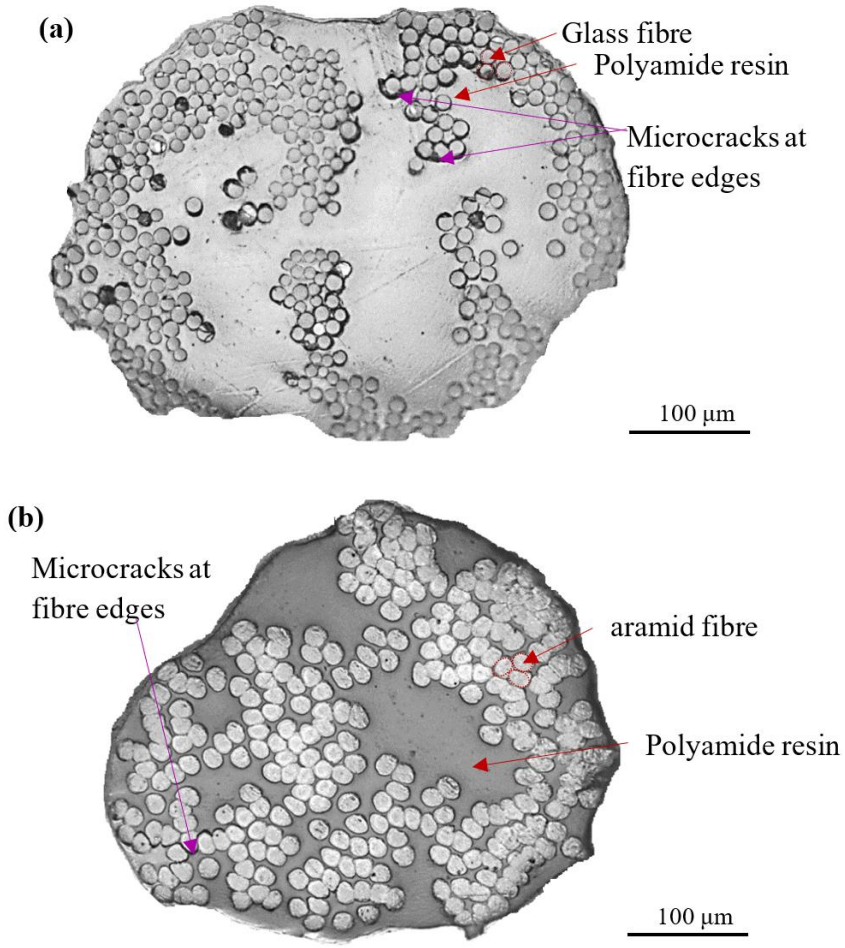

Figure 4-1 *Optical micrographs showing the cross-section of (a) glass- and (b) aramid-polyamide filaments in the as-received (Stage 1) condition.*

4.2.2 FDM printing process

The continuous carbon fibres within the FDM polyamide filament are weakened during the 3D printing process, and this was investigated in the previous chapter for the four stages. The four stages in order are: (i) as-received filament is fed into the FDM machine by (ii) gear mechanism consisting of a serrated roller which grips the filament and then (iii) draws it into the heater chamber to soften the polyamide matrix and is then extruded through a circular nozzle to be (iv) printed onto the flat build platform. The effect of these stages on fibre damage and the tensile properties of the glass and aramid filaments was determined.

4.2.3 Filament specimen preparation

The glass and aramid filaments retained their quasi-cylindrical shape throughout the FDM process until the final print stage, when they were flattened by the printer head on the build platform (as described for carbon filament in **Chapter 3**). In this study, the gap between the exit point of the nozzle and the build platform was set at 0.1 mm, as recommended by Markforged®. The gap is smaller than the filament diameter, and so the printer head flattened the filaments into a rectangular-like cross-sectional shape when printed on the build platform.

The printing parameters are fixed in the Markforged® Marktwo printer for specific polymer and fibre materials, with the extrusion temperature set at ~260°C, the filament print rate at 15 mm/s, and the printed single filament thickness at ~100 μm for glass- and aramid-polyamide due to the gap set between the nozzle head and build platform. Dynamic mechanical analysis (DMA) and thermogravimetric analysis (TGA) [147] reveals that the glass transition temperature of aramid fibre is ~240-260°C and decomposition temperature is ~510-560°C (both in nitrogen and air atmospheres). Therefore, the aramid undergoes glass transition softening during printing but does not experience any decomposition. The width of a single filament after being printed on the build platform is ~1 mm. The build platform was at room temperature, leading to a rapid solidification of the matrix phase as the hot filament (~260°C) exited the printer nozzle.

4.2.4 Microstructural examination

The effect of each stage of the FDM process on damage to the glass and aramid fibres in the FDM filaments was evaluated by physical examination and mechanical testing. The FDM filaments were examined using optical microscopy and scanning electron microscopy

(SEM). The SEM was performed using a TM4000PLUS (HITACHI), with the FDM filaments coated with a thin iridium film prior to the examination to avoid electron beam charging effects. To expose the fibres inside, a resin burn-off test was conducted on the glass-polyamide filaments. Filaments were heated at 500°C in a vacuum furnace for 5 hours, and then the recovered fibres were examined using SEM.

4.2.5 Mechanical property testing

Tensile tests were performed on the FDM filaments after being extracted from each stage of the FDM process. The filament preparation and tensile test method were the same as that described in **Chapter 3**. At least fifteen filament specimens from each of the four stages were tensile tested.

In this study, the acoustic emission (AE) system (MISTRAS-2001, China) and a wide-band transducer (R15, China) with a frequency range of 20-1000 kHz were used to monitor the glass and aramid filaments from different stages during the tensile tests. AE monitoring was used so that the differences in the fracture of the composite filaments with or without fibre damage can be identified. The AE signals detected by the transducer were magnified using a preamplifier with a gain of 40 dB and additional amplification of 20 dB using the AE system. A viscous coupling agent (silicone gel) was used to ensure transmission of acoustic waves from the filament specimen to the transducer with minimal attenuation at the interface. The acquisition parameters of the AE system were set at an amplitude threshold of 50 dB, peak definition time (PDT) of 30 µs, hit definition time (HDT) of 150 µs, hit lockout time (HLT) of 300 µs, and the waveform data point recording rate of 3 M/s. A single transducer was held on the tab during tensile testing. The gauge length of the filament specimens used in this case was 150 mm. A minimum of five FDM filaments from Stage 1 and 4 were monitored using AE.

4.3 Results and Discussion

4.3.1 Effects of FDM stages on damage to glass- and aramid-polyamide filaments

Figure 4-2 and **Figure 4-3** show respectively the surface texture of the glass and aramid filaments at Stages 1-3 of the FDM process. Many fibres are visible on the filament surface in Stages 1 and 2, and the filaments underwent changes to the surface texture as they passed through the hot printer nozzle (Stage 3). From **Figure 4-2c**, resin with a fish-scale

pattern can be seen along the glass-polyamide filament with small holes left due to melting of the matrix. The aramid fibres within the filament showed waviness due to the fibre softening (**Figure 4-3c**).

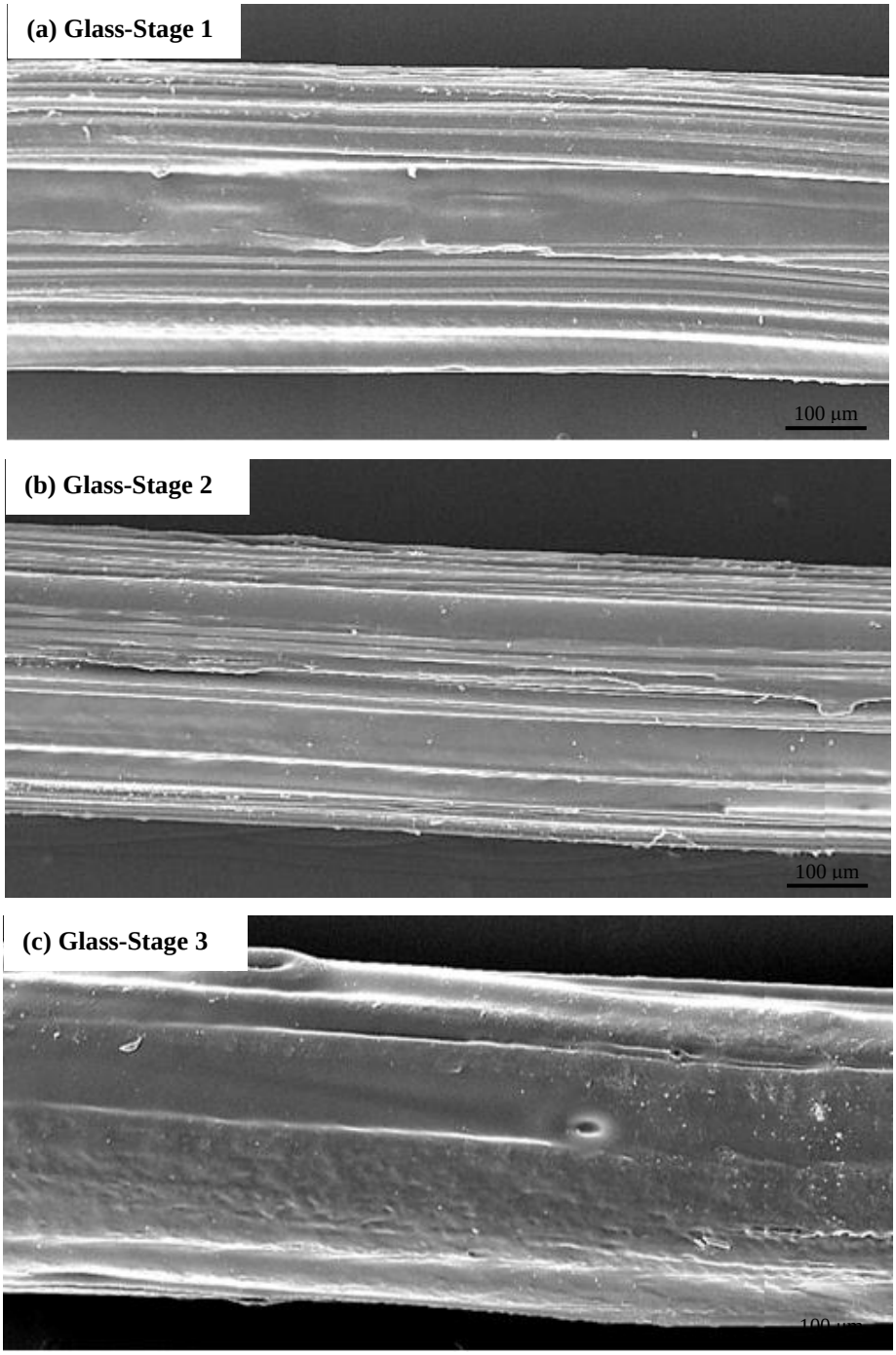

Figure 4-2 *Surface of glass-polyamide filament in Stages (a) 1, (b) 2 and (c) 3.*

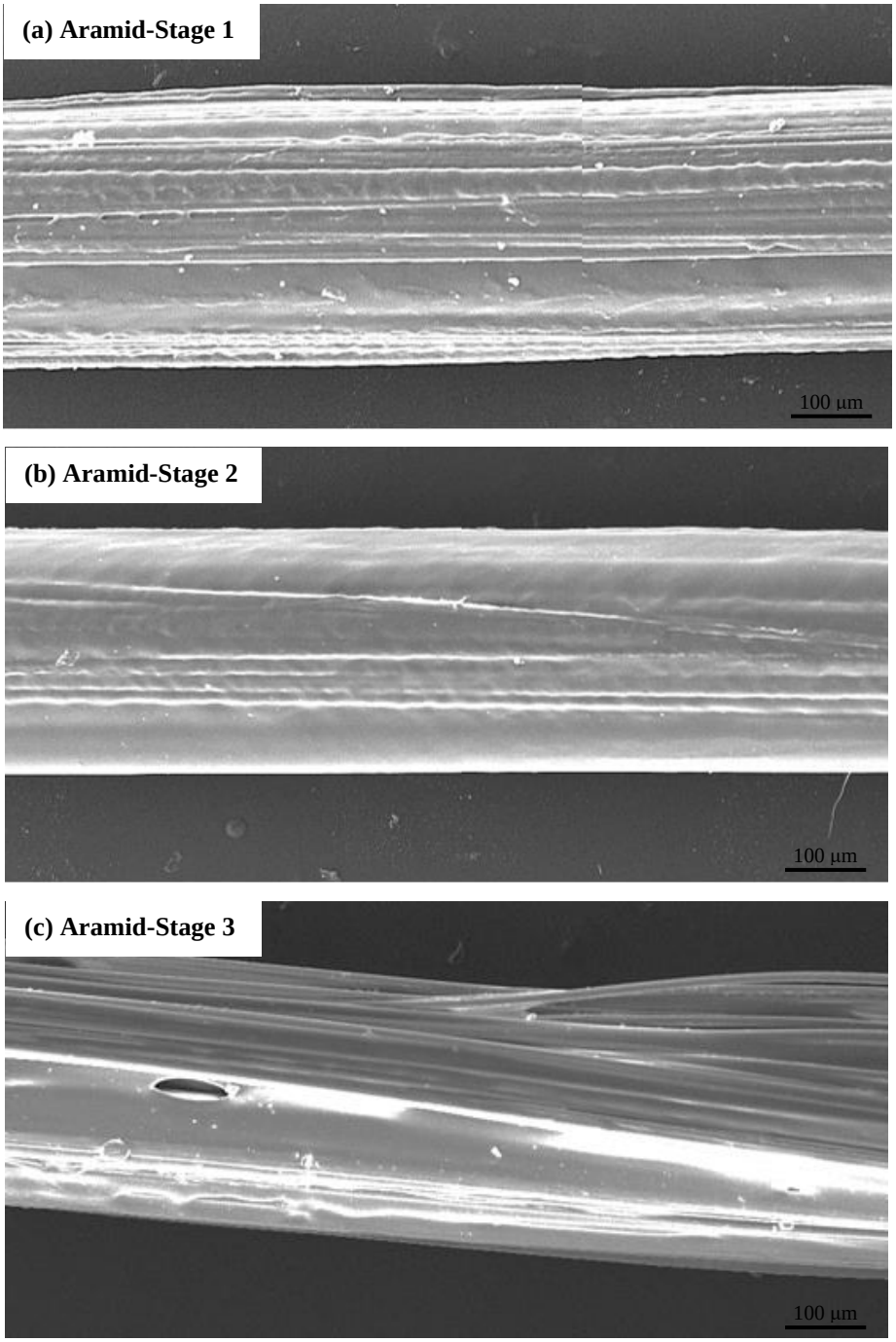

Figure 4-3 *Surface of aramid-polyamide filament in Stages (a) 1, (b) 2 and (c) 3.*

Figure 4-4 and **Figure 4-5** show respectively the cross-section and surface texture of the flattened glass- and aramid-polyamide filaments in Stage 4. When the filament is bent 90° during deposition onto the build platform, the upper surface undergoes compression and the lower surface (in contact with the platform) experiences tension (**Figure 3-15**). **Figure 4-4** shows broken glass fibres near the upper and lower filament surfaces indicating fibre fracture occurs under compression and tension. Many of the aramid fibres buckled over a relatively short length (< 500 µm) near the surfaces, but there was no evidence of fibre breakage

(**Figure 4-5b**). The waviness angles of the aramid fibres at buckled area on the filament surface was measured between approximately ±15° using ImageJ (Directionality).

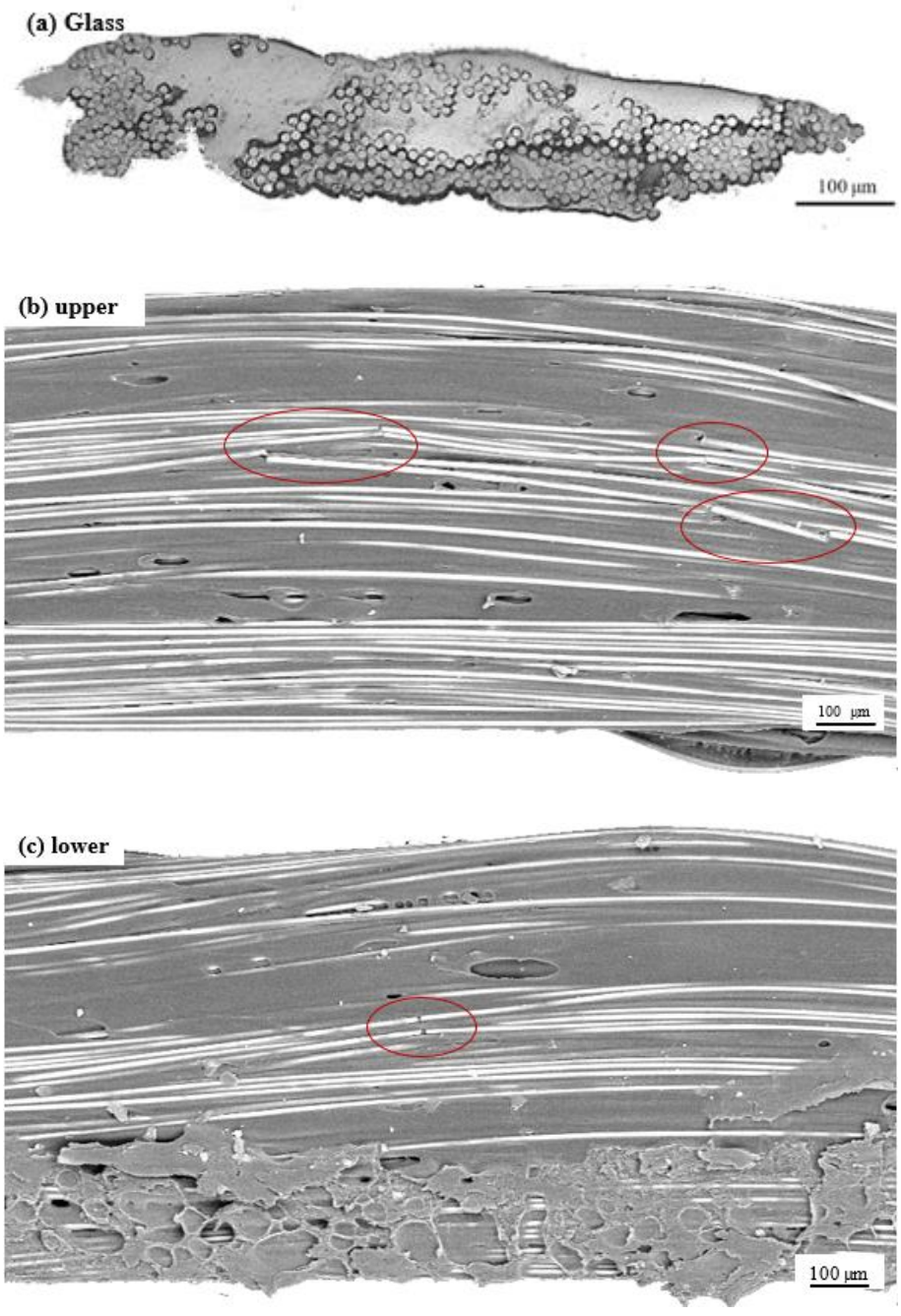

Figure 4-4 *(a) Cross-section and (b) upper and (c) lower surfaces of the glass-polyamide filament in Stage 4. Fibre breakages on the upper surface are circled in (b).*

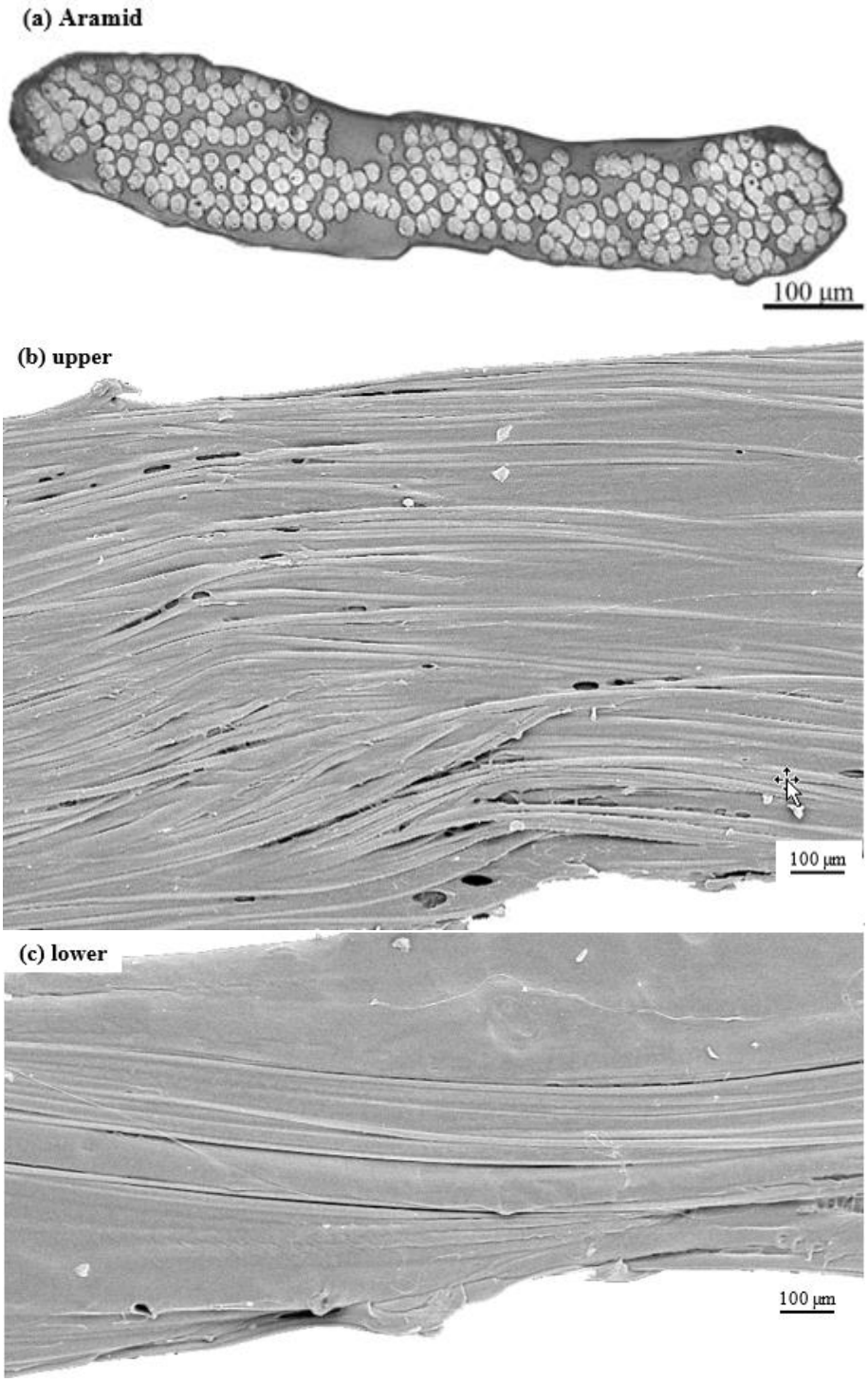

Figure 4-5 *(a) Cross-section and (b) upper and (c) lower surfaces of the aramid-polyamide filament in Stage 4. Fibre buckling on the upper surface is circled in (b).*

Damage sustained by the glass-polyamide filament was investigated by burning off the polyamide matrix to expose the fibres. Glass fibres at the FDM filament surface for each stage are shown in **Figure 4-6**. Five 30 mm long filament specimens for each stage were scanned in the longitudinal direction to count the number of broken fibres. The density of

broken fibres was determined from the total number of broken fibres divided by the scanned area of the filament surface. **Figure 4-7a** shows the number density of broken glass fibres increased as the FDM filament progressed through the different stages. Abrasion to the FDM filament as it passed through the serrated gears broke glass fibres (Stage 2), however no further fibre breakage occurred in Stage 3. The number of broken fibres doubled when the FDM filament was deposited on the build platform (Stage 4), which involved the FDM printer head pressing and sliding against the filament as well as the filament being bent by 90^{o}. However, the measured number of broken glass fibres was much less than for carbon fibres following the FDM process (**Figure 4-7b**). The measurements indicate that about 30x more carbon fibres are broken in the FDM process compared to glass fibres, with aramid fibres not experiencing any breakages. This can be attributed to the higher strain-to-failure of glass, and particularly aramid fibres. When the filament is bent into a sharp angle, the fibres near the upper and lower surface experience significant compressive and tensile failure strain. Fibres with high failure strain can undergo bending without being damaged due to the tensile and compressive stresses. Fracture toughness is another factor affecting the damage of fibres during deposition. **Table 4-1** shows the fracture toughness values for single carbon, glass and aramid fibres [148, 149]. The glass and aramid fibres with higher fracture toughness can hinder the surface crack from propagating through the fibre under loading, minimising the fibre breakage after 3D printing. As mentioned in **Chapter 3**, abrasion caused by the printing device to the composite filament during the FDM process can cause surface damage, including to the fibres. The fibre with higher fracture toughness, like glass fibre and, in particular, the aramid fibre, which shows a tendency to fibrillate and thereby dissipate higher fracture energy, resulting in a higher resistance to damage during loading compared to the carbon fibre. Furthermore, the glass fibres (9 μm) and aramid fibres (12 μm) are slightly wider in diameter than the carbon fibres (7 μm), which will also provide some additional resistance to fracture during the FDM process.

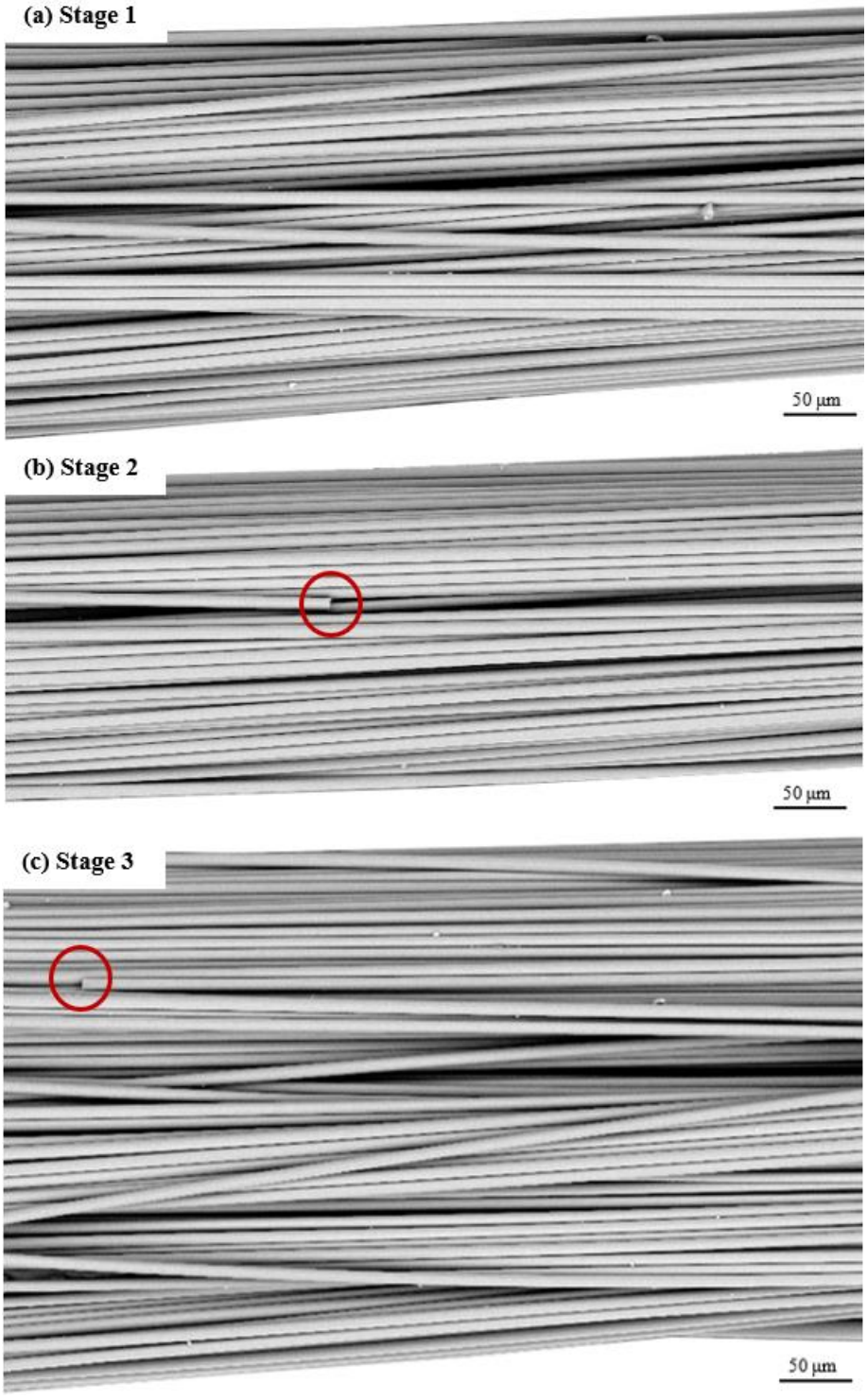
(a) Stage 1
50 µm
(b) Stage 2
50 µm
(c) Stage 3
50 µm

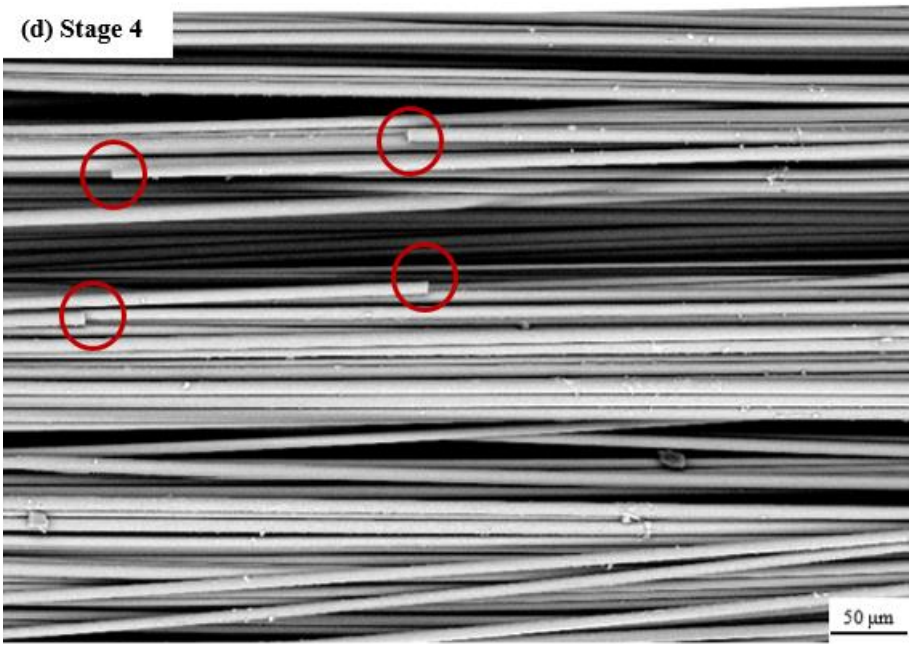

Figure 4-6 *Longitudinal SEM images of glass-polyamide filament with polymer burn off in Stages (a) 1, (b) 2, (c) 3 and (d) 4. The circles indicate where fibres are broken.*

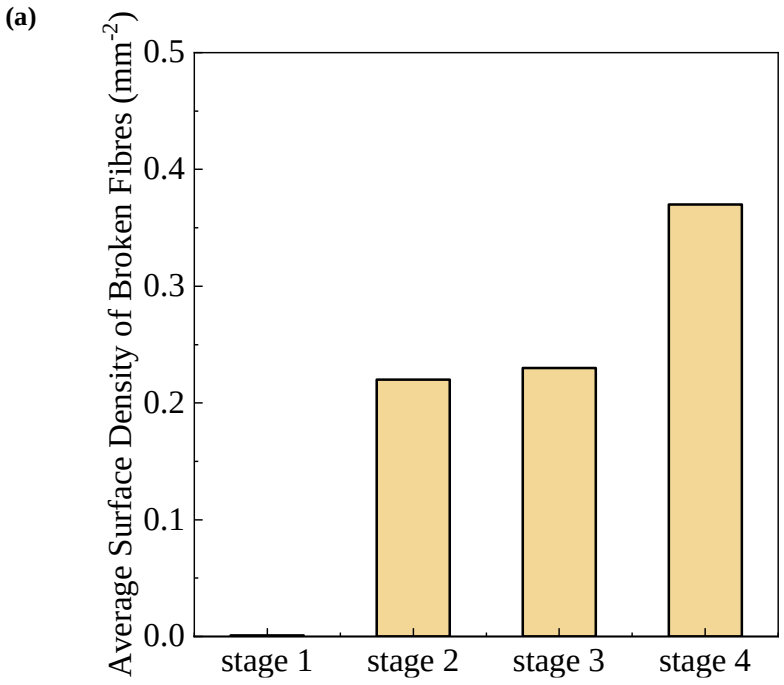

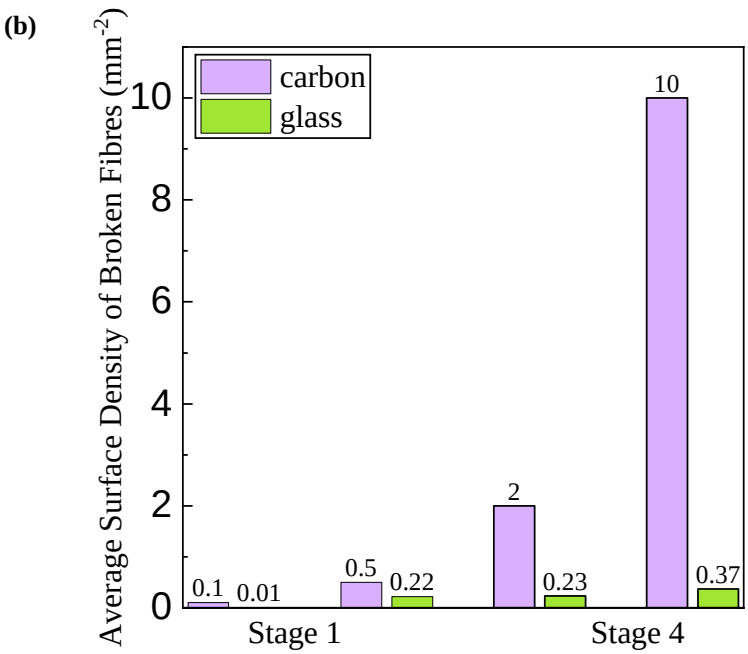

Figure 4-7 *(a) Surface density of broken glass fibres for four stages. (Determined from five sample, with each sample 30 mm long). (b) Comparison of surface density of broken carbon and glass fibres for the four stages. No aramid fibres were broken, and therefore they are not included.*

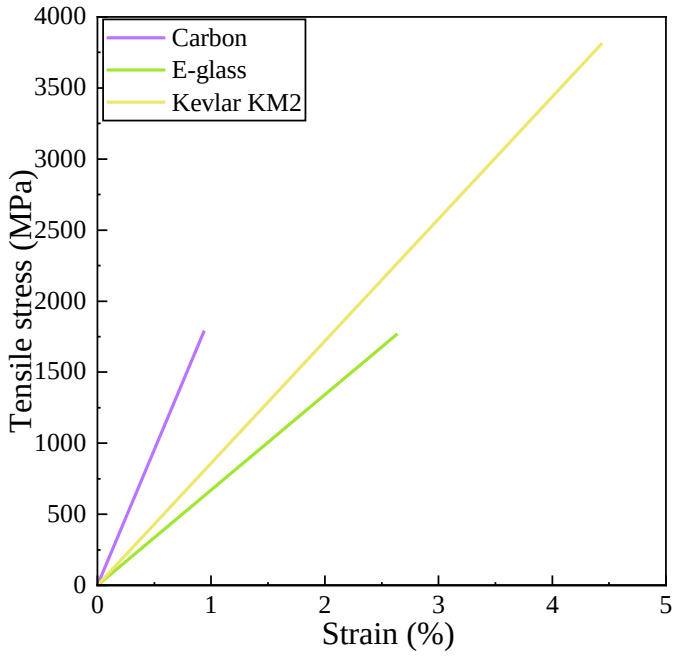

Figure 4-8 *Tensile stress-strain curves of single carbon, glass (E-glass) and aramid (Kevlar KM2) fibres. The values of carbon fibre is from* ***Chapter 3****, the other two are from the literature [148].*

Table 4-1 *Fracture toughness of single carbon, glass and aramid fibres from the literature.*

Fibre type	Crack length (μm)	Fracture toughness (MPa.m$^{1/2}$)
Carbon IM 600 [149]	0.1	1
E-glass [148]	0.1	1.08
Kevlar KM2 [148]	0.1	6.63

4.3.2 Effects of FDM stages on tensile properties of glass- and aramid-polyamide filaments

The FDM process reduced the tensile properties of the glass-polyamide and aramid-polyamide filaments as shown in **Figure 4-9**. Included in the figure are the properties for the carbon filament (which were reported in the previous chapter).

Table 4-2 presents the percentage knock-down to the tensile modulus and strength for the three types of filaments at different stages compared to the initial values in the as-received condition (Stage 1). The tensile modulus and strength of the glass-polyamide filament were reduced as it proceeded from the original stock material through the FDM machine to be printed on the build platform. The average modulus value of the glass filament decreased progressively stage-by-stage, with a final reduction of ~15% following stage 4 which is attributed mostly to breakage of glass fibres by the FDM machine during its deposition on the build platform. The failure stress of the glass filament showed a different dependence on the process stages to that measured for modulus. The average failure stress dropped by ~4% (Stage 2) after being drawn into the printer head, although the reduction is not statistically significant. After the glass-polyamide filament was contacted with the nozzle of the FDM machine under high temperature (Stage 3), the strength dropped by a further 8%, although there is large scatter in the measured filament strengths for this stage. The failure stress dropped further after the glass FDM filament was printed on the build platform, and the residual strength was ~68% of the initial value. These results reveal again that multiple stages of the FDM process are responsible for reducing the tensile properties of inherently brittle FDM filament materials such as glass. The less severe tensile property degradation for glass than for carbon is due to fewer fibres being broken by the FDM machine.

The tensile modulus and failure stress of the aramid filament did not change significantly following Stage 2 of the FDM process, and was reduced slightly in Stage 3. Due

to thermal softening of the aramid fibres, which has a glass transition softening temperature similar to the print temperature, some of the fibres became wavy when passing through the heater section of the FDM machine. In Stage 4, the tensile properties of the aramid filament were reduced further, and this was due to increasing fibre waviness when bent by 90^{o} and then deposited on the build platform. Unlike the carbon and glass fibres which were broken in the FDM process, causing a reduction of the tensile properties of their filaments, the aramid fibres were not broken and instead the properties were reduced due to increased fibre waviness caused by glass transition softening of the aramid fibres and polyimide matrix.

Table 4-2 *Percentage reduction to the tensile modulus and strength for the three types of filaments at different stages compared to initial values of the as-received condition (Stage 1).*

	Carbon-Polyamide		**Glass-Polyamide**		**Aramid-Polyamide**	
	Modulus	**Strength**	**Modulus**	**Strength**	**Modulus**	**Strength**
Stage 2	7%	3%	4%	4%	3%	6%
Stage 3	14%	5%	11%	12%	8%	10%
Stage 4	21%	42%	15%	32%	24%	16%

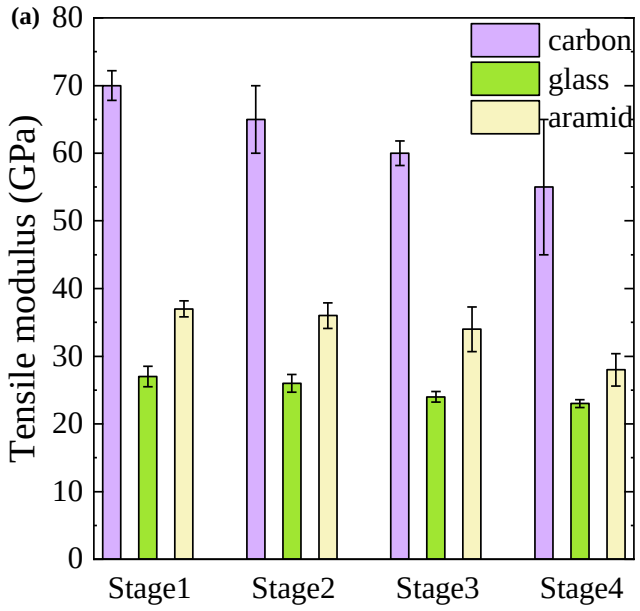

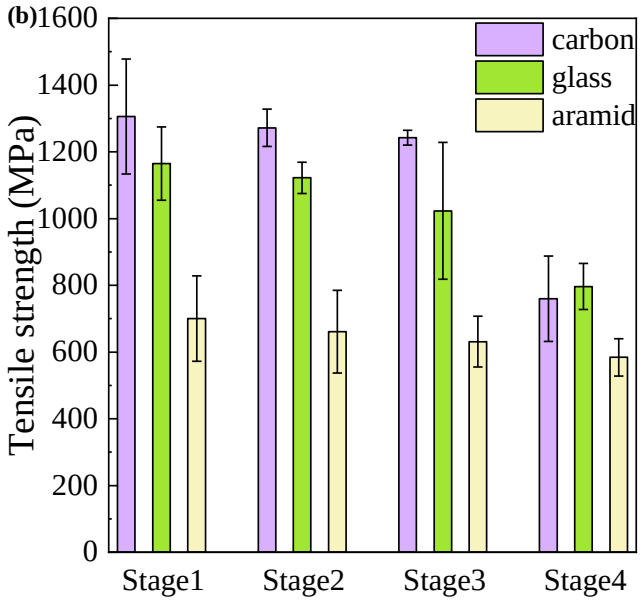

Figure 4-9 *Tensile (a) modulus and (b) strength values of carbon-, glass- and aramid-polyamide filaments in different stages of FDM process.*

During tensile testing of the FDM filaments, AE monitoring was used to track the initiation and accumulation of damage events (which are mostly fibre breakages) leading to final failure. AE monitoring was performed on filaments from different stages of the FDM process. However, little difference was measured using AE due to the small number of fibre damages caused by Stages 2 and 3. Considering that Stage 4 specimen is the 'building block' of the 3D printed structures, the properties of which are the most important for industry, in this study only the AE results of Stage 1 and 4 specimens are presented. **Table 4-3** presents the total number of AE event counts for the three types of filament in Stage 1 and Stage 4. The reduction in the number of AE events for the carbon and glass filaments in the printed condition (Stage 4) is due mostly to a significant number of fibres having been broken during the FDM process before tensile loading. The AE count number for the aramid filament shows no statistically significant difference in the two stages considering the scatter. The curves of normalised applied tensile stress to the normalised number of cumulative AE events for the three filament types are shown in **Figure 4-10**. The AE event count is normalised to the total number measured in a test while the stress is normalised to the ultimate failure stress of the filament. The curves for the three types of filament in the original (Stage 1) condition are similar, with the initial AE events occurring when the applied stress reached ~80% with these events indicating onset fracture of the weakest fibres in the filament. Following the initial onset of fibre fracture, the AE hits increased nearly exponentially with increasing stress to

final failure for the three filament types in the Stage 1 condition, and this trend is common for unidirectional tows and laminates in which the AE events are dominated by fibre fracture. For the Stage 4 filaments, the onset of fibre breakage occurred at lower stress (~30-40%) for the three fibre types. When the filament is processed by the FDM mahine, the abrasion to the filament can also damage the fibre surface, especially for carbon and glass fibres. This surface damage does not completely fracture the fibres, but can reduce their fracture stress, as described in **Chapter 3**. These weakened carbon and glass fibres break at a relatively low stress and thereby cause the early onset of AE events. Aramid fibres are less susceptible to surface damage from the FDM process due to their high fracture toughness and resistance to abrasion, but the increased fibre waviness observed for the printed aramid filaments will result in an early onset of AE events during loading. The rate of increase of AE events for the carbon filament was greater than for the glass and aramid, which were similar, indicating more damage occurs to the carbon fibres during the FDM process.

Table 4-3 *AE count number for the carbon-, glass- and aramid-polyamide filament in Stage 1 and Stage 4.*

	Stage 1	**Stage 4**
Carbon-Polyamide	10455±1774	8579±1343
Glass-Polyamide	4857±625	4294±508
Aramid-Polyamide	1531±238	1615±396

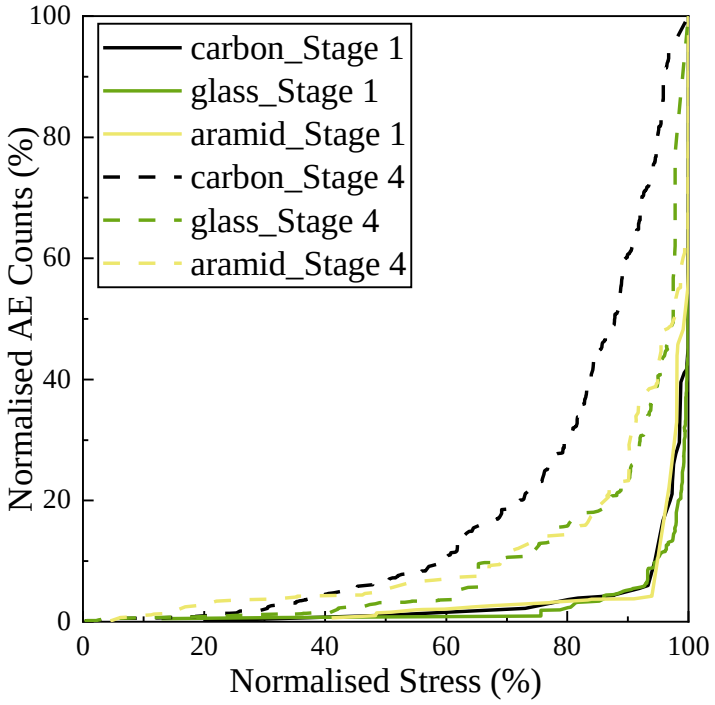

Figure 4-10 *Curves of normalised percentage tensile stress to normalised percentage AE event counts for the carbon-, glass- and aramid-polyamide filament in Stage 1 and Stage 4.*

Figure 4-11 shows the AE hit frequency distributions for the three types of filament at Stages 1 and 4. Symmetric frequency distributions were measured for the filaments over a similar range of 200-550 kHz. A slightly wider frequency range with a lower mean frequency was measured for the Stage 4 filaments compared to Stage 1. The more recorded signals in the carbon-polyamide filaments is attributed to the larger number of fibres and fibre/matrix interfaces within the filament, leading to more damage events. A bell-shaped symmetric frequency distribution is indicative of a single damage mechanism prevailing in the composite [150], which in the case of the filaments is dominated by fibre fracture. In other words, fibre rupture in the filaments reinforced with carbon-, glass- or aramid generates acoustic waves with frequencies of 200-550 kHz, with the median value of ~370 kHz. The values are in the range of the frequency results between 350-700 kHz for the fibre breakage obtained from conventional carbon, glass and aramid fibre composite systems (frequency signature was similar for the fibre types) [151-158]. The relatively low frequency median value for the fibre fracture determined in this study can be attributed to the different fibre type and lower fibre volume fraction of the composites produced by the FDM process. The frequency analysis of the AE signal showed efficiency in distinguishing the fracture mode of fibre breakage. The results will be referred to in the study presented in the next chapter to investigate the failure mechanism of the composite laminates, considering the specific microstructure relative to the FDM process.

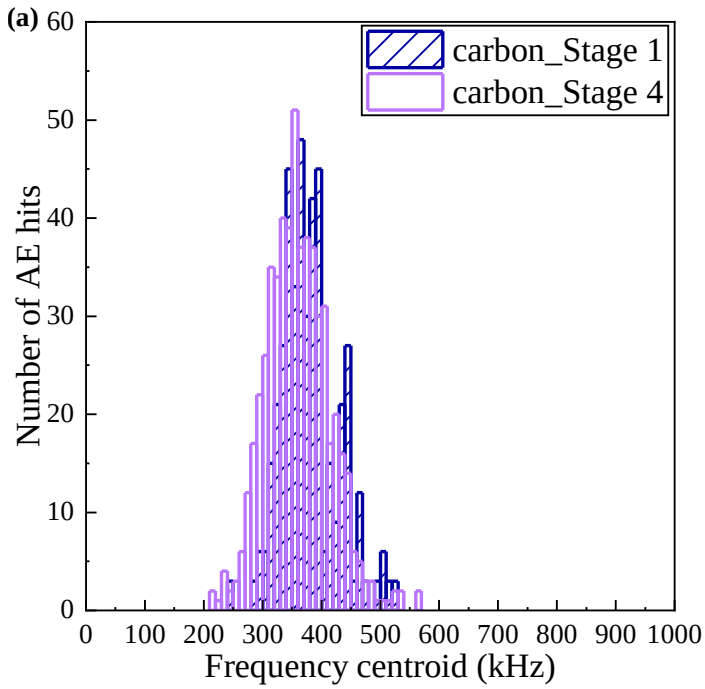
(a)
carbon_Stage 1
carbon_Stage 4
Number of AE hits
Frequency centroid (kHz)
0
10
20
30
40
50
60
0
100
200
300
400
500
600
700
800
900
1000

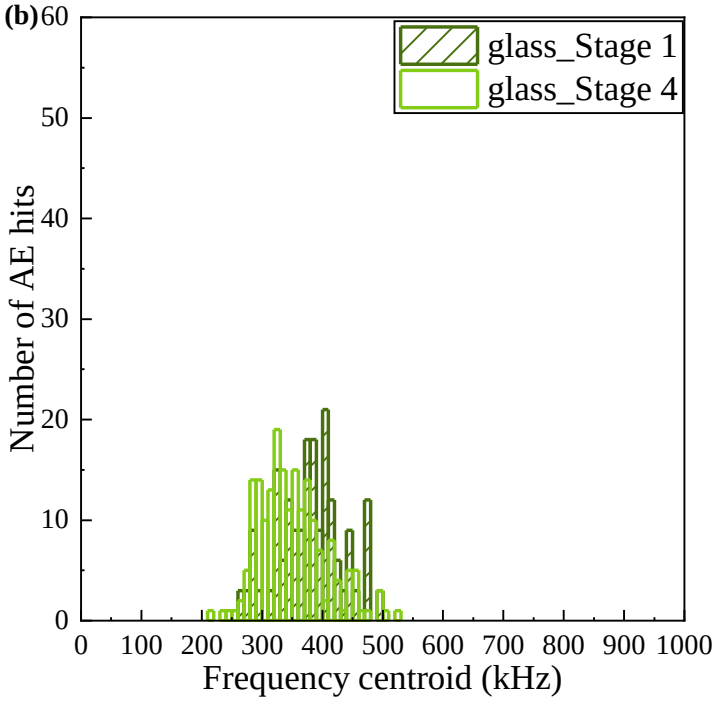
(b)
glass_Stage 1
glass_Stage 4
Number of AE hits
Frequency centroid (kHz)
0
10
20
30
40
50
60
0
100
200
300
400
500
600
700
800
900
1000

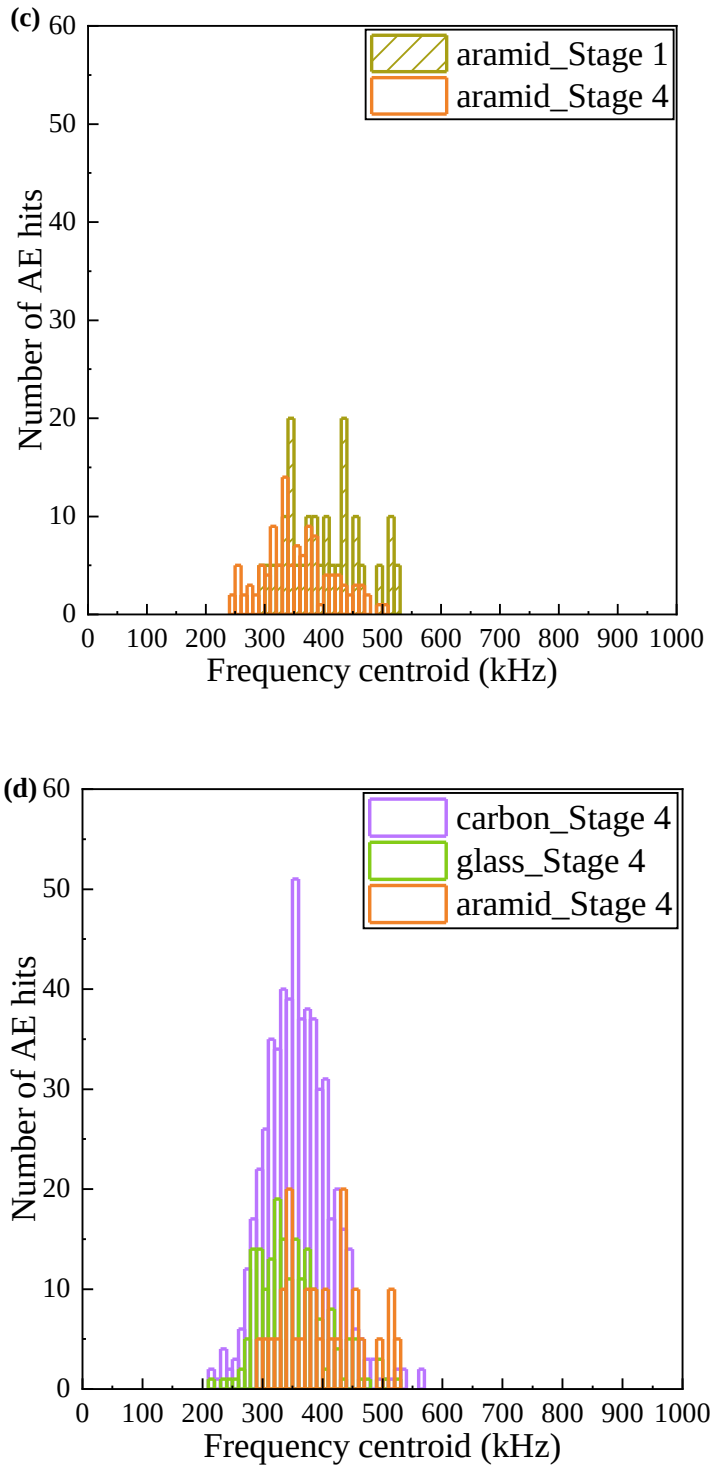

Figure 4-11 *AE frequency centroid distributions of Stage 1 and Stage 4 filaments for (a) carbon, (b) glass and (c) aramid. (d) Comparison of three types of Stage 4 filament.*

4.4 Conclusions

To use 3D printed composite materials in load-bearing structures, the microstructure and its effect on the mechanical properties must be established. This study has demonstrated

that the degree of fibre damage and the residual strength of FDM filaments depends on the fibre type. The surface of the FDM filament is abraded when it passes through the different stages of the FDM process, such as by the gripping action of the gear mechanism used to pull the filament (Stage 2) and during contact with the nozzle (Stage 3). Filament abrasion could damage brittle fibres such as carbon and glass. Damage is also caused to the fibres as the FDM filament is bent through 90^{o} when deposited on the build platform (Stage 4). This bending causes a large increase in the number of broken fibres in the carbon and glass filaments and crimped fibres in the aramid filament. FDM-induced damage reduces the tensile strength and modulus values of the glass-polyamide filament studied here by ~32% and ~15%, respectively. The reductions are less than measured for the carbon filament, which is due to its lower failure strain and the lower fracture toughness of the carbon fibres. The aramid filament showed the least reduction in mechanical properties due to the FDM process, and this was because of its higher failure strain and toughness. However, the ductile aramid filaments were warped and crimped in Stage 4 of the FDM process, which reduced the modulus and failure stress (albeit less than that experienced by the carbon and glass).

CHAPTER 5: PHYSICAL AND MECHANICAL PROPERTIES OF CURVED FDM COMPOSITE FILAMENTS

Abstract

An advantage of 3D printing continuous fibre composites using the FDM process is the ability to bend and curve the filaments during deposition to create intricately shaped products. However, little is known about the effect of bending on the properties of FDM filaments when printing curved sections. This chapter presents an experimental investigation into the effect of 3D printing curvature on the microstructure and mechanical properties of the FDM filaments. FDM polyamide-based filaments containing continuous carbon, glass or aramid fibres were printed as curved sections on the build platform of the FDM machine with different radii ranging between 1 mm and 30 mm. Straight FDM filaments without any curvature were also studied as the benchmark condition. It is found that curved printing using the MarkForgered® MarkTwo machine lacks high dimensional accuracy, particularly at small radii, causing the machine set radius and the actual print radius to be different. The effect of the curved printing process on the microstructure and tensile strength of the FDM filaments is determined. Significant fibre breakage occurred in the carbon- and glass- filaments when the radius was smaller than ~10 mm due to the relatively low bending fracture strain of these fibres. In comparison, the aramid fibre filament sustained no fibre breakage, even when printed at very tight radii, due to its higher flexibility and failure strain. However, the aramid fibres sustain kinking and micro-buckling damage when 3D printed at a tight angle. It is also found that internal longitudinal tearing of the polyamide matrix occurs at tight angles. The fibre and matrix damage caused by printing at tight radii reduced the tensile strength of the filaments. For example, the tensile strength values of the carbon-, glass- and aramid-polyamide filaments with a radius under 5 mm were just 31%, 40% and 64%, respectively, compared to the straight printed filaments. The causes of the damage and the resultant reduction to the tensile strength of the FDM filaments during curved 3D printing are identified.

5.1 Introduction

Traditional manufacturing methods for composites typically use prepregs or fabrics in which the continuous fibres are aligned in specific directions, such as the 0^o and 90^o orientations. Notches and holes often need to be created in these composites by drilling and cutting because it is not practical to deflect the fibres around where the cut-outs need to be located. The machining of notches and holes causes local damage to the fibres and thereby weakens the composite material. Notches and holes also create a geometric stress concentration which can reduce the failure stress. The automated fibre placement method can be used to deposit thin strips of prepreg with complex curvatures to avoid or minimise the need for notches and holes [159, 160]. However, AFP technology is limited by the dimensions of the fibre tow, compaction roller and placement head. Attempting to fabricate composites with a tight bend radius can cause fibres to wrinkle, twist and peel, thereby damaging the material [161].

It is possible to introduce curvature into continuous fibre composites by bending filaments using 3D printing through the FDM process. Studies have proven that by bending the filaments during printing it is possible to control the internal stress distribution [28, 56, 59, 130] or fabricate three-dimensional core shapes [23, 99, 100]. However, errors in the printing path can occur during printing curved sections of filament, as shown for example in **Figure 5-1a**. Also, filament undulation, twisting, peeling from the base, and fibre breakages can occur, especially when the curvature radius is tight, as shown in **Figure 5-1b** [29, 101]. These defects affect the microstructure, quality and properties of 3D printed composite products, although only a few studies have investigated the effect of curved printing using the FDM process. Ishii et al. [104] bent a curved FDM filament to fracture and proposed a failure model for the filament with different curvature radii. The fracture criterion defines the behaviour of the fibre bundle using bending beam analysis. However, the filament curvature studied by Ishii and colleagues was created through heat treatment to the filament in the as-received condition without FDM printing, and damage caused directly by the FDM process was not investigated. Matsuzaki et al. [102] determined the printability of continuous carbon fibre-ABS composites with curvature under 20 mm using the FDM process. Fibre bundle sizes of 1K, 4K and 8K in the ABS matrix filaments were studied. It was found that the increased bundle size reduced the minimum achievable radius for printing. Matsuzaki and colleagues also investigated the folding mechanism that occurs in the curved section of the

filaments and evaluated fibre damage via electrical resistance measurements [105]. The fibre damage and stress distribution of a FDM printed carbon-polyamide filament with curvature radii ranging from 2.5 to 20 mm were investigated by Zhang et al. [162] using microstructural analysis and FE modelling. However, only the elastic properties of the composite were considered, and therefore no fibre damage could be predicted using FE analysis.

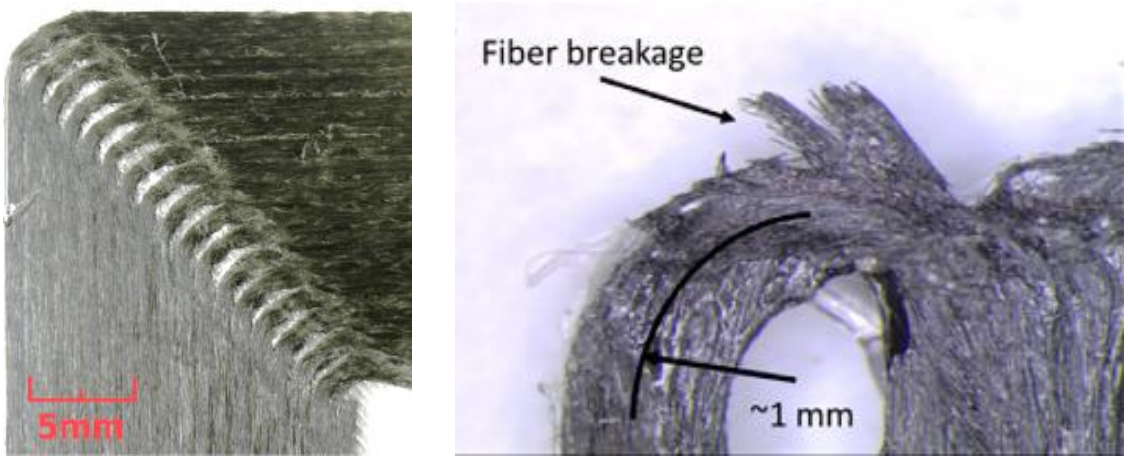

(a) **(b)**

Figure 5-1 *Curved FDM carbon filaments at corner showing microstructural and fibre damage. [29, 32]*

The effect of the printing curvature radii on the microstructure and mechanical properties of 3D printed composites have yet to be fully studied, which is essential to understand the properties of 3D printed structures with complex geometry containing curved and bent filaments.

This chapter presents an experimental study into the microstructure and tensile properties of FDM filaments printed with different curvatures. The study was conducted on carbon-, glass- and aramid-polyamide filaments printed using the FDM process. Damage to the continuous fibres and filament structure when printed at different curvatures was determined. The effect of curvature damage on the tensile strength of the filaments printed with different radii was also determined. The study identifies the limits to bending of different filament types during FDM printing of continuous fibre composites.

5.2 Methodology

5.2.1 Filament specimen preparation

The FDM filaments used in this investigation are carbon-, glass- and aramid-polyamide filaments supplied by Markforged®. (These are the same filament types studied in the previous two chapters). The microstructure of the filaments in the as-received and straight printed conditions have been described in detail in the previous chapters.

In this study, a single FDM filament with a set curvature radius was deposited on the build platform of the Markforged MarkTwo® printer at the temperature of 254°C and print rate of 15 mm/s. These are the same conditions used for printing the straight filaments described in Chapters 3 and 4. The schematic in **Figure 5-2** shows the curvature of a single filament desposited on the printer build platform as well as specimen preparation for tensile testing. The printing path was a 90 mm × 90 mm four-sided frame with round corners having a defined, constant radius. The three filament types were printed with radii of 1 mm, 3 mm, 5 mm, 8 mm, 10 mm and 30 mm. The filament was printed in a concentric pattern following the frame outline, as shown in **Figure 5-2**, with the blue line indicating the path.

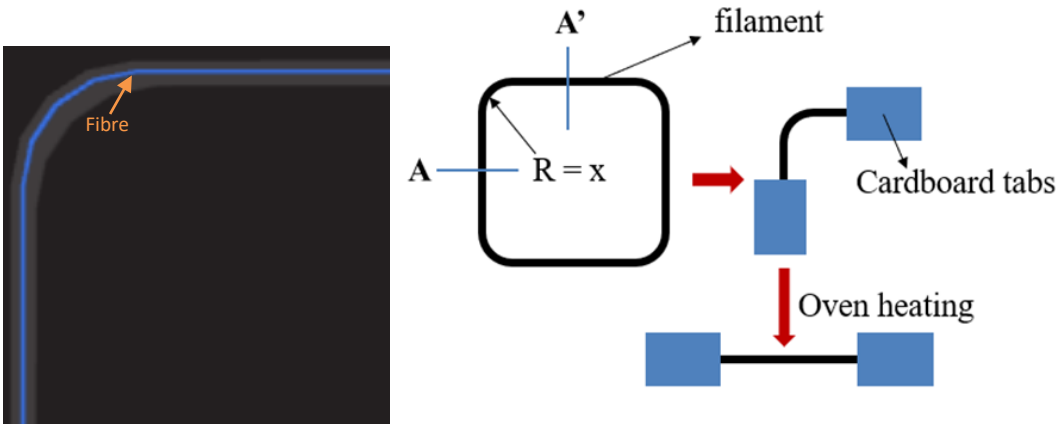

Figure 5-2 *Schematic of curved filament sample which is straigthened for tension testing. R is the specimen radius before straigthening, x is the set printing radius of 1 mm, 3 mm, 5 mm, 8 mm, 10 mm or 30 mm.*

The curved sections were cut at the points marked A and A' in **Figure 5-2**, which are the middle points of the adjacent edges. The ends of the curved filament were then bonded to 20 mm × 20 mm cardboard pieces using an adhesive, and these were used as tabs for tensile testing. The filament specimens were heated in an oven at ~220°C for 10 seconds to soften the polyamide matrix in order to straighten the curved section to enable axial tensile testing, which is not possible when curved. The specimen was hung up on one side with a three-gram weight on another side. (The heat treatment was also performed on the straight printed filament specimens). The tensile properties of the Stage 4 filaments (in the straight condition)

with/without heat performed in an oven was compared, and the results showed no statistical difference. Therefore, the heating treatment had no effect on the tensile properties of the filament specimens when straightened. Additionally, the weight applied to the specimens to straighten the filaments was very low, which is unlikely to cause additional damage to fibres within the filament; all damage was caused during the original printing process and no further damage by straightening.

5.2.2 Experimental methods

Tensile tests were performed on the curved and then straightened FDM filaments with a gauge length of 50 mm at an extension rate of 0.5 mm/min until failure using a 10 kN load capacity Instron machine (CSS 88010, China). The cross-sectional area of each filament was determined at the fracture surface following tensile testing using optical microscopy images processed with ImageJ software. This was necessary because of variations in the cross-sectional area of the filaments after 3D printing (as described later). A minimum of ten FDM filaments for each radius value were tested under identical conditions to determine the average and scatter to the tensile stiffness and strength.

The microstructure of the filaments was examined using optical microscopy and scanning electron microscopy (SEM). Optical microscopy was performed using an OLYMPUS GX41 microscope. SEM was performed using a TM4000PLUS (HITACHI). The SEM inspection parameters were 61 μA and 15 kV for emission current and accelerating voltage, respectively. The SEM working distance was 12 mm. Before SEM examination, the filament sample was coated with a thin film of iridium to avoid electron beam charging effects. The inside (R_{inner}) and outside (R_{outer}) radius values of the curved filaments were measured from SEM images. The mean value was the print radius at the mid-plane line of the filament, and was used for evaluating the printing accuracy.

Polymer burn-off tests were conducted on the curved FDM filaments to expose the fibres and thereby observe any fibre breakages. The curved section of the filament was cut and then held on a 25 mm × 25 mm aluminium sheet. Clips were used to maintain the filament curvature during the burn-off process. Carbon- and glass-polyamide filaments were heated at 500°C in a vacuum furnace for 5 hours to remove the polyamide matrix, while the temperature was lowered to 400°C for the aramid-polyamide filament due to the relatively

low degradation temperature of the aramid fibres. Although the aramid fibres appeared brown due to partial degradation, this had no influence on the fibre shape integrity.

5.3 Results and Discussion

5.3.1 Microstructure of filaments with different curvature radii

Table 5-1 presents the radius values set for the MarkForged FDM printer and the actual mean radius values measured using SEM analysis. The percentage difference between the machine set and actual values depends on the filament type, and increases in the order: aramid, glass, carbon. The inaccuracy of the printing path is likely due to the different path lengths of a printed strip at the inner and outer edges (which is described below) and the mismatch in the diameters of the printer nozzle (~1 mm) and the filament (~0.38 mm).

Table 5-1 *Measured curvature radii following the equation of* $R_{measure} = \frac{R_{inner}+R_{outer}}{2}$ *for the three filament types compared to the radii set for the FDM machine.*

Set radius value	Carbon-Polyamide (mm)	Glass-Polyamide (mm)	Aramid-Polyamide (mm)
1 mm	0.56 ± 0.16	1.08 ± 0.12	1.41 ± 0.07
3 mm	1.22 ± 0.27	2.03 ± 0.27	2.41 ± 0.34
5 mm	3.25 ± 0.88	3.75 ± 0.74	4.13 ± 0.95
8 mm	6.73 ± 1.04	6.75 ± 0.04	7.33 ± 0.72
10 mm	8.61 ± 0.55	9.11 ± 0.41	9.25 ± 0.67
30 mm	21.83 ± 1.73	27.77 ± 0.69	28.32 ± 0.72

Figure 5-3 compares the microstructure of the three filament types for the different radius values. The SEM images show that when the radius increases then the folding angle, which is the angle between the inner and folded outer edge at the folding point, decreases. The measured values of the folding angle for three filament types are summarised in **Table 5-2**. With the tightest radius of ~1 mm, a noticeable folding over of the filament occurs for

three fibre types accompanied by a complete switch of the inner and outer filament edges. A schematic of filament folding is shown in **Figure 5-4**.

Table 5-2 *Measured folding angles of the three filament types for the different set radii.*

Set radius value	Carbon-Polyamide (mm)	Glass-Polyamide (mm)	Aramid-Polyamide (mm)
1 mm	80 ± 5	25 ± 5	23 ± 3
3 mm	50 ± 7	19 ± 4	19 ± 3
5 mm	21 ± 3	16 ± 3	11 ± 2
8 mm	10 ± 4	10 ± 2	/
10 mm	/	/	/
30 mm	/	/	/

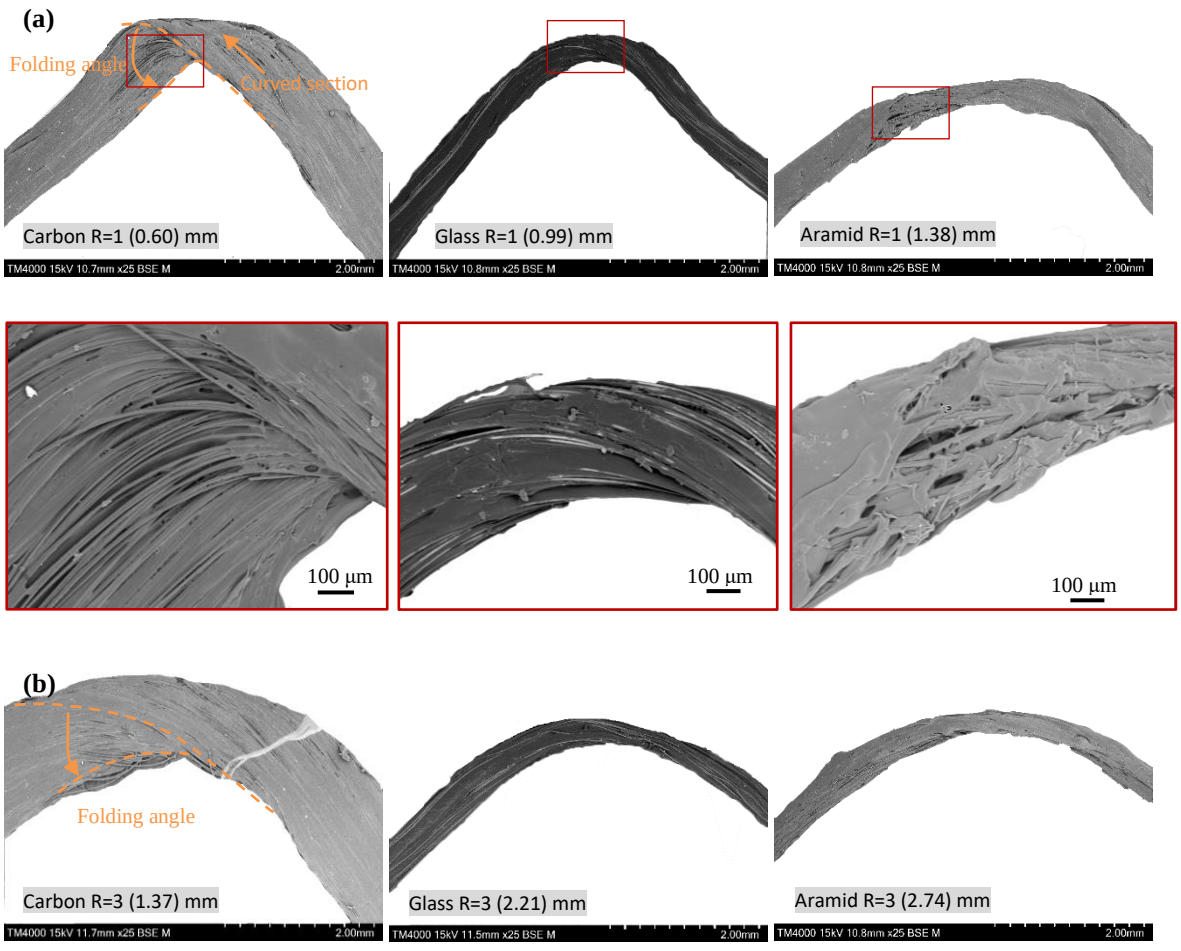

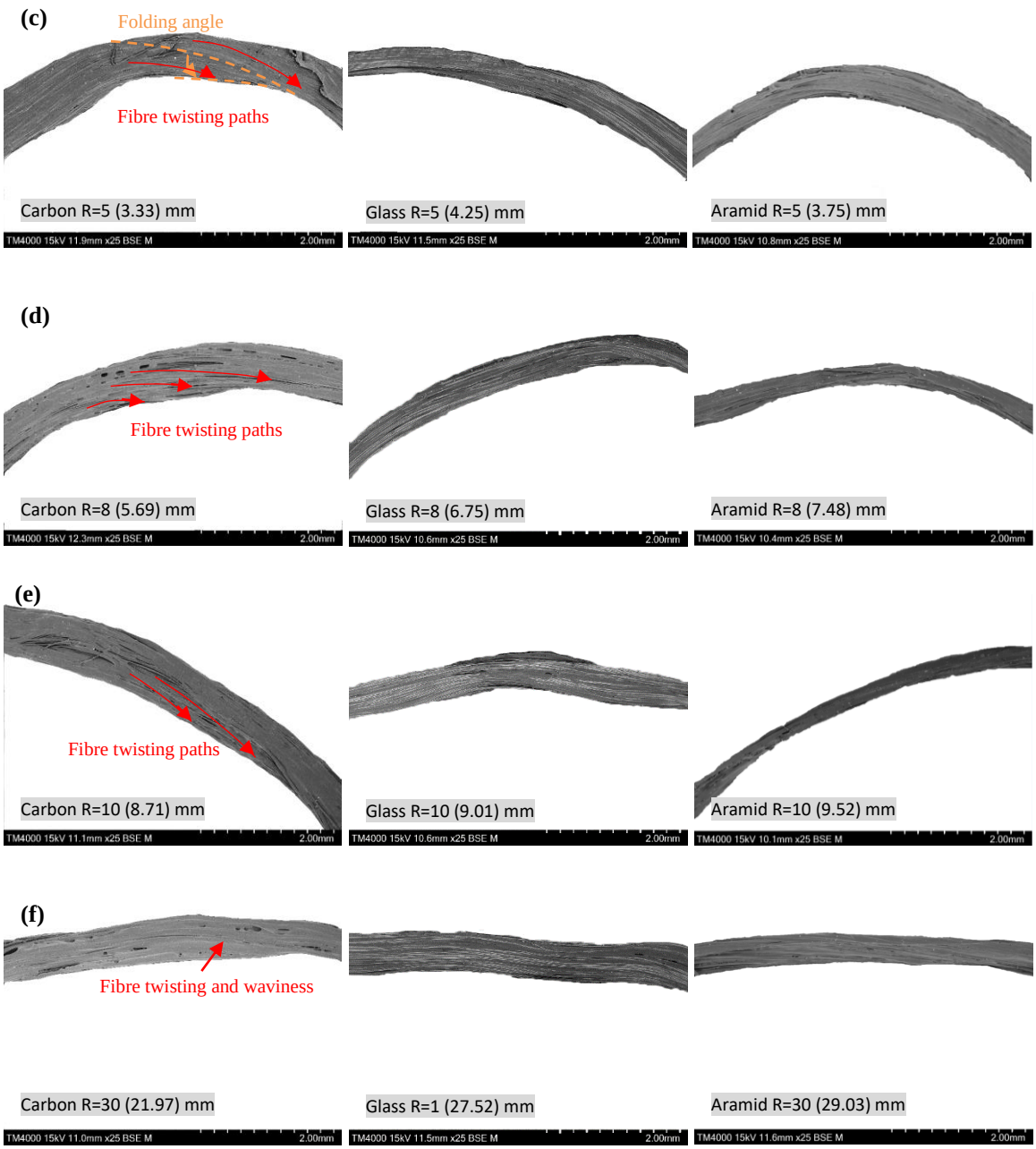

Figure 5-3 *FDM filaments with the printer set radius of R = 1, 3, 5, 8, 10, 30 mm from (a) to (f) for three fibre types. The value in parenthes is the actual (measured) radius. Images with red border on the bottom of (a) are the closer inspection showing the damage in the matrix phase.*

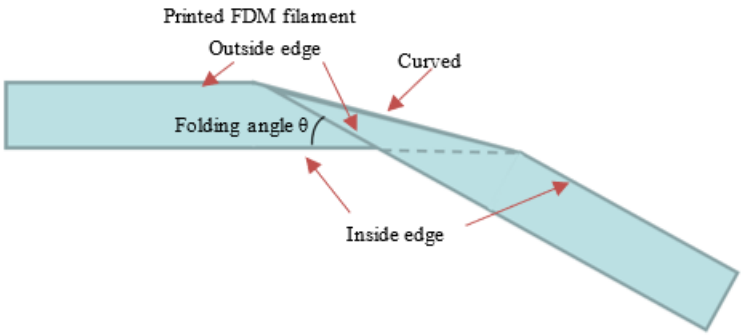

Figure 5-4 *Schematic of filament folding during curved 3D printing.*

The carbon-polyamide filament, in which the fibres are much stiffer than the glass and aramid fibres, results in more fibre waviness and breakage near the inner side due to the compressive strain created from the bending during curved printing. Additionally, when the composite filament bent through a tight radius, some carbon fibres on the inside of the filament pulled away from the main filament, with longitudinal tearing of the polyamide matrix appearing between some of the carbon fibres, as shown in the closer inspection of **Figure 5-3a**. This is caused by the through-thickness stress generated in the filament during fibre bending and twisting. Because the carbon fibre is stiffer and does not bend as easily as glass and aramid fibres (the Young's modulus of the three fibre filaments are given in **Chapter 4**), it will pull away when the bend radius is tight, which can generate the through-thickness stress leading to the tearing within the matrix. This matrix tearing damage will be retained within the 3D printed laminate as localised voids in the matrix, increasing the porosity level. Also, the fibre architechture of the structure will not necessarily follow the bend with some of the fibres pulled away in the curved section, compromising the dimensional accuracy of the 3D printing process for curved sections. Furthermore, the folding process reduces the average width of the printed filament at the curved section (**Table 5-3**), leading to the gaps inside the printed filaments [32], which act as a potential local weakness. For the machine bend radius of 10 mm, the folding back of the printed filament does not occur although the fibres are still twisted at the curved section. For the machine radius of 30 mm, the local fibre alignment is very close to that of a straight printed filament, and the filament width is roughly consistent along the printed section.

Table 5-3 *Percentage of the filament widths at the bend radius point compared to the straight filament section for the different printer radius values.*

Set radius value	Carbon-Polyamide	Glass-Polyamide	Aramid-Polyamide
1 mm	55%	73%	60%
3 mm	68%	83%	77%
5 mm	70%	85%	78%
8 mm	87%	90%	84%
10 mm	91%	96%	94%
30 mm	94%	99%	99%

Filament twisting and folding was caused by the movement limitation set to the printer nozzle of the FDM machine, with which only translation and no rotation is allowed. This forces the inner and outer sides of the filament to inverse or flip in order to form a curved section with a tight radius. For this reason, folding was more severe with the smaller print radius. The folding was the most severe for the carbon filament, due to the higher stiffness of the fibres, and was the least severe for the aramid filament due to the higher flexibility of these fibres which are printed at the glass transition softening temperature.

The cylindrical-shaped filament is flattened into a thin sheet by the printer during deposition on the build platform. During the curved printing process, the difference in the path lengths between the inside and outside of the filament induces an uneven stress field at the cross-section. When the turning section becomes sharp, in other words, the printing curvature radius becomes tight, the tensile force at the outer edge of a filament increases beyond the adhesion force to the build platform and this generates a torque peeling the filament from the build platform and twisting it.

5.3.2 Fibre damage within printed FDM filaments with various curvature radii

Fibre damage to the FDM filaments during curved printing was investigated by burning off the polyamide resin to expose the fibres. SEM images presented in **Figure 5-5** to **Figure 5-7** show the fibres for the three types of filament for different bend radii. Fibre breakage was the most extensive in the carbon-polyamide filament, with many broken fibres

near the outer edge of the curved section when the radius was under 10 mm. Crushed carbon fibres occurred near the inner edge of the folded segment to the filament for the tightest radius values of 1 mm and 3 mm. Fibre breakages also occurred at the outside edge of the glass-polyamide filament with radius of 1 mm, 3 mm and 5 mm. In contrast, no fibre breakage was detected in the aramid-polyamide filament, even at the tightest curvature of 1 mm. However, the aramid fibres sustained local buckling/kinking at the folded region for the radius of 1 mm and 3 mm.

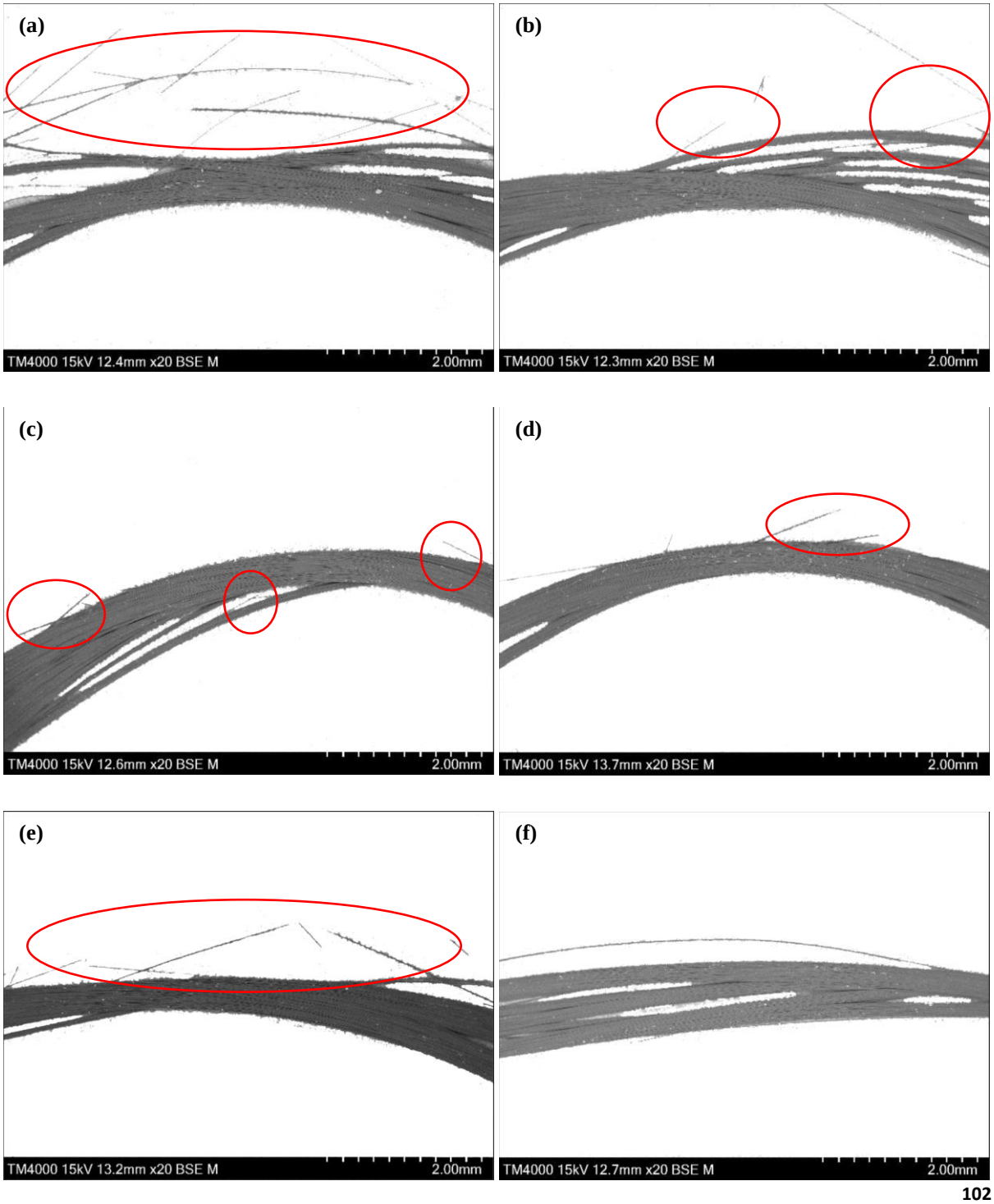

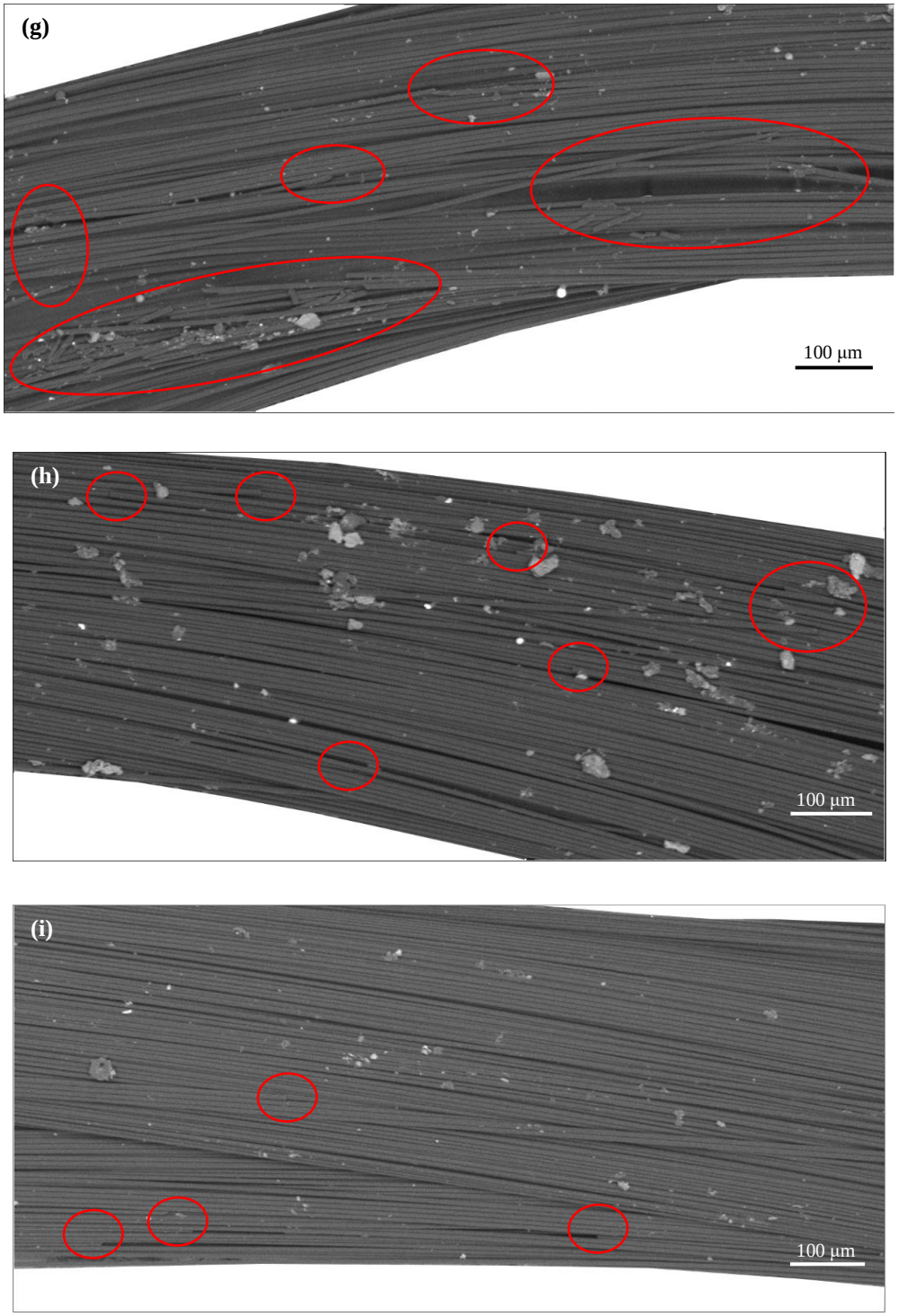

Figure 5-5 *Curved carbon fibre filament (a-f) with FDM machine set R values = 1, 3, 5, 8, 10, 30 mm after polymer burn-off. (g-i) are magnified images of R = 3, 8, 30 mm. The circles indicate where fibres are broken.*

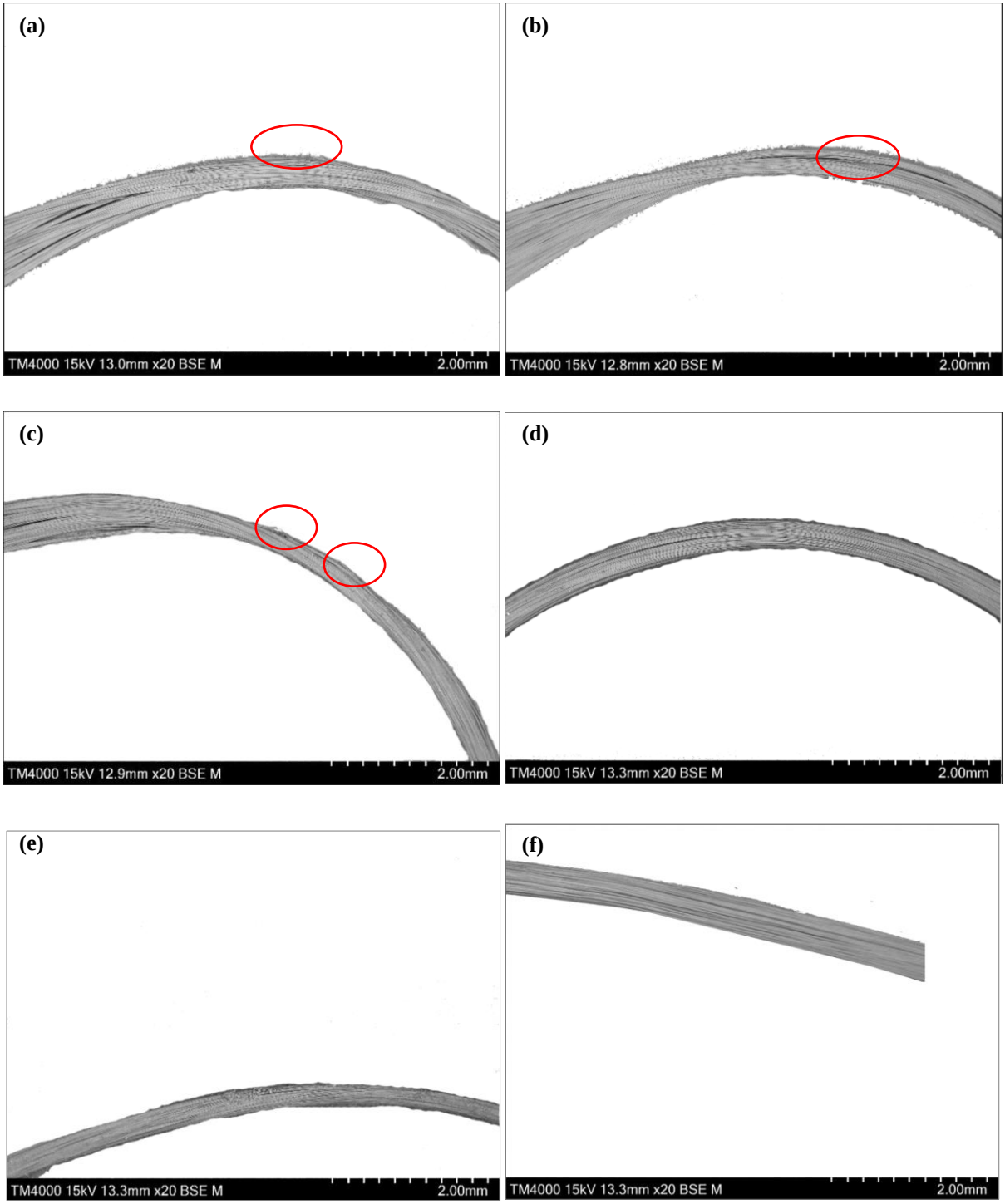
(a)
TM4000 15kV 13.0mm x20 BSE M
2.00mm
(b)
TM4000 15kV 12.8mm x20 BSE M
2.00mm
(c)
TM4000 15kV 12.9mm x20 BSE M
2.00mm
(d)
TM4000 15kV 13.3mm x20 BSE M
2.00mm
(e)
TM4000 15kV 13.3mm x20 BSE M
2.00mm
(f)
TM4000 15kV 13.3mm x20 BSE M
2.00mm

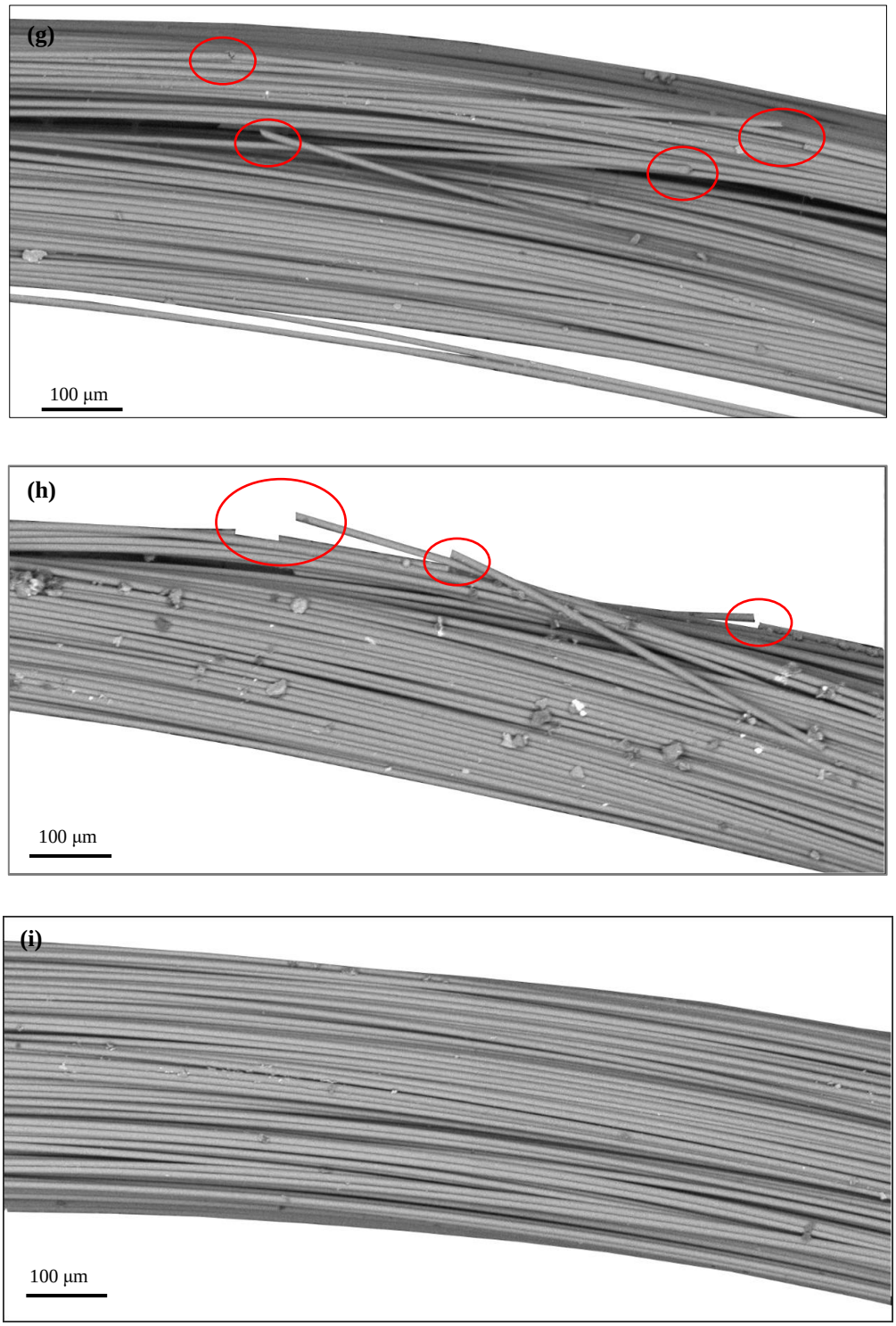

Figure 5-6 *Curved glass fibre filament (a-f) with FDM machine set R values = 1, 3, 5, 8, 10, 30 mm after polymer burn-off. (g-i) are magnified images of R = 3, 8, 30 mm. The circles indicate where fibres are broken.*

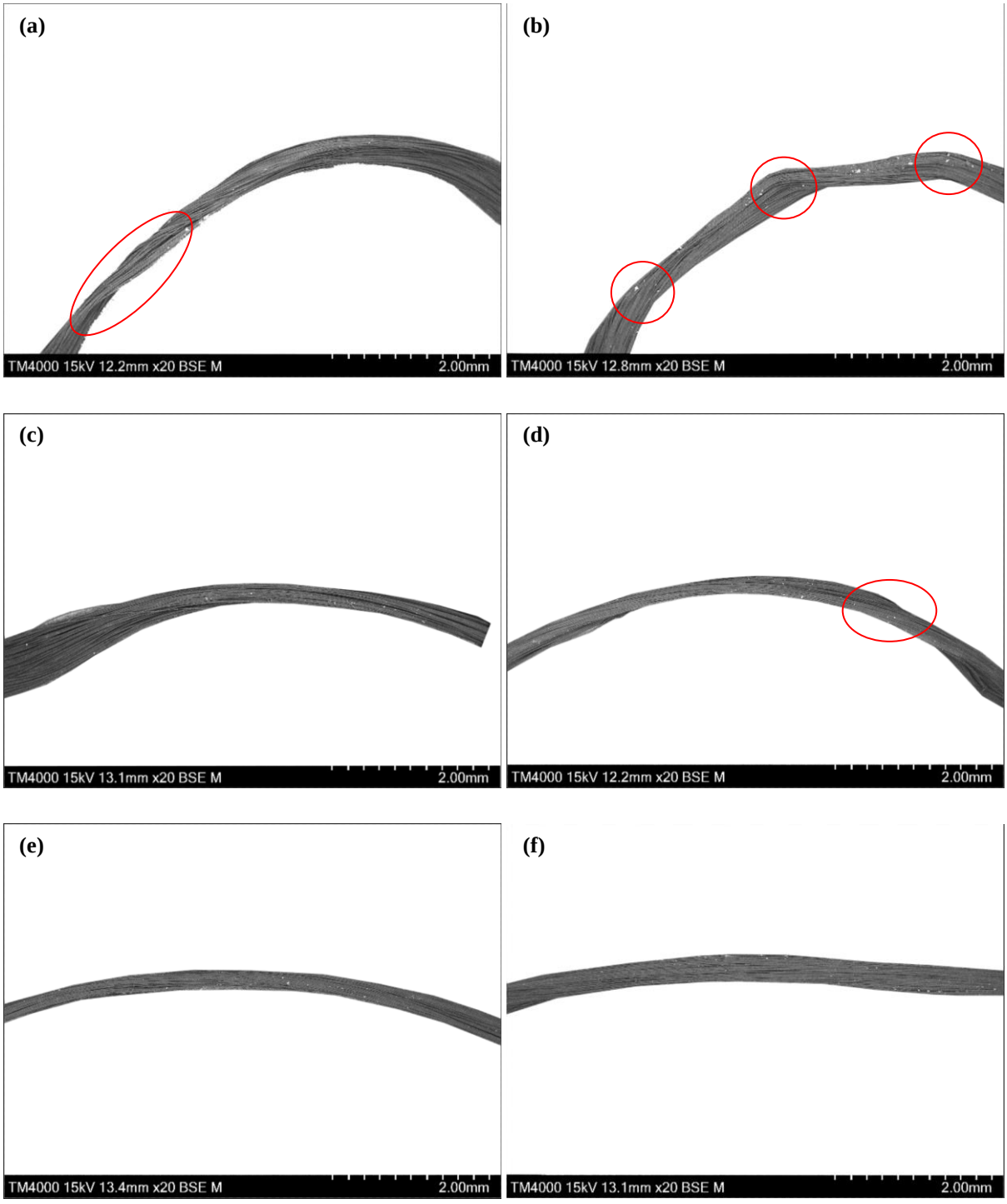
(a)
TM4000 15kV 12.2mm x20 BSE M
2.00mm
(b)
TM4000 15kV 12.8mm x20 BSE M
2.00mm
(c)
TM4000 15kV 13.1mm x20 BSE M
2.00mm
(d)
TM4000 15kV 12.2mm x20 BSE M
2.00mm
(e)
TM4000 15kV 13.4mm x20 BSE M
2.00mm
(f)
TM4000 15kV 13.1mm x20 BSE M
2.00mm

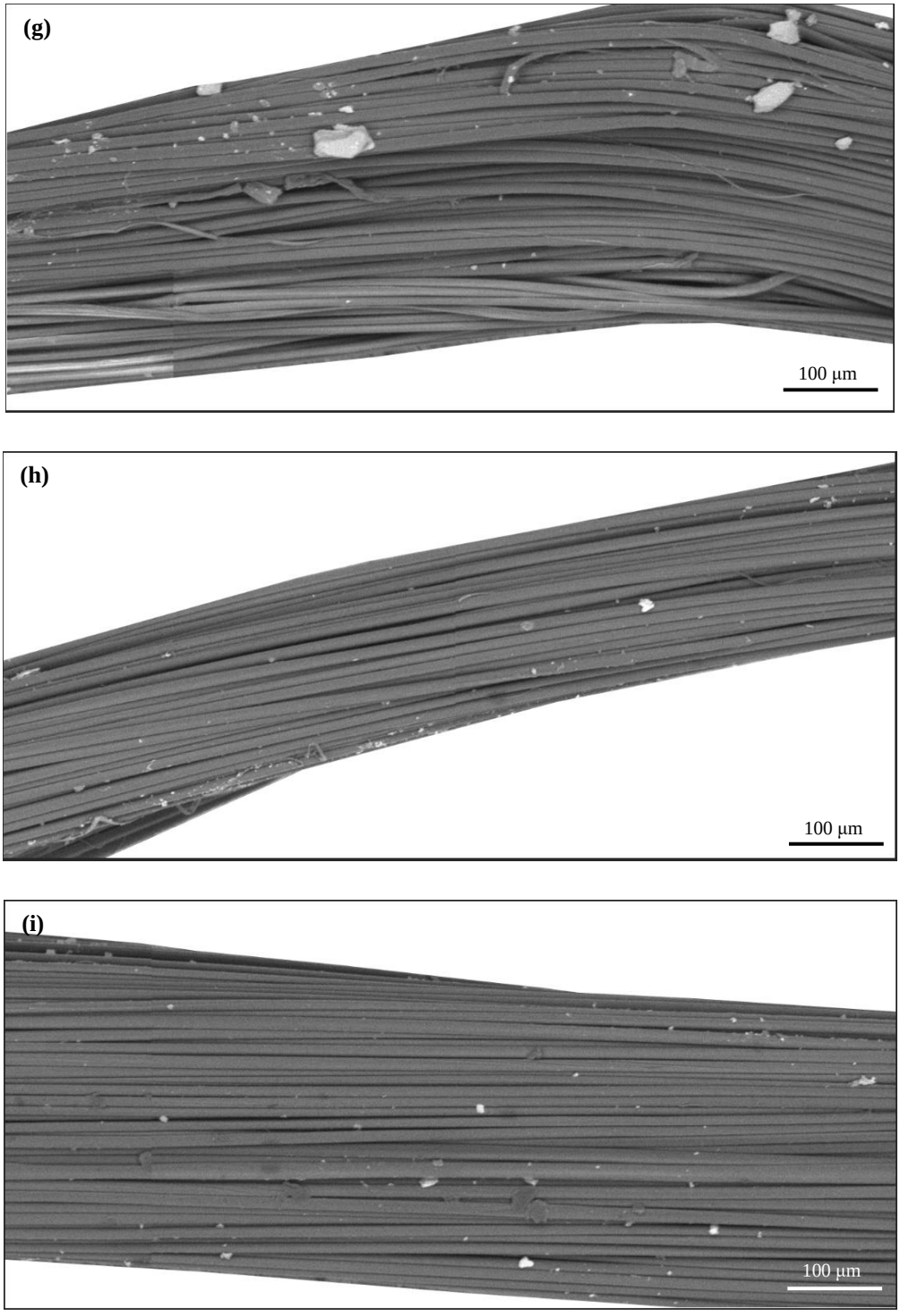

Figure 5-7 *Curved aramid fibre filament (a-f) with FDM machine set R values = 1, 3, 5, 8, 10, 30 mm after polymer burn-off. (g-i) are magnified images of R = 3, 8, 30 mm. The circles indicate where fibres are twisting and buckling.*

When the filaments were formed into a curved shape during the 3D printing process, the material was still hot although it cooled rapidly on the build platform. In the hot, soften condition, the polyamide matrix to the filaments cannot effectively transfer the bending stress

between fibres. Furthermore, every single fibre within the soften matrix can effectively bend independently when following the curved printing path, with tensile and compressive stresses generated within the fibres located at the outer and inner edges of the filament, respectively. The rapid cooling of the filament on the build platform effectively locks-in residual stresses caused by bending and (at tight radius when folding occurs) by twisting [163]. The axial elastic compressive and tension strains in a single fibre in a printed curved filament can be approximated using elastic beam theory:

$$\epsilon_{c_{max_{fibre}}} = \frac{\frac{1}{2}d_{fibre}}{R_{inner}+\frac{1}{2}d_{fibre}} \geq \epsilon_{Lc_{fibre}} \quad (1)$$

$$\epsilon_{t_{max\_fibre}} = \frac{\frac{1}{2}d_{fibre}}{R_{outer}+\frac{1}{2}d_{fibre}} \geq \epsilon_{Lt_{fibre}} \quad (2)$$

where d_{fibre} is the fibre diameter, R_{inner} and R_{outer} are the inner and outer radii of the filament, and ϵ_{Lc_fibre} and ϵ_{Lt_fibre} are the compressive and tensile failure strains of the fibre. In the case of 3D printing using the FDM process, the maximum compressive strain $\epsilon_{c_{max\_fibre}}$ is generated at the inside edge of the curved filament whereas the maximum tensile strain $\epsilon_{t_{max\_fibre}}$ is at the outside edge. **Table 5-4** gives the calculated bending strain values at the inside and outside edges of the three filament types with different curvature values. Taking carbon fibre, whose failure strain is the lowest of the three fibre types, as an example, $d_{fibre} = 0.007\ mm$, $\epsilon_{Lc_{fibre}}$=0.5% and $\epsilon_{Lt_{fibre}}$=1.5% [164, 165] in equation (1) and (2), then the fracture radius values are calculated to be $R_{inner_{min}}$ = 0.70 mm and $R_{outer_{min}}$ = 0.23 mm, which means that any printed radius size below these values will cause fibre fracture. The limit sizes are much lower for glass and aramid fibres because they have higher failure strains and larger fibre diameters (**Table 5-5**). However, carbon fibre breakage was observed experimentally for radius values up to 10 mm, which is much higher than the calculated critical radius. This is because the fibre twisting and folding are not considered in the calculation using elastic beam theory. The intense geometric deformation increases the strain on the fibres at the curved section and thereby raises the critical radius value to cause fibre fracture. For instance, for the carbon-polyamide filament with the set radius of 1 mm, the measured actual radius of some fibre paths in the folded region are as small as ~0.1 mm, which is lower than the calculated critical values to cause fibre breakage. The results agree with the microstructural features observed using SEM.

Table 5-4 *Measured bending strains at the inner and outer surfaces of the three filament types for the different FDM radius values.*

Set radius value	Carbon-Polyamide		Glass-Polyamide		Aramid-Polyamide	
	inside	**Outside**	**inside**	**Outside**	**inside**	**Outside**
1 mm	1.05%	0.51%	0.62%	0.31%	0.87%	0.28%
3 mm	0.52%	0.20%	0.24%	0.17%	0.27%	0.23%
5 mm	0.14%	0.09%	0.14%	0.10%	0.18%	0.12%
8 mm	0.09%	0.04%	0.08%	0.07%	0.10%	0.09%
10 mm	0.05%	0.04%	0.05%	0.05%	0.06%	0.06%
30 mm	0.02%	0.02%	0.02%	0.02%	0.02%	0.02%

Table 5-5 *Critical radius of the three filament types for the different measured curvatures. The values in parenthesis are the fibre failure strains from the literature [164, 165].*

Critical radius	Carbon-Polyamide	Glass-Polyamide	Aramid-Polyamide
	(mm)	**(mm)**	**(mm)**
Compressive to fracture	0.70 (0.5%)	0.40 (1.1%)	0.39 (1.5%)
Tensile to fracture	0.23 (1.5%)	0.11 (3.8%)	0.22 (2.7%)

5.3.3 Tensile strength of curved fibre-polymer filaments

Figure 5-8 presents the tensile force-displacement curves of the carbon-, glass- and aramid-polyamide filaments with curvature radii of 1 mm, 5 mm, 10 mm and 30 mm. The curve of the straight filaments are also shown. All the curves are linear elastic to tensile failure, which always occurred at the curved section due to weakening and fracture of the fibres caused by the curved printing process. The curves show that the stiffness and failure stress of the three filament types is dependent on their initial curvature. It is worth noting that the force-displacement slopes presented here can only show a qualitative relation between the curvature radius value and filament tensile properties. This is because the specimens with

different printing radii in this study had different curved section lengths, which significantly influence the recorded values of displacement and thereby the stiffness. **Figure 5-9** shows the tensile properties of the carbon-, glass- and aramid-polyamide filaments in the straight and curved conditions after 3D printing. **Table 5-6** and **Table 5-7** gives the percentage reductions to the filament stiffness and strength due to curvature relative to the straight filament.

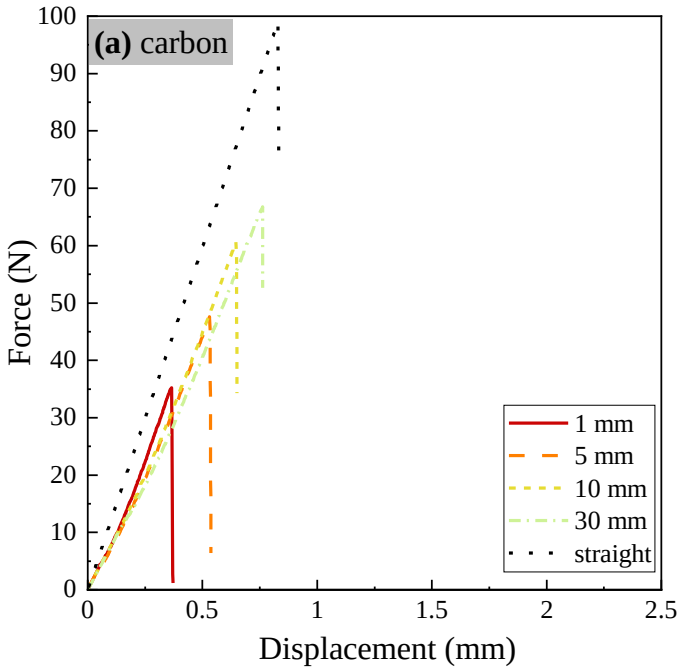

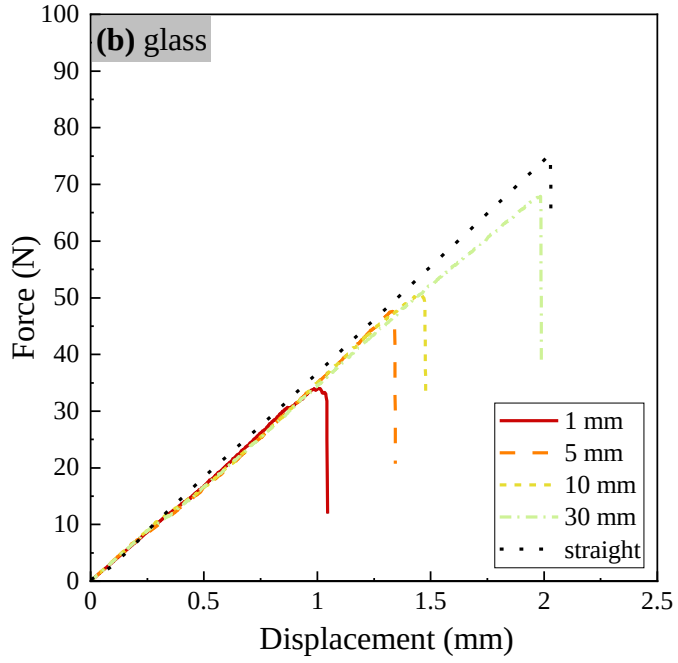

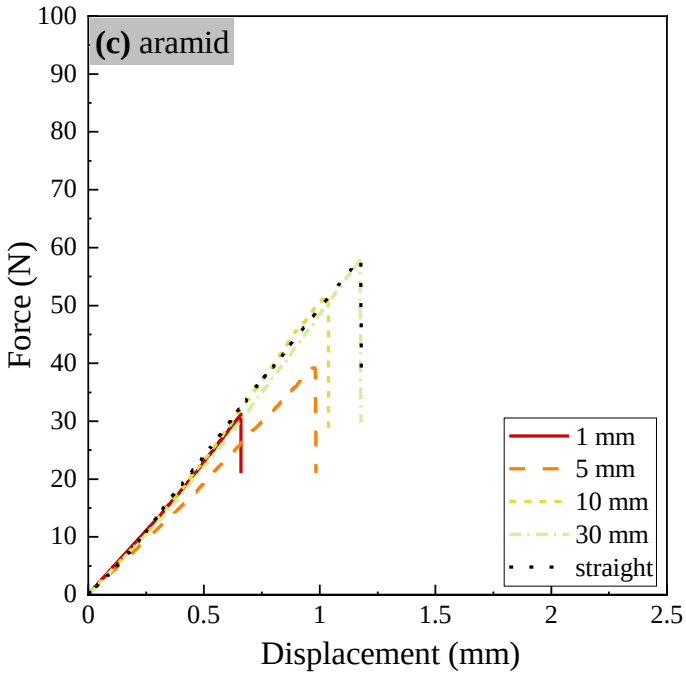

Figure 5-8 *Tensile force-displacement curves of the (a) carbon, (b) glass and (c) aramid filaments with print radius of 1 mm, 5 mm, 10 mm and 30 mm and straight.*

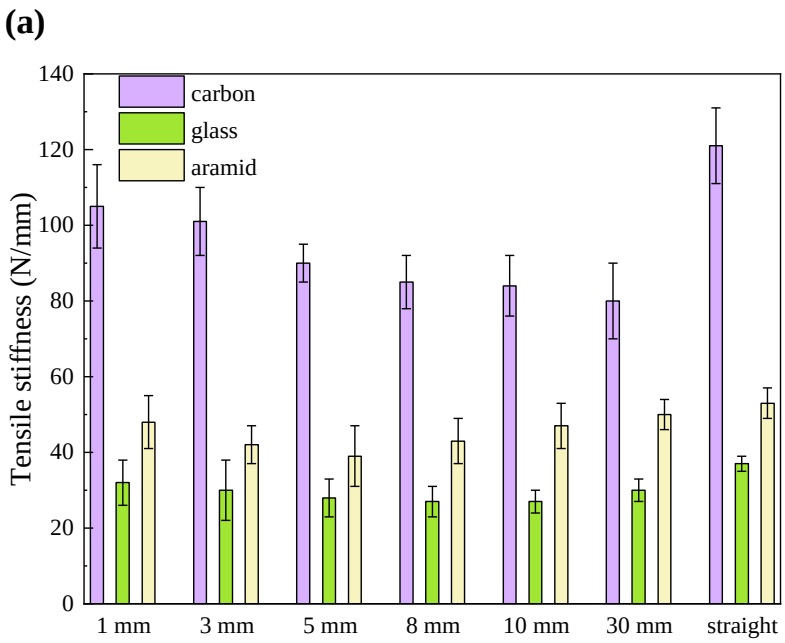

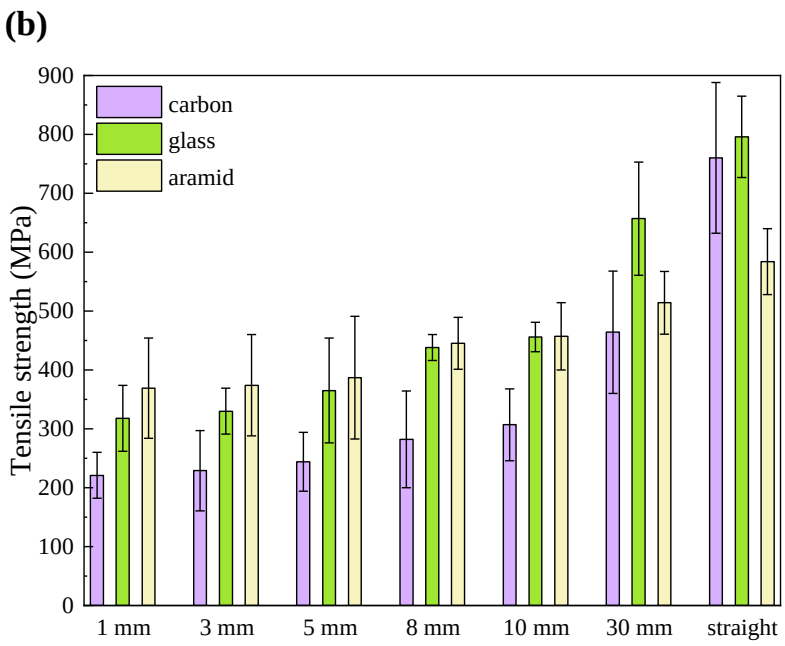

Figure 5-9 *Effect of FDM machine print radius on the tensile (a) stiffness and (b) strength of the filaments.*

Table 5-6 *Percentage reduction to the filament stiffness due to curvature relative to the straight filament.*

Set radius value	Carbon-Polyamide	Glass-Polyamide	Aramid-Polyamide
1 mm	13%	14%	9%
3 mm	16%	19%	21%
5 mm	26%	24%	26%
8 mm	30%	27%	19%
10 mm	31%	27%	11%
30 mm	34%	19%	6%

Table 5-7 *Percentage reduction to the filament strength due to curvature relative to the straight filament.*

Set radius value	Carbon-Polyamide	Glass-Polyamide	Aramid-Polyamide
1 mm	71%	60%	37%
3 mm	70%	59%	36%
5 mm	68%	54%	34%
8 mm	63%	45%	24%
10 mm	60%	43%	22%
30 mm	39%	18%	12%

The tensile stiffness of the curved filaments were lower than that of the straight filament for the three fibres. The result of the curved carbon-polyamide filament decreased with increasing the curvature radius. The tensile stiffness highly depends on the length of the specimen going through extension during loading. For the 3D printed filament with curvature, the weakening and geometric deformation can raise the stress concentration at the curved section, restricting the extension of the material to a region much shorter than the overall length. The tighter the printing radius is, the shorter the curved section is. Therefore, although the fibre fracture at the curved section is more severe for the carbon fibre filament with a tight curvature radius, as shown in **Figure 5-5**, the extension of the filament can be the crucial factor leading to higher tensile stiffness than filaments with lower curvature. A similar trend was found for the glass-polyamide filament with a curvature radius lower than 10 mm, as well as for the aramid-polyamide filament with a curvature radius lower than 8 mm. The increased stiffness of the glass and aramid fibre filaments printed with a loose curvature radius can be attributed to the increased load-bearing capacity benefiting from less sensitivity of the flexible fibre to the twisting.

The tensile strength of the curved filaments are relatively low and constant when the radius size is below ~5 mm. When the radius was below 5 mm, the average filament strengths were only 30%, 41% and 64% compared to the straight printed filament for the carbon-, glass- and aramid-polyamide, respectively. The strengths of the filaments increased with the radius above ~5 mm, although the rate of increase was dependent on the fibre type. For example, the tensile strength of the carbon-, glass- and aramid-polyamide filaments with the

radius of 30 mm was 61%, 82% and 88%, respectively, of that of their straight filament. Two factors are responsible for the reduction in the measured tensile strength: fibre breakage and fibre twisting. As reported above, the amount of fibre breakage and twisting decreased with increasing radius and therefore the filament strength was reduced less.

5.4 Conclusions

The study presented in this chapter reveals that the FDM process to 3D print curved filaments using a Markforged® printer can cause significant deformation and damage, particularly at small radius values. Microstructural analysis of curved filaments printed at various radii reveals that folding and twisting occurs at tight curvatures. The folding angle decreases with increasing print radius for the three filament types. When the print radius exceeds ~10 mm, the folding process does not occur and instead fibre twisting occurs within the curved section of the filament. Additionally, the radii of some fibre printing paths at the folded region are lower than the calculated limit value to fracture in the case of a small set radius (1 mm and 3 mm), causing carbon fibre breakage.

The fibre damage and twisting in the curved section reduces the tensile stiffness and strength of the printed FDM filaments. Longitudinal tearing of the polyamide matrix at tight curvatures may contribute to the reduced strength. The fibre twisting occurred in a curved geometry induces considerable shear stress to the fibre under longitudinal tensile load, leading to a premature failure of the filaments for all three fibre types. The tensile strength values of the carbon-, glass- and aramid-polyamide filament increases with the print radius. With a radius lower than 5 mm, the residual strength values obtained here are only 30%, 41% and 64% for the carbon, glass and aramid filaments, respectively, compared to the straight printed filament, revealing that a complex geometry with a tight curvature radius should always be avoided in 3D printed load-bearing composite components.

It is worth noting that the printing speed and temperature were not varied in this study because they are fixed for the MarkForged printer used. While the speed and temperature may affect the folding and twisting of the filament, these were not studied. These process parameters could influence the amount of filament twisting and, in particular, the filament folding as well as the curvature radius value when these occur. It is also possible that the critical radius value at which twisting and folding occurs is dependent on the fibre content of the filament. Increasing the fibre content, and therefore the stiffness, of the filament is likely

to increase the critical radius value, however this was not explored due to the fibre content of the filaments used in this study being fixed. The effect of printing parameters and fibre content on the curvature of 3D printed filaments, including the amounts of twisting and fibre damage, is a topic worthy of investigation

CHAPTER 6: EFFECT OF 3D PRINTING DAMAGE ON THE TENSILE PROPERTIES OF FDM CONTINUOUS FIBRE-POLYMER COMPOSITES

Abstract

The damage caused to continuous carbon, glass and aramid fibres in the 3D printing process using an FDM printer was investigated in Chapters 3 and 4. The research revealed that the amount and types of fibre damage caused by the FDM process and the resultant reduction to the tensile properties of the FDM filament are dependent on the fibre type. This chapter presents an experimental study to determine the tensile properties and damage mechanisms of 3D printed unidirectional composites containing multiple filaments made using the FDM process. Investigations were conducted on carbon-, glass- and aramid-polyamide composites made by the layer-by-layer deposition of filaments using a MarkForged® printer. The microstructural and tensile properties of the three types of 3D printed composite are investigated. For comparison, hot moulded unidirectional composites fabricated using the FDM filaments, but without being subjected to the FDM printing process, were also investigated. The hot moulded composites had the same fibre type and similar fibre content and fibre orientation and the same polyimide matrix as the FDM printed composites. This comparison enables the effect of 3D printing-induced microstructural defects on the tensile properties of FDM composites to be quantified. The microstructure of the 3D printed composites contained a higher void content as well as more micro-cracks and broken fibres than the hot moulded composites with the same composition. As a result, the tensile modulus and failure stress properties of the carbon-, glass- and aramid-polyimide composites produced using the FDM process were lower than the composites made using hot moulding. The tensile failure mechanism of the composites was also altered by 3D printing.

6.1. Introduction

The layer-by-layer filament deposition process of additive manufacturing makes it possible to fabricate continuous fibre composite parts with intricate geometries, which would be challenging or impossible using conventional manufacturing techniques such as manual layup, pultrusion, hot compression moulding and resin transfer moulding. However, the 3D printing process can affect part quality, including creating large voids, high void content, uneven fibre distribution, and poor bonding of the filaments [14, 16, 23, 28, 29, 32], as reported in **Chapter 2**. Several studies have characterised the mechanical properties of FDM printed composites under various load conditions, and attributed the lower-than-expected properties to voids and imperfect filament fusion. As reported in **Chapter 2**, factors such as poor compatibility between the polymer matrix and fibres and the lack of high pressure during filament deposition are responsible for the high porosity of composites made using the FDM process. Many efforts have been made to reduce the void content by fibre surface modification [21, 166] or post-processing of the 3D printed composite using heat treatment [167] or compression forming [91]. Several studies [28, 29, 32, 99] have reported fibre fracture and pull-out as the most critical failure processes in 3D printed continuous fibre composites under tensile loading. However, the tensile failure mechanisms related to printing process-induced defects and consequently the tensile properties are still not fully understood. Such an understanding is essential to maximise the microstructural quality and mechanical properties of 3D printed composites fabricated using the FDM process.

This chapter presents an experimental study to investigate the microstructure and tensile properties of 3D printed unidirectional composites made by the layer-by-layer deposition of carbon-, glass- or aramid-polyamide filaments using the FDM process. Composites containing the filaments were also made by hot moulding to avoid damage caused by the FDM process, and their properties are compared to the 3D printed composites. The filament types and processing temperature used for hot moulding the composites were consistent with FDM manufacturing, and their fibre content was similar to the 3D printed composites. Using microstructural analysis techniques, the study identifies process-induced defects during the 3D printing of continuous fibre composites using the FDM process. The tensile modulus, strength and failure mode of the 3D printed composites are determined, and compared to the composites made by hot moulding. Acoustic emission (AE) is used to

monitor fracture initiation and progression as well as to identify the damage types during tensile testing of the 3D printed and hot moulded composites.

6.2 Materials and Experimental Methodology

6.2.1 Materials and specimen conditions

The composite materials were fabricated using the same FDM filaments studied in the previous chapter, i.e. unidirectional carbon-, glass- and aramid-polyamide filaments supplied by Markforged®. The physical and microstructural properties of these filaments were described in detail in **Chapters 3** and **4**. The individual 3D printed filament consisting of fibrous tow in polyamide matrix represents the 'basic building block' of the 3D printed composites using the filament-by-filament, layer-by-layer deposition process illustrated in **Figure 3-2**. Unidirectional $[0°]_{16}$ carbon-, glass- and aramid-polyimide composites fabricated using the 3D printing and hot moulding methods were used to compare the microstructures, mechanical properties and tensile fracture modes. The two manufacturing processes are described below in the next two sub-sections.

The fibre volume fractions of the 3D printed $[0°]_{16}$ composites containing carbon-, glass- or aramid-polyamide was ~29.1%, ~26.5% and ~35.7% and for the hot moulded composites was ~30.6%, ~30.7% and ~38.6%, respectively. The slightly higher fibre volume contents to the hot moulded composites were caused by the higher consolidation pressure applied during the composite manufacturing, which decreased the void content and thereby increased the fibre volume fraction. However, the fibre contents of the hot moulded composites were still lower than the Stage 1 filaments (as-received condition) with 34%, 32% and 41% for carbon, glass and aramid FDM filament, respectively, as presented in **Chapter 3** and **4**. The void contents of the different composites are discussed later in the chapter. It is worth noting that the difference in fibre content (under ~4%) is within the range of scatter in the measured tensile properties of the composite materials, as reported later.

The fibre contents of the carbon- and glass-polyamide composites fabricated using the 3D printing and hot moulding methods were determined in accordance to ASTM D3171-15 [168]. Burn-off test was performed in a vacuum furnace to remove the polymer matrix. The materials were heated at the constant rate of 5°C/min to 500°C and kept at the temperature for 8 hours. The mass of the material before and after the burn-off test were measured using a gas pycnometer (Ultrapyc 3000) to within an accuracy of 0.1 mg. The fibre

contents of the aramid-polyamide composites were measured by phase-contrast imaging (ImageJ). As mentioned in **Chapter 4**, the pyrolysis method was not employed to measure the aramid fibre content because of the temperature used is close to the degradation temperature of aramid.

6.1.1.1. 3D printed composites

3D printing of the unidirectional carbon-, glass- and aramid-polyamide composites was performed using the Markforged® printer described in **Chapter 3**. The printer settings were the same as those used in **Chapters 3** and **4** to print the single filaments, with the extrusion temperature set at 254°C and the filament deposition rate at 15 mm/s. The filaments were deposited onto the build platform (which was at room temperature) of the FDM printer in a unidirectional pattern. The printed single ply thickness was ~125 μm for carbon-polyamide and ~100 μm for glass- and aramid-polyamide, as fixed in the FDM printer setting. The 3D printed unidirectional composite specimens used for tensile testing were designed according to ASTM D3039 [169]. The specimens contained 16 unidirectional layers of the fibre-polyamide filaments deposited side-by-side and layer-by-layer, with the external polymer-rich surfaces and sides [23] removed after printing. The specimen dimensions are given in **Table 6-1**. **Figure 6-1** shows top-down views of the three types of 3D printed composite showing the filament-by-filament pattern. The filaments were looped backwards at the edges to enable a continuous printing process, however these loops were removed from the tensile specimens. Fibre waviness and elongated voids between adjacent filaments can be observed at the specimen surface.

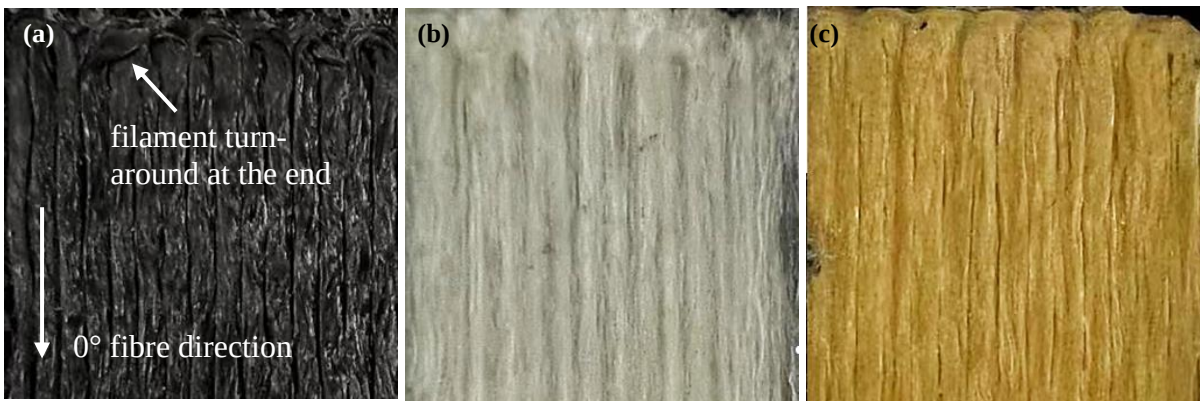

Figure 6-1 *Top-view of 3D printed (a) carbon-, (b) glass- and (c) aramid-polyamide composites. The longitudinal direction is parallel to the 0° fibre orientation in the unidirectional specimen and the transverse direction is normal to the 0° fibre orientation.*

***Table 6-1**. Tensile test specimen dimensions and fibre contents.*

Composite	Material	Dimension (L × W × T, mm)	Measured fibre volume content
3D printed $[0°]_{16}$	carbon	200 × 15 × 2	29.1%
	glass	200 × 15 × 1.6	26.5%
	aramid	200 × 15 × 1.6	35.7%
hot moulded $[0°]_{16}$	carbon	200 × 15 × 2	30.6%
	glass	200 × 15 × 1.6	30.7%
	aramid	200 × 15 × 1.6	38.6%

6.1.1.2. Hot moulded composites

Hot moulding of the undirectional composites involved the use of heat and pressure in processing the FDM feedstock filaments in the as-received (i.e. Stage 1) condition. **Figure 6-2** indicates the process stages to the hot moulding method. The as-received filaments were cut into 220 mm lengths. Then fifteen filaments were arranged side-by-side in a unidirectional orientation and then fused slightly using hot gun heating to form a rectangular-shaped sheet (**Figure 6-3**). Sixteen sheets were then laid up in layers in a [0°] ply pattern inside a steel mould which was pre-heated to 254^{o}C. The internal dimensions of the mould were 200 mm long, 15 mm wide and 2 mm deep for the carbon-polyamide composite. The depth of the mould for the glass-polyamide and aramid-polyamide composites was 1.6 mm. (The mould was thinner for these materials to match the thickness of the 3D printed glass-polyamide and aramid-polyamide composites). The mould was then bolted close and heated to 254^{o}C (identical to the FDM print temperature) in an oven for 15 minutes to melt the polyamide matrix and fuse filaments. The mould was bolt tightened to reach the target thickness of the composites. The hot moulded composite was held in the mould until cooled to room temperature to limit the shrinkage and deformation. Excess material was cut-off once the coupon was fabricated (**Figure 6-5**).

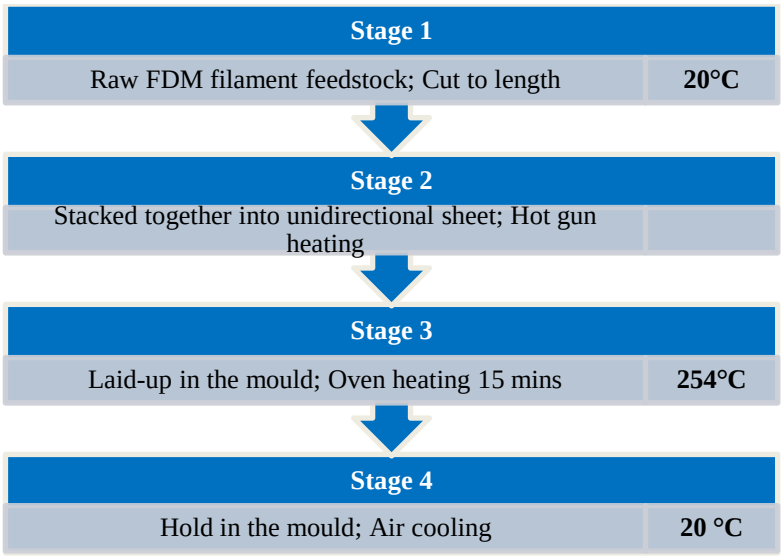

Figure 6-2 *Flowchart of the hot moulding process stages.*

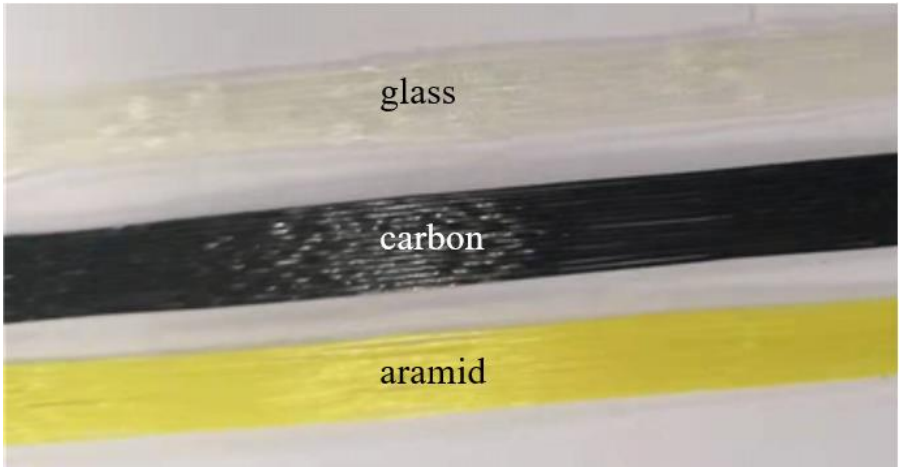

Figure 6-3 *Unidirectional sheets of carbon-, glass- and aramid-polyamide with filaments arranged side-by-side.*

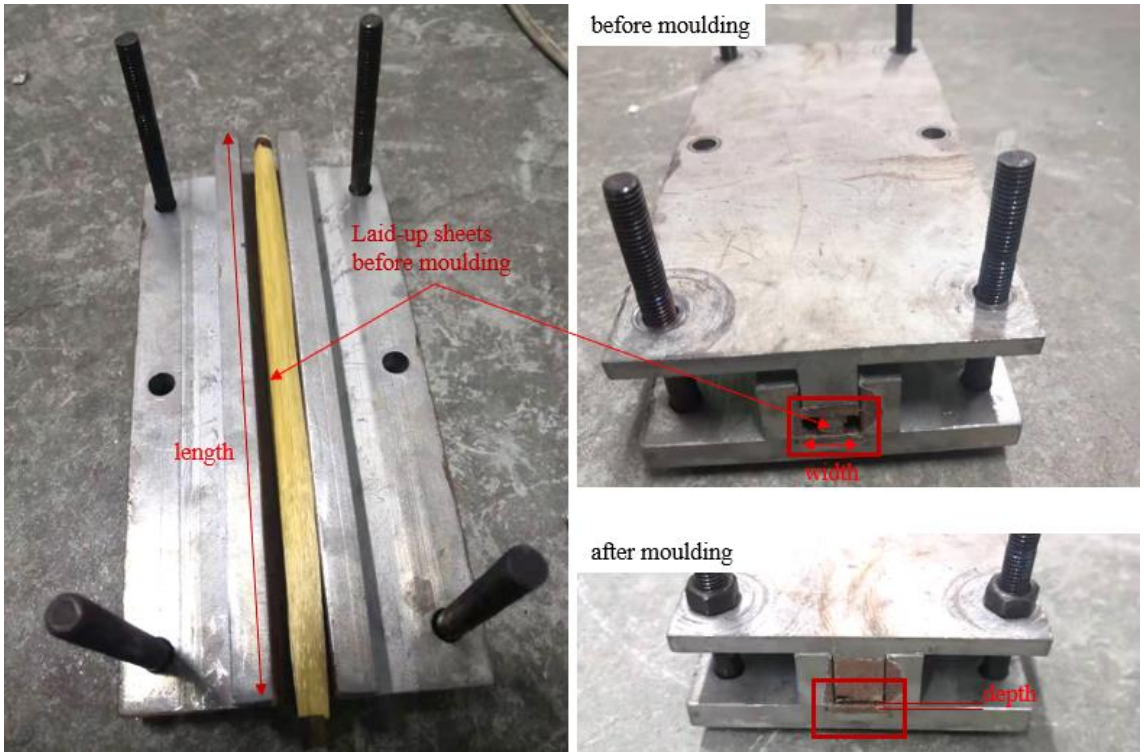

Figure 6-4 *Steel mould with composite sheets laid-up in the cavity before and after moulding.*

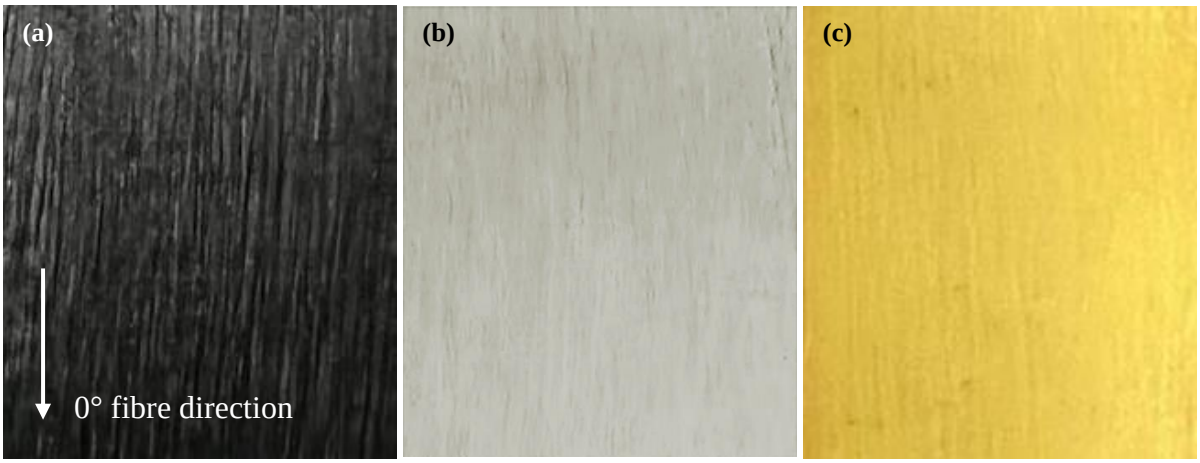

Figure 6-5 *Top-view of hot moulded (a) carbon-, (b) glass- and (c) aramid-polyamide composites. The longitudinal direction is parallel to the 0° fibre orientation in the unidirectional specimen and the transverse direction is normal to the 0° fibre orientation.*

6.2.2 Microstructural examination of composites

The microstructures of the 3D printed and hot moulded composites were examined using X-ray Computed Tomography (CT) and Scanning Electron Microscopy (SEM). The X-ray CT was performed using a GE Phoenix Vo|tome|xs high resolution system with a tungsten X-ray tube. The CT inspection parameters were 140 µA and 50 kV for current and

voltage, respectively. The composite specimens used for the X-ray CT scanning were 10 mm long x 10 mm wide, and contained 16 filament layers. SEM was performed using a TM4000PLUS (Hitachi), with the samples coated with a thin film of iridium prior to examination to avoid electron beam charging effects. The SEM inspection parameters were 55 μA and 15 kV for emission current and accelerating voltage, respectively, and the working distance was 16 mm.

The fibre waviness in the composites was measured from X-ray CT images using the ImageJ (NIH) post-processing software (using the orientationJ plugin), with a minimum of 15 images per sample (6.0 mm long x 4.5 mm high).

6.2.3 Tensile property testing of composites

The 3D printed and hot moulded composites were tensile tested with AE monitoring. The tensile properties of the composites were measured in the fibre direction [0°] using a 50 kN load capacity universal testing machine (Wance TSE504C, China) operated at an extension rate of 0.5 mm/min until failure. The tensile tests were conducted at room temperature. The specimens were 200 mm long (with a gauge length of 150 mm), with the ends reinforced with 25 mm long x 2 mm thick glass–epoxy tabs to avoid damage when gripped in the tensile machine. The tensile modulus of composites was measured using an extensometer with a gauge length of 50 mm. At least five specimens of each composite type were tested to determine the average and scatter to the tensile properties.

The AE system (MISTRAS-2001, China) and a wide-band transducer (R15, China) with a frequency range of 20-1000 kHz was used to monitor the composites during tensile testing. The AE signals detected by the transducer were magnified using a preamplifier with a gain setting of 40 dB and additional amplification of 20 dB using the AE system. A coupling agent (silicone gel) was used to ensure transmission of acoustic waves from the specimen to the transducer with minimal attenuation at the interface. The acquisition parameters of the AE system were set at an amplitude threshold of 50 dB, peak definition time (PDT) of 30 μs, hit definition time (HDT) of 150 μs, hit lockout time (HLT) of 300 μs, band-pass of 100-1000 kHz and recording rate of 3 M/s. A single transducer with a diameter of 8 mm was held against the coupon at the mid-point of the gauge section during the tensile test.

6.3 Results and Discussion

6.3.1 Effects of 3D printing on microstructure of continuous fibre-reinforced polyamide composites

This section describes and compares the microstructures of the 3D printed and hot moulded composites. The SEM images presented in **Figure 6-6** show the 3D printed composites in cross-section. The composites show significant material inhomogeneity with distinct fibre clusters and resin-rich regions. Voids of different sizes also occurred in the 3D printed composites; **Figure 6-7** and **Figure 6-8** present histograms of the shape (aspect ratio) and size of voids obtained from X-ray CT imaging. The porosity contents to the 3D printed composites were 11.9%, 10.6% and 5.5% for carbon-, glass- and aramid-polyamide, respectively. The measured porosity contents of the carbon and glass composites are similar to those reported in [29, 58]. However, there is no previously published information on the void content of aramid-polyamide composites manufactured using the FDM process. The higher porosity content for the 3D printed carbon composite can be explained by the larger number of small voids within the filaments. As shown in **Figure 6-6a**, small voids (under tens of microns) and micro-cracks mostly appeared in the carbon fibre clusters, and larger voids (up to ~500 μm wide) occurred in the polymer-rich fusion zones between filaments and layers. The porosity content of the 3D printed glass composite is mainly due to large-sized voids between the non-overlapped filaments, which even extended through multiple layers (maximum void volume of up to 6×10^8 μm^3), as shown in **Figure 6-6b**. In comparison, the aramid composite contained fewer micro-voids within the filament and the gaps between the filaments were narrower (maximum void value of up to 5×10^8 μm^3) than those in the glass composite. Therefore, the 3D printed aramid composite had the lowest porosity content. **Figure 6-7** presents the shape of voids in the 3D printed composites. The void shape is represented by the aspect ratio, which was calculated by dividing the void length (measured in the longitudinal [0] direction) by the void width (measured in the transverse direction). A void with an aspect ratio above 1 represents a void elongated in the fibre and/or through-thickness directions. It is shown that void cross-sections for the carbon composite were mostly in circular or elliptical shape, with an aspect ratio between 0.5-1.5. In comparison, the 3D printed glass and aramid composites contained fewer voids with an aspect ratio no more than 2 but much more elongated voids with a large aspect ratio (up to ~8 and ~6, respectively, **Figure 6-7b** and **c)**.

Micro-cracks and voids within fibre clusters inside the 3D printed carbon composite are caused by insufficient impregnation of polymer into the carbon fibre clusters. During 3D printing, the melted polymer cools rapidly below the T_g and solidifies shortly after the filament is deposited on the build platform. The slight pressure applied by the nozzle to the filament is not enough for the melt polymer to completely fill in the fibre clusters, especially when the fibres are tightly compacted. Cracks may possibly be caused by the rapid cooling and solidification generating thermal residual stresses due to the mismatch in the coefficient of thermal expansion between the fibres and polymer matrix. As shown in **Figure 6-8**, small voids with the volume of thousands of cubic micrometres most commonly occurred in the 3D printed composites. However, larger-sized voids (volume over 1×10^6 μm^3) between the printed adjacent filaments represented the major part of the global void content, which was around 44% for the carbon, 91% for glass and 75% for aramid. The significant filament non-overlap in the glass and aramid composites is due to their smaller FDM filament diameters (0.32 mm and 0.33 mm, respectively) compared to the carbon composite (0.37 mm). When the as-deposited filament is flattened by the nozzle during 3D printing, an FDM filament with a smaller diameter will be deformed into a sheet with a smaller width, leading to less overlap between flattened filaments. Additionally, because the build platform is levelled manually according to the user guide provided by Markforged®, it is challenging to precisely adjust the gap opening between the nozzle and build platform to the optimum setting. Any tens of micrometres variance from the optimum gap opening can significantly affect the flattening and width of the filament during deposition. As measured from SEM images, the width of a single glass filament (in the printed condition) in the bottom layer was only ~0.6 mm, while that of aramid and carbon composites was ~0.7 mm and ~0.8 mm, respectively. The less overlap between adjacent filaments in the 3D printed glass- and aramid-polyamide composites compared to 3D printed carbon composites has also been reported in previous studies [29, 58] using a Markforged® commercial desktop printer. The temperature of the build platform is another factor affecting the fusion between filaments. Because the build platform is at room temperature, the material printed on it experiences a very fast cool down to the solid state, which can cause insufficient fusion between filaments leading to large voids.

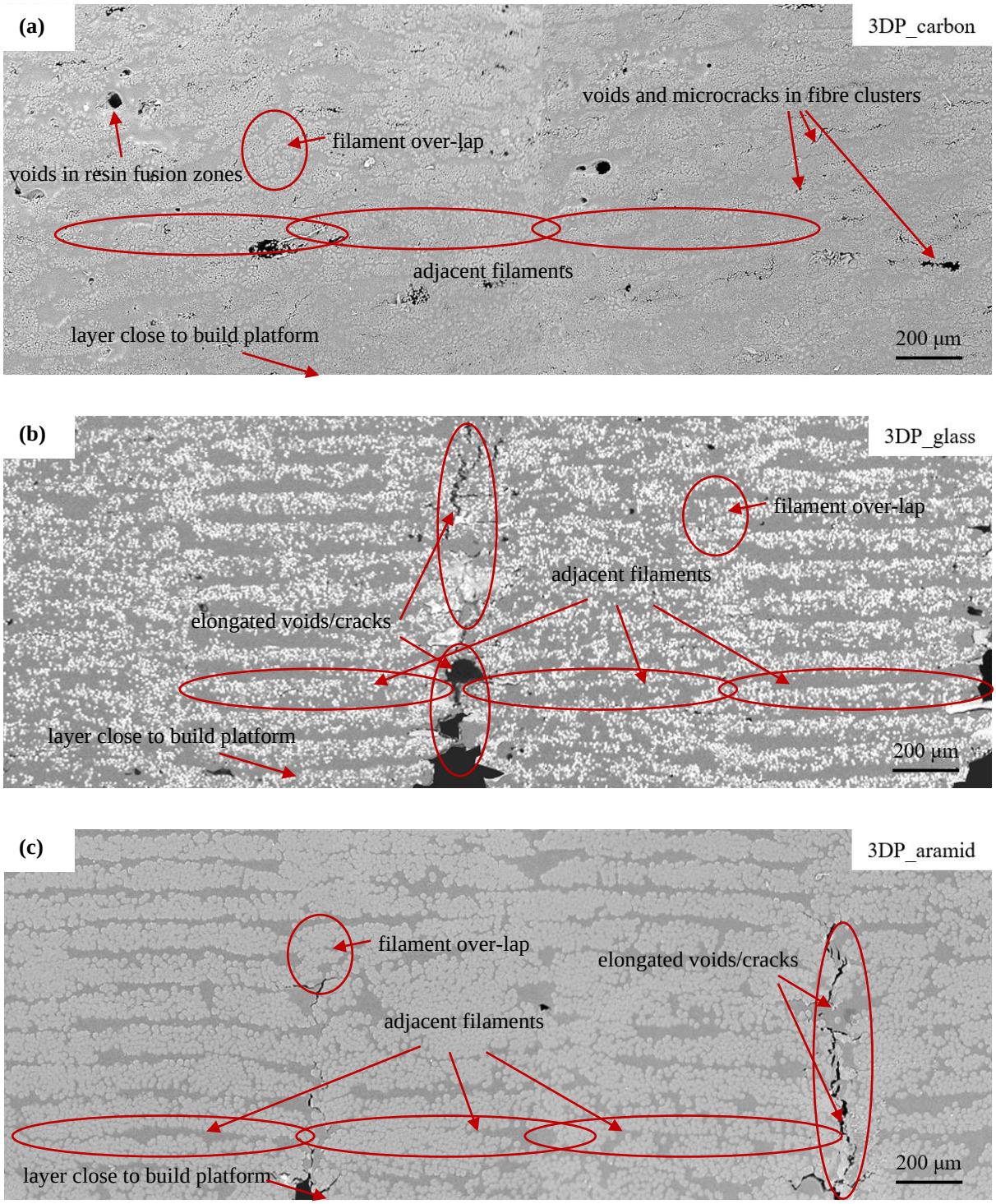

Figure 6-6 *Cross-sections of 3D printed (a) carbon-, (b) glass- and (c) aramid-polyamide composites. The processing-induced defects, including voids and microcracks, are indicated.*

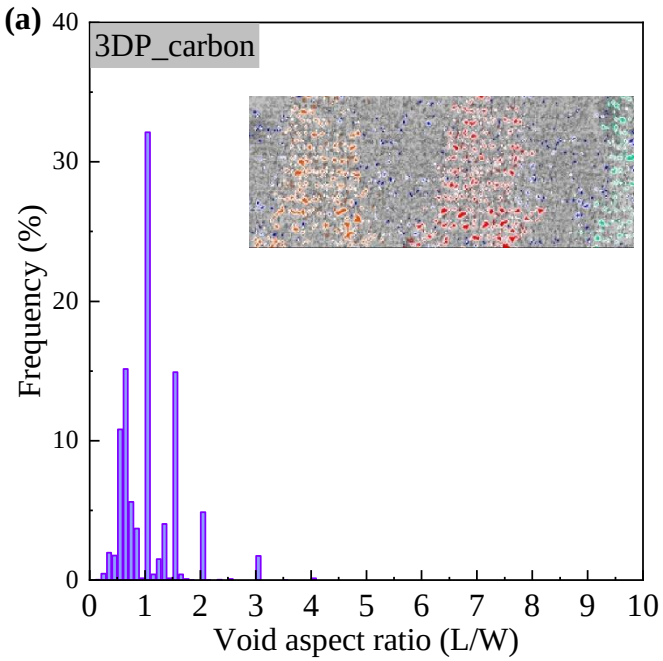
(a)
3DP_carbon
Frequency (%)
Void aspect ratio (L/W)
0
10
20
30
40
0
1
2
3
4
5
6
7
8
9
10

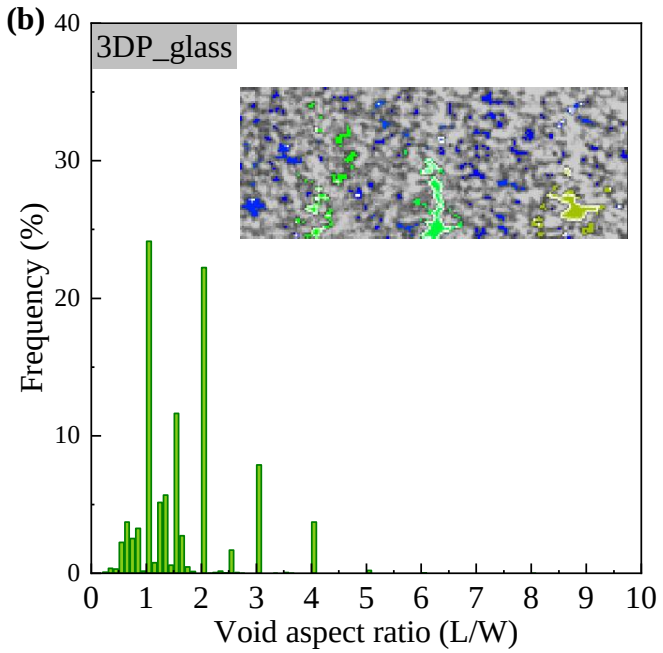
(b)
3DP_glass
Frequency (%)
Void aspect ratio (L/W)
0
10
20
30
40
0
1
2
3
4
5
6
7
8
9
10

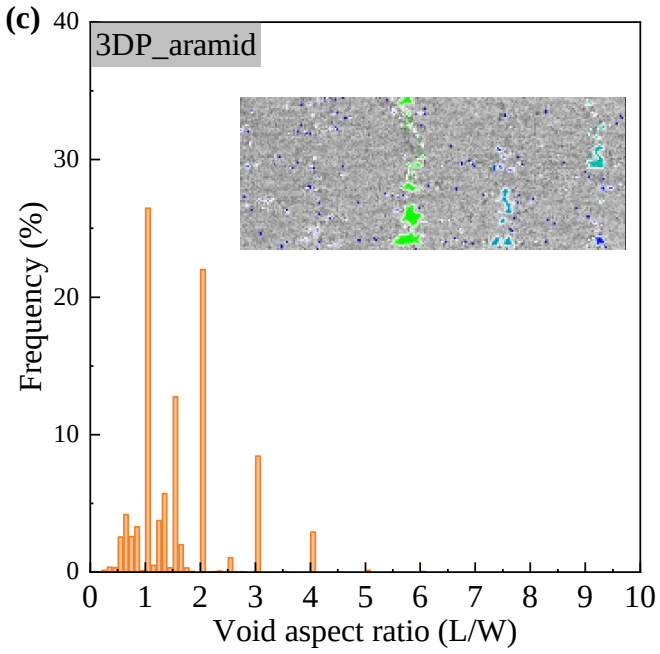

Figure 6-7 *Histogram of void aspect ratio for 3D printed (a) carbon-, (b) glass- and (c) aramid-polyamide composites. The aspect ratio is the void length (L, in the longitudinal direction) divided by void width (W, in the transverse direction). The high value represents an elongated void/crack. X-ray CT image inserted in the plot is the cross-section of the analysed region, with the voids colored. (Note: X-CT images are taken by Huanxin Zhang).*

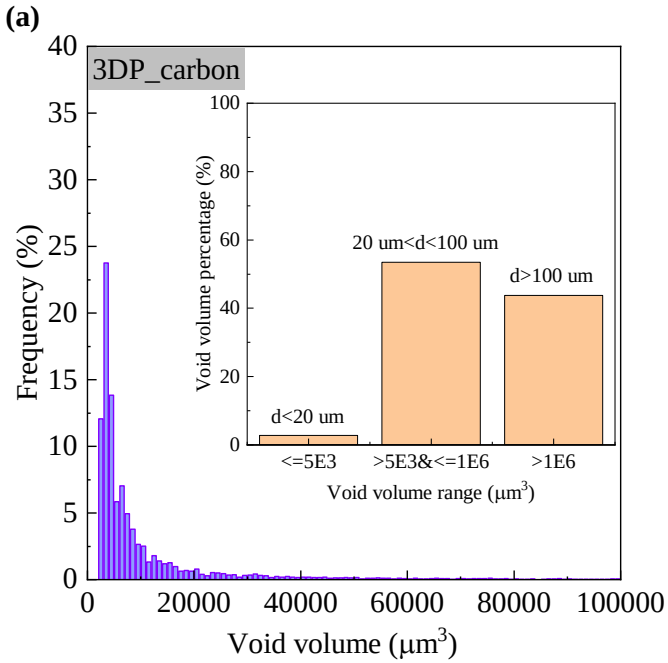

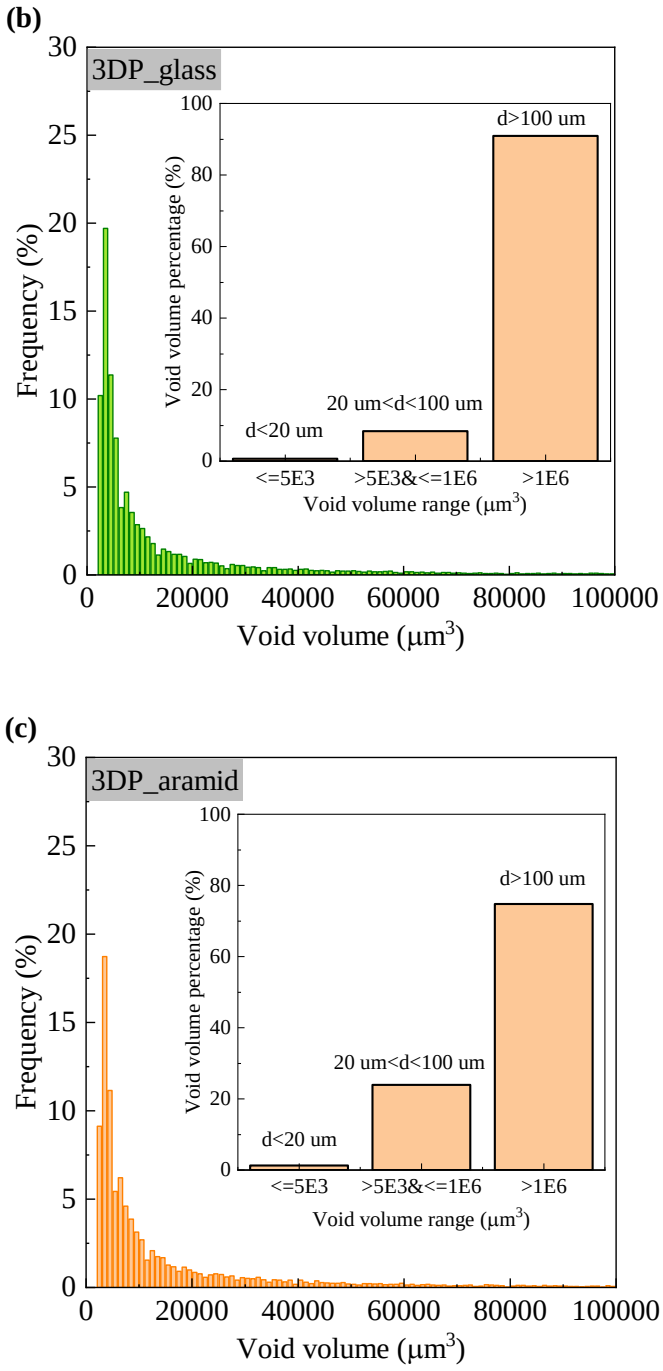

Figure 6-8 *Histograms of void size for 3D printed (a) carbon-, (b) glass- and (c) aramid-polyamide composites. Large voids with volumes over 100000 μm³ are not presented in the plots due to their very low occurrence. The insert plot shows the volume percentage (void volume divided by total porosity volume) of the small (d under 20 μm), intermediate (d between 20 and 100 μm) and large voids (d above 100 μm), where 'd' is the void diameter if regard the void as a sphere.*

The cross-sections and void analysis of the hot moulded composites are shown in **Figure 6-9**, **Figure 6-10** and **Figure 6-11**. As shown in **Figure 6-9**, the fibre distribution was more even than for the 3D printed composites. However, resin-rich areas still occurred due to the inhomogeneous distribution of the fibre and matrix phases in the FDM filament. Furthermore, the uniform heat and pressure applied during the hot moulding process aided better compaction, consolidation and fusion of the filaments, reducing the porosity content to 0.5%, 1.5%, and 0.7% for the carbon, glass and aramid composites, respectively. Microcracks and voids, which were much fewer in number, were mainly in fibre clusters for the hot moulded carbon composite while the glass and aramid composites had voids and microcracks in both the resin-rich regions and at fibre/matrix interfaces.

The average void size in the hot moulded composites was also smaller than the 3D printed composites. As shown in **Figure 6-10**, the maximum void aspect ratios of the hot moulded composites for the three fibre types (no more than 4) were lower than 3D printed composites. This is because the hot moulded composites do not have the filament non-overlap issue (thereby no elongated voids in the through-thickness direction). **Figure 6-11** presents histograms of the volume percentage of voids with different sizes for the hot moulded composites. Benefiting from the uniform pressure and longer heating period applied during the hot moulding process, the probability of the medium- to large-sized voids (volume over 2×10^4 μm^3) was much lower compared to the 3D printed composites (**Figure 6-8**) and the maximum void volumes of the hot moulded carbon, glass and aramid composites were two orders of magnitude smaller than their 3D printed counterparts.

SEM images in **Figure 6-9** show that voids in the resin-rich regions were larger in the hot moulded glass composite than in the carbon and aramid composites. This agrees with the results presented in **Figure 6-11**, which show that the volume percentage of voids over 1×10^6 μm^3 was higher in the hot moulded glass composite (~7%) than in the carbon (~1%) and aramid (0%) composites. This may be attributed to the lower thermal conductivity of the glass-polyamide composite which hinders filament fusing, particularly in the centre of the composite. It is well known that the standard carbon fibre has higher thermal conductivity (of up to 180 W/mK) that exceeds that of glass (~1 W/mK) and aramid (~3 W/mK) fibres [96, 170-172]. Therefore, heat transfer occurred more effectively through the carbon composite compared to the glass and aramid composites, resulting in better filament fusion and fewer voids in the resin-rich area. The smaller void size and lower void content in the aramid

composite can benefit from the highest fibre volume fraction and higher thermal conductivity of aramid fibres compared to glass fibre.

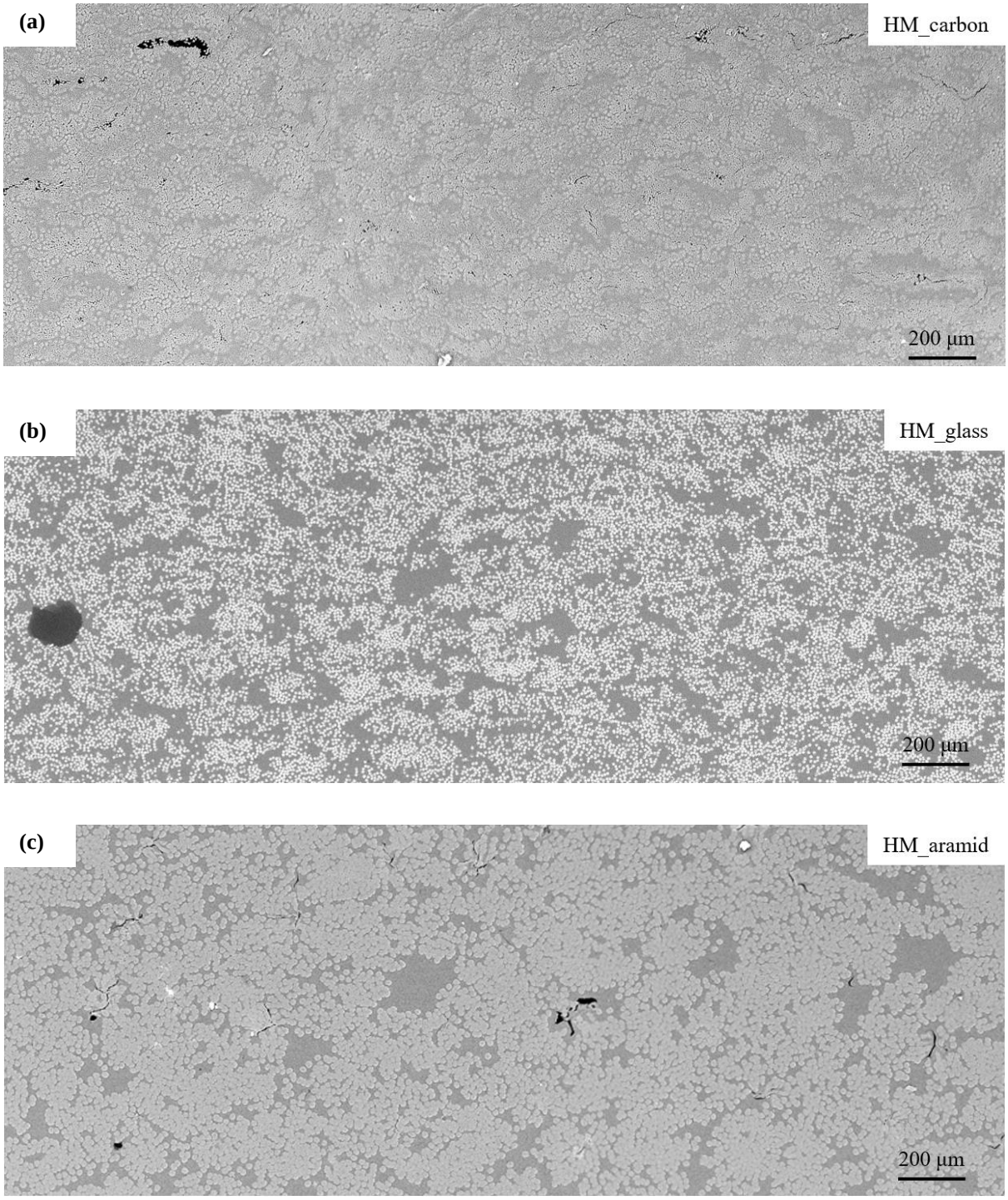

Figure 6-9 *Cross-sections of the hot moulded (a) carbon-, (b) glass- and (c) aramid-polyamide composites. The dark regions are voids.*

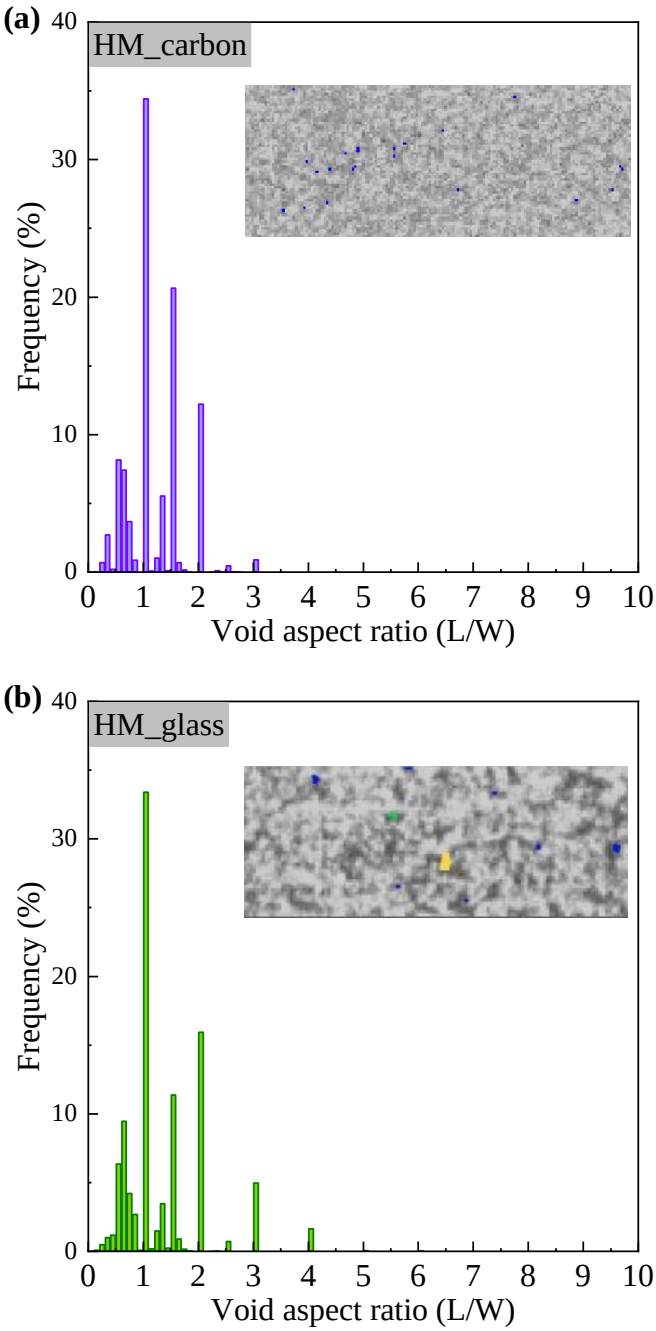
(a)
HM_carbon
Frequency (%)
Void aspect ratio (L/W)
(b)
HM_glass
Frequency (%)
Void aspect ratio (L/W)

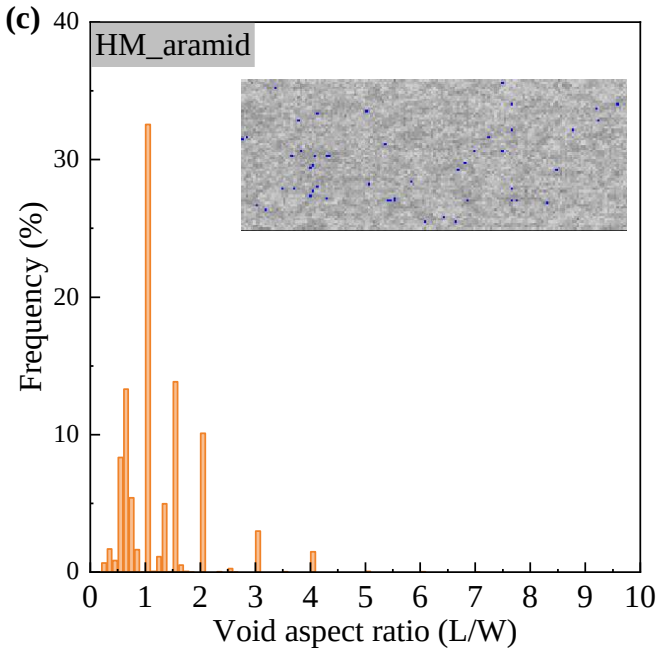

Figure 6-10 *Histograms of void aspect ratio for hot moulded (a) carbon-, (b) glass- and (c) aramid-polyamide composites. The aspect ratio is the void length (L, in the longitudinal direction) divided by void width (W, in the transverse direction). The high value represents an elongated void. X-ray CT image inserted in the plot is the cross-section of the analysed region with the voids coloured. (Note: X-ray CT images were taken by Huanxin Zhang).*

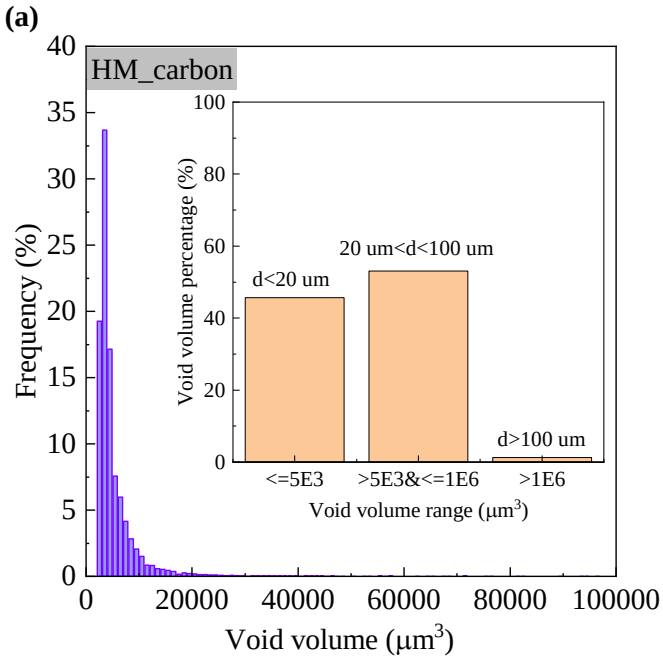

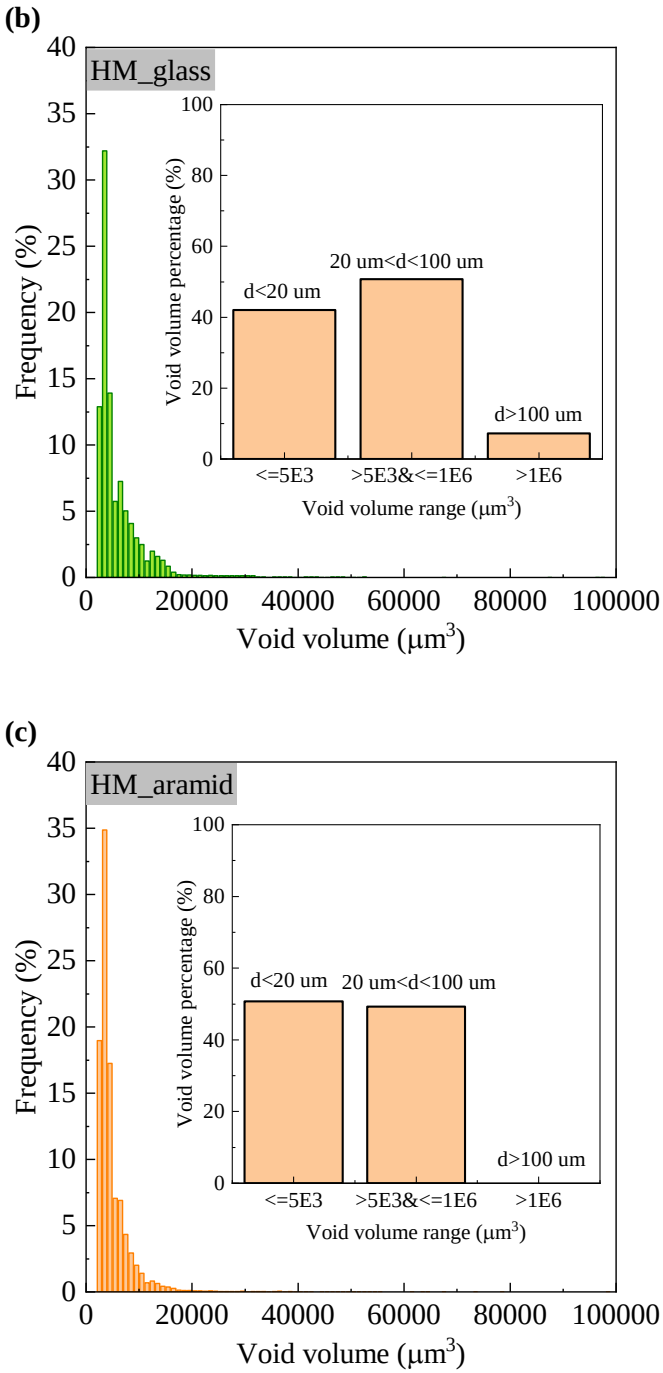

Figure 6-11 *Histograms of void size for hot moulded (a) carbon-, (b) glass- and (c) aramid-polyamide composites. The large-sized voids with volumes over 100000 µm³ are not presented in the plots due to their very low occurrence frequency. The inserted plot shows the volume percentage (void volume divided by total porosity volume) of the small, medium and large voids, and 'd' is the void diameter if regard the void as a sphere.*

To investigate the effect of the 3D printing process on fibre alignment in unidirectional composites, X-ray CT images of the 3D printed and hot moulded composites in the longitudinal [0] direction were post-processed by ImageJ software to measure the fibre alignment. **Figure 6-12** presents the reconstructed X-ray CT images and the fibre

misalignment probability distribution for the 3D printed and hot moulded composites. Because the distributions of the fibre alignment for the three types of composite materials were similar, only the carbon fibre composite is presented as an example. The X-ray CT revealed higher local fibre waviness in the 3D printed composites. The alignment of fibres to the 0^o direction is not as close for the 3D printed composite (waviness angles between approximately $+15^o$ and -15^o) compared to the hot moulded composite (angles within $\pm 10^o$), as shown in **Figure 6-12c**. The fibres in the 3D printed composites are wavier due to the low tension applied to the filament and insufficient adhesion force from the build platform during deposition. When the printing device bent and squashed the filament at the nozzle tip, the fibres spread out in the molten matrix and tended to become wavy without the filament tension provided by the nozzle. Fibre waviness caused during the FDM process has been reported in the literature [106, 164, 173]. However, only Galos et al. [164] quantified the fibre waviness using the fibre deviation angle measured from X-ray CT images. The deviation angle reported in the paper is smaller (within $\pm 5^o$) than the results in this study. Additionally, the local waviness of fibres in 3D printed composites can be caused by slight vibrations of the printer head when moving across the build platform. In contrast, the filaments used in the hot moulding process are laid-up together and pressed uniformly, resulting in smaller deviation angles (within ±10°). The fibre misalignment in the hot moulded composite probably results mostly from the local heating using a hot gun and the manual handling process.

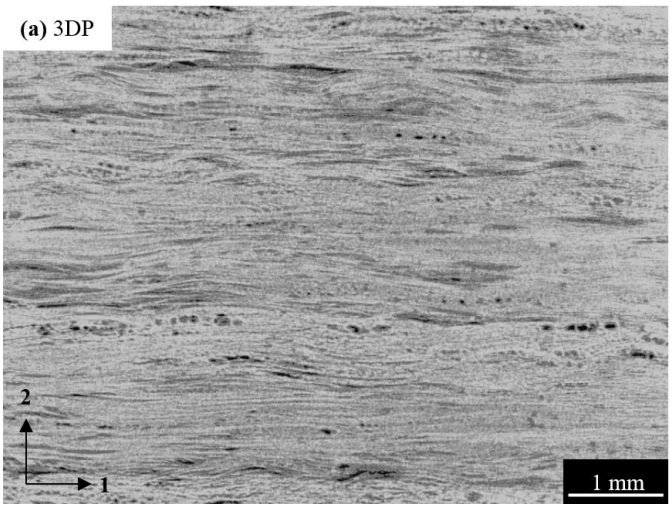

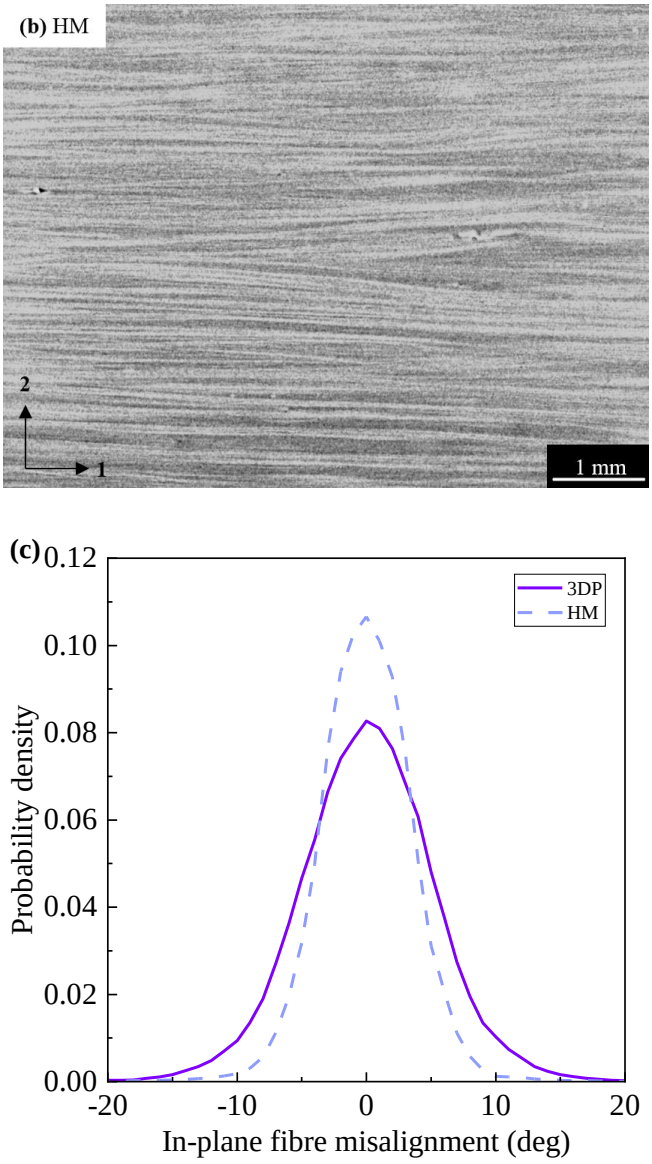

Figure 6-12 *X-ray CT images of the (a) 3D printed and (a) hot moulded carbon composites showing alignment of fibres. 1 and 2 refer to the longitudinal (0°) and transverse (90°) directions, respectively. (c) In-plane fibre misalignment probability distribution of unidirectional composites made by 3D printing and hot moulding. Fibre misalignment angles were measured relative to the longitudinal direction of the composite.* (Note: X-CT images taken by Huanxin Zhang).

6.3.2 Effects of 3D printing on tensile properties of continuous fibre-reinforced polyamide composites

Figure 6-13 presents tensile stress-strain curves measured in the longitudinal direction for the 3D printed and hot moulded composites. All of the composites showed linear elastic deformation to tensile failure. This behaviour is similar to that observed for the single FDM filaments presented in **Chapter 3** and **4**. The tensile properties of the 3D printed

composites are presented in **Figure 6-14**, and compared to the hot moulded composites. Within the bounds of experimental scatter (as defined by the error bars), the hot moulded carbon-, glass- and aramid-polyamide composites had modulus values that are 16%, 17% and 41% higher than those of the 3D printed composites, respectively. The hot moulded composites also had higher tensile strength values of 41%, 67% and 34% compared to the 3D printed composites with carbon, glass or aramid fibres, respectively. The tensile properties measured for the 3D printed composites in this study are higher than the values reported in many studies [23, 26-30, 58, 71, 174]. **Figure 6-15** compares the tensile properties measured for the 3D composites studied here against property values published in the literature, and generally the modulus and failure stress values are higher. This is because the published tensile property values are generally for composites with fibre layers sandwiched between or separated by polyamide layers. In contrast, the composites used in this research consist only pre-impregnated fibre/polymer FDM filaments, thereby maximising the fibre volume fraction. Similar tensile properties for a 3D printed carbon-polyamide composite were reported in [91]. However, the tensile strength of the 3D printed composites are still lower than the values provided by the Markforged® company [165]. **Figure 6-15** also compares the tensile properties of the 3D printed and hot moulded composites obtained in this study to continuous fibre composites made using conventional processes and aluminium alloy (AA7075). The hot moulded carbon composite had comparable tensile properties to glass/epoxy and aramid/epoxy composites made using conventional processes, although with a lower fibre volume fraction. The carbon composites evaluated in this study also had higher tensile strength than the aluminium alloy with comparable tensile modulus.

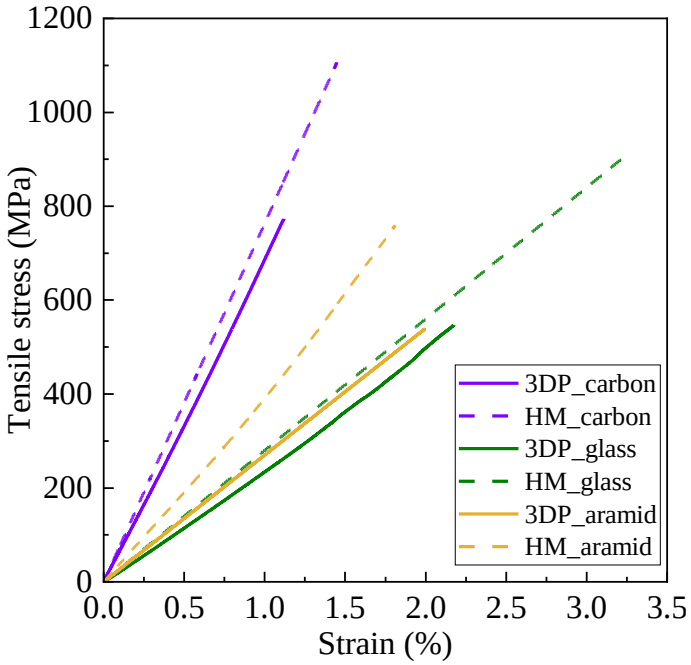

Figure 6-13 *Tensile stress-strain curves of carbon, glass and aramid composites made using the 3D printing and hot moulding process.*

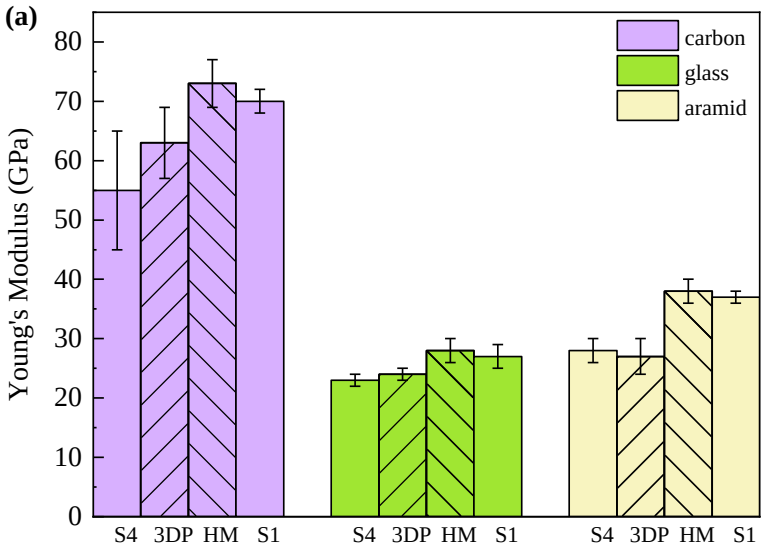

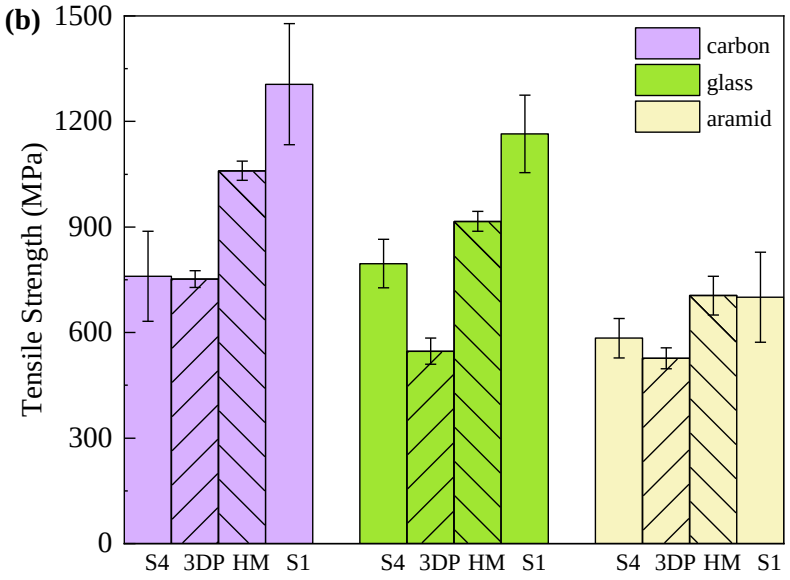

Figure 6-14 *Tensile (a) modulus and (b) strength of carbon-, glass- and aramid-polyamide composites fabricated using 3D printing and hot moulding. Tensile properties of Stage 4 (S4, 'building block' of 3D printed composites) and Stage 1 filament (S1, 'building block' of hot moulded composites) obtained in Chapters 3 and 4 are also presented in the plots as reference.*

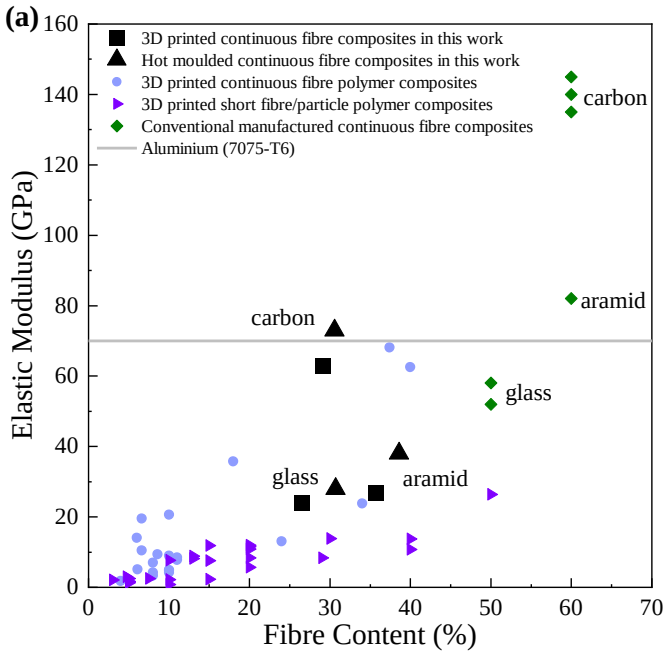

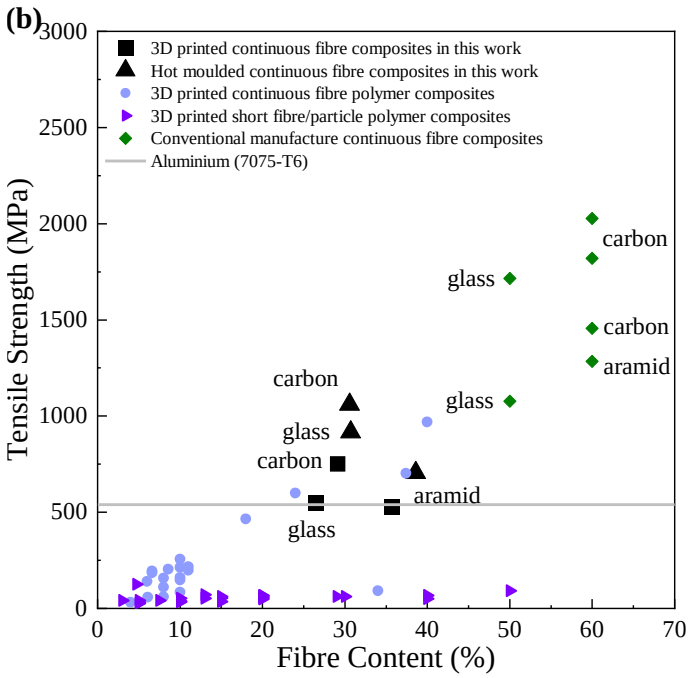

Figure 6-15 *Comparison of (a) Young's modulus and (b) tensile strength of 3D printed composites using the FDM process and hot moulding obtained in this study with literature data for 3D printed short fibre composites, continuous fibre composites, conventionally manufactured composites, and an aluminium alloy [12-30, 74].*

The main factors that resulted in the lower tensile modulus of the 3D printed composites compared to their hot moulded counterparts are the lower fibre volume fraction and higher void content. **Table 6-2** present modulus values predicted from the Stage 1 (in the printed condition) and Stage 4 filament (in the printed condition), which are the feedstock material of these composites, using rule-of-mixture calculation. The hot moulded carbon, glass and aramid composites showed higher tensile modulus values of 34%, 36% and 43% compared to the 3D printed composite, respectively, considering the fibre and void contents. Fibre waviness is another factor contributing to the lower modulus of 3D printed composites. As presented in **Figure 6-12**, the 3D printed composites had wavier fibres (of ±15°) compared to the hot moulded composites (angles within ±10°) thereby resulting in lower tensile modulus values. However, as can be seen in **Figure 6-14**, the tensile modulus values of the composites (both 3D printed and hot moulded) were all close to their feedstock filaments.

Table 6-2 *Comparison of the measured tensile modulus of 3D printed and hot moulded composites to the values calculated using rule-of-mixtures.*

Composite	Method	Measured modulus (GPa)	Calculated modulus (GPa)
Carbon	3DP	63±6	47
	HM	73±4	63
Glass	3DP	24±1	19
	HM	28±2	26
Aramid	3DP	27±3	24
	HM	38±2	35

The 3D printed composites also had lower tensile strength compared to the hot moulded materials. Fibre damage, higher fibre waviness and higher porosity are the main reasons leading to the lower tensile strength of the 3D printed composites. As discussed in **Chapter 3** and **4**, fibre damage and breakage (carbon and glass) and fibre crimp (aramid) caused by the 3D printing process weaken the filaments, which then decreased the tensile strength of the 3D printed composites. Voids occur in the fibre clusters and fibre/matrix interface due to insufficient impregnation of polyamide matrix during 3D printing. The voids adversely affect the load transfer between fibres under tensile loading. Furthermore, voids with large sizes (up to ~200 μm) in the polymer-rich fusion zones between adjacent filaments and layers can lead to delamination cracking and longitudinal splitting of the 3D printed composites under tension, especially in glass- and aramid-polyamide composites which had lower fusion between filaments caused by the more inter-filament voids. This can be evidenced by the tensile fracture modes for the 3D printed and hot moulded composite specimens presented in **Figure 6-16**. The carbon-polyamide composites manufactured using the two methods had a similar failure mode, with extensive splitting cracking longitudinal to and multi-point fractures perpendicular to the tensile loading direction due to fibre breakage. The glass- and aramid-polyamide composites had different failure modes when fabricated using the different processes. The 3D printed composites showed extensive longitudinal splitting which was caused by weak fusion bonding between filaments. Delamination

cracking also occurred in the 3D printed glass-polyamide composite. In contrast, the hot moulded composites showed limited longitudinal splitting cracking, and fibre breakage was the dominant failure mode in both the glass and aramid composites.

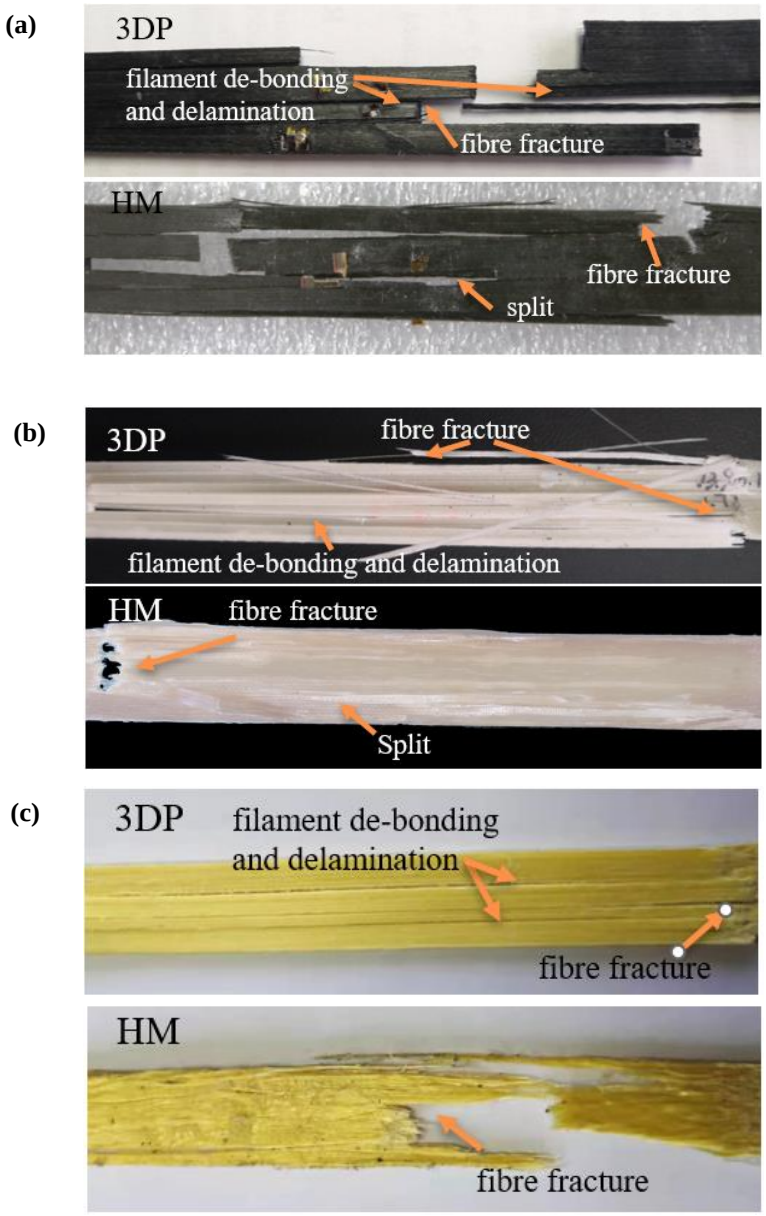

Figure 6-16 *Tensile fracture modes of (a) carbon-, (b) glass- and (c) aramid-polyamide composites manufactured using 3D printing and hot moulding, respectively.*

In contrast, the hot moulded composites had a much lower void content due to a more uniform pressure applied during fabrication and the longer heating time, which aided in better consolidation and fusion between filaments. However, the tensile strengths of the hot moulded carbon- and glass-polyamide composites were lower than their feedstock materials (Stage 1 filament). This can be partly attributed to the fibre waviness. Although the fibre

misalignment in the hot moulded composites is not as high as the 3D printed composites, the deviation angle of ±10° is still large compared to that of Stage 1 filament, the fibres within which are almost perfectly straight. The hot moulded composites with a global fibre misalignment can suffer significant shear stress during tensile loading. This will reduce the tensile strength of the composites, especially for carbon and glass which are more brittle. Also, the hot moulded composites still showed material heterogeneity with fibre clusters and polymer-rich areas due to limited pressure applied for fabrication.

The AE signature properties of the 3D printed and hot moulded composites measured in the fibre [0°] direction were determined under increasing tensile loading to final failure. **Table 4-3** presents the total number of AE event counts recorded for the 3D printed and hot moulded composites with three fibre types. The 3D printed composites had fewer AE events, presumably due to a significant number of carbon and glass fibres having been broken during the FDM process (as described in the previous chapter). The fewer AE event counts for the 3D printed composites, particularly for glass and aramid, can also be attributed to filament de-bonding before fibre breakage.

Table 6-3 *Total AE count number for the carbon-, glass- and aramid-polyamide composites fabricated using 3D printing and hot moulding process.*

	3DP ($\times 10^4$)	**HM ($\times 10^4$)**
Carbon-Polyamide	19.7±2.1	23.6±1.9
Glass-Polyamide	10.0±1.3	14.7±3.8
Aramid-Polyamide	4.9±0.7	6.8±0.4

Curves of cumulative AE events and applied tensile stress against tensile strain for the 3D printed and hot moulded composites are shown in **Figure 6-17****Figure 4-10**. The initiation of AE events occurred at lower stress values in the 3D printed composites, presumably due to the higher density of microstructural defects which aid tensile damage processes. The higher void content to the 3D printed composites is a factor responsible for the AE events at this stress level. The voids at and between filaments can act as geometric stress raisers and initiate cracks in the matrix phase at relatively low stress, which will generate AE signals. For the 3D printed carbon and glass composites, the weakest fibres damaged by the FDM machine can also fracture at relatively low stress and thereby generate the early AE events at relatively low stress. Following the initial onset, the AE hits increased nearly

exponentially with increasing stress to final failure for both the 3D printed and hot moulded composites.

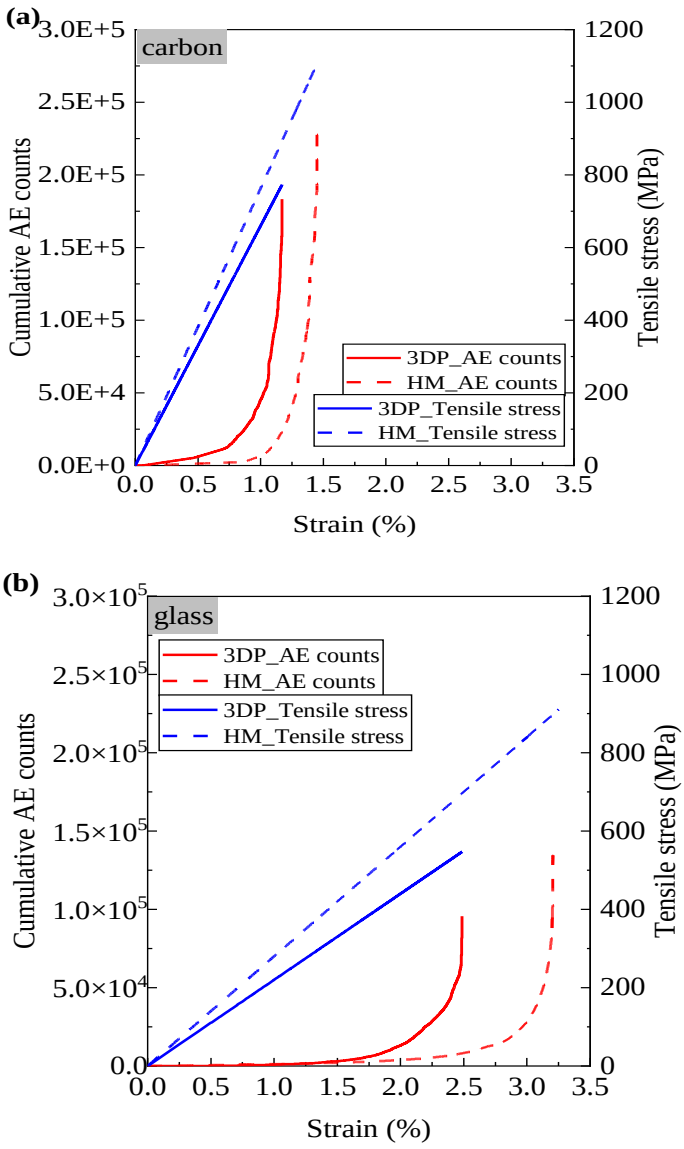

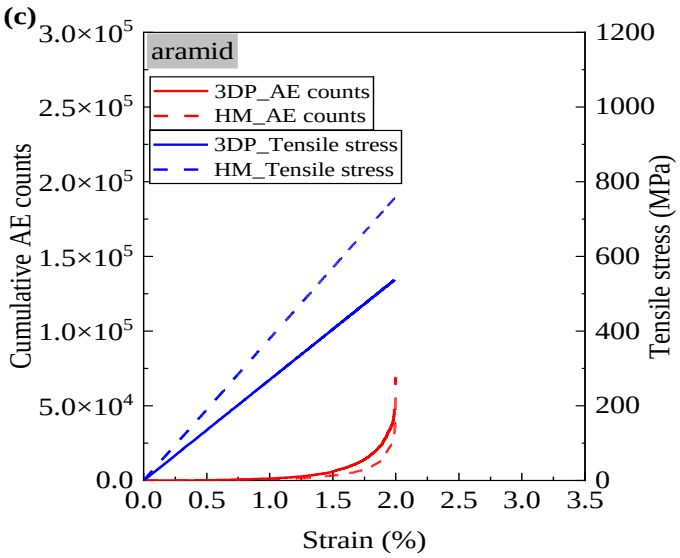

Figure 6-17 *Curves of AE counts to tensile strain and tensile stress to tensile strain for the 3D printed and hot moulded (a) carbon-, (b) glass- and (c) aramid-polyamide composites.*

Figure 6-18 compares the AE frequency distributions of the 3D printed and hot moulded composites. The two types of carbon-polyamide composites had similar symmetric AE frequency distributions over ~200-600 kHz with the medium value at ~370 kHz. The frequency distributions were consistent with that obtained for the single FDM carbon filament presented in **Chapter 4**, representing the frequency range for the breakage of carbon fibres, which agrees with the frequency results for carbon fibre laminates reported in other studies [155, 157, 158]. In contrast, the glass- and aramid-polyamide composites showed different frequency distributions for the two fabrication methods. The 3D printed glass composites displayed a bimodal frequency distribution with some overlapping at ~350-400 kHz, indicating multiple damage mechanisms had occurred during loading. The frequency distribution with a relatively low peak value at ~350 kHz is in the range of matrix cracking obtained from conventional carbon- and glass-polymer composites [175-177]. This frequency distribution can be generated by the filament de-bonding, longitudinal splitting and delamination cracking in the 3D printed composite, while the distribution with a high peak value at ~400 kHz is indicative of glass fibre breakage. The frequency distribution in the hot moulded glass composites was more concentrated in the range of 350-450 kHz, implying that the fibre fracture was more dominant in the failure process. A fibre-controlled damage mechanism had also occurred in the hot moulded aramid composite, with the AE frequency distributed in the similar range of 350-450 kHz. The aramid-polyamide composite fabricated by 3D printing presented more AE signals in the relatively low frequency with a peak value

at ~350 kHz, indicating that the fibre and matrix fracture were two main failure mechanism under tensile loading.

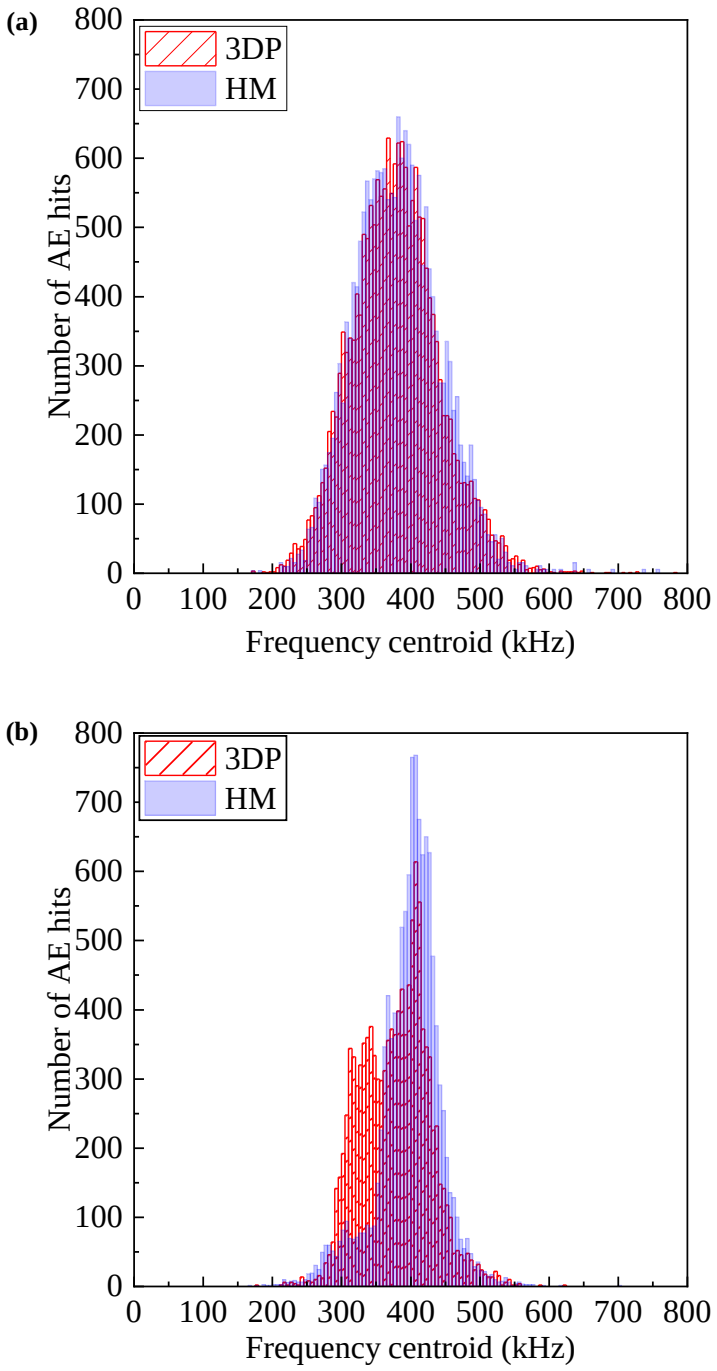

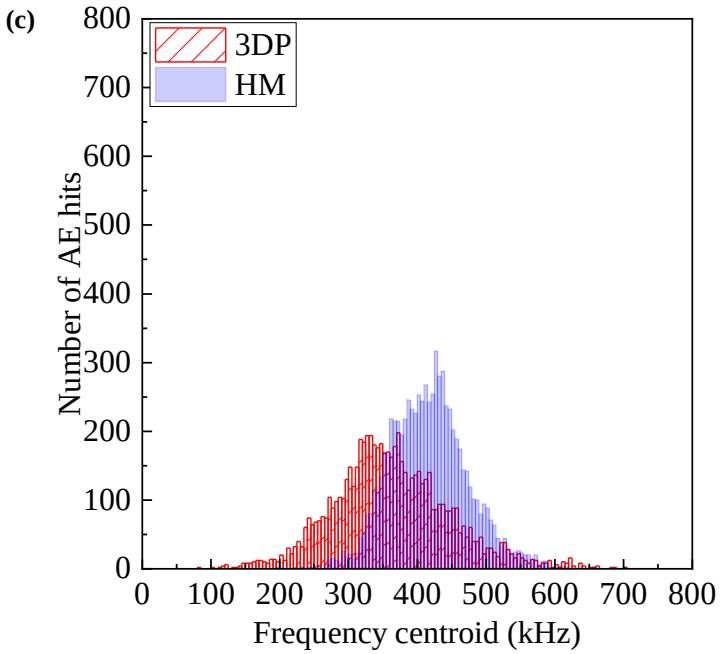

Figure 6-18 *AE frequency histogram plots of 3D printed and hot moulded (a) carbon-, (b) glass- and (c) aramid-polyamide composites.*

6.4 Conclusions

The microstructures, tensile properties, tensile damage mechanisms and tensile failure modes of 3D printed continuous carbon-, glass- and aramid-polyamide composites were experimentally determined. Void contents of 11.9%, 10.6% and 5.5% were measured in the 3D printed carbon, glass and aramid composites, respectively. The relatively high porosity was caused by insufficient fusion between the filaments, incomplete impregnation of the polymer into the fibre bundles during deposition and filament build-up, and insufficient consolidation pressure applied by the FDM nozzle. In contrast, the higher and more uniform pressure applied in the hot moulding process as well as the longer heating time decreased the void size and reduced the porosity level to ~1% for the three types of hot moulded composites. The 3D printed composites also had greater fibre waviness (within ±15°) than the hot moulded composites (within ±10°) due to the low filament tension and printer head vibration during printing.

The tensile properties and failure mechanisms of the 3D printed composites were investigated and compared to the hot moulded composites fabricated with the same material and similar fibre content. The tensile modulus values of 3D printed composites were 16%, 17% and 41% lower and the tensile strength values were 41%, 67% and 34% lower than hot

moulded composites for carbon, glass and aramid composites, respectively. The lower tensile modulus is mainly caused by the fibre damage, fibre waviness, higher void content and slightly lower fibre content resulting from the FDM process. FDM process-induced fibre damage and waviness, as well as voids within and between the filaments, reduced the tensile strength of 3D printed composite. The voids within the composites can contribute to the failure process by acting as geometric stress concentration sites for the initiation of damage, such as matrix cracking. However, the effect of voids on the tensile properties is complex, being dependent on a multitude of factors including void size, void shape and void location. These factors vary between 3D printed and hot moulded composites studied here, and therefore can contribute to the difference between the measured tensile properties. However, it is not possible to readily 'separate' the contributions of FDM-induced voids and FDM-induced fibre damage on the lower tensile properties of the FDM composites.

CHAPTER 7: MICROSTRUCTURAL AND MECHANICAL PROPERTIES OF 3D PRINTED HYBRID COMPOSITES

Abstract

3D printing of continuous fibre composites using the FDM process can be used to fabricate lightweight structures with complex material combinations and designs such as fibre hybridisation. However, little is known about the microstructural and mechanical properties of 3D printed hybrid composites containing two or more types of continuous fibre. This chapter presents an experimental investigation into the hybridisation effects of carbon layer ratio and carbon layer distribution on the tensile properties of 3D printed carbon+glass-polyamide and carbon+aramid-polyamide composites. The composites were printed using the FDM process with the carbon fibre filaments sandwiched between or separated by filaments containing glass or aramid fibres, which have higher failure strain. The carbon fibre layer ratio in the hybrid composites ranged between 11% and 50%, and were compared to composites containing only carbon fibres or no carbon fibres (i.e. 100% glass or aramid fibres). It is found that fibre hybridisation increased the failure strain of the composites, although all the hybrid composites failed by rupture of the carbon layers. The experimentally measured tensile modulus values of the 3D printed hybrid composites can be predicted using rule-of-mixtures. The tensile strength was controlled by the glass or aramid fibres and not by the carbon fibres. The carbon layer distribution in the hybrid carbon+aramid composites had little influence on the tensile properties. In contrast, for the 3D printed carbon+glass composites, sandwiching the carbon layers between the glass layers resulted in higher tensile properties at the relatively low carbon layer ratio of 25%, while the separated conditions performed better at the high carbon layer ratio of ~50%.

7.1 Introduction

The high specific mechanical properties, fatigue strength and corrosion resistance make continuous carbon fibre reinforced polymer composites suitable materials for lightweight structures such as motor cars and aircraft. It is estimated that the replacement of steel with carbon fibre composites in structural components can result in 40%-60% weight reduction [178]. However, the adoption rate for carbon fibre composites remains low compared to steel and other fibre types (e.g. glass) due to the high cost. Combining carbon fibres with lower-cost fibres such as glass to create hybrid fibre composites can reduce material cost without a large loss in some structural and other properties.

It is also well known that brittle carbon fibres can significantly increase the tensile modulus and strength but compromise the fracture toughness and failure strain of the composite material. In most cases, more damage-resistant and less brittle materials are ideal for load-bearing composite structures. Fibre hybridisation by combining continuous carbon fibres with other fibres having higher failure strain, such as glass and aramid, is a promising strategy to toughen composite materials and offer a better balance in the mechanical properties [179-183]. For example, Zhang et al. [184] hybridised woven carbon and glass fibre layers and obtained improvements of between 10% to 31% to the tensile failure strain of the hybrid composite by varying the carbon layer content (25% and 50%). Zhang and colleagues also investigated the effect of fibre layer distribution on the tensile, compressive and flexural strengths. The research revealed that the tensile strength was insensitive to the stacking sequence of the carbon and glass layers. However, hybrid composites with glass layers sandwiched between carbon layers had higher flexural properties, while alternating the carbon and glass layers provided the highest compressive strength. The impact damage resistance of composite materials can also be improved by fibre hybridisation. For example, Sayer et al. [185] and Park et al. [186] found that incorporating glass or aramid fibre layers to the underside of carbon fibre composites can improve the penetration impact resistance by up to 30%. Park attributed the improvement to the energy absorption through delamination and the higher bending failure strain in the aramid layer. In contrast, Jang et al. [187] showed that placing the fibres with high failure strain on the impact side is more beneficial to the impact resistance.

3D printing continuous fibre/polymer composites using the FDM process is potentially an effective method to fabricate hybrid composites, as the filaments can be precisely placed in desired paths and locations, and the fibre types can be easily changed during the printing process. However, few studies have investigated the mechanical properties of 3D printed continuous fibre reinforced polymer composites [11-14]. Peng et al. [116, 188] investigated the flexural properties and energy absorption of 3D printed short and continuous carbon fibre reinforced polyamide composites. That is, this hybrid composite consisted of different fibre lengths rather than different fibre types. Peng and colleagues found that the properties are dependent on the printing angle of continuous carbon fibre filaments. They also showed that separating continuous carbon fibre layers by short carbon fibre layers can improve the interfacial strength and impede crack propagation. Wang et al. [124] investigated the effect of fibre layer position on the indentation properties of 3D printed carbon/aramid composites. They determined that placing aramid fibre layers at the rear side can achieve the highest indentation force, while positioning carbon fibre layers at the rear side can lead to the highest energy absorption capability. Huang et al. [73] investigated the potential of achieving pseudo-ductility through 3D printing hybrid composites with carbon layers sandwiched between glass layers. The study showed that controlled fragmentation of the carbon layers induced a pseudo-ductile response, and that this was achieved with thicker carbon layers (between 100-200 μm) compared to the need to use thin-ply carbon plies (29-84 μm) in traditional hybrid laminates.

The investigations presented in Chapters 4 and 6 show that the 3D printed composites with different fibre types had similar tensile strength values at the filament level, but different at the coupon level due to different void characteristics. To evaluate the effect of hybridisation on the microstructures and mechanical properties of the 3D printed composites, this chapter presents an experimental study into the microstructure and tensile properties of 3D printed hybrid composites containing two types of continuous fibres fabricated using the FDM process. The study was conducted on continuous carbon+glass- and continuous carbon+aramid-polyamide hybrid composites. The effects of the carbon layer ratio and carbon layer distribution on the tensile properties and damage mechanisms to the 3D printed hybrid composites were determined. The study also evaluates the cost efficiency of the 3D printed hybrid composites by comparing the normalised tensile properties (by material densities and filament prices) to those of the composites containing carbon, glass or aramid fibres only. The hybridisation presented in this study would be much effective if the hybrid

composites could show property/density values higher than non-hybrid carbon composites (carbon fibre is strong and the lightest) and property/price values higher than non-hybrid glass composites (glass fibres is the cheapest).

7.2 Methodology

7.2.1 Hybrid composite design

The materials used for 3D printing the hybrid composites are carbon-, glass- and aramid-polyamide filaments supplied by Markforged®. The physical and mechanical properties of these filaments have been described in the previous chapters. In this study, unidirectional carbon+glass- and carbon+aramid-polyamide hybrid composites were fabricated using a Markforged® MarkTwo FDM printer. The printing conditions are similar to those used for the filament and non-hybrid composites described in the earlier chapters. The printed single layer thickness for the carbon-, glass- and aramid-polyamide are ~125 μm, ~100 μm and ~100 μm, respectively, based on the default settings of the FDM printer. The hybrid composites were fabricated by pausing the printing (~1 min) and changing the fibre filament type for specific layers. **Figure 7-1** shows an example of overprinting layers with different filament types.

Two types of hybrid specimens were fabricated: (i) carbon fibre/polyamide layers sandwiched between glass fibre/polyamide or aramid fibre/polyamide layers and (ii) carbon fibre/polyamide layers separated by glass fibre/polyamide or aramid fibre/polyamide layers. **Figure 7-2** shows schematics of the two specimen conditions. To evaluate the effects of carbon layer ratio on the tensile properties of the 3D printed hybrid composites, the number of carbon layers in the two conditions was varied from one to four plies. **Table 7-1** summarises the composite types investigated in this study. All of the composites were printed with a unidirectional orientation to the filaments.

Table 7-1 *Hybrid composite types indicating the carbon layer distribution and carbon layer ratio.* G, A *and* C *indicate glass-, aramid- and carbon-polyamide layers, respectively. The subscript number '*n*' indicates* n *consecutive layers with the same fibre type of carbon, glass or aramid.*

Composite Condition	Specimen Thickness (mm)	Carbon Layer Ratio (Carbon layer number/Total layer number)
$[G]_{16}$	1.6	0
$[A]_{16}$	1.6	0
$[C]_{16}$	2	100%
$[G_4/C/G_4]$	0.92	11%
$[A_4/C/A_4]$		
$[G_3/C_2/G_3]$	0.85	25%
$[A_3/C_2/A_3]$		
$[G_2/C_4/G_2]$	0.90	50%
$[A_2/C_4/A_2]$		
$[G/C_2/G_2/C_2/G]$	0.90	50%
$[A/C_2/A_2/C_2/A]$		
[G/C/G/C/G/C/G/C/G]	1.00	44%
[A/C/A/C/A/C/A/C/A]		
$[G_2/C/G/C/G/C/G_2]$	0.98	33%
$[A_2/C/A/C/A/C/A_2]$		
$[G_2/C/G_2/C/G_2]$	0.85	25%
$[A_2/C/A_2/C/A_2]$		

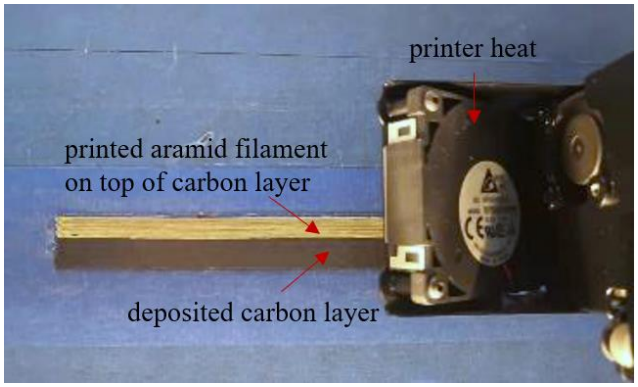

Figure 7-1 *Overprinting aramid-polyamide filaments (yellow) onto a carbon fibre layer (black) using the MarkTwo® printer.*

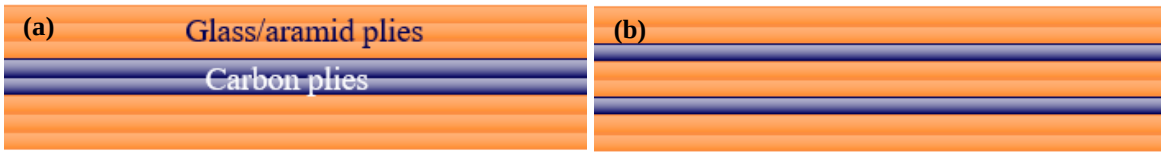

Figure 7-2 *Schematics of 3D printed hybrid composites with the carbon fibre layer in the (a) sandwiched and (b) dispersed conditions.*

7.2.2 Mechanical property characterisation

Tensile tests were performed on the 3D printed unidirectional hybrid composites under displacement control at the loading rate of 0.5 mm/min using a 10 kN universal machine (CSS 88010, China). All the specimens were printed with the dimensions of 200 mm × 15 mm with a gauge length of 100 mm. The tensile modulus of the composite specimens was measured using an extensometer with a gauge length of 50 mm. A minimum of three samples of each composite type listed in **Table 7-1** were tensile tested to failure. Emery paper was used as an interface between the grips to the loading machine and the sample, as per ASTM D3039 recommendation [169]. All of the specimens failed in the gauge area, indicating the validity of the test results in this study.

An acoustic emission (AE) system (MISTRAS-2001, China) having a wide-band transducer (R15, China) with a frequency range of 20-1000 kHz was used to monitor the initiation and accumulation of damage in the composite specimens under increasing tensile loading to failure. The single transducer was mounted in the middle of the specimen. The

parameter settings are the same as those used for the non-hybrid composites, and are given in **Chapter 6**.

The tensile properties of the 3D printed hybrid composites were normalised by the densities and prices of the feedstock filament materials to evaluate the efficiency of hybrid 3D printing using the FDM process. The physical properties and cost of the filament materials are presented in **Table 7-2**.

Table 7-2 *Density and cost of the feedstock material from the Markforged datasheet [165]. The price was taken in January 2022.*

Material	Density (g/cm^3)	Price (US$/cm^3)
Carbon-polyamide filament	1.4	3
Glass-polyamide filament	1.5	1.6
Aramid-polyamide filament	1.2	2

7.2.3 Microstructural analysis of filaments and composites

The microstructures of the hybrid composites were examined using scanning electron microscopy (SEM). A TM4000PLUS (HITACHI) microscope was operated at the accelerating voltage of 15 kV and emission current of 75 μA. The SEM working distance was 5.6 mm. The SEM samples were coated with a thin film of iridium before the examination to minimise electron beam charging effects.

7.3 Results and Discussion

7.3.1 Microstructure characterisation of 3D printed hybrid composites

In this section the effect of 3D printing on the microstructures of the hybrid carbon+glass-polyamide and carbon+aramid polyamide composites are discussed. Cross-sections of the 3D printed hybrid composites with different specimen types are shown in **Figure 7-3** and **Figure 7-4**. The ply at the bottom border of the image is the bottom layer printed directly on the build platform to the FDM machine. Regardless of the composition of

the hybrid composite they contained voids, which are also present in the non-hybrid materials as described in **Chapter 6**. Voids up to ~50 μm occurred in the resin-rich regions within the carbon filaments forming the carbon layers to the hybrid composites. In contrast, elongated voids occurred between adjacent filaments in the glass and aramid layers, and this was due to incomplete filament overlapping during the 3D printing of these filament types. These microstructural defects are similar to those in the 3D printed non-hybrid continuous fibre composites, as described in the previous chapter. Similar microstructural features are also reported in [58]. Additionally, voids that were hundreds of microns wide occurred in the bottom glass and aramid plies caused by insufficient fusion between filaments. Because the build platform was at room temperature, the filaments cooled and solifidied rapidly which hindered the spread and fusion of the polymer matrix phase.

When a carbon ply was sandwiched between thicker glass layers, elongated voids always occurred along the glass filament interfaces throughout the thickness, although voids were larger in the bottom layers closest to the build platform, as shown in **Figure 7-3a**. When the carbon core in the hybrid composite was relatively thick, then the porosity content decreased in the carbon layer. For example, the measured void content of the 4-ply carbon core was ~1%, which is lower than that of the 1-ply carbon core of ~6%. During 3D printing, the newly deposited filament material, which is at high temperature, can reheat the underlying plies leading to better fusion and improved bonding between filaments. Because the thermal conductivity of the carbon fibre filament is much higher than that of glass fibre filament, the 3D printing of carbon layers has higher heat transfer thereby reducing the void content in the carbon layers and at the carbon/glass interfaces, as shown in **Figure 7-3b**. Another factor benefitting polymer fusion in the carbon fibre layers is the amorphous nylon used in the material, which requires less heat for movement of the polymer molecules compared to semi-crystalline nylon used in glass and aramid composites [143]. Also, as shown in **Figure 7-4**, specimens with alternatively placed carbon and aramid layers had higher void content (of ~3%) compared to the specimen types with carbon layers sandwiched as the core (~1%).

In the hybrid composite specimens having the carbon layer separated by glass layers, both the void size and void content decreased from the build platform to the top surface as the plies were 3D printed layer-by-layer. This was due to the build-up of heat within the hybrid composites as the layers were printed, resulting in better fusion between filaments.

Additionally, as shown in **Figure 7-3d**, 3D printing the carbon layer directly onto the glass layer can infill the voids between the glass filaments. However, large voids between adjacent filaments caused by insufficient filament overlap, especially in the layers close to the build platform, remained (**Figure 7-3c**).

Micro-cracks always occurred at the carbon/glass interfaces to the hybrid composites. This might be attributed to pausing the 3D printing process in order to change the filament type (which took ~1 minute), which allowed cooling of the material that hindered interfacial fusion of dissimilar layers. The 3D printed carbon+aramid hybrid composites had similar microstructural feastures to the carbon+glass composites.

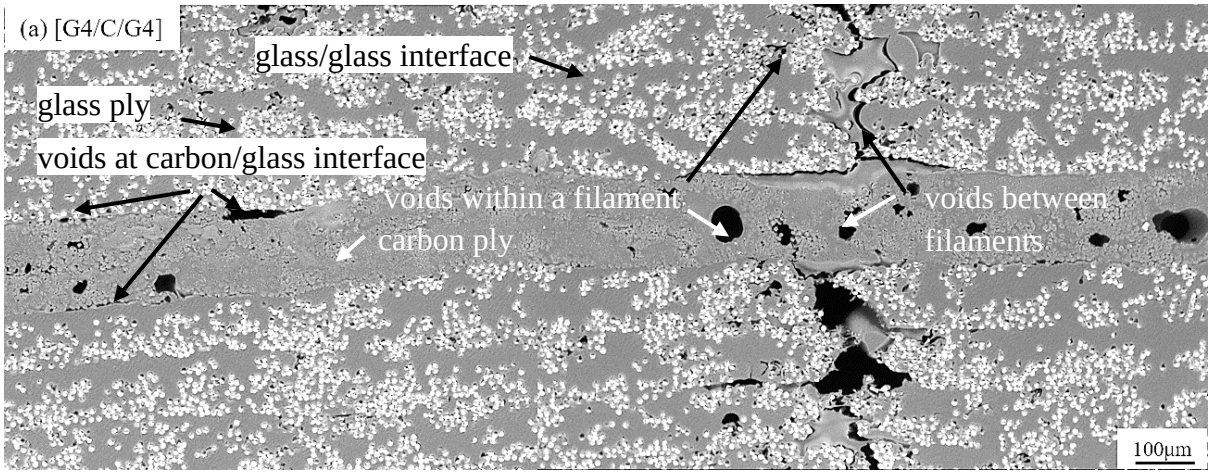

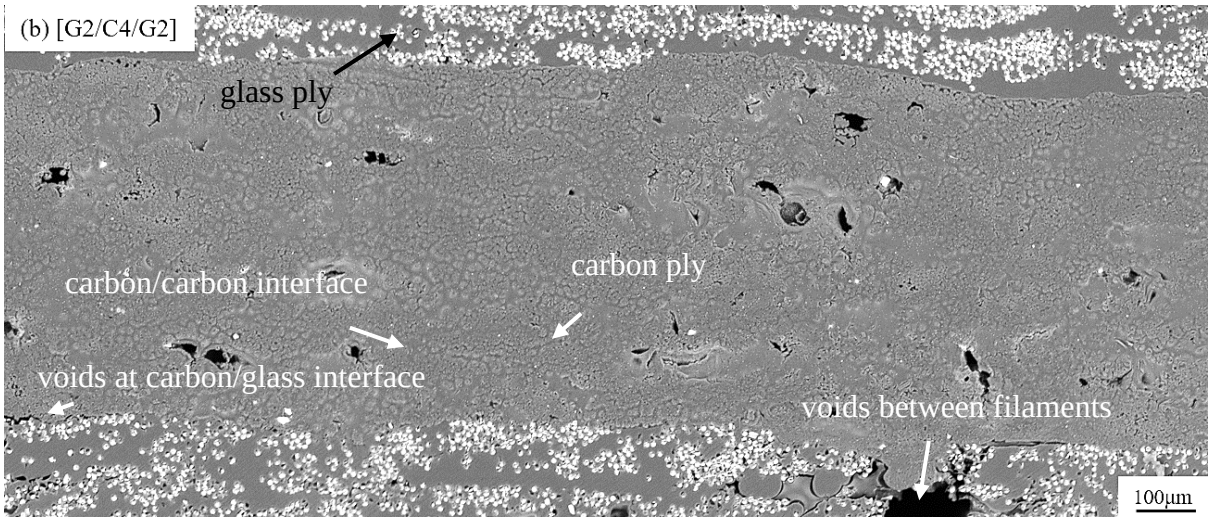

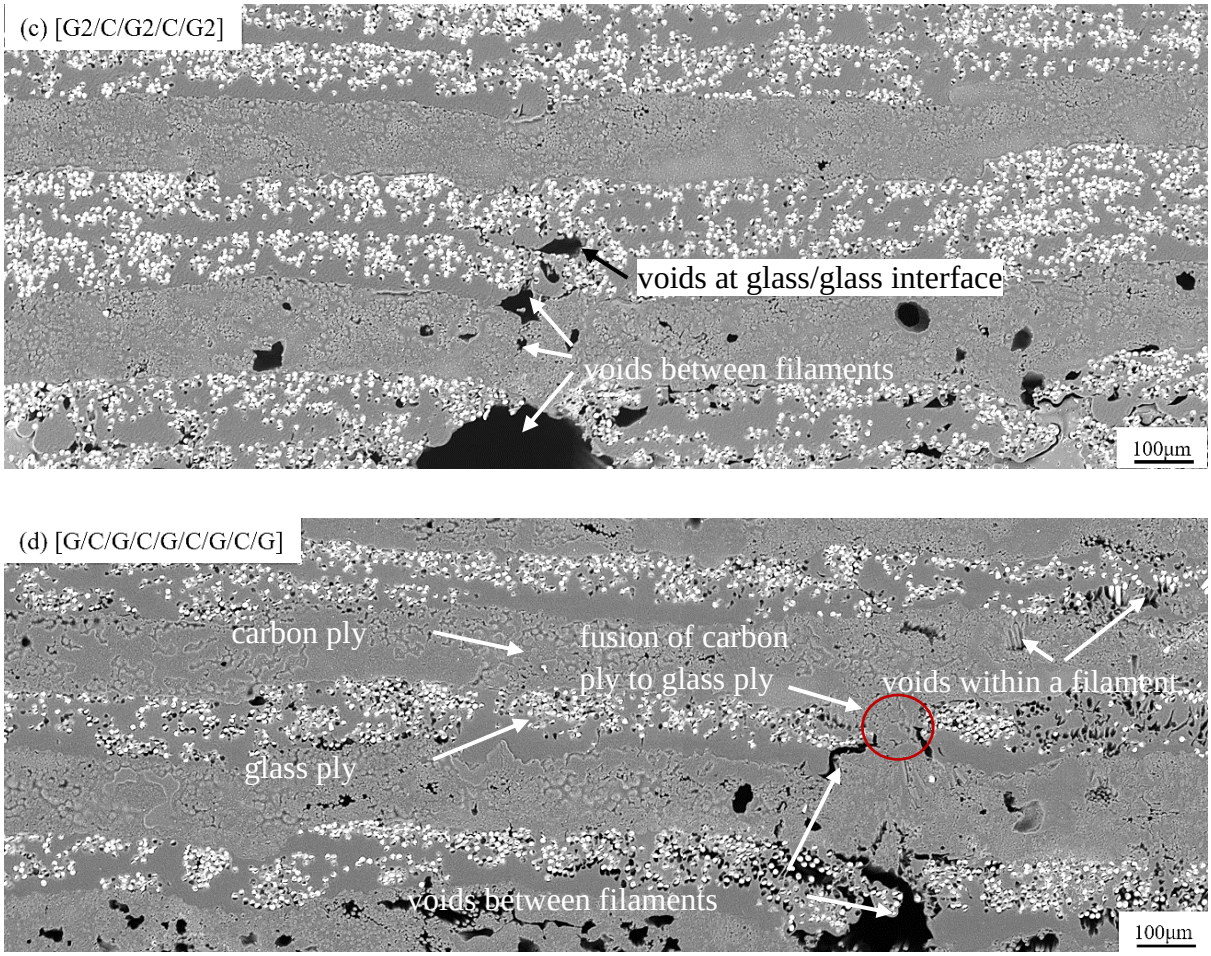

Figure 7-3 *Cross-sections of 3D printed carbon+glass-polyamide composites with specimen types of [G_4/C/G_4], [G_2/C_4/G_2], [G_2/C/G_2/C/G_2], and [G/C/G/C/G/C/G/C/G] showing the microstructures of the glass and carbon layers in different stackings.*

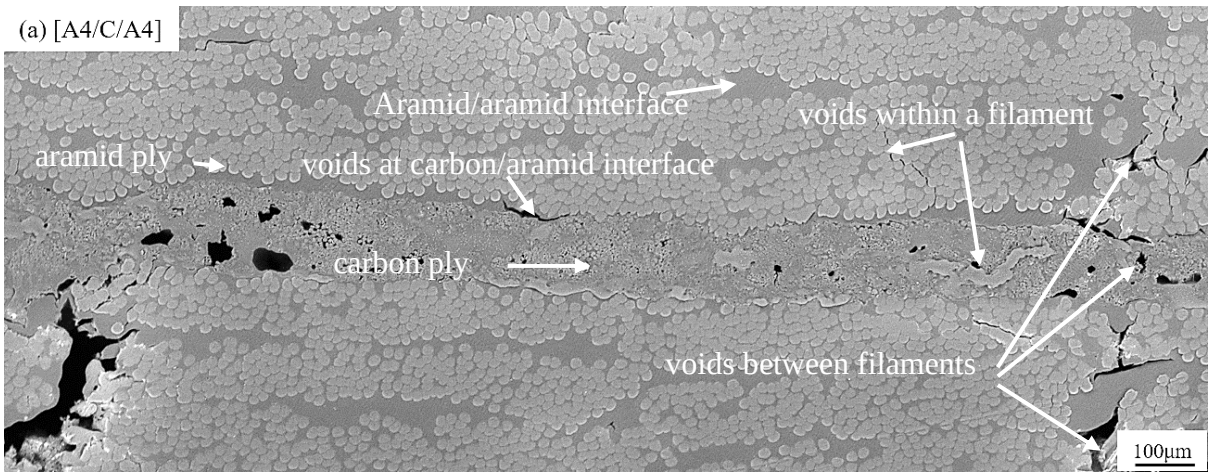

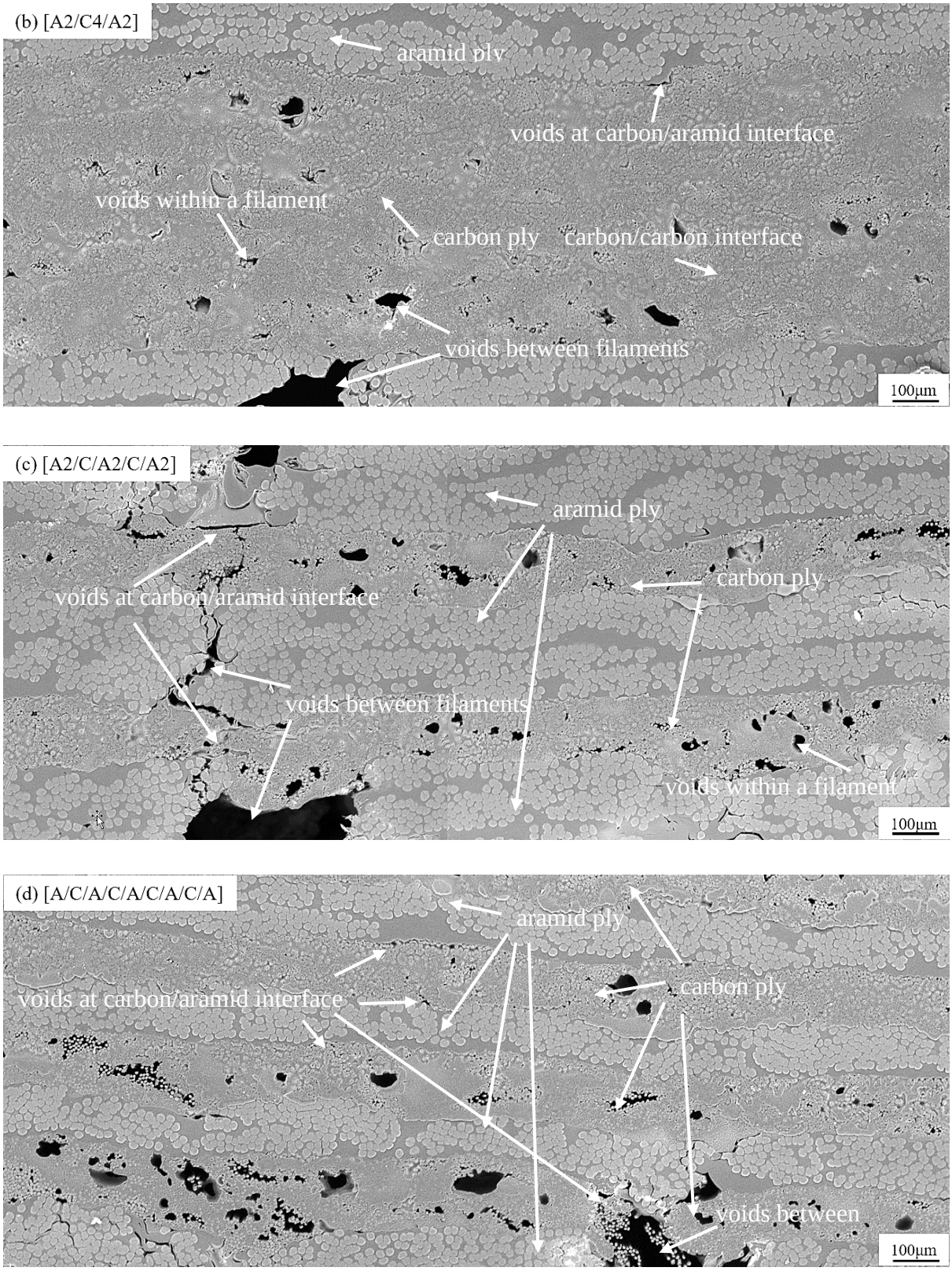

Figure 7-4 *Cross-sections of 3D printed carbon+aramid-polyamide composites for specimen types of [A_4/C/A_4], [A_2/C/A_2/C/A_2], [A_2/C_4/A_2] and [A/C/A/C/A/C/A/C/A] showing the microstructures of aramid and carbon layers in different stackings.*

7.3.2 Tensile properties of carbon-, glass- and aramid-polyamide composites

Tensile stress-strain curves for the 3D printed non-hybrid and hybrid composites are shown in **Figure 7-5**. In both the carbon+glass- polyamide and carbon+aramid-polyamide composites, tensile rupture of the carbon filaments coincided with final failure of hybrid composites and no further load-carrying by the glass or aramid fibre layers occurred despite their higher failure strain. The results show that the carbon fibre hybridisation improved the tensile modulus of the 3D printed hybrid composites compared to the non-hybrid glass or aramid composites.The failure strain of the hybrid composites, representing the tensile failure strain of the continuous carbon fibre reinforced composites, also increased in most cases to different levels besides [G/C_2/G_2/C_2/G], [A/C_2/A_2/C_2/A] and [A_2/C_4/A_2].

It is also worth noting that the stress-strain curves for the different hybrid composites were linearly elastic to final failure, with no ductility. As mentioned, Huang et al. [73] found tensile pseudo-ductility by hybrising carbon and glass filaments within 3D printed composites. The psedo-ductile strain response was activated via controlled tensile fragmentation of the carbon layers when sandwiched between glass layers. However, such a pseudo-ductile effect was not generated in any of the hybrid composites studied here because of the sudden failure of the carbon layers. Inducing a psedo-ductile response depends on many factors, including the carbon layer thickness, bonding between the filaments, and microstructural defects which influence the initiation and progression of the tensile damage.

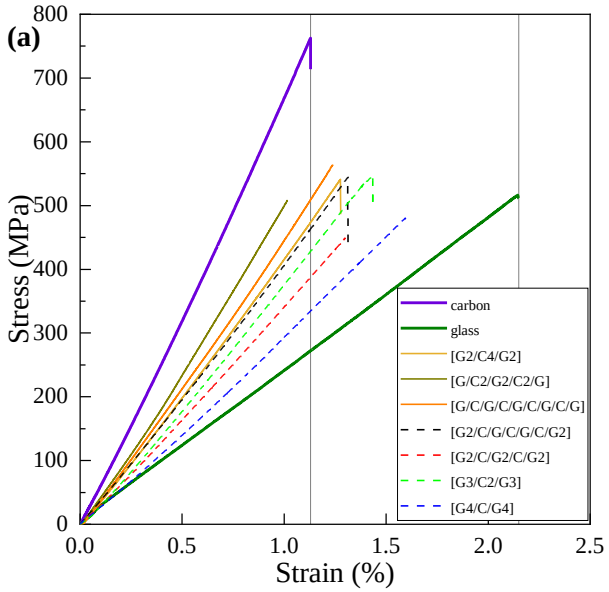

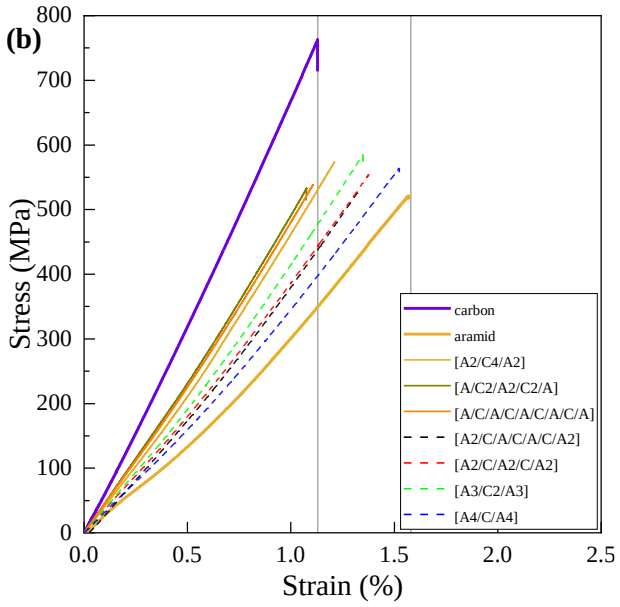

Figure 7-5 *Tensile stress-strain curves of 3D printed non-hybrid and hybrid composites.*

Figure 7-6 and **Figure 7-7** present the tensile modulus and failure stress values of 3D printed carbon+glass-polyamide and carbon+aramid-polyamide composites as a function of carbon content. Included in the figures are the predicted values based on rule-of-mixtures (RoM). The RoM values were calculated from the tensile properties of 3D printed non-hybrid carbon-, glass- and aramid-polyamide composites determined in **Chapter 6**, which include the effect of void content. The equation is expressed by:

$$E_{hybrid} = E_1 R_1 + E_2 R_2 \quad (1)$$

$$X_{hybrid} = X_1 R_1 + X_2 R_2 \quad (2)$$

where E is the tensile modulus, X is the tensile strength, subscripts '1' and '2' are the two fibre types used for 3D print hybrid composites, and R is the layer ratio.

As shown in **Figure 7-6**, the tensile modulus values of the 3D printed hybrid composites followed the ROM for increasing carbon fibre content. When the carbon layer ratio was relatively low (up to ~30%), the effect of layer distribution on the tensile modulus of 3D printed hybrid composites was negligible for the two fibre combinations (i.e. carbon+glass and carbon+aramid). The layer distribution became more influential on the modulus when the carbon layer ratio increased. The sandwiched hybrid composites [$G_2/C_4/G_2$] and [$A_2/C_4/A_2$] showed modulus values that were respectively 12% and 8% lower than the hybrid composites in the separated condition of [$G/C_2/G_2/C_2/G$] and [$A/C_2/A_2/C_2/A$], and the

value was even lower to that of the fully dispersed [G/C/G/C/G/C/G/C/G] and [A/C/A/C/A/C/A/C/A] composites, which had lower carbon fiber content. This can be caused by the poor interfacial bonding between different filament types that cannot effectively transfer the load from the face sheets to the thick carbon core for the sandwich condition. Whereas for the separaed or fully dispersed configurations, the even distribution of the stiffer carbon plies would promote effective stress transfer between the less stiff aramid or glass layers, thereby improving the modulus of the hybrid laminate.

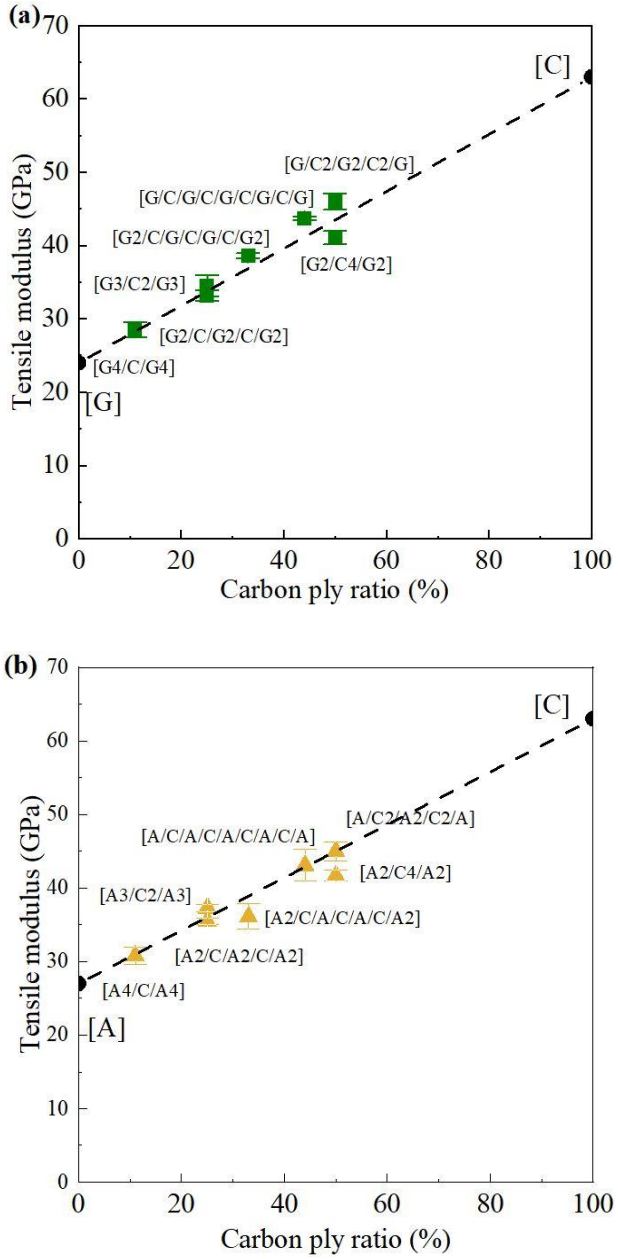

Figure 7-6 *Comparison between measured and calculated (ROM) tensile modulus of 3D printed unidirectional (a) carbon+glass- and (b) carbon+aramid-polyamide composites.*

As presented in **Figure 7-7**, the effect of carbon layer ratio on the tensile strength of 3D printed hybrid composites is different to its effect on tensile modulus. For carbon+glass composites, the strength showed a linear increase from 485 MPa to 553 MPa (similar to the strength of 3D printed non-hybrid glass composite) when the carbon layer ratio increased from 11% to 44%. The separated layer distribution showed a positive effect on the tensile strength, especially when the carbon layer ratio was high. The tensile strength of [G/C/G/C/G/C/G/C/G] was only 3% higher (which is within the bounds of experimental scatter) than [$G_2/C_4/G_2$] although with a lower carbon layer ratio (44% vs. 50%). The lower tensile strength of [$G_2/C_4/G_2$] is due to high fracture energy released from the thick carbon layer core, which can be beyond the interlayer strength of the glass/carbon layer interface, leading to a premature failure of delamination and lower tensile strength. The lower-than-expected tensile strength values of [$G_2/C/G_2/C/G_2$] and [$G/C_2/G_2/C_2/G$] can be caused by the elongated voids between glass filaments in the central plies, as shown in **Figure 7-3c**. The voids can act as geometric stress raisers to initiate cracks. The cracks propagate parallel to the glass filaments along the filament-to-filament and layer-to-layer interfaces. Similar fracture mechanism of delamination for the 3D printed non-hybrid glass composite was also reported in **Chapter 6** and other studies [29, 58].

For the 3D printed hybrid carbon+aramid composites, the tensile strength can be predicted using RoM when the carbon ratio is lower than 30%. When [$A_3/C_2/A_3$] configuration is compared to [$A_2/C/A_2/C/A_2$], the fibre layer distribution had almost no effect on the tensile strength at such a low carbon layer ratio. The tensile strength decreased as the carbon layer ratio increased from 25% to 50% when the carbon layers are separated in the hybrid composites. The strength of [$A/C_2/A_2/C_2/A$] was only 523 MPa, which is similar to that of 3D printed non-hybrid aramid composite. The tensile strength of [$A_2/C_4/A_2$] was 9% higher than that of [$A/C_2/A_2/C_2/A$], which can be caused by the lower porosity level in the sandwich condition described in the previous section.

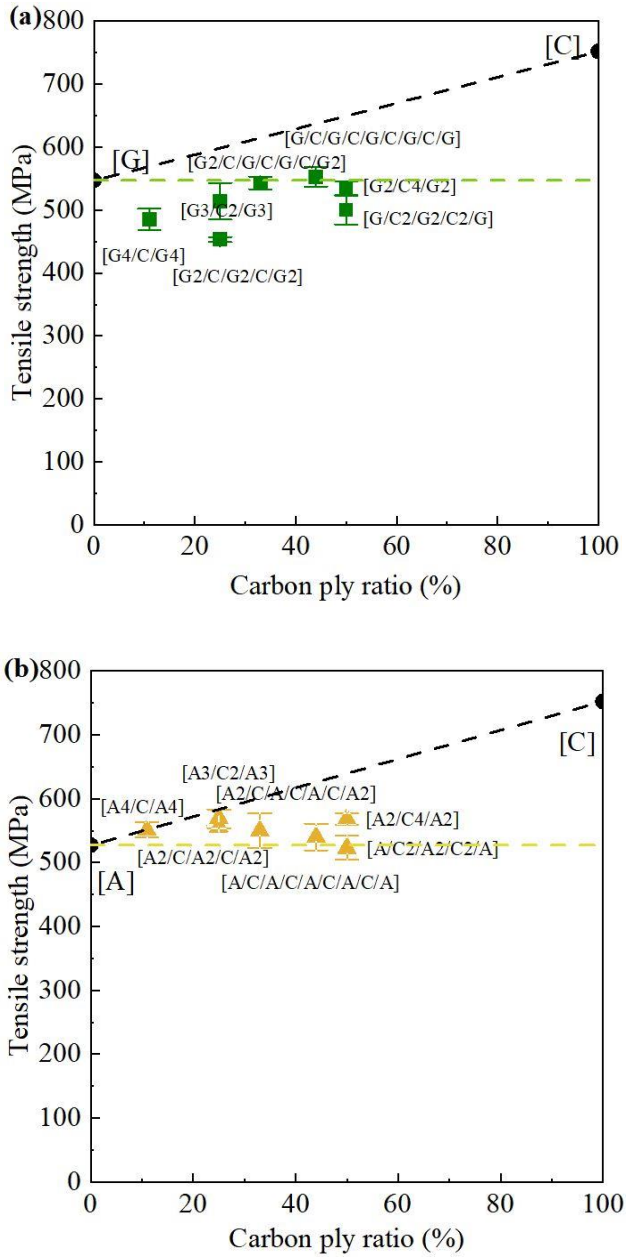

Figure 7-7 *Comparison between measured and calculated (ROM) tensile strength of 3D printed (a) carbon+glass- and (b) carbon+aramid-polyamide composites for different composite conditions.*

Table 7-3 and **Table 7-4** present the tensile failure strain values of the 3D printed hybrid composites. The results indicate that the failure strain can be improved when the carbon plies are sandwiched between fibre layers with higher failure strain (i.e. glass or aramid). Large improvements of 42% and 34% occurred for [G_4/C/G_4] and [A_4/C/A_4], respectively, and the failure strain increased with decreasing carbon layer ratio. The limited improvement of the tensile failure strain for [G_2/C_4/G_2] and [A_2/C_4/A_2] is due to the premature delamination between the carbon core layers and glass or aramid surface layers. The specimen conditions of [G/C_2/G_2/C_2/G] and [A/C_2/A_2/C_2/A] had a negative effect on the

tensile failure strain due to premature de-bonding and delamination in the glass and aramid layers positioned in the centre. The failure strain of 3D printed composites showed an increase in the specimen type with carbon layers completely seperated by higher failure strain layers of glass or aramid as the carbon layer ratio decreased from 44% to 25%. The relatively low enhancement of 15% for [G_2/C/G_2/C/G_2] can be caused by the premature de-bonding and delamination in the glass plies.

Table 7-3 *Tensile failure strain of 3D printed carbon+glass-polyamide hybrid composites compared to the 3D printed non-hybrid carbon-polyamide composite.*

Composite Condition	**Carbon Layer Ratio**	**Tensile Failure Strain (%)**	**Failure Strain Improvement (%)**
[C]	100%	1.13 ± 0.03	/
[G_4/C/G_4]	11%	1.61 ± 0.09	42
[G_3/C_2/G_3]	25%	1.38 ± 0.08	22
[G_2/C_4/G_2]	50%	1.23 ± 0.05	9
[G/C_2/G_2/C_2/G]	50%	1.04 ± 0.04	-8
[G/C/G/C/G/C/G/C/G]	44%	1.25 ± 0.13	11
[G_2/C/G/C/G/C/G_2]	33%	1.32 ± 0.02	17
[G_2/C/G_2/C/G_2]	25%	1.30 ± 0.02	15
[G]	0%	2.15 ± 0.03	/

Table 7-4 *Tensile failure strain of the 3D printed carbon+aramid-polyamide hybrid composites compared to the 3D printed non-hybrid carbon-polyamide composite..*

Composite Condition	Carbon Layer Ratio	Tensile Failure Strain (%)	Failure Strain Improvement (%)
[C]	100%	1.13 ± 0.03	/
[A_4/C/A_4]	11%	1.52 ± 0.05	34
[A_3/C_2/A_3]	25%	1.33 ± 0.02	18
[A_2/C_4/A_2]	50%	1.21 ± 0.02	7
[A/C_2/A_2/C_2/A]	50%	1.07 ± 0.04	-5
[A/C/A/C/A/C/A/C/A]	44%	1.13 ± 0.03	0
[A_2/C/A/C/A/C/A_2]	33%	1.30 ± 0.03	15
[A_2/C/A_2/C/A_2]	25%	1.38 ± 0.03	22
[A]	0%	1.58 ± 0.02	/

During tensile testing of the 3D printed hybrid composites, AE monitoring was used to track the initiation and accumulation of damage events leading to final failure, including fibre breakage and matrix fracture. **Table 7-5** presents the number of AE hits for the different types of 3D printed hybrid composites. The AE hit number indicates the number of damage events that occurred during the test. The largest AE hit number for the 3D printed carbon+glass-polyamide composites occurred with [G_4/C/G_4]. The number decreased with increasing carbon layer ratio when the carbon layers were sandwiched by the glass layers. When the carbon layer ratios were similar, the distribution of carbon layers completely separated by glass layers can lead to a much larger AE hit number compared to the sandwiched condition. In the cases where the carbon layers were separated by the glass layers, the carbon layer ratio can have two opposite effects on the AE count number. On the one hand, because the carbon filament has more fibres than the glass filament (i.e. 1000 vs. 400), the event number of fibre breakage decreases with the decreased carbon layer ratio. On the other hand, the elongated voids in the overlapped glass plies can generate more events of matrix fracture due to the poor filament adhesion in the glass composites. Therefore, it is

possible that [G_2/C/G_2/C/G_2] can produce more AE signals than [G_2/C/G/C/G/C/G_2]. A similar trend was also found for 3D printed carbon+aramid-polyamide composites, and the largest AE hit number was for [A_2/C/A/C/A/C/A_2]. The significant difference of the AE hit numbers between the 3D printed carbon+glass and carbon+aramid composites with same specimen condition can be attributed to the different fibre number within the glass and aramid (270 fibres) filaments. The different filament and layer adhesion in the two hybrid composite types is another factor that can determine the number of AE events.

Table 7-5 *AE hit number of 3D printed hybrid composites for different composite conditions.*

Composite Condition	**Number of AE Count (×10^4)**	**Composite Condition**	**Number of AE Count (×10^4)**	**Carbon Layer Ratio**
[G_4/C/G_4]	13.0 ± 2.3	[A_4/C/A_4]	5.6 ± 1.3	11%
[G_3/C_2/G_3]	8.6 ± 0.3	[A_3/C_2/A_3]	4.4 ± 1.1	25%
[G_2/C_4/G_2]	1.4 ± 0.3	[A_2/C_4/A_2]	3.3 ± 0.3	50%
[G/C_2/G_2/C_2/G]	3.7 ± 0.7	[A/C_2/A_2/C_2/A]	3.3 ± 1.0	50%
[G/C/G/C/G/C/G/C/G]	6.3 ± 1.6	[A/C/A/C/A/C/A/C/A]	5.7 ± 1.1	44%
[G_2/C/G/C/G/C/G_2]	5.0 ± 0.3	[A_2/C/A/C/A/C/A_2]	5.3 ± 1.8	33%
[G_2/C/G_2/C/G_2]	6.7 ± 0.4	[A_2/C/A_2/C/A_2]	5.4 ± 0.4	25%

The curves of the normalised number of cumulative AE counts to the normalised applied tensile stress for the 3D printed hybrid composites are shown in **Figure 7-8** and **Figure 7-9**. The AE count number is normalised to the total count number measured in the test, while the stress is normalised to the ultimate failure stress of the filament. For the 3D printed carbon/glass composites with carbon layers sandwiched by glass layers (**Figure 7-8a**), the initial AE event occurred when the applied stress reached ~45%. Following the onset of fracture, [G_4/C/G_4] presented a nearly exponential increase in the number of AE events with increasing stress to final failure. This trend is typical for unidirectional laminates in which the AE events are dominated by fibre fracture. [G_3/C_2/G_3] and [G_2/C_4/G_2] showed greater rates of increase in the AE hits before the final failure of these composites. These two hybrid composites have higher carbon filament contents, and thereby more weakened carbon fibres

(as discussed in **Chapter 3**) can break at low to the medium stress level, generating more AE hits of fibre fracture during this period. The carbon layer ratio significantly changed the curves of normalised cumulative AE hits for the composites with carbon layers completely separated by glass layers. The composites with higher carbon content showed the initial AE hits at a lower stress, and presented a more steady increase of AE hits to the final fracture, indicating more progressive failure events occurred during loading. The significant matrix damage can be due to the higher void content in the glass layers between filaments and at the carbon+glass interfaces, which was shown in **Figure 7-3**. **Figure 7-8c** compares the AE results between the hybrid composites with the same carbon layer number but different layer distributions. The AE hits showed a more steady increase when the carbon layers were more dispersed in the composites. Both [$G_2/C_4/G_2$] and [$G/C_2/G_2/C_2/G$] showed a sudden increase of AE hits at the stress value of ~98% and 95%, respectively, which can indicate a premature delamination before the final fracture.

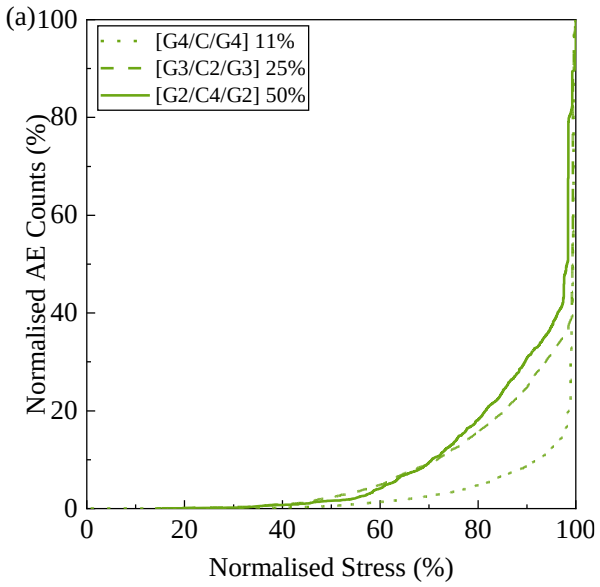

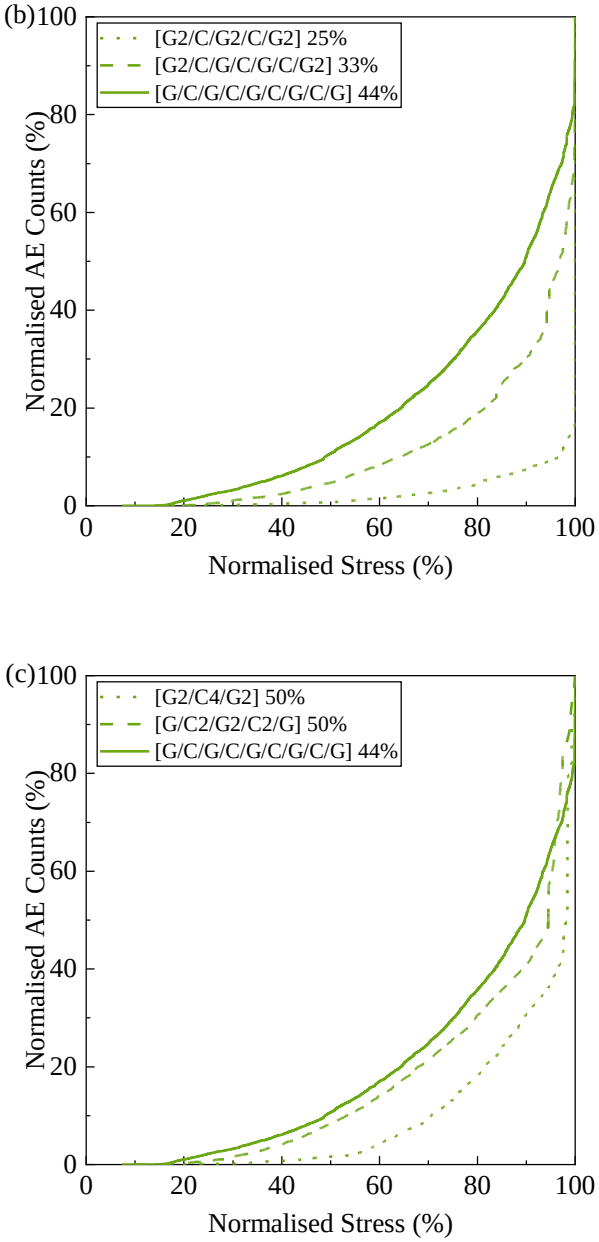

Figure 7-8 *Curves of normalised percentage AE counts to normalised percentage tensile stress for different 3D printed hybrid composites: (a) carbon layers (C) sandwiched by the glass (G) layers; (b) carbon layers dispersed by glass layers; (c) similar carbon layer ratio but a different number of consecutive carbon layers. The percentage in the legend is the carbon layer ratio of the condition.*

The effects of carbon layer ratio and carbon layer distribution on the cumulative AE hits for 3D printed carbon+aramid composites were different compared to carbon+glass composites. As shown in **Figure 7-9a**, the curves are similar for the composites with different carbon layer ratio when the carbon layers are sandwiched between aramid layers. After the onset of damage at a normalised stress of ~40%, the AE hits increased at a steady rate to the final fracture for the three specimen types. When the carbon layers were completely separated

by aramid layers, [A_2/C/A/C/A/C/A_2] showed the onset of fracture at the lower normalised stress of ~20% than the other two specimen types (~30%). The rate of AE hits for [A_2/C/A/C/A/C/A_2] was also greater. **Figure 7-9c** shows that the onset of fracture can be hindered when the carbon layers are sandwiched by aramid layers, which presented the initial AE hits at higher stress of ~30%, compared to the specimen type with carbon layers separately distributed. The increase of AE hits after the onset of fracture were similar for [A_2/C_4/A_2] and [A/C/A/C/A/C/A/C/A], which were greater than that for [A/C_2/A_2/C_2/A].

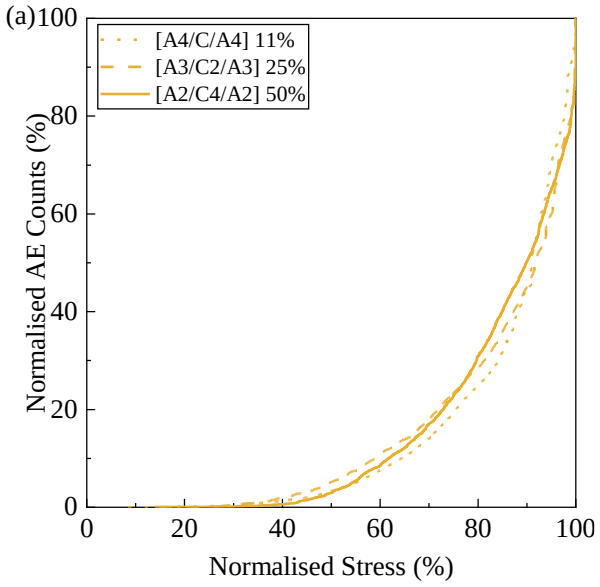

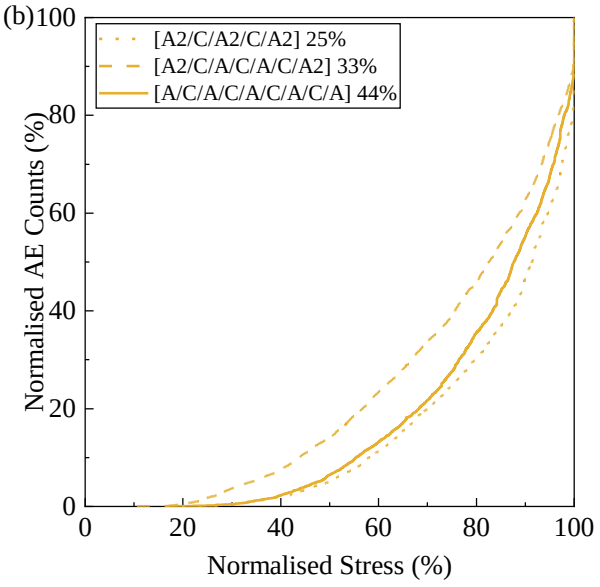

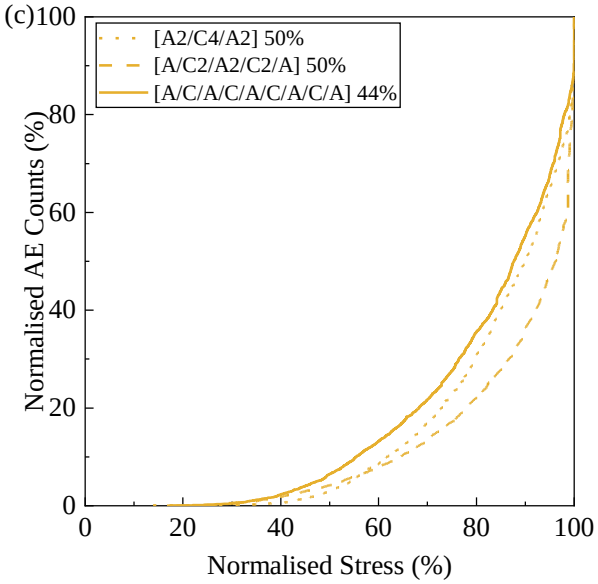

Figure 7-9 *Curves of normalised percentage AE counts to normalised percentage tensile stress for different 3D printed hybrid composites: (a) carbon layers (C) sandwiched by glass (G) or aramid (A) layers; (b) carbon layers dispersed by glass or aramid layers; (c) similar carbon layer ratio but a different number of consecutive carbon layers. The percentage in the legend is the carbon layer ratio of the condition.*

Figure 7-10 and **Figure 7-11** show the AE hit frequency distributions for the different 3D printed hybrid composites, which are presented to distinguish different fracture modes under tension. The AE frequency distributions of 3D printed non-hybrid composites, which have been presented in **Chapter 6**, are also shown in **Figure 7-10d** and **Figure 7-11d** as a comparison. 3D printed non-hybrid glass and aramid composites had a large number of AE signals with relatively lower frequency around ~350 kHZ, which indicates significant matrix fracture accompany fibre breakage during tensile loading. The hybridisation with carbon layer changed the fracture mode of glass and aramid composites to more fibre-fracture dominant, especially when the carbon layer ratio is low. It is worth noting that the difference in the AE hit numbers for the 3D printed hybrid and non-hybrid composites is due to the different layer number used in the tensile specimens.

As shown in **Figure 7-10**, for 3D printed carbon/glass composites, a high carbon layer ratio leads to more matrix fracture with AE signals presenting frequency close to ~350 kHz. **Figure 7-10a** shows the frequency results of 3D printed carbon+glass composites with the carbon layers sandwiched by glass layers. [G_4/C/G_4] presented a frequency distribution with the medium value of ~400 kHz, indicating a fibre fracture dominant mechanism occurred in this composite. When the carbon layer ratio increased, more AE signals shifted to a lower

frequency range between 300-400 kHz, generating another peak value of ~350 kHz. These AE events can be caused by an increasing number of matrix fractures between the thick carbon core and glass face sheets. A symmetric-like frequency distribution presented by [$G_2/C_4/G_2$] with the medium value of ~370 kHz can be caused by the significant overlapping of the frequency for carbon fibre fracture and matrix damage. This is due to the relatively low frequency of fibre breakage for the composites used in this research (medium value at ~370 kHz for carbon composites) compared to the traditional composites (350 kHz-700 kHz [175, 177]), as presented in **Chapter 6**. The composites with carbon layers placed separately always presented overlapping multiple fracture modes of fibre fracture and matrix damage as the carbon layer ratio was varied. [G/C/G/C/G/C/G/C/G] with the highest carbon layer ratio showed the largest proportion of signals with frequency in the range of 300-400 kHz, which can possibly be attributed to the significant matrix fractures that occurred at the carbon/glass interfaces and in the glass layer between filaments. The frequency distribution of [$G_2/C/G_2/C/G_2$] also showed significant overlapping of fibre fracture and matrix damage. **Figure 7-10c** shows the effect of carbon layer distribution on AE frequency results of 3D printed carbon/glass composites. [G/C/G/C/G/C/G/C/G] with the most carbon/glass interfaces presented the largest proportion of matrix damage.

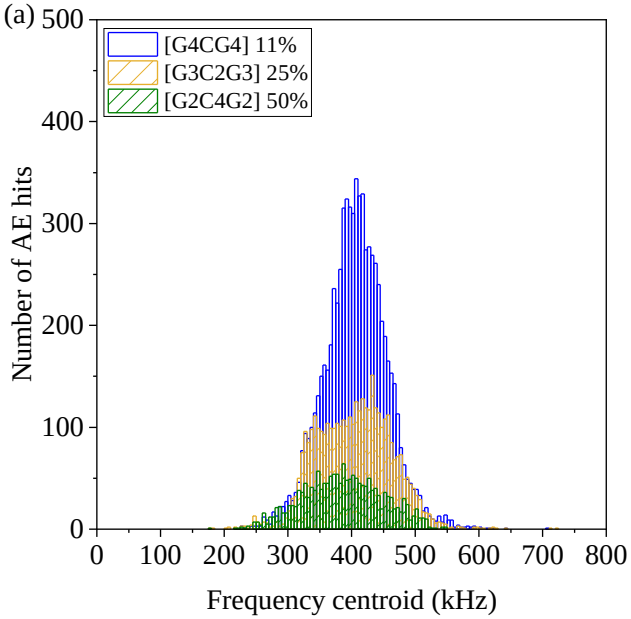

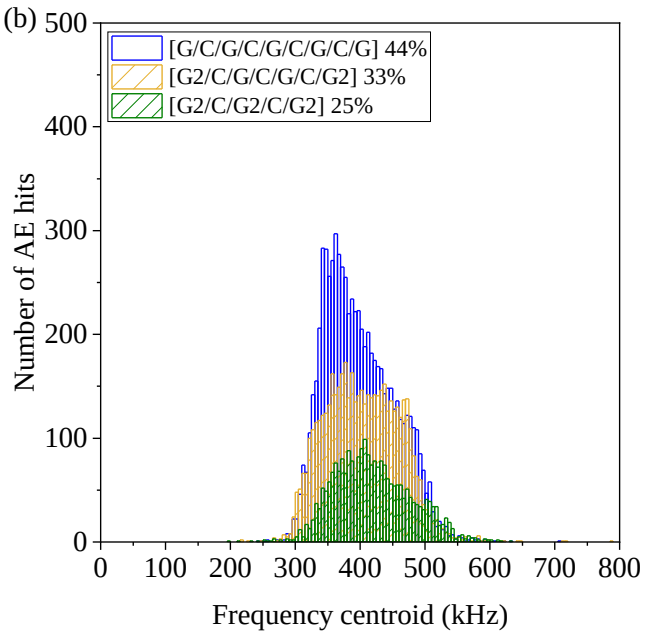
(b)
[G/C/G/C/G/C/G/C/G] 44%
[G2/C/G/C/G/C/G2] 33%
[G2/C/G2/C/G2] 25%
Number of AE hits
Frequency centroid (kHz)
0
100
200
300
400
500
600
700
800

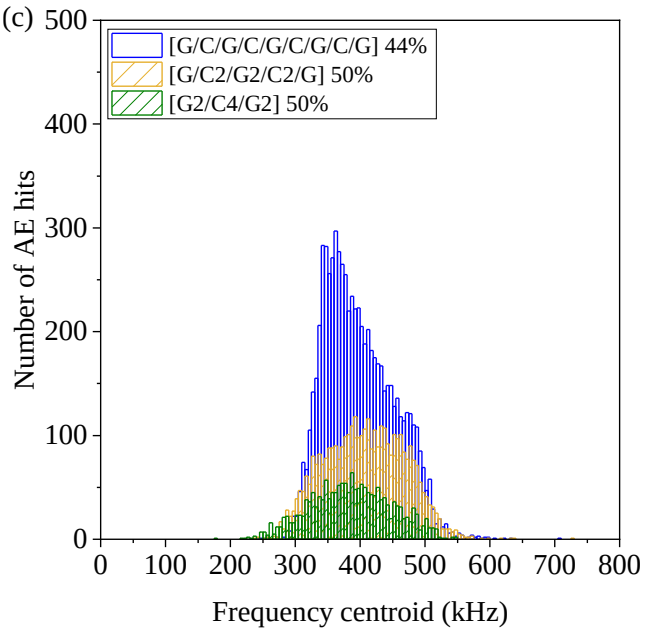
(c)
[G/C/G/C/G/C/G/C/G] 44%
[G/C2/G2/C2/G] 50%
[G2/C4/G2] 50%
Number of AE hits
Frequency centroid (kHz)
0
100
200
300
400
500
600
700
800

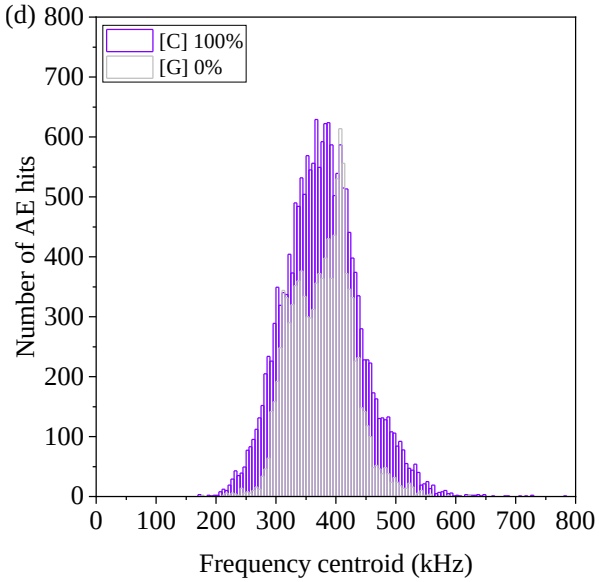

Figure 7-10 *AE frequency centroid distributions of different 3D printed hybrid composites: carbon layers (C) sandwiched by (a) glass (G) layers; carbon layers dispersed by (b) glass layers; similar carbon layer ratio but a different number of consecutive carbon layers separated by (c) glass layers. The percentage in the legend is the carbon layer ratio of the condition.*

The AE frequency results of 3D printed carbon+aramid composites are shown in **Figure 7-11**. When the carbon layers are sandwiched between aramid layers (**Figure 7-11a**), [A_4/C/A_4] and [A_3/C_2/A_3] with lower carbon layer ratio presented frequency distributions with the peak value at ~400 kHz. In contrast, more AE signals shifted to a lower frequency range of 300-400 kHz for [A_2/C_4/A_2], which represent significant matrix fractures occurred under tension. **Figure 7-11b** shows that the carbon layer ratio had limited effect on the frequency results when the carbon layers were dispersed in the 3D printed carbon+aramid composites. Composites with different carbon layer ratio showed similar frequency distributions with dominant fracture modes of fibre and matrix damage. When comparing the frequency results of composites with the same number of carbon layers but different carbon layer distributions, [A/C/A/C/A/C/A/C/A] with carbon layers completely dispersed in the composites presented a frequency distribution shifted to the left, indicating more significant matrix cracking compared to [A/C_2/A_2/C_2/A] and [A_2/C_4/A_2].

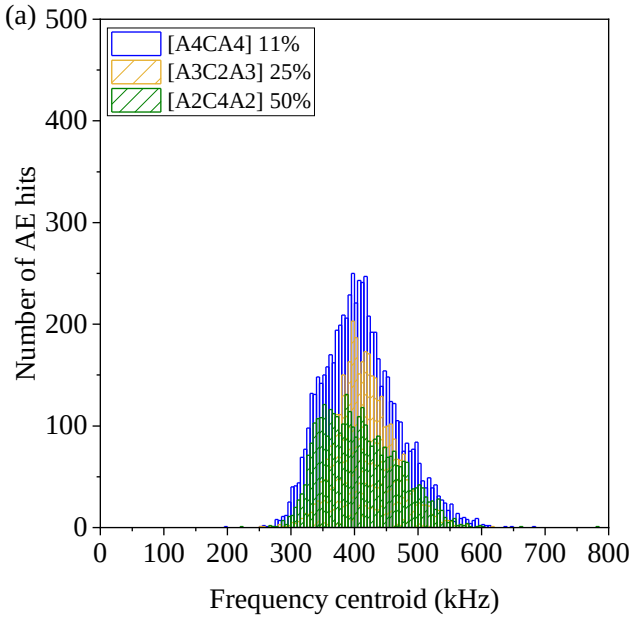
(a)
[A4CA4] 11%
[A3C2A3] 25%
[A2C4A2] 50%
Number of AE hits
Frequency centroid (kHz)
0
100
200
300
400
500
600
700
800

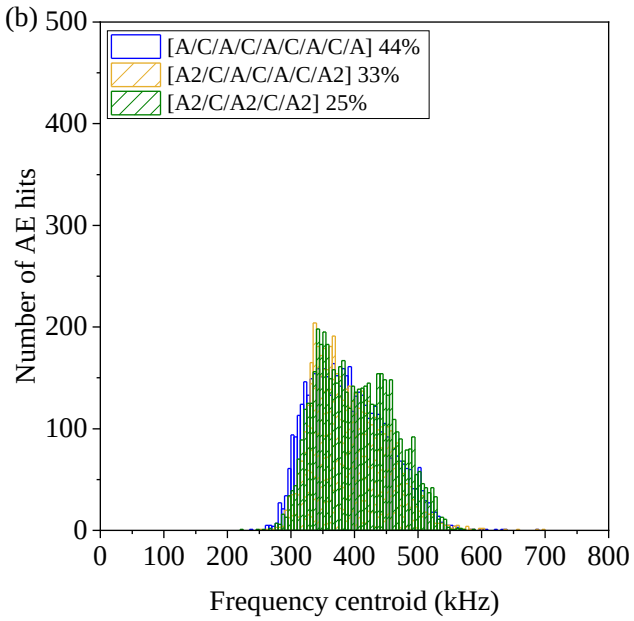
(b)
[A/C/A/C/A/C/A/C/A] 44%
[A2/C/A/C/A/C/A2] 33%
[A2/C/A2/C/A2] 25%
Number of AE hits
Frequency centroid (kHz)
0
100
200
300
400
500
600
700
800

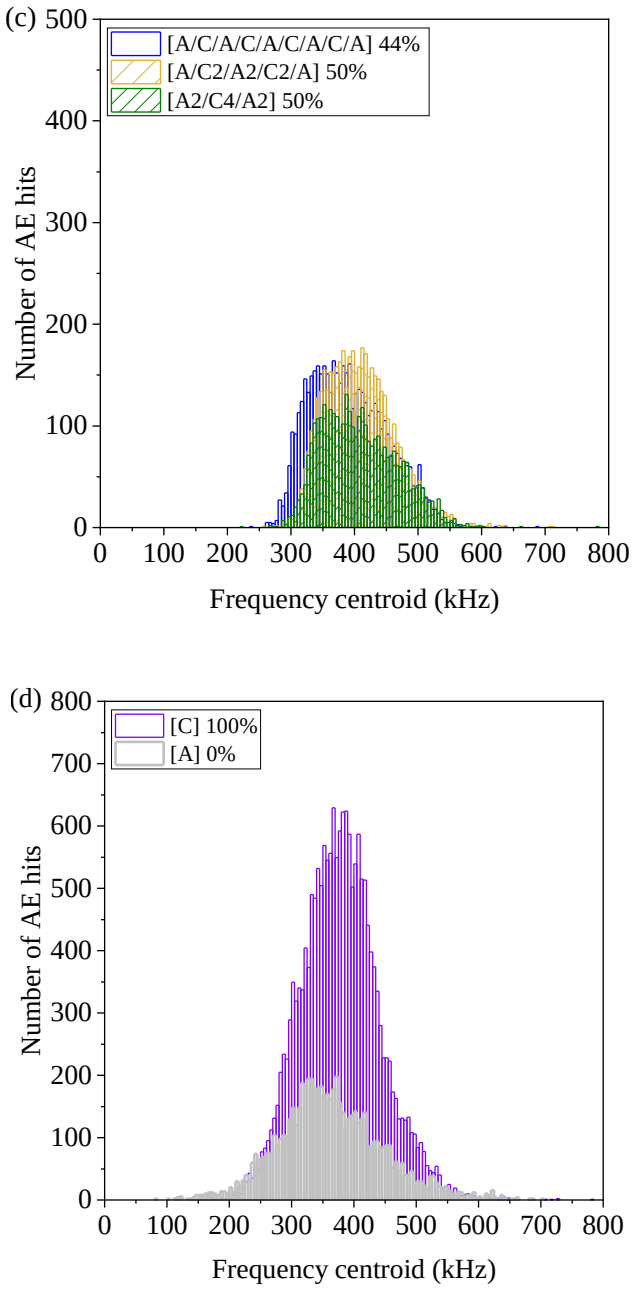

Figure 7-11 *AE frequency centroid distributions of different 3D printed hybrid composites: carbon layers (C) sandwiched by (a) aramid layers; carbon layers dispersed by (b) aramid layers; similar carbon layer ratio but a different number of consecutive carbon layers separated by (c) aramid layers. The AE frequency distributions of 3D printed non-hybrid carbon and glass composites in (d) are also shown as a comparison. The percentage in the legend is the carbon layer ratio of the condition.*

Figure 7-13 and **Figure 7-13** present the normalised tensile properties of 3D printed hybrid composites by the material densities and filament prices. The carbon layer ratio in the plots increases from left to right. Both the 3D printed carbon+glass and carbon+aramid composites had higher normalised tensile modulus than 3D printed non-hybrid glass- or

aramid-polyamide composites in terms of density and cost. Still, the results were all inferior to 3D printed non-hybrid carbon-polyamide composites. The specific tensile strength values of 3D printed hybrid composites were similar to those of 3D printed non-hybrid glass or aramid composites. When normalised by price, the hybrid composites of [G_4/C/G_4], [A_4/C/A_4], [G_3/C_2/G_3] and [A_3/C_2/A_3] demonstrated comparable results to 3D printed non-hybrid carbon-polyamide composites. However, the results of 3D printed hybrid composites lagged behind the non-hybrid glass or aramid composites, particularly with a high carbon ratio.

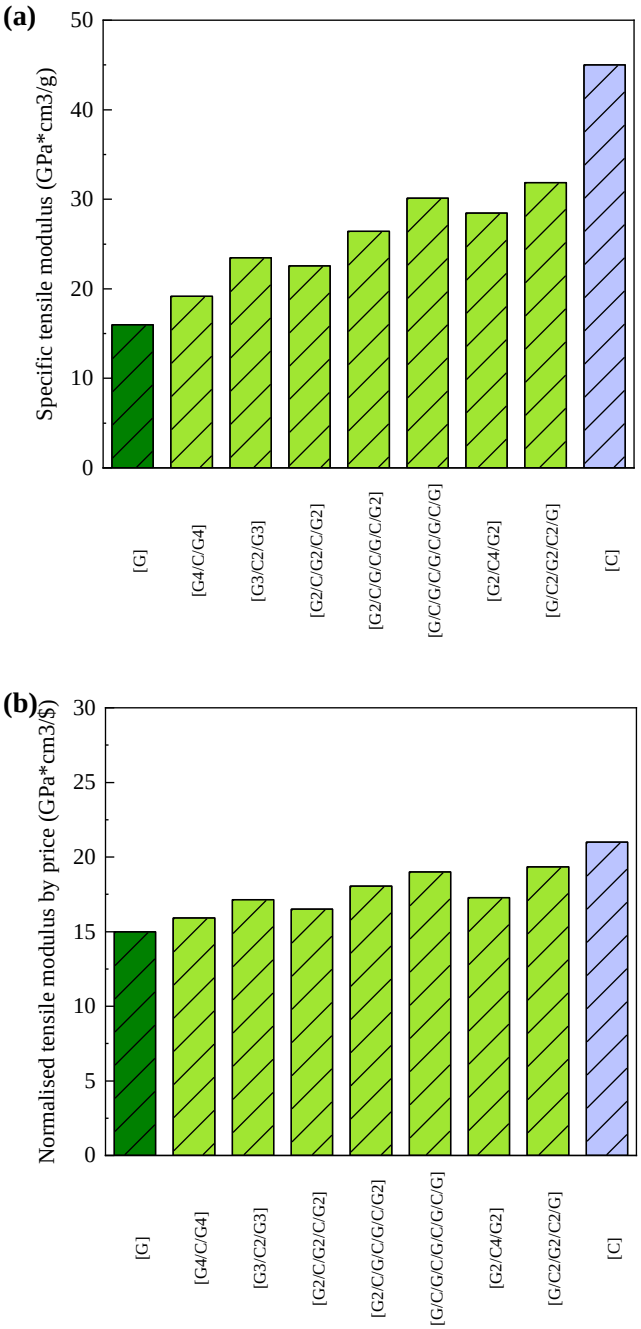

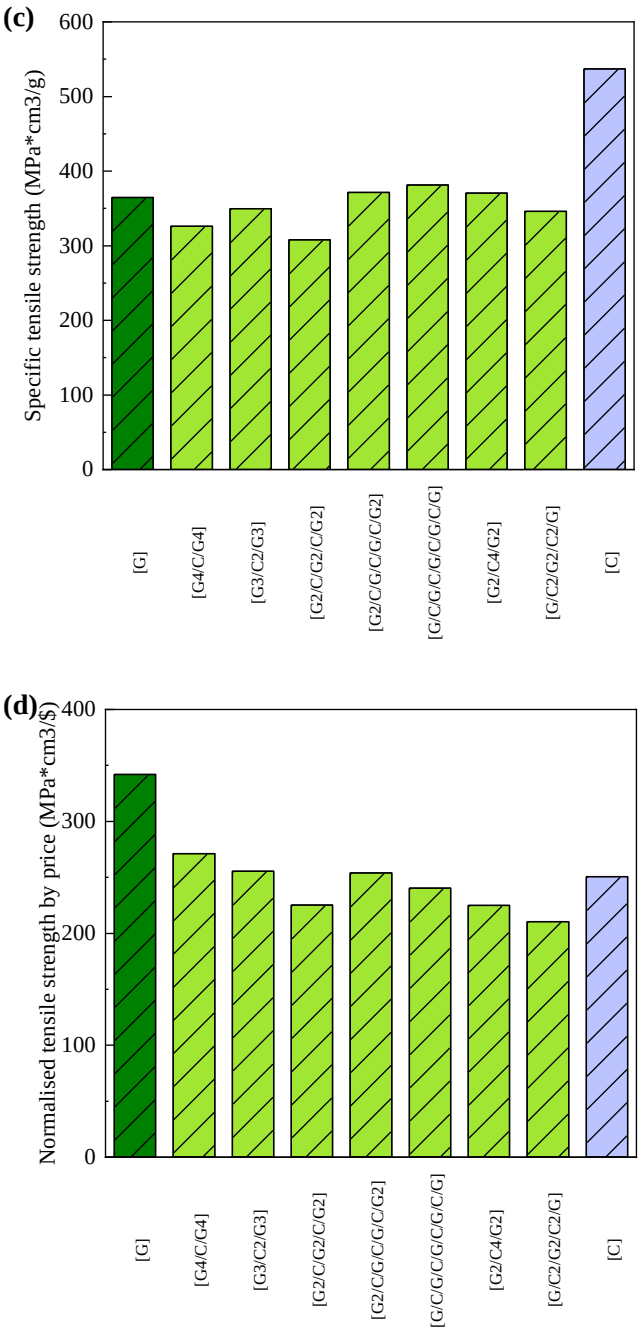

Figure 7-12 *Normalised tensile properties of 3D printed carbon+glass composites by material densiy and price: (a) normalised tensile modulus by density; (b) normalised tensile modulus by price; (c) normalised tensile strength by density; (b) normalised tensile strength by price.*

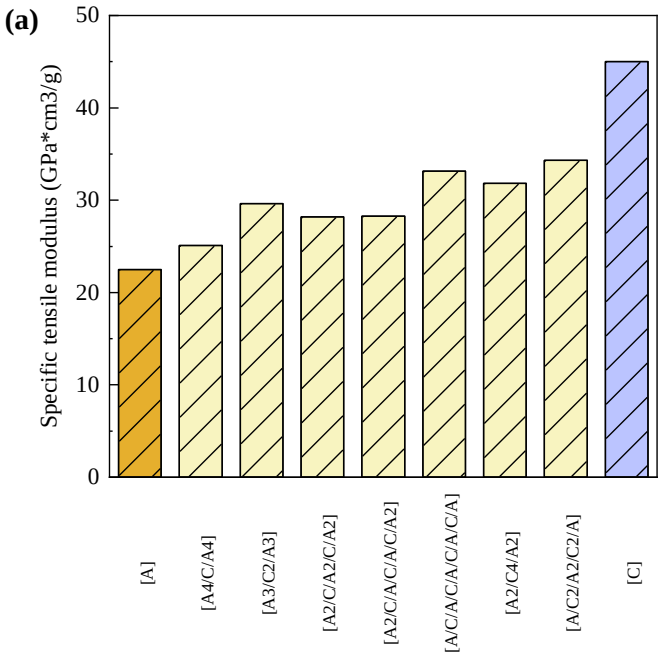
(a)
Specific tensile modulus (GPa*cm3/g)
0
10
20
30
40
50
[A]
[A4/C/A4]
[A3/C2/A3]
[A2/C/A2/C/A2]
[A2/C/A/C/A/C/A2]
[A/C/A/C/A/C/A/C/A]
[A2/C4/A2]
[A/C2/A2/C2/A]
[C]

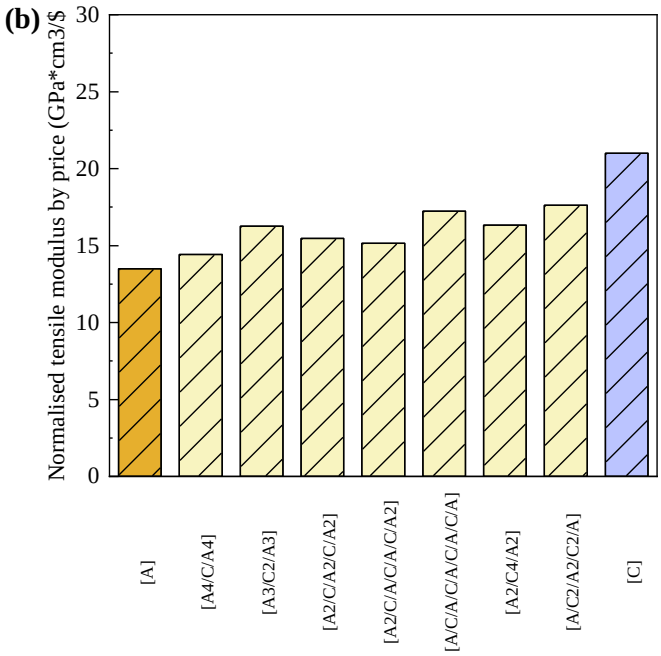
(b)
Normalised tensile modulus by price (GPa*cm3/$
0
5
10
15
20
25
30
[A]
[A4/C/A4]
[A3/C2/A3]
[A2/C/A2/C/A2]
[A2/C/A/C/A/C/A2]
[A/C/A/C/A/C/A/C/A]
[A2/C4/A2]
[A/C2/A2/C2/A]
[C]

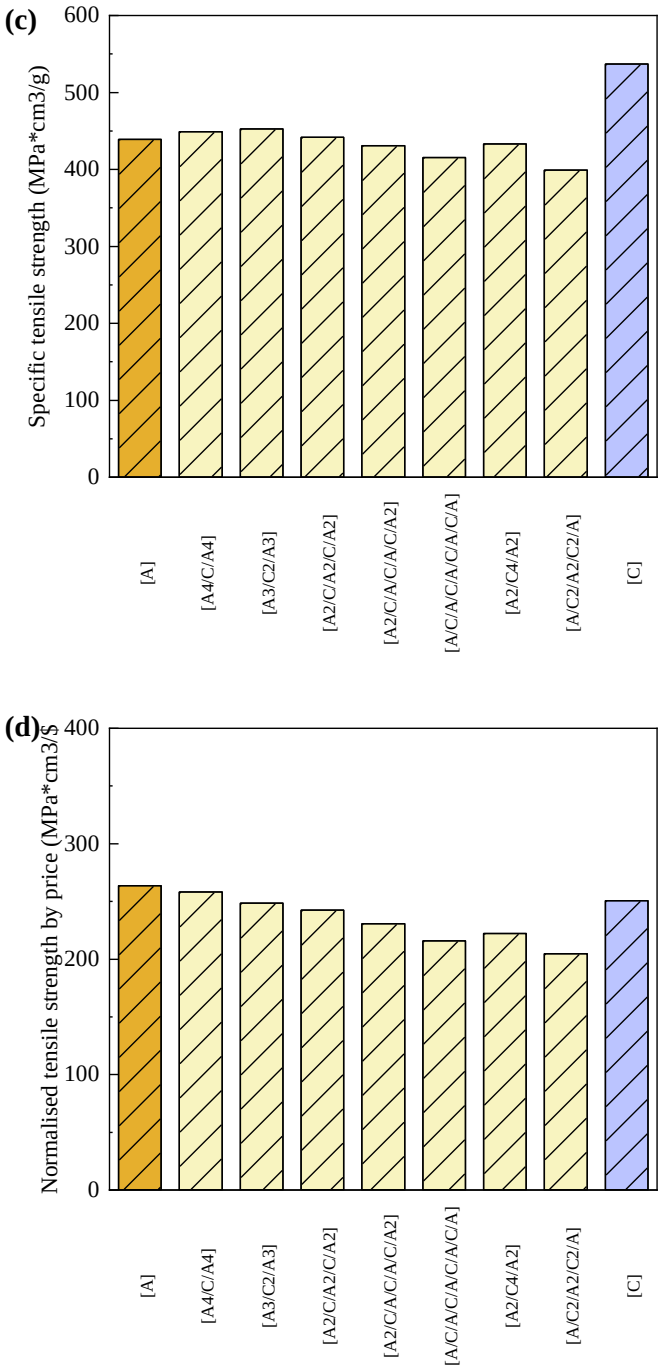

Figure 7-13 *Normalised tensile properties of 3D printed carbon+aramid composites by material densiy and price: (a) normalised tensile modulus by density; (b) normalised tensile modulus by price; (c) normalised tensile strength by density; (b) normalised tensile strength by price.*

7.4 Conclusions

3D printing of the continuous fibre reinforced polymeric composites using the FDM process can also be used to fabricate hybrid fibre composites. This study investigated the effects of carbon layer ratio and carbon layer distribution on the tensile properties of 3D

printed hybrid composites containing glass or aramid filaments. The tensile modulus of the 3D printed carbon+glass-polyamide and carbon+aramid-polyamide composites were well predicted using the rule-of-mixtures (RoM), while the tensile strength of the two types of hybrid composites were more controlled by the strength of the glass- or aramid-polyamide filaments even with carbon layer ratio up to 50%. The lower-than-expected tensile strength of 3D printed hybrid composites is due to the high porosity level, which has also been reported in the 3D printed non-hybrid composites. Although the carbon layer could improve the bonding at layer interfaces, cracks and voids still exist, particularly at the glass/glass and aramid/aramid interfaces. When the composite is under loading, cracks tend to initiate and propagate at the interface, leading to lower-than-expected tensile strength. The poor interfacial bond between different fibre layers is another contributing factor. Additionally, 3D printed hybrid composites showed improvements in normalised modulus values by the material density and price compared to the 3D printed non-hybrid glass- or aramid-polyamide composites without compromising the specific tensile strength.

Due to the failure of the 3D printed hybrid composites being affected by the high porosity level in the glass and aramid layers between adjacent filaments, varying the printing parameters to improve the quality of the printed glass and aramid composites is an important topic for further research. The effect of the processing parameters was not studied in this PhD project because the print conditions are fixed for the MarkForged printer, and cannot be adjusted. Parameters that could be investigated using an adjustable FDM printer include the layer thickness, nozzle travel speed, heating temperature, heating time (slower printing speed can prolong heating time), and ambient temperature (environment temperature). All of these parameters can affect the fusion interface between filaments. Smaller layer thickness and the nozzle travelling distance in the y-axis can lead to more overlap between adjacent filaments. Increasing heating temperature, heating time and ambient temperature benefit the polymer to melt, spread out, and formation of the fusion interface. With a better interface and fewer voids, the in-plane properties of the 3D printed composites could be improved

CHAPTER 8: CONCLUSIONS

8.1 Summary of Main Conclusions

The research work presented in this PhD thesis has contributed to the understanding of the processing, microstructure and mechanical properties of 3D printed continuous fibre/polymer composites fabricated using a MarkForged® FDM printer. The investigations were conducted at multiple dimensional scales spanning the individual fibre, filament, ply and laminate. The factors determining the mechanical properties of 3D printed continuous fibre/polymer composites presented in the literature were reviewed. Research gaps were identified within the scope of the damage caused by the FDM process to the continuous fibre, fibre/polymer filament and composites and the resultant reduction of the mechanical properties.

Chapters 3 and 4 presented experimental investigations into the damage caused by different stages of the FDM process using a Markforged® MarkTwo printer to the continuous fibre and composite filaments. The experiments were conducted on continuous carbon-, glass-, and aramid fibre-polyamide filaments. It was found that the filament surface can be abraded when it passes through the FDM machine prior to printing. The abrasion occurred in the FDM process stage of being fed through the serrated gears (Stage 2). Filament damage also occurred when extruded out of the nozzle (Stage 3), and bent through 90° and pressed onto the build platform (Stage 4). The carbon fibre filament sustained the most severe fibre damage, which reduced the average failure stress of single carbon fibres to only 66% of the initial strength (in the as-received condition). The FDM-induced damage also reduced the tensile and compressive kinking stress values of the carbon-polyamide filament by ~44% and ~25%, respectively. A modification to the FDM printer showed that reducing the abrasion caused by the machine can minimise the reduction in tensile strength. It was also found that the amount and type of fibre damage and the tensile properties of 3D printed filaments processed by the FDM printer depend on the fibre type. Glass fibres were also damaged during 3D printing, but less than carbon fibres, due to their higher flexibility and failure strain. Aramid fibres were not broken, resulting in the smallest loss in tensile properties, although they were more severely crimped by the FDM process due to fibre softening at processing temperature.

Chapter 5 presented an experimental investigation into the effect of 3D printing curvature on the microstructure and mechanical properties of FDM filaments with three fibre types. The study was conducted on the 3D printed filaments with different print curvature radii between 1 mm and 30 mm. It was found that curved printing using the Markforged® MarkTwo printer can cause significant deformation and damage to filaments, particularly at small radius values. Filament folding and twisting occured at tight curvatures, which caused fibre breakage in the carbon- and glass-reinforced filaments. Fibre breakage in the folded region is due to the relatively low bending fracture strain of these fibres, particularly the carbon. Some carbon fibres also pulled away from the main filament when the print radius was under ~5 mm accompanied by longitudinal tearing of the polyamide matrix between fibres. The aramid filament sustained no fibre breakage during curved printing due to its higher flexibility, toughness and failure strain. As the print radius increased to over 10 mm, only twisting occurred instead of filament folding. The fibre damage, filament twisting and matrix tearing damage reduced the tensile properties of the FDM filaments for the three fibre types. The tensile strength of the 3D printed filaments increased as the print radii increased. The results showed that a complex geometry with a tight curvature radius should always be avoided in 3D printed load-bearing composite components.

Chapter 6 presented a study into the microstructure and mechanical properties of the 3D printed continuous fibre/polymer composites made using the FDM process. A comparative assessment between the 3D printed and hot moulded composites containing the same FDM filaments of carbon-polyamide, glass-polyamide and aramid-polyamide was conducted. The tensile modulus values of 3D printed composites were very similar to those of 3D printed filaments, while the ultimate failure stress of 3D printed glass and aramid composites were lower than their ‘building block’ filament in the Stage 4 condition. This is due to the elongated voids that occurred at the fusion interface between adjacent filaments and ply layers in the 3D printed glass and aramid composites, which lead to premature delamination and de-bonding under tension. In contrast, although containing a large density of small voids within the filament, carbon fibre damage caused by the FDM process is the main factor in determining the tensile strength of the 3D printed carbon composite. The hot moulded composites without FDM-induced damage (e.g. fibre breakage, voids, cracks) had higher tensile modulus and strength properties.

Chapter 7 presented an experimental investigation into the microstructure and mechanical properties of 3D printed hybrid composites made using the FDM process. The hybrid composites were 3D printed using the combination of carbon+glass or carbon+aramid filaments. The carbon fibre/polyamide layers in the 3D printed hybrid laminates were sandwiched between or separated by glass/polyamide or aramid fibre/polyamide layers. The effects of material combination, carbon layer ratio (11% - 50%) and carbon layer distribution on the tensile properties of 3D printed hybrid composites were investigated. The tensile modulus values of the 3D printed carbon+glass and carbon+aramid composites were determined by the carbon layer ratio, and the values can be well predicted using rule-of-mixtures. The tensile strength values of the 3D printed hybrid composites are more controlled by the strength of glass and aramid filaments, particularly at a high carbon layer ratio of over 30%. The distribution of the carbon layers separated by the fibre layers with high failure strain showed a positive effect on the tensile strength of 3D printed carbon+glass composites as the carbon layer ratio increased, which in contrast caused a decrease in the strength of carbon+aramid composites with increasing carbon layer ratio. The lower-than-expected tensile strength of the 3D printed hybrid composites containing carbon fibres is attributed to the poor interfacial quality between the different filament layers and their lower failure strain. It was also found that fibre hybridisation can increase the normalised modulus values by the material density and price compared to the 3D printed non-hybrid glass- or aramid-polyamide composites without compromising the specific tensile strength.

8.2 Future Research Considerations

Significant progress has been achieved in this PhD project in determining the FDM process-related factors that cause relatively low mechanical properties for 3D printed continuous fibre polymer composites. However, further experimental and analytical research is required to expand the current research presented in this PhD thesis.

8.2.1 A non-destructive detection method for 3D printed continuous carbon fibre composites

Chapter 3 reported that the continuous carbon fibres within the filament is damaged as it passes through the different stages of the FDM process. The fibre damage reduces the tensile modulus and strength of the composites in the fibre direction. Additionally, our research investigated that fibre damage and fibre waviness can reduce the electrical

conductivity of the unidirectional composites (results were presented in a journal paper [164]). Therefore, it is possible to quantify the relationship between the electrical and tensile properties of 3D printed composites using machine learning. The model can be used as a non-destructive detection method for 3D printed continuous carbon materials to evaluate printing quality and monitor damage.

8.2.2 Microstructure and mechanical properties of 3D printed continuous fibre composites hybridised at the tow level

Hybridising fibres at the tow level is an effective and standard method for manufacturing hybrid fibre composites. However, fabricating a hybrid composite mat is challenging and expensive. In contrast, the 3D printing process opens an avenue by printing continuous fibres tow-by-tow; the prerequisite of which is only fabricating rolls of hybrid fibre filaments. Fibre damages caused by bending and abrasion during the 3D printing process have been identified for different fibre types (i.e. carbon, glass, aramid) in this PhD project. Using hybrid pre-impregnated fibre filaments should also have the potential to reduce fibre damage by covering more brittle fibres with tougher fibres. In this case, material development is crucial and needs to address the following questions. How to choose a matrix that is compatible with the hybrid fibre tows? What kind of fibre surface treatment is efficient in manufacturing hybrid fibre filaments? How do the fibre sizes, fibre distribution and different fibre ratios affect the microstructure and mechanical properties of the 3D printed hybrid fibre filaments and composites? What is the optimum ratio of different fibre types used in the same FDM filament? These questions are all worth studying in the future.

8.2.3 Effects of printing temperature and printing speed on the microstructure and mechanical properties of 3D printed continuous fibre composites

This PhD project was conducted on a commercial desktop 3D printer with a default setup of printing parameters that cannot be changed, such as the printing temperature and printing speed. These parameters have been regarded as essential factors affecting the bond quality between fibre and matrix, adjacent filaments and plies, particularly in the FDM process using the in-situ impregnating method. However, their effects on the fibre damage and void formation in the composites fabricated from pre-impregnated FDM filaments are not well understood. And its efficiency in fabricating composites with complex geometry is also

unknown. These aspects will be helpful to product designers in fabricating continuous fibre composite structures.

8.2.4 Fracture toughness of 3D printed non-hybrid and hybrid continuous fibre composites

The results presented in **Chapter 6** and **7** showed that the voids in the polymer-rich fusion zones reduced the filament-to-filament and layer-to-layer adhesion in the 3D printed composites, thereby reducing the tensile strength. It is expected that voids can affect the initiation and propagation of cracks at the interlayer. However, the effects of void size and distribution on the modes I and II interlaminar fracture toughness properties of 3D printed continuous fibre/polymer composites is not well understood. Additionally, fibre damage caused by the FDM process might increase fibre bridging during delamination crack growth, which may increase the interlaminar fracture toughness. Furthermore, the void formation and fibre damage have been proved to depend on the fibre type, and therefore the interlaminar fracture properties and delamination crack growth mechanisms of hybrid composites might be different from the 3D printed non-hybrid composites, which is worth investigating.

REFERENCES:

[1] K. Yassin, M. Hojjati, Processing of thermoplastic matrix composites through automated fiber placement and tape laying methods, Journal of Thermoplastic Composite Materials, 31(12), (2018), 1676-1725.

[2] R. Pitchumani, J.W. Gillespie Jr, M.A. Lamontia, Design and optimization of a thermoplastic tow-placement process with in-situ consolidation, Journal of Composite Materials, 31(3), (1997), 244-275.

[3] R. Pitchumani, S. Ranganathan, R.C. Don, J.W. Gillespie Jr, M.A. Lamontia, Analysis of transport phenomena governing interfacial bonding and void dynamics during thermoplastic tow-placement, International Journal of Heat and Mass Transfer, 39(9), (1996), 1883-1897.

[4] C.M. Stokes-Griffin, P. Compston, T.I. Matuszyk, M.J. Cardew-Hall, Thermal modelling of the laser-assisted thermoplastic tape placement process, Journal of thermoplastic composite materials, 28(10), (2015), 1445-1462.

[5] V. Agarwal, R.L. McCullough, J.M. Schultz, The thermoplastic laser-assisted consolidation process - Mechanical and microstructure characterization, Journal of thermoplastic composite materials, 9(4), (1996), 365-380.

[6] D. Modi, A. Comer, R.M. O'Higgins, M.A. McCarthy, Thermoplastic composites: In-situ consolidation or in-situ welding, 19th International Conferences on Composite Materials, Montreal, Canada, 2013, pp. 649-655.

[7] S.K. Mazumdar, S.V. Hoa, Experimental determination of process parameters for laser assisted processing of PEEK/carbon thermoplastic composites, International SAMPE Symposium and Exhibition (Proceedings), 1993, pp. 189-204.

[8] A.J. Comer, D. Ray, W.O. Obande, D. Jones, J. Lyons, I. Rosca, R.M. O'Higgins, M.A. McCarthy, Mechanical characterisation of carbon fibre-PEEK manufactured by laser-assisted automated-tape-placement and autoclave, Composites Part A: Applied Science and Manufacturing, 69, (2015), 10-20.

[9] G.D. Goh, Y.L. Yap, S. Agarwala, W.Y. Yeong, Recent progress in additive manufacturing of fiber reinforced polymer composite, Advanced Materials Technologies, 4(1), (2019), 180027.

[10] Z. Quan, A. Wu, M. Keefe, X. Qin, J. Yu, J. Suhr, J.-H. Byun, B.-S. Kim, T.-W. Chou, Additive manufacturing of multi-directional preforms for composites: opportunities and challenges, Materials Today, 18(9), (2015), 503-512.

[11] E. MacDonald, R. Salas, D. Espalin, M. Perez, E. Aguilera, D. Muse, R.B. Wicker, 3D printing for the rapid prototyping of structural electronics, IEEE Access, 2, (2014), 234-242.
[12] H.J. O'Connor, D.P. Dowling, Evaluation of the influence of low pressure additive manufacturing processing conditions on printed polymer parts, Additive Manufacturing, 21, (2018), 404-412.
[13] A. Sebert, J.W. Nelson, G. Bertacco, Anisotropic mechanical performance of 3D printed polymers, Conference of Advanced Materials - TechConnect Briefs, 2017, pp. 170-173.
[14] R.T.L. Ferreira, I.C. Amatte, T.A. Dutra, D. Bürger, Experimental characterization and micrography of 3D printed PLA and PLA reinforced with short carbon fibers, Composites Part B: Engineering, 124, (2017), 88-100.
[15] L.J. Love, V. Kunc, O. Rios, C.E. Duty, A.M. Elliott, B.K. Post, R.J. Smith, C.A. Blue, The importance of carbon fiber to polymer additive manufacturing, Journal of Materials Research, 29(17), (2014), 1893-1898.
[16] F. Ning, W. Cong, J. Qiu, J. Wei, S. Wang, Additive manufacturing of carbon fiber reinforced thermoplastic composites using fused deposition modeling, Composites Part B: Engineering, 80, (2015), 369-378.
[17] H.L. Tekinalp, V. Kunc, G.M. Velez-Garcia, C.E. Duty, L.J. Love, A.K. Naskar, C.A. Blue, S. Ozcan, Highly oriented carbon fiber–polymer composites via additive manufacturing, Composites Science and Technology, 105, (2014), 144-150.
[18] C.E. Duty, V. Kunc, B. Compton, B. Post, D. Erdman, R. Smith, R. Lind, P. Lloyd, L. Love, Structure and mechanical behavior of Big Area Additive Manufacturing (BAAM) materials, Rapid Prototyping Journal, 23(1), (2017), 181-189.
[19] C. Hill, K. Rowe, R. Bedsole, J. Earle, V. Kunc, Materials and process development for direct digital manufacturing of vehicles, International SAMPE Technical Conference, 2016.
[20] R. Matsuzaki, M. Ueda, M. Namiki, T.K. Jeong, H. Asahara, K. Horiguchi, T. Nakamura, A. Todoroki, Y. Hirano, Three-dimensional printing of continuous-fiber composites by in-nozzle impregnation, Scientific Reports, 6, (2016), 23058.
[21] N. Li, Y. Li, S. Liu, Rapid prototyping of continuous carbon fiber reinforced polylactic acid composites by 3D printing, Journal of Materials Processing Technology, 238, (2016), 218-225.
[22] X. Tian, T. Liu, Q. Wang, A. Dilmurat, D. Li, G. Ziegmann, Recycling and remanufacturing of 3D printed continuous carbon fiber reinforced PLA composites, Journal of Cleaner Production, 142, (2017), 1609-1618.

[23] A.N. Dickson, J.N. Barry, K.A. McDonnell, D.P. Dowling, Fabrication of continuous carbon, glass and Kevlar fibre reinforced polymer composites using additive manufacturing, Additive Manufacturing, 16, (2017), 146-152.
[24] B. Brenken, E. Barocio, A. Favaloro, V. Kunc, R.B. Pipes, Fused filament fabrication of fiber-reinforced polymers: A review, Additive Manufacturing, 21, (2018), 1-16.
[25] M.L. Shofner, K. Lozano, F.J. Rodríguez-Macías, E.V. Barrera, Nanofiber-reinforced polymers prepared by fused deposition modeling, Journal of Applied Polymer Science, 89(11), (2003), 3081-3090.
[26] G.W. Melenka, B.K.O. Cheung, J.S. Schofield, M.R. Dawson, J.P. Carey, Evaluation and prediction of the tensile properties of continuous fiber-reinforced 3D printed structures, Composite Structures, 153, (2016), 866-875.
[27] F.V.D. Klift, Y. Koga, A. Todoroki, M. Ueda, Y. Hirano, R. Matsuzaki, 3D printing of continuous carbon fibre reinforced thermoplastic (CFRTP) tensile test specimens, Open Journal of Composite Materials, 6(1), (2016), 18-27.
[28] J. Justo, L. Távara, L. García-Guzmán, F. París, Characterization of 3D printed long fibre reinforced composites, Composite Structures, 185, (2018), 537-548.
[29] G.D. Goh, V. Dikshit, A.P. Nagalingam, G.L. Goh, S. Agarwala, S.L. Sing, J. Wei, W.Y. Yeong, Characterization of mechanical properties and fracture mode of additively manufactured carbon fiber and glass fiber reinforced thermoplastics, Materials & Design, 137, (2018), 79-89.
[30] L. Pyl, K.-A. Kalteremidou, D. Van Hemelrijck, Exploration of specimen geometry and tab configuration for tensile testing exploiting the potential of 3D printing freeform shape continuous carbon fibre-reinforced nylon matrix composites, Polymer Testing, 71, (2018), 318-328.
[31] T. Liu, X. Tian, Y. Zhang, Y. Cao, D. Li, High-pressure interfacial impregnation by micro-screw in-situ extrusion for 3D printed continuous carbon fiber reinforced nylon composites, Composites Part A: Applied Science and Manufacturing, 130, (2020), 105770.
[32] L.G. Blok, M.L. Longana, H. Yu, B.K.S. Woods, An investigation into 3D printing of fibre reinforced thermoplastic composites, Additive Manufacturing, 22, (2018), 176-186.
[33] Composites, C. A fundamental shift in manufacturing. 2021 <https://www.continuouscomposites.com/technology>, (Accessed September 30th.2021).

[34] S.M.F. Kabir, K. Mathur, A.F.M. Seyam, A critical review on 3D printed continuous fiber-reinforced composites: History, mechanism, materials and properties, Composite Structures, 232, (2020), 111476.
[35] N. Krajangsawasdi, L. Blok, I. Hamerton, M. Longana, B. Woods, D. Ivanov, Fused deposition modelling of fibre reinforced polymer composites: A parametric review, Journal of Composites Science, 5(1), (2021), 29.
[36] T.N.A.T. Rahim, A.M. Abdullah, H. Md Akil, Recent developments in fused deposition modeling-based 3D printing of polymers and their composites, Polymer Reviews, 59(4), (2019), 589-624.
[37] T. Sathies, P. Senthil, M.S. Anoop, A review on advancements in applications of fused deposition modelling process, Rapid Prototyping Journal, 26(4), (2020), 669-687.
[38] F. Calignano, D. Manfredi, E.P. Ambrosio, S. Biamino, M. Lombardi, E. Atzeni, A. Salmi, P. Minetola, L. Iuliano, P. Fino, Overview on Additive Manufacturing Technologies, Proceedings of the IEEE, 105(4), (2017), 593-612.
[39] D.E. Karalekas, Study of the mechanical properties of nonwoven fibre mat reinforced photopolymers used in rapid prototyping, Materials & Design, 24(8), (2003), 665-670.
[40] D. Karalekas, K. Antoniou, Composite rapid prototyping: overcoming the drawback of poor mechanical properties, Journal of Materials Processing Technology, 153-154, (2004), 526-530.
[41] A.A. Ogale, T. Renault, R.L. Dooley, A. Bagchi, C.C. Jaraalmonte, 3-D photolithography for composite development - Discontinuous reinforcements, SAMPE Quarterly-Society for the Advancement of Material and Process Engineering, 23(1), (1991), 28-38.
[42] A. Gupta, A.A. Ogale, Dual curing of carbon fiber reinforced photoresins for rapid prototyping, Polymer Composites, 23(6), (2002), 1162-1170.
[43] G.V. Salmoria, C.H. Ahrens, V.E. Beal, A.T.N. Pires, V. Soldi, Evaluation of post-curing and laser manufacturing parameters on the properties of SOMOS 7110 photosensitive resin used in stereolithography, Materials & Design, 30(3), (2009), 758-763.
[44] I. Gibson, D.W. Rosen, B. Stucker, Additive Manufacturing Mechnologies: Rapid Prototyping To Direct Digital Manufacturing, Springer Publishing Company, 2010.
[45] D. Klosterman, R. Chartoff, G. Graves, N. Osborne, A. Lightman, G. Hah, A. Bezeredi, S. Rodrigues, Direct fabrication of ceramics and composites through Laminated Object

Manufacturing (LOM), International SAMPE Symposium and Exhibition (Proceedings), 1998, pp. 693-705.
[46] D. Klosterman, R. Chartoff, G. Graves, N. Osborne, B. Priore, Interfacial characteristics of composites fabricated by laminated object manufacturing, Composites Part A: Applied Science and Manufacturing, 29(9), (1998), 1165-1174.
[47] J.R.C. Dizon, A.H. Espera, Q. Chen, R.C. Advincula, Mechanical characterization of 3D-printed polymers, Additive Manufacturing, 20, (2018), 44-67.
[48] M. Chapiro, Current achievements and future outlook for composites in 3D printing, Reinforced Plastics, 60(6), (2016), 372-375.
[49] A.K. Sood, R.K. Ohdar, S.S. Mahapatra, Parametric appraisal of mechanical property of fused deposition modelling processed parts, Materials & Design, 31(1), (2010), 287-295.
[50] G. Liao, Z. Li, Y. Cheng, D. Xu, D. Zhu, S. Jiang, J. Guo, X. Chen, G. Xu, Y. Zhu, Properties of oriented carbon fiber/polyamide 12 composite parts fabricated by fused deposition modeling, Materials & Design, 139, (2017), 283-292.
[51] A. Torrado, D. Roberson, R. Wicker, Fracture surface analysis of 3D-printed tensile specimens of novel ABS-based materials, Journal of Failure Analysis and Prevention, 14(3), (2014), 343-353.
[52] M. Luo, X. Tian, J. Shang, W. Zhu, D. Li, Y. Qin, Impregnation and interlayer bonding behaviours of 3D-printed continuous carbon-fiber-reinforced poly-ether-ether-ketone composites, Composites Part A: Applied Science and Manufacturing, 121, (2019), 130-138.
[53] B. Akhoundi, A.H. Behravesh, A. Bagheri Saed, Improving mechanical properties of continuous fiber-reinforced thermoplastic composites produced by FDM 3D printer, Journal of Reinforced Plastics and Composites, 38(3), (2019), 99-116.
[54] H. Mei, Z. Ali, I. Ali, L. Cheng, Tailoring strength and modulus by 3D printing different continuous fibers and filled structures into composites, Advanced Composites and Hybrid Materials, 2(2), (2019), 312-319.
[55] H. Al Abadi, H.-T. Thai, V. Paton-Cole, V.I. Patel, Elastic properties of 3D printed fibre-reinforced structures, Composite Structures, 193, (2018), 8-18.
[56] M. Araya-Calvo, I. López-Gómez, N. Chamberlain-Simon, J.L. León-Salazar, T. Guillén-Girón, J.S. Corrales-Cordero, O. Sánchez-Brenes, Evaluation of compressive and flexural properties of continuous fiber fabrication additive manufacturing technology, Additive Manufacturing, 22, (2018), 157-164.

[57] M.A. Caminero, J.M. Chacón, I. García-Moreno, J.M. Reverte, Interlaminar bonding performance of 3D printed continuous fibre reinforced thermoplastic composites using fused deposition modelling, Polymer Testing, 68, (2018), 415-423.
[58] G. Chabaud, M. Castro, C. Denoual, A. Le Duigou, Hygromechanical properties of 3D printed continuous carbon and glass fibre reinforced polyamide composite for outdoor structural applications, Additive Manufacturing, 26, (2019), 94-105.
[59] M.A. Caminero, J.M. Chacón, I. García-Moreno, G.P. Rodríguez, Impact damage resistance of 3D printed continuous fibre reinforced thermoplastic composites using fused deposition modelling, Composites Part B: Engineering, 148, (2018), 93-103.
[60] M.A. Caminero, I. García-Moreno, G.P. Rodríguez, J.M. Chacón, Internal damage evaluation of composite structures using phased array ultrasonic technique: Impact damage assessment in CFRP and 3D printed reinforced composites, Composites Part B: Engineering, 165, (2019), 131-142.
[61] W. Zhong, F. Li, Z. Zhang, L. Song, Z. Li, Research on rapid-prototyping/part manufacturing (RP&M) for the continuous fiber reinforced composite, Materials and Manufacturing Processes, 16(1), (2001), 17-26.
[62] Y. Song, Y. Li, W. Song, K. Yee, K.Y. Lee, V.L. Tagarielli, Measurements of the mechanical response of unidirectional 3D-printed PLA, Materials & Design, 123, (2017), 154-164.
[63] H. Li, T. Wang, S. Joshi, Z. Yu, The quantitative analysis of tensile strength of additively manufactured continuous carbon fiber reinforced polylactic acid (PLA), Rapid Prototyping Journal, 25(10), (2019), 1624-1636.
[64] X. Tian, T. Liu, C. Yang, Q. Wang, D. Li, Interface and performance of 3D printed continuous carbon fiber reinforced PLA composites, Composites Part A: Applied Science and Manufacturing, 88, (2016), 198-205.
[65] D. Jiang, D.E. Smith, Anisotropic mechanical properties of oriented carbon fiber filled polymer composites produced with fused filament fabrication, Additive Manufacturing, 18, (2017), 84-94.
[66] D. Young, N. Wetmore, M. Czabaj, Interlayer fracture toughness of additively manufactured unreinforced and carbon-fiber-reinforced acrylonitrile butadiene styrene, Additive Manufacturing, 22, (2018), 508-515.

[67] M. Heidari-Rarani, M. Rafiee-Afarani, A.M. Zahedi, Mechanical characterization of FDM 3D printing of continuous carbon fiber reinforced PLA composites, Composites Part B: Engineering, 175, (2019), 107147.
[68] A.A. Stepashkin, D.I. Chukov, F.S. Senatov, A.I. Salimon, A.M. Korsunsky, S.D. Kaloshkin, 3D-printed PEEK-carbon fiber (CF) composites: Structure and thermal properties, Composites Science and Technology, 164, (2018), 319-326.
[69] C. Yang, X. Tian, D. Li, Y. Cao, F. Zhao, C. Shi, Influence of thermal processing conditions in 3D printing on the crystallinity and mechanical properties of PEEK material, Journal of Materials Processing Technology, 248, (2017), 1-7.
[70] C. Yang, B. Wang, D. Li, X. Tian, Modelling and characterisation for the responsive performance of CF/PLA and CF/PEEK smart materials fabricated by 4D printing, Virtual and Physical Prototyping, 12(1), (2017), 69-76.
[71] G. Dong, Y. Tang, D. Li, Y.F. Zhao, Mechanical properties of continuous Kevlar fiber reinforced composites fabricated by fused deposition modeling process, Procedia Manufacturing, 26, (2018), 774-781.
[72] F.d.A. Silva, N. Chawla, R.D.d.T. Filho, Tensile behavior of high performance natural (sisal) fibers, Composites Science and Technology, 68(15-16), (2008), 3438-3443.
[73] C. Huang, M.W. Joosten, 3D printed continuous fibre-reinforced composites: Design and characterisation of advanced pseudo-ductile hybrid laminates, Composites Part A: Applied Science and Manufacturing, 146, (2021), 106403.
[74] P. Zhuo, S. Li, I.A. Ashcroft, A.I. Jones, Material extrusion additive manufacturing of continuous fibre reinforced polymer matrix composites: A review and outlook, Composites Part B: Engineering, 224, (2021), 109143.
[75] I. Fidan, A. Imeri, A. Gupta, S. Hasanov, A. Nasirov, A. Elliott, F. Alifui-Segbaya, N. Nanami, Trends and challenges of fiber reinforced additive manufacturing, International Journal of Advanced Manufacturing Technology, 102(5), (2019), 1801-1818.
[76] G. Cicala, D. Giordano, C. Tosto, G. Filippone, A. Recca, I. Blanco, Polylactide (PLA) filaments a biobased solution for additive manufacturing: Correlating rheology and thermomechanical properties with printing quality, Materials, 11(7), (2018), 1191.
[77] W. Zhong, F. Li, Z. Zhang, L. Song, Z. Li, Short fiber reinforced composites for fused deposition modeling, Materials Science and Engineering: A, 301(2), (2001), 125-130.

[78] T. Liu, X. Tian, M. Zhang, D. Abliz, D. Li, G. Ziegmann, Interfacial performance and fracture patterns of 3D printed continuous carbon fiber with sizing reinforced PA6 composites, Composites Part A: Applied Science and Manufacturing, 114, (2018), 368-376.
[79] M. Luo, X. Tian, J. Shang, J. Yun, W. Zhu, D. Li, Y. Qin, Bi-scale interfacial bond behaviors of CCF/PEEK composites by plasma-laser cooperatively assisted 3D printing process, Composites Part A: Applied Science and Manufacturing, 131, (2020), 105812.
[80] O.S. Carneiro, A.F. Silva, R. Gomes, Fused deposition modeling with polypropylene, Materials & Design, 83, (2015), 768-776.
[81] E. Yasa, L.v.l.m. Ersoy, Dimensional accuracy and mechanical properties of chopped carbon reinforced polymers produced by material extrusion additive manufacturing, Materials, 12(23), (2019), 3885.
[82] E.V.d. Toro, J.C. Sobrino, A. Martínez, V.M. Eguía, J.A. Perez, Investigation of a Short Carbon Fibre-Reinforced Polyamide and Comparison of Two Manufacturing Processes: Fused Deposition Modelling (FDM) and Polymer Injection Moulding (PIM), Materials, 13, (2020), 672.
[83] E. Yasa, Anisotropic impact toughness of chopped carbon fiber reinforced nylon fabricated by material-extrusion-based additive manufacturing, Anadolu University Journal of Science and Technology. A : Applied Sciences and Engineering, 20, (2019), 195-203.
[84] A.D. Pertuz, S. Díaz-Cardona, O.A. González-Estrada, Static and fatigue behaviour of continuous fibre reinforced thermoplastic composites manufactured by fused deposition modelling technique, International Journal of Fatigue, 130, (2020), 105275.
[85] A. Kehinde Aworinde, S. Oluropo Adeosun, F. Adekunle Oyawale, E. Titilayo Akinlabi, S.A. Akinlabi, Parametric effects of fused deposition modelling on the mechanical properties of polylactide composites: A review, Journal of Physics: Conference Serise, 2019, p. 022060.
[86] W.C. Smith, R.W. Dean, Structural characteristics of fused deposition modeling polycarbonate material, Polymer Testing, 32, (2013), 1306-1312.
[87] F. Ning, W. Cong, Y. Hu, H. Wang, Additive manufacturing of carbon fiber-reinforced plastic composites using fused deposition modeling: Effects of process parameters on tensile properties, Journal of Composite Materials, 51, (2017), 451 - 462.
[88] A.N. Dickson, K.-A. Ross, D.P. Dowling, Additive manufacturing of woven carbon fibre polymer composites, Composite Structures, 206, (2018), 637-643.

[89] R. Omuro, M. Ueda, R. Matsuzaki, A. Todoroki, Y. Hirano, Three-dimensional printing of continuous carbon fiber reinforced thermoplastics by in-nozzle impregnation with compaction roller, 21th International Conferences on Composite Materials, 2017.
[90] M. Yamawaki, Y. Kouno, Fabrication and mechanical characterization of continuous carbon fiber-reinforced thermoplastic using a preform by three-dimensional printing and via hot-press molding, Advanced Composite Materials, 27, (2018), 209 - 219.
[91] Q. He, H. Wang, K. Fu, L. Ye, 3D printed continuous CF/PA6 composites: Effect of microscopic voids on mechanical performance, Composites Science and Technology, 191, (2020), 108077.
[92] D.D.L. Chung, Processing-structure-property relationships of continuous carbon fiber polymer-matrix composites, Materials Science and Engineering R: Reports, 113, (2017), 1-29.
[93] A. D'Amore, L. Grassia, P. Verde, Modeling the fatigue behavior of glass fiber reinforced thermoplastic and thermosetting matrices, 6th International Conference on Times of Polymers & Composites, 2012.
[94] P.G. Partridge, C.M. Ward-Close, Processing of advanced continuous fibre composites: Current practice and potential developments, International Materials Reviews, 38(1), (1993), 1-24.
[95] H. Brooks, S. Molony, Design and evaluation of additively manufactured parts with three dimensional continuous fibre reinforcement, Materials & Design, 90, (2016), 276-283.
[96] Z. Qin, B.G. Compton, J.A. Lewis, M.J. Buehler, Structural optimization of 3D-printed synthetic spider webs for high strength, Nature Communications, 6, (2015), 7038.
[97] H. Zhang, D. Yang, Y. Sheng, Performance-driven 3D printing of continuous curved carbon fibre reinforced polymer composites: A preliminary numerical study, Composites Part B: Engineering, 151, (2018), 256-264.
[98] Y. Yamanaka, A. Todoroki, M. Ueda, Y. Hirano, R. Matsuzaki, Fiber line optimization in single ply for 3D printed composites, Open Journal of Composite Materials, 6(4), (2016), 121-131.
[99] C. Oztan, R. Karkkainen, M. Fittipaldi, G. Nygren, L. Roberson, M. Lane, E. Celik, Microstructure and mechanical properties of three dimensional-printed continuous fiber composites, Journal of Composite Materials, 53(2), (2019), 143-154.
[100] S. Liu, Y. Li, N. Li, A novel free-hanging 3D printing method for continuous carbon fiber reinforced thermoplastic lattice truss core structures, Materials & Design, 137, (2018), 235-244.

[101] H. Shiratori, A. Todoroki, M. Ueda, R. Matsuzaki, Y. Hirano, Mechanism of folding a fiber bundle in the curved section of 3D printed carbon fiber reinforced plastics, Advanced Composite Materials, 29(3), (2020), 247-257.
[102] R. Matsuzaki, T. Nakamura, K. Sugiyama, M. Ueda, A. Todoroki, Y. Hirano, Y. Yamagata, Effects of set curvature and fibre bundle size on the printed radius of curvature by a continuous carbon fibre composite 3D printer, Additive Manufacturing, 24, (2018), 93-102.
[103] K. Sugiyama, R. Matsuzaki, M. Ueda, A. Todoroki, Y. Hirano, 3D printing of composite sandwich structures using continuous carbon fiber and fiber tension, Composites Part A: Applied Science and Manufacturing, 113, (2018), 114-121.
[104] K. Ishii, A. Todoroki, Y. Mizutani, Y. Suzuki, Y. Koga, R. Matsuzaki, M. Ueda, Y. Hirano, Bending fracture rule for 3D-printed curved continuous-fiber composite, Advanced Composite Materials, 28, (2018), 1-13.
[105] H. Shiratori, A. Todoroki, M. Ueda, R. Matsuzaki, Y. Hirano, Mechanism of folding a fiber bundle in the curved section of 3D printed carbon fiber reinforced plastics, Advanced Composite Materials, 29, (2019), 247 - 257.
[106] H. Zhang, J. Chen, D. Yang, Fibre misalignment and breakage in 3D printing of continuous carbon fibre reinforced thermoplastic composites, Additive Manufacturing, 38, (2021).
[107] A. Beakou, M. Cano, V. Verney, Modelling slit tape buckling during automated prepreg manufacturing: A local approach, Composite Structures, 93, (2011), 2628-2635.
[108] C.G. Mahajan, D. Cormier, 3D printing of carbon fiber composites with preferentially aligned fibers, Industrial and Systems Engineering Research Conference, 2015.
[109] T. Hofstätter, D.B. Pedersen, G. Tosello, H.N. Hansen, State-of-the-art of fiber-reinforced polymers in additive manufacturing technologies, Journal of Reinforced Plastics and Composites, 36, (2017), 1061 - 1073.
[110] D. Luca, Design and manufacture of optimized continuous composite fiber filament using additive manufacturing systems, Journal of Material Sciences & Engineering, 6(4), (2017), 1-5.
[111] W. Ye, G. Lin, W. Wu, P. Geng, X. Hu, Z. Gao, J. Zhao, Separated 3D printing of continuous carbon fiber reinforced thermoplastic polyimide, Composites Part A: Applied Science and Manufacturing, 121, (2019), 457-464.

[112] A.V. Azarov, F.K. Antonov, M.V. Golubev, A.R. Khaziev, S.A. Ushanov, Composite 3D printing for the small size unmanned aerial vehicle structure, Composites Part B: Engineering, 169, (2019), 157-163.
[113] A.V. Azarov, F. Antonov, V.V. Vasil ev, M.V. Golubev, D. Krasovskii, A.F. Razin, V.A. Salov, V. Stupnikov, A. Khaziev, Development of a two-matrix composite material fabricated by 3D printing, Polymer Science, Series D, 10, (2017), 87-90.
[114] Y. Ming, Z. Xin, J. Zhang, Y. Duan, B. Wang, Fabrication of continuous glass fiber-reinforced dual-cure epoxy composites via UV-assisted fused deposition modeling, Composites Communications, 21, (2020), 100401.
[115] Y. Ming, S. Zhang, W. Han, B. Wang, Y. Duan, H. Xiao, Investigation on process parameters of 3D printed continuous carbon fiber-reinforced thermosetting epoxy composites, Additive Manufacturing, 33, (2020), 101184.
[116] Y. Peng, Y. Wu, K. Wang, G.-j. Gao, S. Ahzi, Synergistic reinforcement of polyamide-based composites by combination of short and continuous carbon fibers via fused filament fabrication, Composite Structures, 207, (2019), 232-239.
[117] T.A. Dutra, R.T.L. Ferreira, H.B. Resende, A. Guimarães, Mechanical characterization and asymptotic homogenization of 3D-printed continuous carbon fiber-reinforced thermoplastic, Journal of the Brazilian Society of Mechanical Sciences and Engineering, 41(3), (2019), 133.
[118] Z. Guerdal, R. Olmedo, Composite laminates with spatially varying fiber orientations - 'Variable stiffness panel concept', 33rd Structures, Structural Dynamics and Materials Conference, 1992.
[119] W. Hao, Y. Liu, H. Zhou, H. Chen, D. Fang, Preparation and characterization of 3D printed continuous carbon fiber reinforced thermosetting composites, Polymer Testing, 65, (2018), 29-34.
[120] C. Yang, X. Tian, T. Liu, Y. Cao, D. Li, 3D printing for continuous fiber reinforced thermoplastic composites: Mechanism and performance, Rapid Prototyping Journal, 23(1), (2017), 209-215.
[121] M. Iragi, C. Pascual-González, A. Esnaola, C.S. Lopes, L. Aretxabaleta, Ply and interlaminar behaviours of 3D printed continuous carbon fibre-reinforced thermoplastic laminates; effects of processing conditions and microstructure, Additive Manufacturing, 30, (2019), 100884.

[122] P. Bettini, G. Alitta, G. Sala, L. Di Landro, Fused deposition technique for continuous fiber reinforced thermoplastic, Journal of Materials Engineering and Performance, 26, (2016), 843-848.
[123] J.M. Chacón, M.A. Caminero, P.J. Núñez, E. García-Plaza, I. García-Moreno, J.M. Reverte, Additive manufacturing of continuous fibre reinforced thermoplastic composites using fused deposition modelling: Effect of process parameters on mechanical properties, Composites Science and Technology, 181, (2019), 107688.
[124] K. Wang, S. Li, Y. Wu, Y. Rao, Y. Peng, Simultaneous reinforcement of both rigidity and energy absorption of polyamide-based composites with hybrid continuous fibers by 3D printing, Composite Structures, 267, (2021), 113854.
[125] G.D. Goh, V. Dikshit, J. An, W.Y. Yeong, Process-structure-property of additively manufactured continuous carbon fiber reinforced thermoplastic: an investigation of mode I interlaminar fracture toughness, Mechanics of Advanced Materials and Structures, 29(10), (2022), 1418-1430.
[126] Y. Swolfs, I. Verpoest, L. Gorbatikh, Recent advances in fibre-hybrid composites: materials selection, opportunities and applications, International Materials Reviews, 64(4), (2019), 181-215.
[127] R. Alagirusamy, R. Fangueiro, V. Ogale, N.V. Padaki, Hybrid yarns and textile preforming for thermoplastic composites, Textile Progress, 38(4), (2006), 1-71.
[128] K. Wang, S. Li, Y. Rao, Y. Wu, Y. Peng, S. Yao, H. Zhang, S. Ahzi, Flexure behaviors of abs-based composites containing carbon and Kevlar fibers by material extrusion 3D printing, Polymers, 11(11), (2019), 1878.
[129] D. Yavas, Z. Zhang, Q. Liu, D. Wu, Interlaminar shear behavior of continuous and short carbon fiber reinforced polymer composites fabricated by additive manufacturing, Composites Part B: Engineering, 204, (2021), 108460.
[130] S. Dul, L. Fambri, A. Pegoretti, Fused deposition modelling with ABS–graphene nanocomposites, Composites Part A: Applied Science and Manufacturing, 85, (2016), 181-191.
[131] H. Yu, M.L. Longana, M. Jalalvand, M.R. Wisnom, K. Potter, Pseudo-ductility in intermingled carbon/glass hybrid composites with highly aligned discontinuous fibres, Composites Part A: Applied Science and Manufacturing, 73, (2015), 35-44.
[132] G. Czél, T. Rev, M. Jalalvand, M. Fotouhi, M.L. Longana, O.J. Nixon-Pearson, M.R. Wisnom, Pseudo-ductility and reduced notch sensitivity in multi-directional all-carbon/epoxy

thin-ply hybrid composites, Composites Part A: Applied Science and Manufacturing, 104, (2018), 151-164.
[133] G. Czél, M.R. Wisnom, Demonstration of pseudo-ductility in high performance glass-epoxy composites by hybridisation with thin-ply carbon prepreg, Composites Part A: Applied Science and Manufacturing, 52, (2013), 23-30.
[134] M.L. Longana, H. Yu, M. Jalalvand, M.R. Wisnom, K. Potter, Aligned discontinuous intermingled reclaimed/virgin carbon fibre composites for high performance and pseudo-ductile behaviour in interlaminated carbon-glass hybrids, Composites Science and Technology, 143, (2017), 13-21.
[135] M.Y. Zakaria, A.B. Sulong, J. Sahari, H. Suherman, Effect of the addition of milled carbon fiber as a secondary filler on the electrical conductivity of graphite/epoxy composites for electrical conductive material, Composites Part: Engineering, 83, (2015), 75-80.
[136] M.M. Shokrieh, M.J. Omidi, Reinforcement of metallic plates with composite materials, Journal of Composite Materials, 39, (2005), 723-744.
[137] B. Cai, Y. Liu, C. Ren, Z. Liu, X. Tian, A. Abulimiti, Experimental study of galvanic corrosion behaviour of carbon fibre composite coupled to aluminium in artificial seawater, Corrosion Engineering, Science and Technology, 47, (2012), 289-296.
[138] N. Soohyun, L. Dongyoung, C. Ilbeom, L. Gil, Smart cure cycle for reducing the thermal residual stress of a co-cured E-glass/carbon/epoxy composite structure for a vanadium redox flow battery, Composite Structures, 120, (2015), 107-116.
[139] E. Frank, L.M. Steudle, D. Ingildeev, J.M. Spörl, M.R. Buchmeiser, Carbon fibers: precursor systems, processing, structure, and properties, Angewandte Chemie International Edition, 53(21), (2014), 5262-5298.
[140] A.L.-V. Centeno, R. Santamaría, M. Granda, R. Menéndez, C. Blanco, Thermal curing of mesophase pitch: An alternative to oxidative stabilisation for the development of carboŽ carbon composites, Journal of Analytical and Applied Pyrolysis, 86, (2009), 28-32.
[141] D.A. Baker, T.G. Rials, Recent advances in low-cost carbon fiber manufacture from lignin, Journal of Applied Polymer Science, 130(2), (2013), 713-728.
[142] N. Aliheidari, R. Tripuraneni, A. Ameli, S. Nadimpalli, Fracture resistance measurement of fused deposition modeling 3D printed polymers, Polymer Testing, 60, (2017), 94-101.

[143] C. Pascual-González, M. Iragi, A. Fernández, J.P. Fernández-Blázquez, L. Aretxabaleta, C.S. Lopes, An approach to analyse the factors behind the micromechanical response of 3D-printed composites, Composites Part B: Engineering, 186, (2020), 107820.
[144] ASTM C1557-20 Standard test method for tensile strength and Young's modulus of fibers, ASTM International, West Conshohocken, PA, 2020.
[145] K. Honjo, Fracture toughness of PAN-based carbon fibers estimated from strength-mirror size relation, Carbon, 41(5), (2003), 979-984.
[146] A. Imeri, I. Fidan, M. Allen, D.A. Wilson, S. Canfield, Fatigue analysis of the fiber reinforced additively manufactured objects, International Journal of Advanced Manufacturing Technology, 98(9), (2018), 2717-2724.
[147] C. Chen, X. Wang, F. Wang, T. Peng, Preparation and characterization of para-aramid fibers with the main chain containing heterocyclic units, Journal of Macromolecular Science, Part B: Physics, 59(2), (2020), 90-99.
[148] M. Herráez, A. Fernández, C.S. Lopes, C. González, Strength and toughness of structural fibres for composite material reinforcement, Philosophical Transactions of the Royal Society A: Mathematical, Physical and Engineering Sciences, 374(2071), (2016), 20150274.
[149] S. Ogihara, Y. Imafuku, R. Yamamoto, Y. Kogo, Direct evaluation of fracture toughness in a carbon fiber, 17th International Conferences on Composite Materials, 2009.
[150] I.M. De Rosa, C. Santulli, F. Sarasini, Acoustic emission for monitoring the mechanical behaviour of natural fibre composites: A literature review, Composites Part A: Applied Science and Manufacturing, 40(9), (2009), 1456-1469.
[151] J. Jefferson Andrew, V. Arumugam, D.J. Bull, H.N. Dhakal, Residual strength and damage characterization of repaired glass/epoxy composite laminates using A.E. and D.I.C, Composite Structures, 152, (2016), 124-139.
[152] C. Caneva, I.M. De Rosa, F. Sarasini, Monitoring of impacted aramid-reinforced composites by embedded PVDF acoustic emission sensors, Strain, 44(4), (2008), 308-316.
[153] S. Benmedakhene, M. Kenane, M.L. Benzeggagh, Initiation and growth of delamination in glass/epoxy composites subjected to static and dynamic loading by acoustic emission monitoring, Composites Science and Technology, 59(2), (1999), 201-208.
[154] I. Narisawa, T. Oba, An evaluation of acoustic emission from fibre-reinforced composites - Part 2 The application of acoustic emission techniques to aramid fibre-reinforced model composites, Journal of Materials Science, 20(12), (1985), 4527-4531.

[155] A. Bussiba, M. Kupiec, S. Ifergane, R. Piat, T. Böhlke, Damage evolution and fracture events sequence in various composites by acoustic emission technique, Composites Science and Technology, 68(5), (2008), 1144-1155.
[156] A. Marec, J.H. Thomas, R. El Guerjouma, Damage characterization of polymer-based composite materials: Multivariable analysis and wavelet transform for clustering acoustic emission data, Mechanical Systems and Signal Processing, 22(6), (2008), 1441-1464.
[157] Q.Q. Ni, K. Kurashiki, M. Iwamoto, AE technique for identification of micro failure modes in CFRP composites, Materials Science Research International, 7(1), (2001), 67-71.
[158] M. Giordano, A. Calabro, C. Esposito, A. D'Amore, L. Nicolais, An acoustic-emission characterization of the failure modes in polymer-composite materials, Composites Science and Technology, 58(12), (1998), 1923-1928.
[159] C. Grant, Automated processes for composite aircraft structure, Industrial Robot: An International Journal, 33, (2006), 117-121.
[160] P.K. Vallittu, Flexural properties of acrylic resin polymers reinforced with unidirectional and woven glass fibers, Journal of Prosthetic Dentistry, 81(3), (1999), 318-326.
[161] D.O.H. Adams, M.W. Hyer, Analysis of layer waviness in flat compression-loaded thermoplastic composite laminates, Journal of Engineering Materials and Technology, 118(1), (1996), 63-70.
[162] V. Dikshit, A.P. Nagalingam, G.D. Goh, S. Agarwala, W.Y. Yeong, J. Wei, Quasi-static indentation analysis on three-dimensional printed continuous-fiber sandwich composites, Journal of Sandwich Structures and Materials, 23(2), (2021), 385-404.
[163] H. Zhang, J. Chen, D. Yang, Fibre misalignment and breakage in 3D printing of continuous carbon fibre reinforced thermoplastic composites, Additive Manufacturing, 38, (2021), 101775.
[164] J. Galos, Y. Hu, A.R. Ravindran, R.B. Ladani, A.P. Mouritz, Electrical properties of 3D printed continuous carbon fibre composites made using the FDM process, Composites Part A: Applied Science and Manufacturing, 151, (2021), 106661.
[165] Material datasheet, REV 3.2. 2019 (Collected September 9th 2019).
[166] E.A. Papon, A. Haque, S.K. Spear, Effects of fiber surface treatment and nozzle geometry in structural properties of additively manufactured two-phase composites, AIAA SciTech Forum, 2019.
[167] C. Pascual-González, P. San Martín, I. Lizarralde, A. Fernández, A. León, C.S. Lopes, J.P. Fernández-Blázquez, Post-processing effects on microstructure, interlaminar and thermal

properties of 3D printed continuous carbon fibre composites, Composites Part B: Engineering, 210, (2021), 108652.
[168] ASTM D3171 Standard test methods for constituent content of composite materials, ASTM International, West Conshohocken, PA, 2015.
[169] ATSM D3039/D3039M Standard test method for tensile properties of polymer matrix composite materials, ASTM International, West Conshohocken, PA, 2008.
[170] S.D. McIvor, M.I. Darby, G.H. Wostenholm, B. Yates, L. Banfield, R. King, A. Webb, Thermal conductivity measurements of some glass fibre- and carbon fibre-reinforced plastics, Journal of Materials Science, 25(7), (1990), 3127-3132.
[171] M. Barucci, G. Bianchini, T. Del Rosso, E. Gottardi, I. Peroni, G. Ventura, Thermal expansion and thermal conductivity of glass-fibre reinforced nylon at low temperature, Cryogenics, 40(7), (2000), 465-467.
[172] G. Ventura, V. Martelli, Thermal conductivity of Kevlar 49 between 7 and 290 K, Cryogenics, 49(12), (2009), 735-737.
[173] O.A. Panina, A.S. Nemov, A.Y. Zobacheva, I.A. Kobykhno, O.V. Tolochko, V.K. Yadykin, Numerical analysis of mechanical behavior of unidirectional thermoplastic-based carbon fiber composite for 3D-printing, Materials Today: Proceedings, 30, (2020), 559-563.
[174] M. Mohammadizadeh, A. Imeri, I. Fidan, M. Elkelany, 3D printed fiber reinforced polymer composites - Structural analysis, Composites Part B: Engineering, 175, (2019), 107112.
[175] K. T., B. J., Selection of acoustic emissions and classification of damage mechanisms in fiber composite materials, Journal of Acoustic Emission, 16(1-4), (1998), S233-S242.
[176] P.J. de Groot, P.A.M. Wijnen, R.B.F. Janssen, Real-time frequency determination of acoustic emission for different fracture mechanisms in carbon/epoxy composites, Composites Science and Technology, 55(4), (1995), 405-412.
[177] K.W. Nam, S.H. Ahn, C.K. Moon, Fracture behavior of carbon fiber reinforced plastics determined by the time-frequency analysis method, Journal of Applied Polymer Science, 88(7), (2003), 1659-1664.
[178] S. Das, The cost of automotive polymer composites: a review and assessment of DOE's lightweight materials composites research, Oak Ridge National Laboratory, Oak Ridge, TN, USA, 2001.
[179] J. Galos, Thin-ply composite laminates: A review, Composite Structures, 236, (2020), 111920.

[180] M. Jalalvand, G. Czél, M.R. Wisnom, Parametric study of failure mechanisms and optimal configurations of pseudo-ductile thin-ply UD hybrid composites, Composites Part A: Applied Science and Manufacturing, 74, (2015), 123-131.
[181] D. Chen, Q. Luo, M. Meng, Q. Li, G. Sun, Low velocity impact behavior of interlayer hybrid composite laminates with carbon/glass/basalt fibres, Composites Part B: Engineering, 176, (2019), 107191.
[182] A.R. Bunsell, B. Harris, Hybrid carbon and glass fibre composites, Composites, 5(4), (1974), 157-164.
[183] G. Czél, M. Jalalvand, M.R. Wisnom, Design and characterisation of advanced pseudo-ductile unidirectional thin-ply carbon/epoxy–glass/epoxy hybrid composites, Composite Structures, 143, (2016), 362-370.
[184] J. Zhang, K. Chaisombat, S. He, C.H. Wang, Hybrid composite laminates reinforced with glass/carbon woven fabrics for lightweight load bearing structures, Materials & Design, 36, (2012), 75-80.
[185] M. Sayer, N.B. Bektaş, O. Sayman, An experimental investigation on the impact behavior of hybrid composite plates, Composite Structures, 92(5), (2010), 1256-1262.
[186] R. Park, J. Jang, Impact behavior of aramid fiber/glass fiber hybrid composite: Evaluation of four-layer hybrid composites, Journal of Materials Science, 36(9), (2001), 2359-2367.
[187] B.Z. Jang, L.C. Chen, C.Z. Wang, H.T. Lin, R.H. Zee, Impact resistance and energy absorption mechanisms in hybrid composites, Composites Science and Technology, 34(4), (1989), 305-335.
[188] Y. Peng, Y. Wu, S. Li, K. Wang, S. Yao, Z. Liu, H. Garmestani, Tailorable rigidity and energy-absorption capability of 3D printed continuous carbon fiber reinforced polyamide composites, Composites Science and Technology, 199, (2020), 108337.

Appendix A1

Publications

1. **Y. Hu**, R.B. Ladani, M. Brandt, Y. Li, A.P. Mouritz, "***Carbon fibre damage during 3D printing of polymer matrix laminates using the FDM process***", Materials & Design 205 (2021) 109679.

2. **Y. Hu**, Y. Li, B. Li, S. Shen, "***3D printed fibre-reinforced polymer composites—Review of the fused deposition modeling process and mechanical performance of products.***" [J]. Acta Materiae Compositae Sinica, 38(4) (2021) 979-996.

3. J. Galos, **Y. Hu**, A.R. Ravindran, R.B. Ladani, A.P. Mouritz, "***Electrical properties of 3D printed continuous carbon fibre composites made using the FDM process***", Composites Part A: Applied Science and Manufacturing 151 (2021) 106661.